CYCLIC STRESS EFFECT ON STRESS CORROSION CRACKING OF DUPLEX STAINLESS STEEL IN CHLORIDE AND CAUSTIC SOLUTIONS

A Dissertation

Presented to

The Academic Faculty

By

Di Yang

In Partial Fulfillment

Of the Requirements for the Degree

Doctor of Philosophy in the

School of Mechanical Engineering

Georgia Institute of Technology

December, 2011

CYCLIC STRESS EFFECT ON STRESS CORROSION CRACKING OF DUPLEX STAINLESS STEEL IN CHLORIDE AND CAUSTIC SOLUTIONS

Approved by:

Dr. Preet M. Singh, Advisor
School of Materials Science and Engineering
Georgia Institute of Technology

Dr. Richard W. Neu, Co-advisor
School of Mechanical Engineering and
Materials Science and Engineering
Georgia Institute of Technology

Dr. W. Steven Johnson
School of Mechanical Engineering and
Materials Science and Engineering
Georgia Institute of Technology

Dr. Naresh Thadhani
School of Mechanical Engineering and
Materials Science and Engineering
Georgia Institute of Technology

Dr. Hamid Garmestani
School of Materials Science and Engineering
Georgia Institute of Technology

Date Approved: October 7, 2011

ACKNOWLEDGEMENTS

TABLE OF CONTENTS

LIST OF TABLES

LIST OF FIGURES

XIII

SUMMARY

Duplex stainless steel (DSS) is a dual-phase material with approximately equal volume amount of austenite and ferrite. It has both great mechanical properties (good ductility and high tensile/fatigue strength) and excellent corrosion resistance due to the mixture of the two phases.

Cyclic loadings with high stress level and low frequency are experienced by many structures. However, the existing study on corrosion fatigue (CF) study of various metallic materials has mainly concentrated on relatively high frequency range. No systematic study has been done to understand the ultra-low frequency ($\sim 10^{-5}$ Hz) cyclic loading effect on stress corrosion cracking (SCC) of DSSs.

In this study, the ultra-low frequency cyclic loading effect on SCC of DSS 2205 was studied in acidified sodium chloride and caustic white liquor (WL) solutions. The research work focused on the environmental effect on SCC of DSS 2205, the cyclic stress effect on strain accumulation behavior of DSS 2205, and the combined environmental and cyclic stress effect on the stress corrosion crack initiation of DSS 2205 in the above environments.

Potentiodynamic polarization tests were performed to investigate the electrochemical behavior of DSS 2205 in acidic NaCl solution. Series of slow strain rate tests (SSRTs) at different applied potential values were conducted to reveal the optimum applied potential value for SCC to happen. Room temperature static and cyclic creep tests were performed in air to illustrate the strain accumulation effect of cyclic stresses. Test

results showed that cyclic loading could enhance strain accumulation in DSS 2205 compared to static loading. Moreover, the strain accumulation behavior of DSS 2205 was found to be controlled by the two phases of DSS 2205 with different crystal structures. The B.C.C. ferrite phase enhanced strain accumulation due to extensive cross-slips of the dislocations, whereas the F.C.C. austenite phase resisted strain accumulation due to cyclic strain hardening. Cyclic SSRTs were performed under the conditions that SCC occurs in sodium chloride and WL solutions. Test results show that cyclic stress facilitated crack initiations in DSS 2205. Stress corrosion cracks initiated from the intermetallic precipitates in acidic chloride environment, and the cracks initiated from austenite phase in WL environment. Cold-working has been found to retard the crack initiations induced by cyclic stresses.

CHAPTER 1 INTRODUCTION

1.1   Research Objective

The low frequency cyclic loadings can have an important effect on stress corrosion cracking (SCC) initiation and propagation in duplex stainless steels (DSSs). Cyclic stresses have been proved to induce creep deformation which could change the strain accumulation behavior of materials and the strain rate at the crack tip [1-5]. Therefore, cyclic loading will enable the SCC by promoting surface film rupture at the crack tip and assisting film breakdown to take place at an optimum strain rate. In addition, the dual phase microstructure of DSSs adds more complexity to this problem. The two phases of DSSs have different chemical compositions, mechanical properties, residual stresses, as well as SCC susceptibilities. Austenite phase is more susceptible to SCC in sulfide-containing caustic solutions, while ferrite phase undergoes preferential SCC initiation in acidified chloride environments.

However, prior published research has focused on relatively high frequency cyclic loading effects on SCC of DSSs. Since in the high frequency domain the creep effect is suppressed, the effects of high frequency cyclic loading (HFCL) are expected to be different than those of very low frequency cyclic loading (LFCL). Hence, the effects of very low frequency cyclic loading on SCC of DSSs remain unknown. On the other hand, since cold-working is known to reduce the subsequent strain accumulation and causes a

decrease in strain rate, it is also important to investigate the effects of cold-working on SCC of DSSs with and without cyclic loading.

The primary objective of this research is to investigate the very low frequency ($\sim 10^{-5}$ Hz) cyclic stress effects on stress corrosion crack initiation of DSS 2205 in acidic NaCl and caustic white liquor (WL) solutions, as well as the cold-working effects on the stress corrosion crack initiation behavior of DSSs.

1.2   Overall Approach

In order to achieve this primary objective of studying the very low frequency cyclic stress effects on stress corrosion crack initiation of as-received and cold-worked DSS 2205 in acidic NaCl and caustic WL environments, a few tasks were identified for this study, as shown in FIGURE 1.1, as well as the experimental methods used for each task.

The environmental effect on SCC, cyclic stress effect on strain accumulation and the combined environmental and cyclic stress effect on SCC of DSS 2205 have been studied. This dissertation is structured according to the flow chart of FIGURE 1.1.
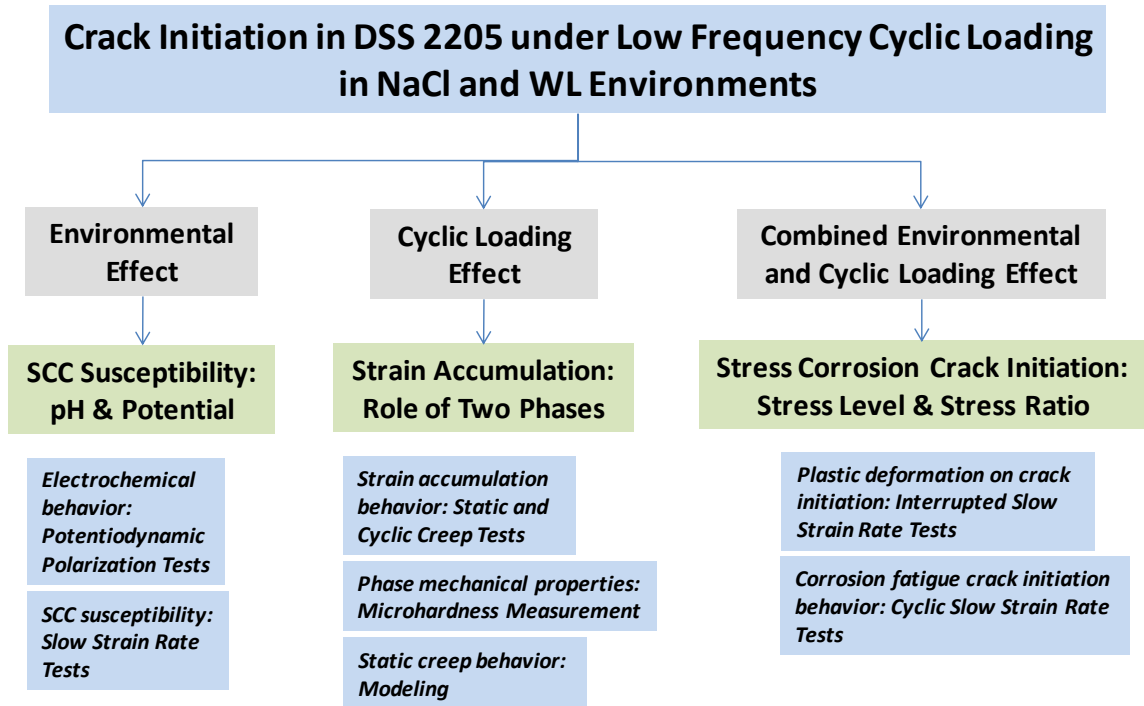
FIGURE 1.1 Flow chart showing the subtopics of this study and the corresponding experimental techniques employed in this study.

CHAPTER 2 introduces the background information and literature review that are relevant to this study.

CHAPTER 3 introduces the experimental techniques and procedures employed in this study.

In CHAPTER 4, the environmental effect is discussed. The results in this chapter help us understand the electrochemical behavior of DSS 2205 in the selected acidic NaCl and caustic WL solutions. The pH and potential effect on SCC susceptibility of DSS 2205 is

discussed. Moreover, the cold-working effect on SCC of DSS 2205 in the two corrosive environments is illustrated as well.

In CHAPTER 5, the cyclic stress effect on strain accumulation behavior of DSS 2205 is evaluated, focusing on the role of the individual phases in this process.

In CHAPTER 6, the results of cyclic slow strain rate tests (SSRT) will be discussed. The crack initiation behavior of DSS 2205 in both acidic chloride and caustic WL environments will be characterized, and the effect of cyclic loading parameters, i.e., maximum stress level and stress ratio, on the crack initiation process is quantified and discussed.

In CHAPTER 7, the results and mechanisms of cyclic stress effect on SCC of DSS 2205 in the two environments are summarized and illustrated by three schematic drawings.

CHAPTER 8 discusses the practical impacts of this study and the recommendations on engineering practice based on the results of this study.

CHAPTER 2 BACKGROUND

2.1 Duplex Stainless Steel

Duplex Stainless Steels (DSSs) are dual phase metallic materials. They are composed of approximately equal volume amount of austenitic (γ) phase and ferritic (α) phase. FIGURE 2.1 shows the microstructures of DSS 2205 in both rolling and transverse directions. The darker phase in the pictures is ferrite, and the lighter phase is austenite. In the manufacturing process of DSSs, the materials are hot-rolled, therefore the phases are elongated in the rolling direction. Due to the different crystal structures of the two phases, austenite (F.C.C.) has very good formability and toughness, while ferrite phase (B.C.C.) has very high tensile and fatigue strength. DSSs usually combine the beneficial properties of the two phases. They exhibit superior mechanical properties and high corrosion resistance as compared to other grades, such as carbon steels and austenitic stainless steels.
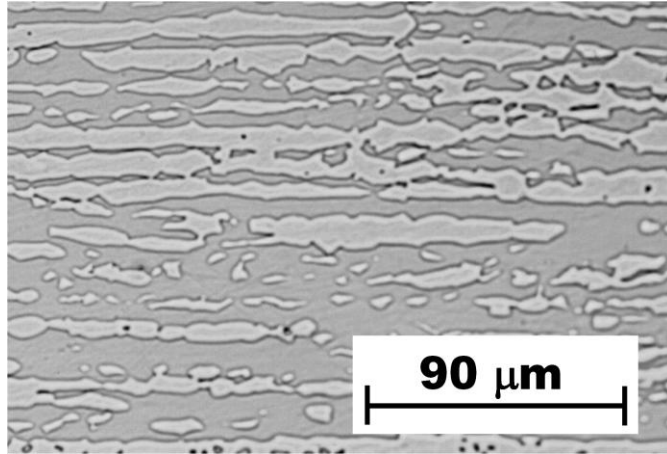
(a)
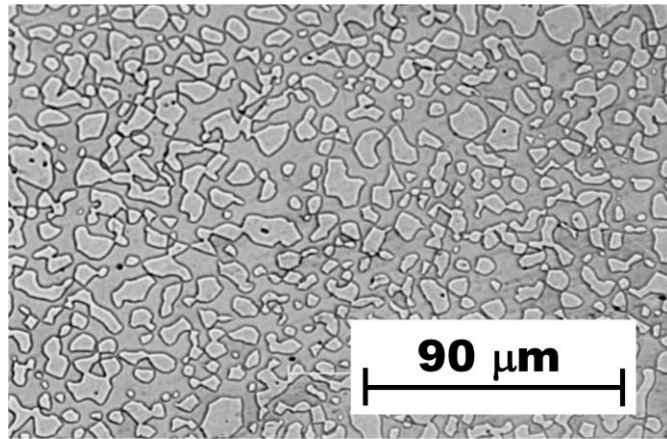
(b)

FIGURE 2.1 Microstructure pictures of DSS 2205 (a) rolling direction (b) transverse

direction.

The major alloying elements of DSSs can be grouped as ferrite stabilizers (such as

chromium, molybdenum, and silicon) and austenite stabilizers (such as nickel,

manganese, and nitrogen). Schaeffler diagram in FIGURE 2.2 illustrates the relationship between chemical compositions and crystal structures of alloys. When the chromium equivalent number (Cr_{eq}) is high and nickel equivalent number (Ni_{eq}) is low, the crystal structure will be B.C.C. ferrite. On the other hand, when the chromium equivalent number is low and nickel equivalent number is high, the crystal structure will be F.C.C. austenite. DSSs have medium Cr_{eq} and Ni_{eq}, so they are in between of austenite and ferrite in Schaeffler diagram and are mixtures of austenite and ferrite.

FIGURE 2.2 Schaeffler diagram. [6]

The typical chemical compositions and mechanical properties of a few duplex grades as well as some traditional stainless steels are summarized in TABLE 2.1. From comparison, DSSs have a higher Cr content but a lower Ni content than austenitic stainless steels (304L, 316L). In terms of mechanical properties, duplex grades have much higher yield and tensile strengths. For example, the yield strength of super DSS 2750 is twice of that of 304L.What makes DSSs more attractive is that they still retain a very good ductility while possessing a high strength. DSS have a ductility of about 35%, which is quite large considering the high strength they have.

TABLE 2.1 Summary of chemical compositions and mechanical properties of various stainless steels. [7]

UNS	Chemical Compositions (wt.%)						Mechanical Properties		
	C	N	Cr	Ni	Mo	Others	Yield Strength (MPa)	Tensile Strength (MPa)	Elongation (%)
304L	0.02	--	18.1	8.1	--	--	280	580	55
316L	0.02	--	17.2	10.1	2.1	--	280	570	55
430	0.04	--	16.5	--	--	--	380	520	25
S32101	0.03	0.22	21.5	1.5	0.3	5Mn	480	700	38
S32304	0.02	0.10	23	4.8	0.3	--	450	670	40
S82441	0.02	0.27	24	3.6	1.6	3Mn	480	680	33
S32205	0.02	0.17	22	5.7	3.1	--	510	750	35
S32760	0.02	0.27	25.4	6.9	3.8	W, Cu	540	830	35
S32750	0.02	0.27	25	7	4	--	560	830	35

DSSs provide a wide range of corrosion resistance to various environments. The resistance to chloride pitting and crevice corrosion increases with the content of chromium, molybdenum and nitrogen. Hence this resistance could be evaluated by the pitting resistance equivalent number (PREN), which is calculated by

$$PREN = wt.\% \, Cr + 3.3 \, (wt.\% \, Mo) + \, 16 \, (wt.\% \, N)$$

The PREN values of a number of duplex and austenitic stainless steel grades are listed in TABLE 2.2, which shows all duplex grades have larger PREN values than austenitic grades.

TABLE 2.2 PREN values for different austenitic and duplex grades.

Steel Grade	PREN
304L	18
316L	24
S32101	26
S32304	26
S82441	33
SS32205	35
S31254	43
S32750	43

Other than the pitting corrosion resistance, DSSs also show better stress corrosion cracking (SCC) resistance than austenitic stainless steels. TABLE 2.3 illustrates that under many of the conditions austenitic grades are susceptible to SCC, DSSs are expected to be immune to SCC. However, it is worth noting that SCC still can be a problem when the combination of the environmental parameters is right. SCC of DSSs will be discussed in Section 2.2.

TABLE 2.3 Comparative SCC Resistance of Unwelded Duplex and Austenitic Stainless Steels in Accelerated Laboratory Tests (various literature sources)*. [8]

Grade	42% MgCl$_2$ boiling 154°C U-bend	35% MgCl$_2$ boiling 125°C U-bend	Drop Evap. 0.1M NaCl 120°C 0.9xY.S.	Wick Test 1500 ppm Cl as NaCl 100°C	33% LiCl$_2$ boiling 120°C U-bend	40% CaCl$_2$ 100°C 0.9xY.S.	25-28% NaCl boiling 106°C U-bend	26% NaCl auto-clave 155°C U-bend	26% NaCl auto-clave 200°C U-bend	600 ppm Cl(NaCl) auto-clave 300°C U-bend	100 ppm Cl(sea salt+0$_2$) auto-clave 230°C U-bend
Type 304L Type 316L											
3RE60											
S32101 S32202											
2205											
25 Cr Duplex											
Superduplex											

Cracking anticipated   Cracking possible   Cracking not anticipated   Insufficient data

DSSs are widely used as structural steels in oil and gas, chemical industry, pulp and paper industry, water systems, desalination plants and nuclear industries. Among all of the DSS grades, the standard grade DSS 2205 is the one that balances the cost and the properties of the material best. Hence most of the duplex grades in services are DSS 2205 hot rolled products. As we mentioned earlier, many of the applications concern highly corrosive environments, such as chemical, chemical tankers, petrochemical, off-shore, pulp and paper industry and sea-water applications). In these applications, DSS 2205 have always been very competitive compared to austenitic stainless steels due to their reduced nickel content and better mechanical properties which make it possible to reduce the thickness of structures. Super DSS grades represent about 10% of total DSS productions and are designed to replace 6Mo austenitic stainless steels in the most severe corrosive applications. Lean DSSs including DSS 2304 and DSS 2101 contribute to slightly more than 10% of the total DSS productions. The lean DSSs are expected to replace austenitic grades 304/316 in volume markets [9]. The production and use of DSS 2205 has a growth of more than 100% in the last decade, as shown in FIGURE 2.3.
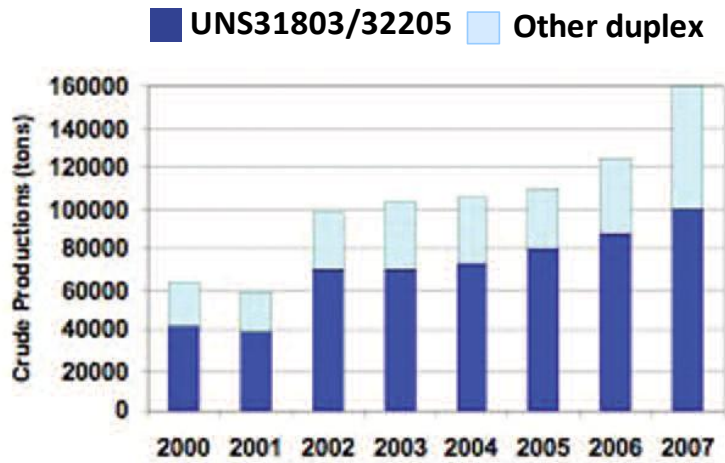
FIGURE 2.3 DSS productions from 2000 to 2007. [9]

2.2   SCC

2.2.1   Definition of SCC

SCC is the brittle failure at a relatively low constant tensile stress of an alloy exposed to a corrosive environment, which means it often leads to sudden brittle fracture of a usually ductile material. SCC is the cracking induced by the combined effects of a tensile stress and a corrosive environment. Generally, SCC is considered to occur when three conditions present simultaneously: a corrosive environment, a tensile stress and a susceptible alloy (FIGURE 2.4).
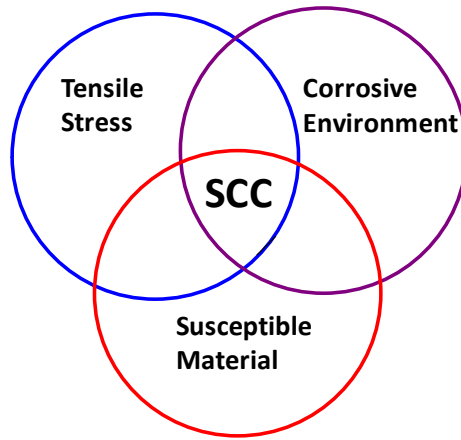
FIGURE 2.4 Three factors that will result in SCC.

Therefore, factors affecting SCC include: material factors such as alloy composition, microstructure, and secondary phases; stress factors such as magnitude of the tensile stress or stress intensity factor, residual stress, and stress state; environmental factors like temperature, pressure, pH, and electrochemical potential.

One characteristic of SCC is its potential dependence. SCC occurs for systems (combination of a susceptible material and a corrosive environment) exhibiting an active-passive transition region in polarization curves. Even for the same system, SCC only happens at certain potential ranges. In FIGURE 2.5, the potential regions where SCC occurs are labeled as zone 1 and zone 2. In zone 1, SCC and pitting are associated in adjacent or overlapping potential ranges. In zone 2, far from the pitting potential range, SCC occurs where the passive film is relatively weak at active potential barely adequate to form the passive film.
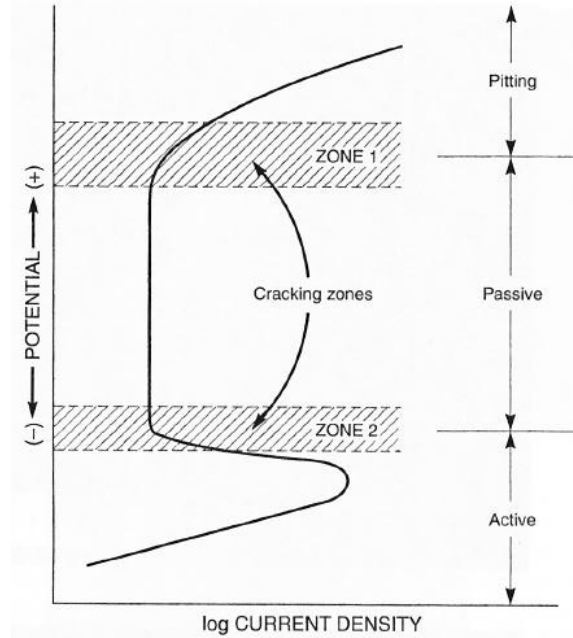
FIGURE 2.5 Schematic anodic polarization curve showing potential zones SCC

frequently occurs. [10]

The passivity of materials can be influenced not only by potential, but also other factors such as pH and concentration of species in solution. Pourbaix diagram is an effective way of showing the metal surface passive film state at various potential and pH values. For example, the Pourbaix diagram of iron superimposed on chromium is illustrated in FIGURE 2.6. At low potential range, Fe is immune to corrosion. At medium potential range, Fe is susceptible to uniform corrosion at lower pH values, but the surface will form Fe_3O_4 at higher pH values. When the potential is further increased, the surface film will change from Fe_3O_4 to Fe_2O_3.
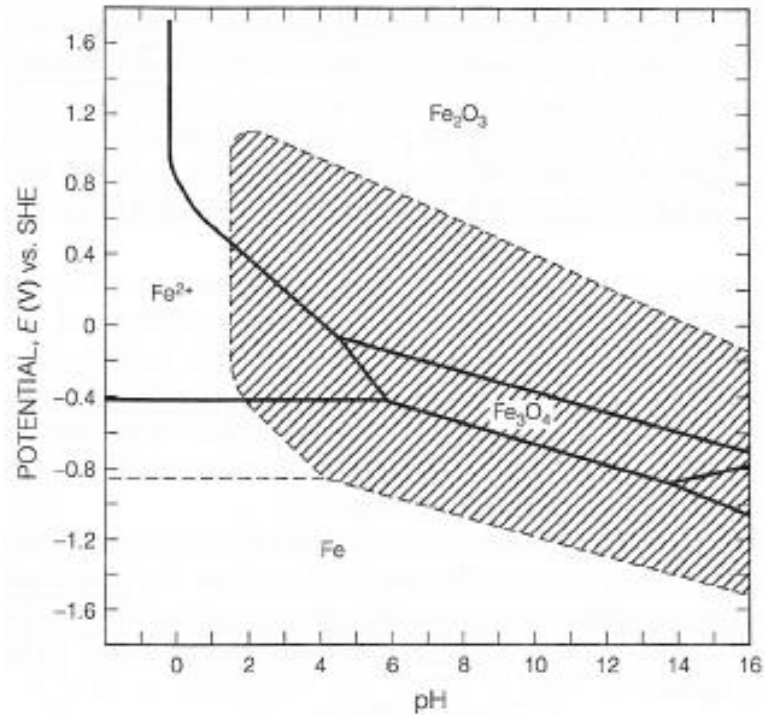
FIGURE 2.6 Pourbaix diagram for iron superimposed on the diagram for chromium designated by dashed lines. Shaded area indicates stability of Cr_2O_3. Approximately unit activity assumed for dissolved species. [11]

2.2.2 Classification of SCC

There are two types of SCC: transgranular SCC and intergranular SCC. In transgranular SCC, cracks propagate through the grains, while in intergranular SCC, cracks grows along the grain boundaries, as shown in FIGURE 2.7. Moreover, besides crack morphology, the fracture surfaces of the two kinds of SCC look different as well (FIGURE 2.8).
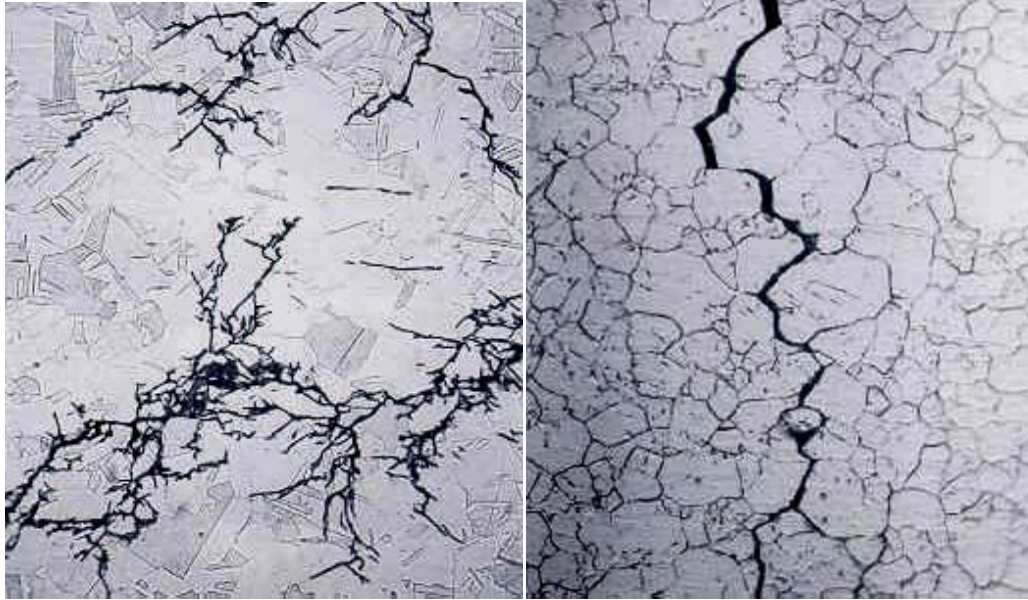
FIGURE 2.7 Metallographic of SCC: (a) Transgranular SCC (b) Intergranular SCC. [12]
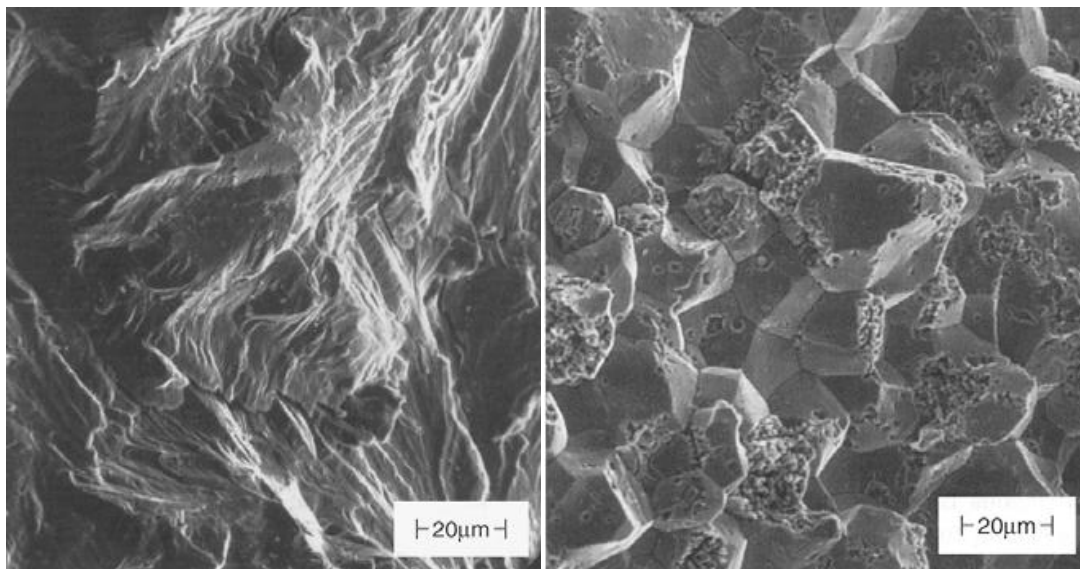
FIGURE 2.8 Fractures surfaces by scanning electron microscopy of (a) transgranular SCC of austenitic stainless steel in hot chloride solution and (b) intergranular SCC of carbon steel in hot nitrate solution, surface cleaned with inhibited HCl. [11]

2.2.3   Mechanisms of SCC

SCC is one type of localized corrosion, which implies that the initiation of SCC are always associated with some localized surface features or surface discontinuities of the material, such as inclusions, grain boundaries, slip bands, corrosion pits and most importantly the rupture sites of protective surface film. Most of the existing SCC mechanisms are concerned about the propagation process, because the crack initiations are relatively difficult to measure and crack initiation has not been precisely defined. For example, it is difficult to define at what point a pit becomes a small crack. Another example is the boundary between intergranular corrosion to intergranular SCC is actually a grey area. In any of the crack initiation studies, researchers are required to define the specific crack length ranges for crack initiations by themselves.

On the other hand, numerous mechanisms have been proposed for SCC propagation process of various systems. Generally speaking, there are two types of models: dissolution models and mechanical fracture models. In dissolution models, crack advances by preferential dissolution at the crack tip. Slip-dissolution model is essentially the most important dissolution model. In mechanical fracture models, stress concentration at the crack root is assumed to be increased to the point of ductile deformation and fracture [13]. Models such as corrosion tunnel model, adsorption enhanced plasticity model, tarnish-rupture model, film induced cleavage model, and localized surface plasticity model are examples of mechanical fracture models. Some people also consider hydrogen embrittlement as one mechanism of mechanical fracture

SCC models. In the following section, only those receiving the greatest current attention and the ones that might be relevant to this study are discussed.

2.2.3.1 Dissolution Mechanisms

2.2.3.1.1 Slip-Dissolution Model

Slip-dissolution model is a relatively mature model, and it has been used to rationalize the kinetics of SCC in many systems [14-18]. It was proposed independently by Champion and Logan [19, 20]. R.N. Parkins has successfully demonstrated a correlation between the crack propagation rate and the current density on a straining electrode surface, as shown in FIGURE 2.9. In this mechanism, fresh metal is assumed to be exposed to the corrosive environment at an emerging slip band, and then the crack grows by anodic dissolution of the unfilmed surface at the rupture site. FIGURE 2.10 is a schematic drawing of the crack propagation by slip-dissolution model. Slip-dissolution model is also referred to as the film rupture model.
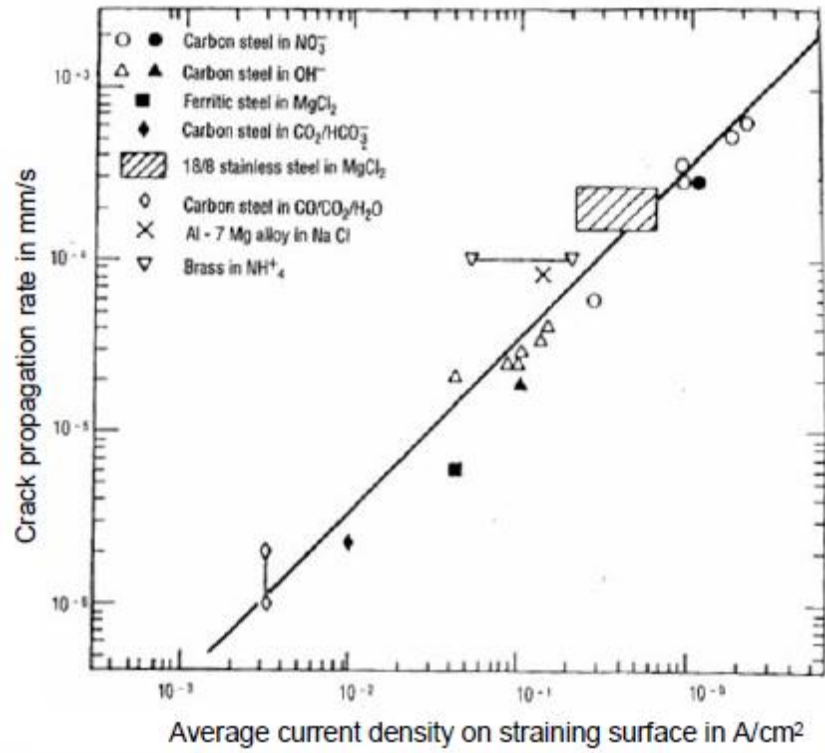
FIGURE 2.9 Correlation between crack growth rate and anodic dissolution current at straining electrode surfaces. [21]
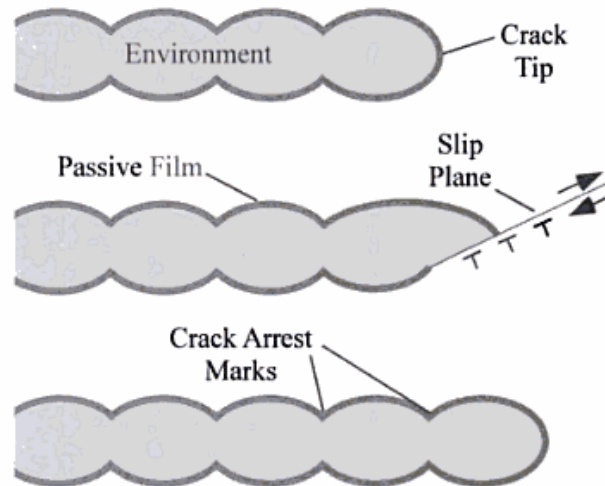
FIGURE 2.10 Schematic representation of crack propagation by slip-dissolution model.

2.2.3.2 Mechanical Fracture Mechanisms

2.2.3.2.1 Corrosion Tunnel Model

In corrosion tunnel model, it is assumed that a small array of tunnels are formed by active corrosion at emerging slip steps, then the small tunnels grow in length and width until the undissolved parts between them are fractured by ductile overload. Thus, the crack propagates by the alternating tunnel growth and ductile fracture, as shown in FIGURE 2.11. Crack propagating by this mechanism will show a grooved fracture surfaces with ductile fracture features on the peaks of the grooves [22].
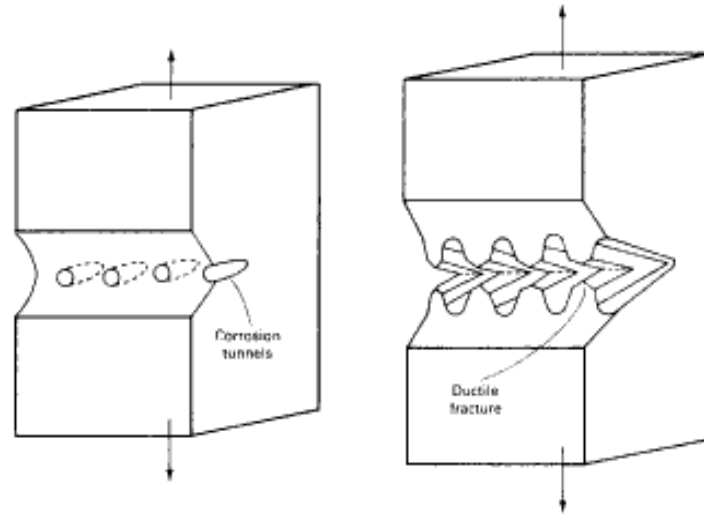
FIGURE 2.11 Schematic representation of crack propagation by corrosion tunnel model.

[23]

2.2.3.2.2   Film Induced Cleavage Model

The film induced cleavage model assumes that there is a brittle film forms on the crack tip and the crack wall. This model was proposed by Sieradzki and Newman in 1980s [24, 25]. When the stress at the crack tip breaks the brittle film because of stress concentration, if the velocity is sufficient the crack could penetrate into the ductile base metal, as shown in FIGURE 2.12. The film induced cleavage mechanism was proposed to explain the discontinuous transgranular crack growth and high transgranular crack growth rates. In this case, the anodic reaction at the crack tip does not necessarily propagate the crack, but it is required to produce the brittle surface film.
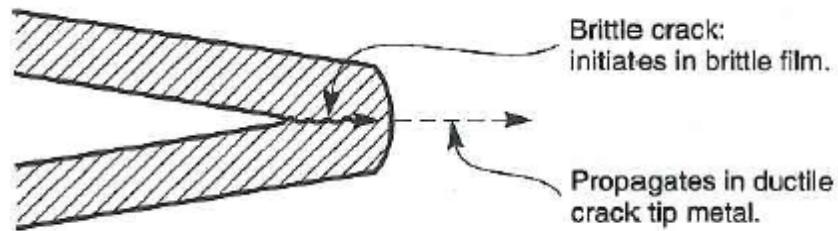
FIGURE 2.12 Schematic representation of crack propagation by film induced cleavage model. [11]

2.2.3.2.3   Hydrogen Embrittlement

It is a popular opinion that the brittle nature of SCC must be associated with a mechanism controlled by hydrogen induced cracking, which shares a similar brittle cleavage-like feature with SCC. Hydrogen embrittlement is characterized by a brittle fracture of a normally ductile alloy under sustained load in the presence of hydrogen. Most of the hydrogen induced cracking theories are based on the proposal about stress-induced diffusion of hydrogen to the region of high stress triaxiality in the metal matrix ahead of a plastically-strained notch or crack [26-29]. The sources of hydrogen can be

a) The hydrogen encountered in the manufacturing process, such as welding, electroplating, and phosphating.

b) The use of cathodic protection for corrosion protection.

c) The hydrogen generated by water or acid reduction as the cathodic reaction of a corrosion reaction:

$$H_2O + e^- \rightarrow H + OH^-$$

$$H^+ + e^- \rightarrow H$$
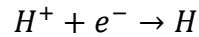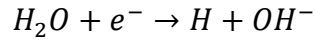
The cracking in hydrogen embrittlement could be transgranular or intergranular, and the cracks usually have sharp tips and minor branching. Although hydrogen embrittlement is a theory that has been extensively studied and used to explain various SCC failures, the mechanism have remained unclear. Several different mechanisms have been proposed, and they are each supported by different sets of experiments, but none of them is able to explain all experimental results. The most common and simple mechanism is that the brittle fracture is caused by the penetration and diffusion of atomic hydrogen into the crystal structure of the crack tip material (FIGURE 2.13). Then the inter-atomic bonds in that region are weakened.
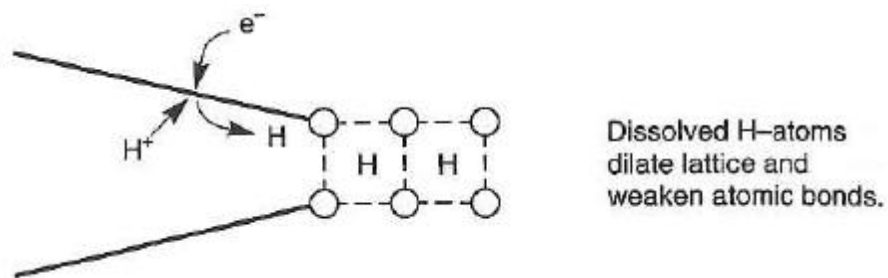
FIGURE 2.13 Schematic representation of crack propagation by hydrogen embrittlement. [11]

Hydrogen embrittlement can be reversed if the material is baked at elevated temperatures, because during this process, the hydrogen could be removed from the material. FIGURE 2.14 shows some results illustrating the effects of this process. Hydrogen embrittlement does not affect all materials equally. High strength steel, aluminum alloys, and titanium alloys are more susceptible to hydrogen embrittlement.
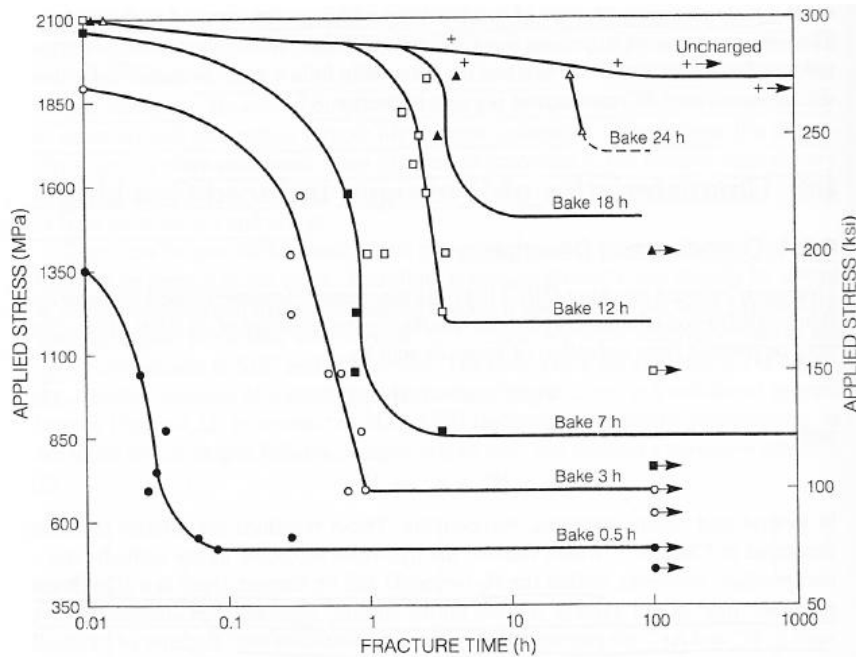
FIGURE 2.14 Fracture of AISI 4340 steel backed at 150°C after initial cathodic hydrogen charging. [30]

2.2.3.2.4   Adsorption Induced Cleavage Model

Adsorption induced cleavage model suggests that the adsorption of selective anions in the solution at the crack tip may lower the inter-atomic bond strength of the base metal, which will lead to a reduction of the stress required to cause a brittle failure, as FIGURE 2.15 illustrated. Potential effect and effects of inhibitor species could be easily explained by this model. However, there are many arguments against this mechanism. A main assumption of this theory is that specific aggressive dissolved species adsorb at "mobile defect sites" [31]. However, the nature and character of such defects have not been specified, and there was no explanation about why some adsorbed species inhibit while others promote SCC.

Adsorption of A
weakens crack tip
bonds.
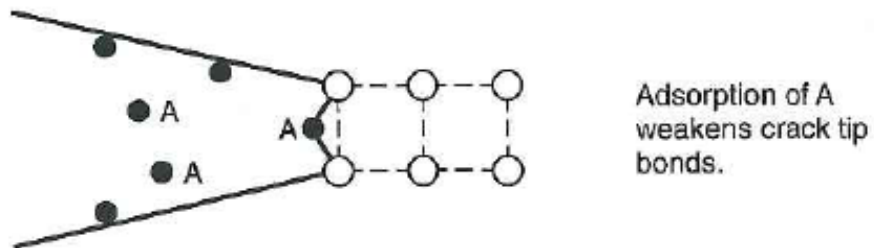
FIGURE 2.15 Schematic representation of adsorption induced cleavage model. [11]

2.2.3.2.5   Localized Surface Plasticity Model

Localized surface plasticity model assumes film rupture initiates large anodic currents

which will produce a softened defect structure at the rupture site by galvanic coupling

of the unfilmed active surface to surrounding noble passive surfaces. Then the following

deformation can only propagate a brittle crack, because the softened crack tip area is

constrained by the surrounding material, and the microstrain within the softened, yet

constrained, crack tip volume produces a triaxial stress state (plane-strain condition),

which suppresses plastic slip [11]. FIGURE 2.16 is a schematic drawing of the localized

surface plasticity SCC mechanism.
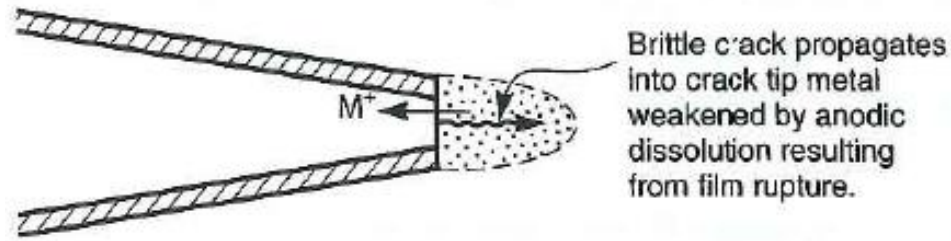
FIGURE 2.16 Schematic representation of crack propagation by localized surface

plasticity model. [11]

2.2.4   SCC of DSSs

SCC of DSSs have been studied in many different environments, such as chloride

solutions [32-43], pure caustic and sulfide-containing caustic solutions [44-50], hydrogen

sulfide environment [40, 51-53], and so on. Various aspects of SCC for DSSs have been investigated by researchers. For instance, the electrochemical behavior of DSS during SCC [35, 42, 45, 47], the material compositional effects [36, 38], material heat treatment effects [39], and environmental effects including potential and electrolyte chemistry effects [32-34, 37, 42, 43].

One of the aspects quite unique for DSSs is the effect of the two phases on SCC under different conditions. It was pointed out in Section 2.2.4 that the two phases of DSSs show different SCC behavior due to the different chemical compositions, crystal structures, residual stresses, and mechanical properties such as yield strength, hardness and ductility. Typical chemical compositions for the two phases are listed in TABLE 2.4, featuring a higher Cr and Mo content in ferrite phase, and a higher Ni and Mn content in austenite phase. As mentioned earlier, the alloying elements in DSSs are not equally distributed in two phases. They serve as stabilizers for either of these phases, as indicated by Schaeffler diagram (FIGURE 2.2).

TABLE 2.4 Composition of the major alloying elements of austenite and ferrite phases in DSS 2205 (wt.%). Results are obtained by EDS. [43]

Element	Fe	Cr	Ni	Mo	Mn
γ phase	69.5	20.4	7.2	1.2	1.7
α phase	68.7	23.5	4.9	2.1	0.8

As a result, it is not surprising to find that austenite phase and ferrite phase have different SCC susceptibility under certain conditions. Tsai and his coworkers have done extensive research on the SCC behavior of DSS 2205 in concentrated chloride-containing solutions [33-36, 43]. Their results revealed a strong potential-dependent SCC behavior of DSS 2205. Based on the results of the potentiodynamic polarization tests and a series of slow strain rate tests (SSRTs), they obtained the potential range within which DSS 2205 is susceptible to SCC in acidified concentrated NaCl solutions at room temperature [34]. Cracking below the primary fracture surface of the sample showed ferrite is more susceptible to SCC than austenite under this condition, as illustrated by FIGURE 2.17. Similarly, selective dissolution of the ferrite phase was also observed under SCC in concentrated NaCl [33] and concentrated $CaCl_2$ solutions [36] at elevated temperatures. FIGURE 2.18 is a micrograph showing the degradation of ferrite phase in $CaCl_2$ solution, leaving austenite phase un-attacked. Tsai and his co-workers explained the preferential dissolution of ferrite phase using the potential difference between the two phases of DSSs. It was found that the potential of ferrite phase was active than austenite phase in DSSs when exposed to H_2SO_4 solution containing either NaCl or HCl [43, 54, 55]. Therefore, near open circuit potential, selective dissolution could happen to the active or less noble phase (in this case, ferrite phase) when the material is being stressed. This localized attack could lead to initiation of SCC in ferrite phase.

FIGURE 2.17 Micrograph of DSS 2205 after testing in 26 wt.% NaCl solution of pH = 2 and at -400 mV (SCE). [34]
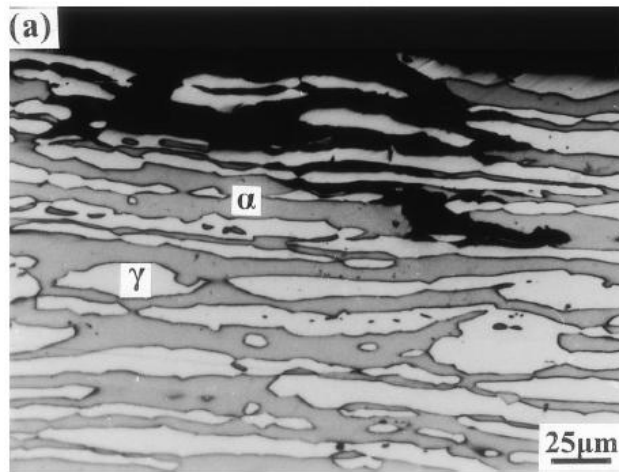
FIGURE 2.18 Selective dissolution of ferrite phase in 40 wt.% $CaCl_2$ solution at 100°C. [36]

On the contrary, in sulfide-containing caustic solutions, austenite phase has been found

to be more susceptible to SCC [44, 50], as shown in FIGURE 2.19. This preferential SCC

attack of the austenite phase was explained by the residual stress state of DSSs, namely,

tensile residual stresses in austenite phase and compressive residual stresses in ferrite

phase [56]. As a result, the tensile residual stresses would promote SCC initiation in

austenite phase through slip-dissolution mechanism, because the slip bands will emerge

in austenite phase more easily [57]. More details about residual stresses of DSSs will be

discussed in the following section.
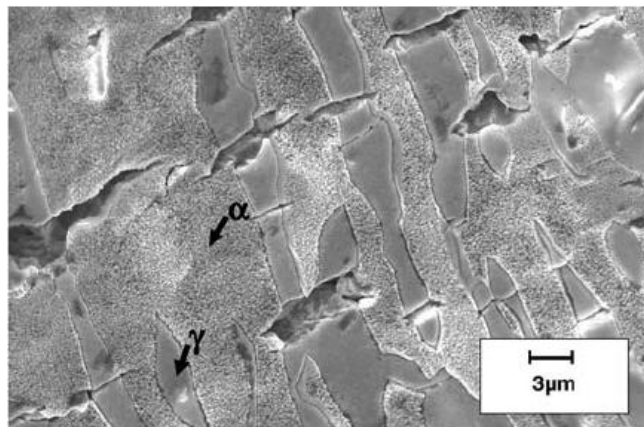
FIGURE 2.19 SEM image of DSS 2205 sample surface after SSRTs in sulfide-containing

caustic solution at 170°C, showing cracks initiating in austenite phase. [50]

2.3 Corrosion Fatigue

2.3.1 Definition and Characteristics

Corrosion fatigue (CF) is defined as the phenomenon of cracking (include both initiation and propagation) in materials under the combined actions of a fluctuating (or cyclic) stress and a corrosive (deleterious) environment [58]. By definition, CF only differs from SCC by the fact that the stresses are no longer static, but cyclic. Similarly to SCC, CF is also influenced by various mechanical, electrochemical and microstructural parameters. There actually exists a very important difference between CF and SCC. That is, the combinations of corrosive environment and susceptible material are not specific [59]. The reason of that will be illustrated by the mechanisms of CF crack initiation.

2.3.2 Mechanisms of CF

Fatigue process can be divided into crack initiation and crack propagation, and so is CF. To summarize the existing CF studies, the crack propagation research has focused on the mechanical aspects, while the crack initiation studies were mainly trying to understand the physics behind the process. In this section, only the mechanisms for CF crack initiation will be discussed, considering the aim of this research work.

Fatigue crack initiation in air is often associated with the intrusions and extrusions causing by the persistent slip bands (PSB). During this process, there are basically two ways that the corrosion process could affect the fatigue crack initiations:

i.   The corrosive environment could preferentially attack the intrusions and extrusions by active dissolution under active corrosion conditions. FIGURE 2.20 shows an example of this mechanism for copper tested in air and NaCl. After a same number of cycles, the crack initiation in NaCl was found to be much larger than the one in air.
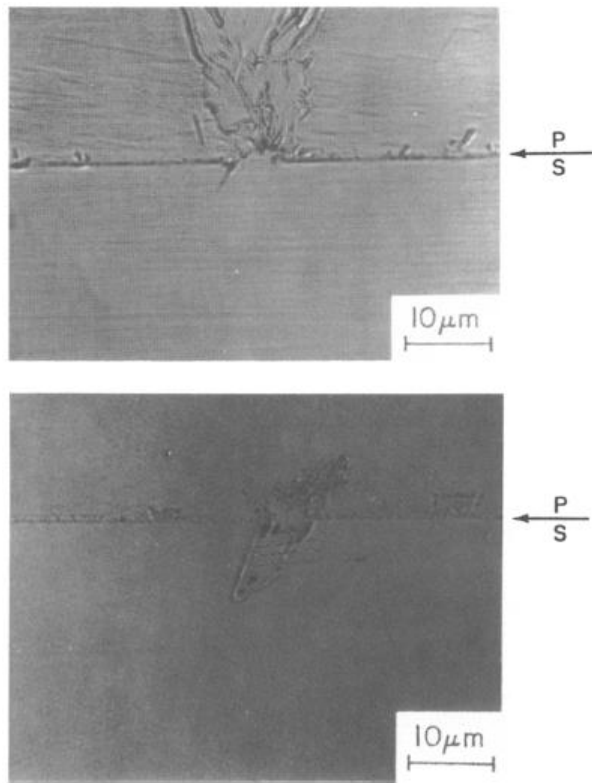
FIGURE 2.20 Cross sections through single crystals of copper after cyclic stressing showing (a) an extrusion and associated crack in air (b) the preferential attack of an extrusion and associated crack in NaCl at an applied anodic current of 100 µA/cm². P indicates copper plate applied after testing to preserve specimen edge and S represents the sample. [60]

ii.   The active dissolution process also alters the distribution and the shape of

PSBs. Research done by Hahn and Duquette [61, 62] have shown that for

both polycrystals and single crystals of pure copper, the number of PSBs was

significantly increased by active dissolution, and the height and breadth of

the bands were enhanced as well (FIGURE 2.21).
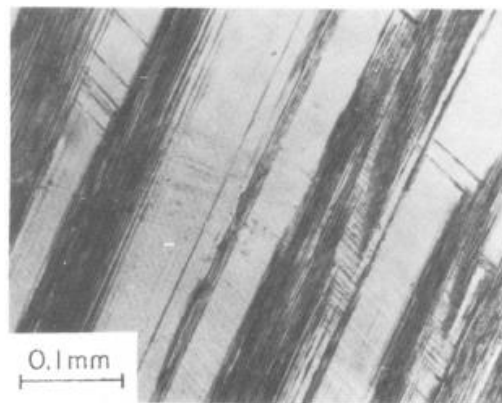
(a)
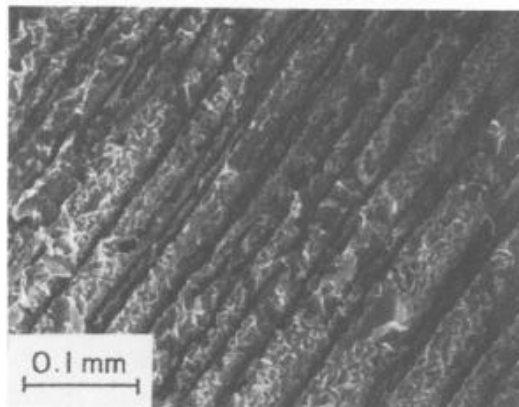
(b)

FIGURE 2.21 Surface slip offsets in single crystals of copper at 90% of fatigue life (a) air

(b) 0.5N NaCl at an applied current density of 100 μA/cm^2. [60]

Since pure metals are not immune to uniform corrosion, they can be attacked by CF, considering the extrusion/intrusion and anodic dissolution induced crack initiation. This is contrary to their observed resistance to SCC, and explained why CF does not require specific combinations of material and corrosive environment [63].

Although in most cases, fatigue crack initiations are accelerated by corrosion processes, there are exceptions. For example, if corrosion rates are sufficiently rapid, crack initiation sites are removed by corrosion, and the crack initiation is retarded [64]. Lo and Tsai [65] found similar effect of anodic dissolution on fatigue of DSS 2205. They found in 2 M H_2SO_4 + 0.7 M HCl aqueous solution, at applied potential -300 mV (SCE) crack initiated in austenite phase, because the slip bands generated in ferrite phase was smoothed out by fast selective dissolution.

2.3.3   Effect of Loading Parameters

Like fatigue in air, CF is also affected by loading parameters such as stress level and stress frequency. Stress level effect on CF is similar to fatigue in air, namely, CF life increases with decreasing of stress level. FIGURE 2.22 shows the S-N curves of AISI 4140 steel in air and NaCl solutions, demonstrating the effect of stress levels on CF.
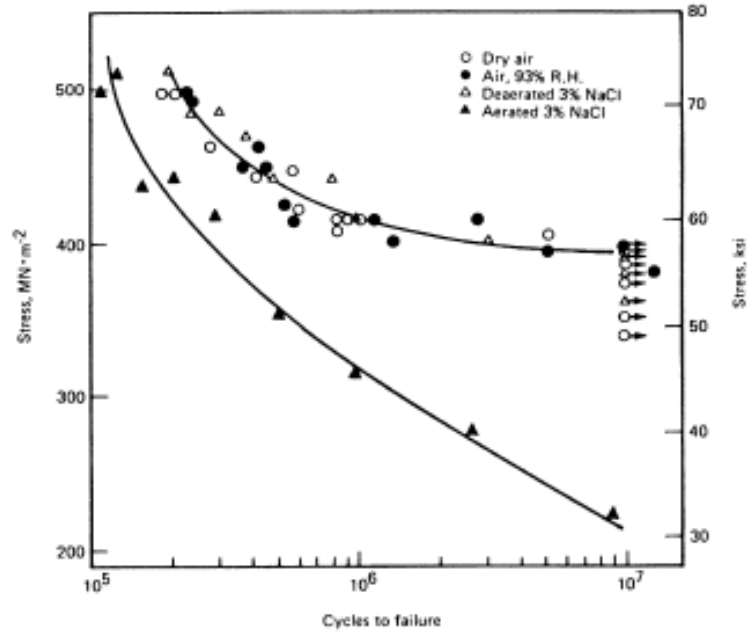
FIGURE 2.22 The deleterious effect of aerated aqueous chloride solution on the HCF life of smooth specimens of tempered martensitic AISI 4140 steel. Symbols with horizontal arrows indicate that CF failure has not occurred after 107 load cycles. [66]

Frequency effects on CF crack propagation have been characterized broadly and modeled based on the hydrogen embrittlement and film rupture mechanisms [67-72]. The general effect of frequency on CF is illustrated in FIGURE 2.23. With decreasing of frequency or strain rate, the CF life also decreases. The reason is that the rate of corrosion damage is limited by the mass transport and electrochemical reaction rate, and environmental cracking may not occur during unloading [67]. The higher the frequency, the shorter the loading time of each cycle, which means there is no sufficient time for the corrosion damage to occur. However, as can be seen in FIGURE 2.23, there

is no CF data available below strain rate of 10^{-5} s^{-1}. This is attributed to the challenge of prolonged test time.
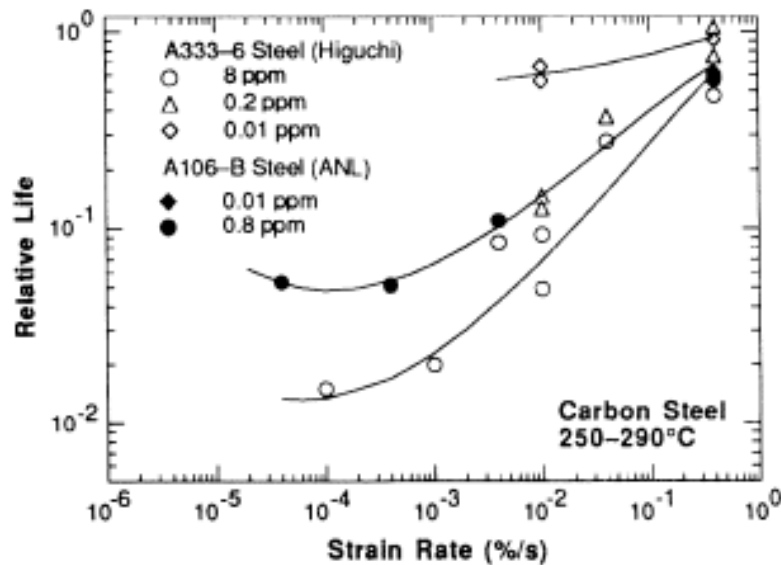
FIGURE 2.23 The effect of strain rate on low cycle CF in the C-Mn steel/high-temperature water system. [73]

2.3.4 Relationship of SCC and CF

Although in practice most of the structures are subjected to the combined action of static and cyclic loads, SCC and CF were usually separately studied. Numerous studies have shown a basic electrochemical similarity of these two processes. Both of them are greatly affected by external polarization. They have similar time-to-failure vs. potential trend, but in low frequency regime, the time-to-failure is much shorter for cyclic loading

36

than static at the same maximum tensile stress. Stepanov and Salomashenko believed that the accelerating failure under cyclic stresses is due to the fact that electrolyte is being squeezed out from the crack tip and the rubbing of the crack walls with subsequent renewal of the electrolyte and crack wall surface [74]. The cyclic stress effect on SCC will be elaborated in one of the following sections.

2.4   Residual Stresses in DSSs

2.4.1   Nature of Residual Stresses in DSSs

Due to the inhomogeneous microstructure of DSSs, different residual stresses in the two phases could be induced by various manufacturing processes, such as hot forging, cold working, and heat treatment [75-77]. More specifically, the inhomogeneity causing residual stresses in DSSs mainly refers to the different coefficients of thermal expansion (CTE) and different mechanical properties (i.e., yield strength, toughness, etc.) of the two phases. TABLE 2.5 shows the typical CTE for the two phases of DSSs changing with temperatures [78]. When the material is quenched from the solutionizing temperature, thermal stresses are generated in the two phases due to the large temperature change and different CTE. On the other hand, when DSSs are subjected to large deformations, mechanical residual stresses are introduced due to the different stress-strain responses of the two phases. For example, when one of the phases yield before the other due to the difference in yield strength and initial residual stress, the permanent plastic deformation in that phase will further induce mechanical residual stresses to the

material. At room temperature, all DSSs have residual stresses, which are known to be compressive in the ferrite phase and tensile in the austenite phase [75]. Kamachi and his co-workers found that the stress-free temperature for a DSS was about 300 °C [79].

TABLE 2.5 Typical coefficients of thermal expansion values for ferrite and austenite phase of DSSs. [78]

Grades	Type	Mean CTE from 0°C to:		
		100°C	315°C	538°C
Ferritic	445	10.4	10.8	11.2
Austenitic	303	17.2	17.8	18.4

2.4.2 Quantification of Residual Stresses in DSSs

The stress field in DSSs can be defined on different scales. The definitions of total stress, macrostress and microstress are given in FIGURE 2.24. Macrostresses ($^{M}\sigma_{ij}$) are the average stresses over a large number of polycrystalline grains, in this case even phases. They can be caused by an external mechanical or thermal treatment due to relative deformation of different areas of the material. Thus by definition macrostresses are the same in both phases. Microstresses ($^{\mu}\sigma_{ij}$), on the other hand, can vary on the microstructure scale of the material, and they must be balanced between phases. The microstresses could be caused by the mismatch in mechanical properties, such as yield

strength and CTE, between phases. The average total stress at any point in phase α is the sum of the macrostress and microstress

$$\langle {}^t\sigma_{ij}^\alpha \rangle = {}^M\sigma_{ij} + \langle {}^\mu\sigma_{ij}^\alpha \rangle \qquad\qquad 2.1$$

Another relationship between these stresses is the equilibrium condition between the two phases of the material,

$$\left(1 - V_f\right)\langle {}^\mu\sigma_{ij}^\alpha \rangle + V_f \langle {}^\mu\sigma_{ij}^\beta \rangle = 0 \qquad\qquad 2.2$$

where V_f is the volume fraction of phase β and where "⟨ ⟩" represents the averages over the appropriate volume [75].
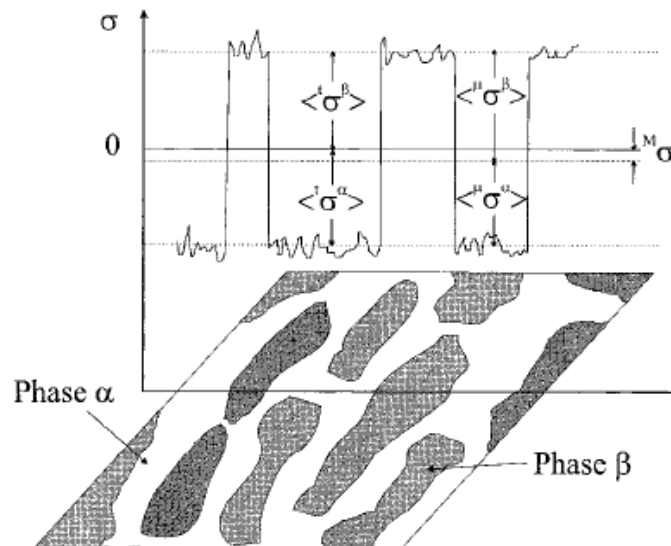
FIGURE 2.24 Definition of total stress, macrostress and microstress in DSSs. [75]

The total stresses can be obtained from measurements, such as diffraction techniques. Then the macrostresses and microstresses could be determined by the above equations. However, such calculations only give an average value of the microstresses within each phase, and no experimental methods could detect the changes of microstresses within phases. Therefore, in order to quantify the microstresses within phases, numerical simulations are usually employed. For the above reasons, in most of the literature, experimental techniques and numerical simulations were usually used together to determine the residual stresses developed in DSSs. Among various approaches, diffraction technique is the most common experimental method used to determine the average total stress of materials. The main advantages of diffraction-based methods are the non-destructive nature and the possibility of obtaining stresses in individual phase of multiphase materials. X-ray diffraction (XRD) [75, 80-84] can measure the surface stress/strain state, while Neutron [77, 85] and Synchrotron [86] radiation can determine the stresses up to a few centimeters inside the material. On the other hand, finite element analysis [75, 84] and self-consistent models [77, 81, 83, 87] have been proved to be the most effective numerical calculation methods in calculating the microstress states in DSSs. Simply speaking, the self-consistent models are used to predict the plastic incompatibility stresses generated due to various elastoplastic deformations of one- and two-phase materials. TABLE 2.6 shows a complete initial residual stress state of SAF 2304 obtained by XRD measurement and calculations using above analytical equations [75]. In another study, principal stresses obtained by XRD and neutron diffraction were compared by Dakhlaoui *et al.* [77], as shown in TABLE 2.7 and TABLE 2.8.

Qualitative agreement between these two techniques was obtained. In other words, stresses in TD (transverse direction) and RD (rolling direction) are small and have similar values, while stresses in ND (normal direction) are relatively large.

TABLE 2.6 Initial total stresses, macrostresses and microstresses in SAF 2304 measured by XRD. [75]

Component	${}^{t}\sigma^{\alpha}$	error	${}^{t}\sigma^{\gamma}$	error	${}^{M}\sigma$	error	${}^{\mu}\sigma^{\alpha}$	error	${}^{\mu}\sigma^{\gamma}$	error
σ_{11} [MPa]	−111.1	15.7	29.1	16.4	−34.0	13.4	−77.1	12.4	63.1	14.3
σ_{22} [MPa]	−213.5	15.7	82.8	14.7	−50.5	18.4	−163.0	17.7	133.4	19.0
σ_{33} [MPa]	−124.8	6.1	74.3	5.7	−15.3	10.8	−109.5	10.6	89.6	11.0
σ_{12} [MPa]	0.3	7.1	2.6	6.2	1.6	4.8	−1.3	4.2	1.1	5.2
σ_{13} [MPa]	−2.0	3.1	−4.4	2.3	−3.3	2.0	1.3	1.7	−1.1	2.1
σ_{23} [MPa]	1.4	3.1	−8.1	2.2	−3.8	2.0	5.2	1.8	−4.3	2.1

TABLE 2.7 Initial principal residual stresses measured by XRD in both phases of DSS UR45N. [77]

	Austenite	Ferrite
Face TD/ND		
σ_{TD}^{ph} (MPa)	42	−35
σ_{ND}^{ph} (MPa)	−130	66
Face RD/ND		
σ_{ND}^{ph} (MPa)	−134	75
σ_{RD}^{ph} (MPa)	43	−66
Face RD/TD		
σ_{RD}^{ph} (MPa)	55	−52
σ_{TD}^{ph} (MPa)	53	−40

TABLE 2.8 Initial principal residual stresses measured by neutron diffraction in both phases of DSS UR45N. [77]

	Austenite	Ferrite
$\sigma_{TD}^{ph} - \sigma_{RD}^{ph}$ (MPa)	-8	36
$\sigma_{ND}^{ph} - \sigma_{RD}^{ph}$ (MPa)	-62	113

2.4.3   Effect of Residual Stresses on SCC of DSSs

The effects of residual stresses on SCC of DSSs have rarely been investigated. A survey of the literature indicates the influence of residual stresses will mainly influence through promoting/retarding plastic deformation of one phase versus the other. Such plastic deformations could promote SCC by breaking the surface film or giving rise to emerging slip bands in a certain phase. Mary *et al.* [80] have found that below the yield strength of DSS 2205, the austenite phase deformed plastically first at a relatively lower strain level (FIGURE 2.25). Considering the lower yield strength of austenite phase compared to the ferrite phase [80, 83], this result is consistent with the initial residual stress state of the two phases. However, the load sharing or strain distribution between the two phases changes with applied stress/strain amplitudes. Lillbacka and Mateo *et al.* [88, 89] observed that for super DSSs under cyclic loading, although plastic deformation starts in the austenite phase, hardness measurements after cyclic loading show that the austenite phase becomes harder than ferrite. The hardening of the austenite leads to the transfer of plastic deformation from austenite to ferrite phase during cyclic loading.

For instance, when super DSS 2507AD (with the addition of nitrogen) is subjected to a relatively larger cyclic straining, slip bands appear mainly in ferrite phase, and also in small parts of austenite phase, as shown in the SEM image of FIGURE 2.26. The difference of plastic deformations observed in DSSs may be attributed to the compositional difference in materials (i.e., nitrogen content) and the different strain levels.
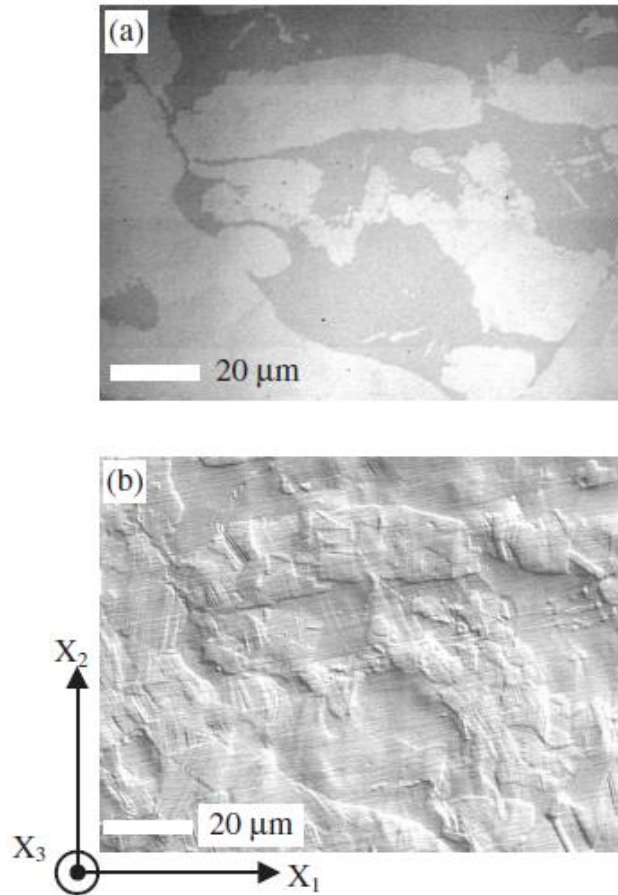
FIGURE 2.25 Surface of DSS 2205 after a tensile test at 400 MPa: (a) bright field image and (b) differential interference contrast image showing numerous slip bands visible in the austenite phase. [80]
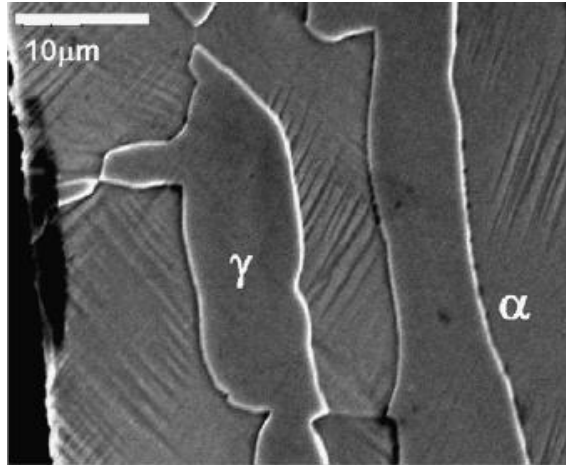
FIGURE 2.26 Fatigue damage in 2507AD steel: SEM picture shows the slip bands formed during cyclic loading a/2 = 1%. [88]

2.4.4   Effect of Stresses on Corrosion and Electrochemical Behavior

Through a series of micro-polarization tests and a finite-element simulation, Vignal *et al.* [90] found that the surface stress in ferrite phase of DSS 2205 induced by polishing has a strong linear relationship with local corrosion potential when tested in 15 M LiCl (pH=3), as shown in FIGURE 2.27. Considering another relationship they obtained between corrosion potential and Cr/Fe ratio in the surface passive film, it can be concluded that the Cr/Fe ratio in the passive film increases with increasing compressive stresses. Vignal *et al.* thought this may explain the beneficial effect of compressive stresses in SCC. These results were supported by the Navaï and his coworkers, who have also found higher Cr content in passive film in compressive stress state compared to the unstrained state, for 302 [91] and 316 [92] stainless steels.
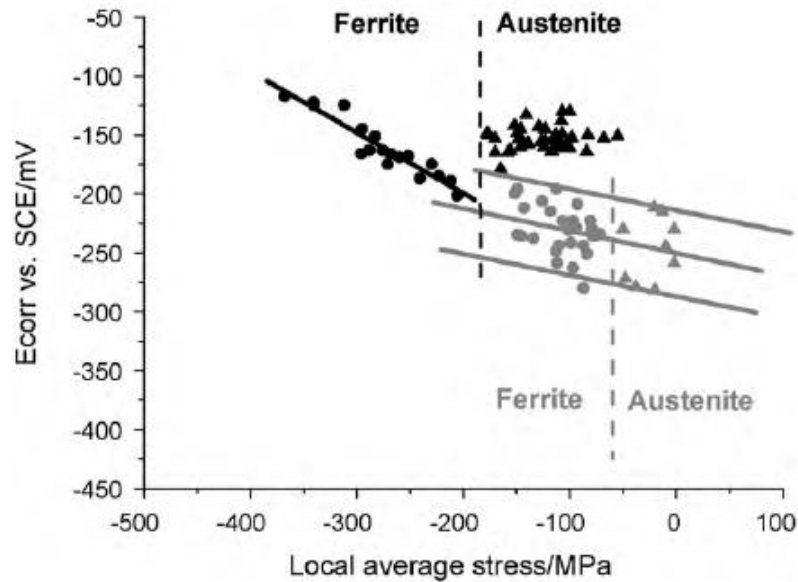
FIGURE 2.27 Relationship between local corrosion potential and local average stress for UNS S31803. Balck dots: surface polished using 1 μm diamond paste and polarization curves in 1.5 M LiCl; Grey dots: surface etched in nitric acid and polarization curves in 1.7 M NaCl. pH = 3 (buffered solution) [90]

2.5 Effect of Cyclic Stresses on SCC of DSSs

2.5.1 Rate Sensitivity of SCC

Before introducing the cyclic stress effect on SCC, there is one concept deserves some discussion, namely, the rate sensitivity characteristic of SCC. The effect of strain rate on SCC is shown in FIGURE 2.28. Since SCC could reduce the ductility of materials, smaller reduction in area (i.e., low ductility) represents more SCC attack. This schematic drawing

tells us SCC only happens when the strain rate of the material falls into a certain critical range. This critical strain rate range corresponding to the film rupture rate is comparable with the rate of passive film formation. Above this range, the film was ruptured by the straining of the material so fast that the passive film cannot form at the rupture site. Moreover, once the cracks initiate, the corrosive environment does not have enough time to take effect at the crack tip before the cracks grow further under the mechanical straining. As a result, the material fails in a ductile matter, like no corrosive environments exist. Below this critical strain rate range, the film formation kinetics is sufficiently rapid that film ruptures are healed before corrosion happens. Past experience has shown that for steels, the most severe SCC was usually observed at a strain rage of about 10^{-6} s^{-1} regardless of the test environment. On the other hand, the strain rate effect for hydrogen-induced cracking is quite different than SCC, as can be seen from FIGURE 2.28. That reason is that the occurring of hydrogen-induced cracking is associated with hydrogen intake, not film rupture. As the strain rate decreases, more and more hydrogen atom could be absorbed by the material, which makes the hydrogen-induced cracking more severe.
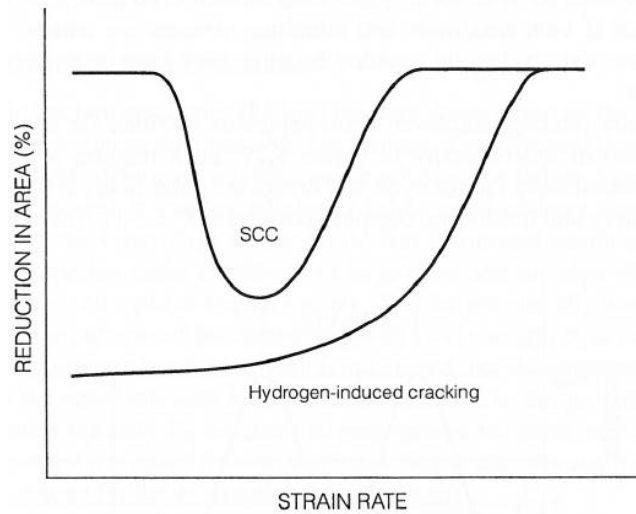
FIGURE 2.28 Schematic effect of strain rate on ductility in SSRTs for SCC and hydrogen induced cracking. [93]

In fact, based on the rate sensitivity nature of SCC, SSRT is widely used to characterize and quantify SCC of materials. In SSRT, the initiation of SCC is accelerated through the application of a dynamic strain in the gage section of a specimen. Moreover, the rate-sensitive characteristic of SCC indicates that in order for SCC to continuously proceed, the strain rate (i.e., film rupture rate) should be comparable with the film formation rate. Hence this critical strain rate was artificially applied to the material to accelerate the SCC process in SSRT. Due to the accelerated nature of this type of testing, the results are not intended to necessarily represent the service performance, but rather to provide a method of material screening in a relatively shorter period of time.

48

2.5.2   Effect of Cyclic Stresses on Crack Tip Creep

In 1952, A.J. Kennedy first reported the phenomenon of cyclic loading induced creep on lead [94]. Through the experiments, he found the influence of a short period of unloading and reloading on creep. Kennedy observed a transient increase in the strain rate, so the creep strain right after each reloading was larger than it would have been if creep was not interrupted, as shown in FIGURE 2.25. This phenomenon was referred as the "Kennedy effect" or "cyclic creep acceleration" in literatures.
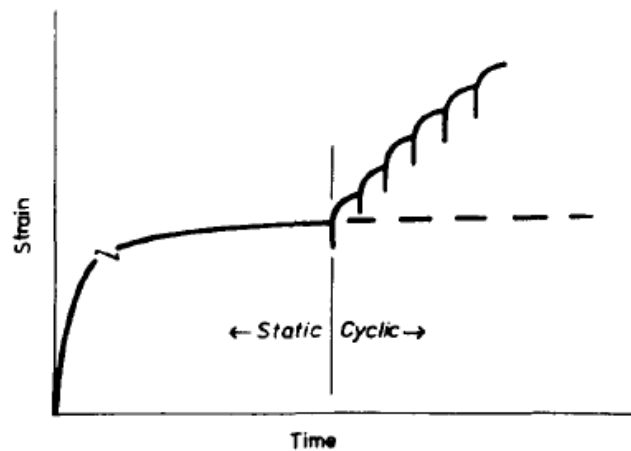
FIGURE 2.29 Schematic illustration of the accumulation of strain by cyclic loading. [1]

The increases in creep rate stimulated by low frequency cyclic loading, or the Kennedy effects have been observed on various materials, such as polycrystalline lead, copper, aluminum, mild steel and pure iron [1-5, 94-96].

In 1970s, Evans, Bennett and Parkins studied the room temperature creep induced by cyclic loading for both pipeline carbon steel [2] and copper [1]. They proved that at room temperature, creep deformation is induced by low frequency cyclic loading in materials with both BCC and FCC crystal structures. Instead of conducting separate static and cyclic creep tests at the same stress level, they prestrained the samples under static loading to exhaust the creep strain, and then started the cyclic loading. Through the observation of the creep strain accumulation, they found that during each cycle upon the application of cyclic stresses, the creep rate or strain rate of the materials largely increased, which resulted in more strain accumulation than it would have been if the stress was static. They studied the effects of applied stress and prestrain. Applied stress was the same for the initial static stress and the cyclic stress. Prestrain was defined as the strain before cycling starts. They concluded that the applied stress was the most important experimental variable in stimulating creep by cyclic loading. FIGURE 2.30 is demonstrating the effects of applied stresses on creep accumulation for carbon steel and copper.
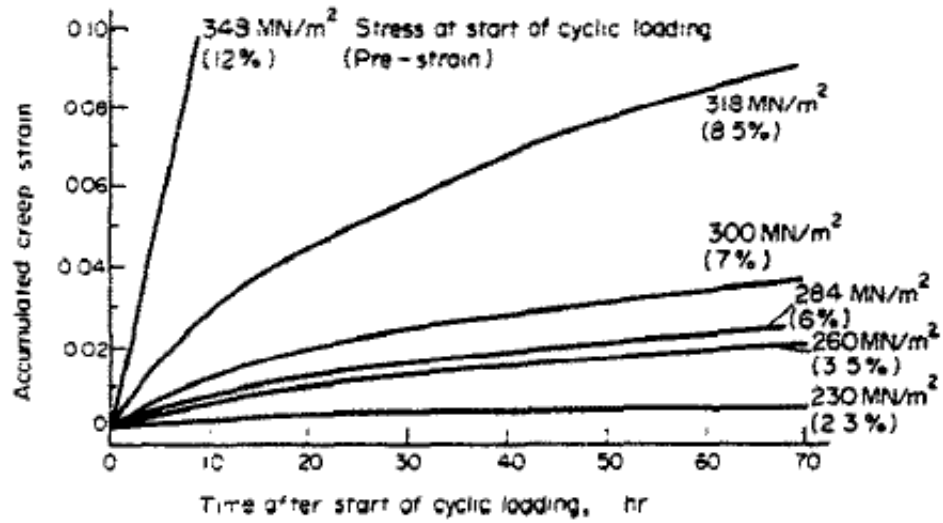
(a)
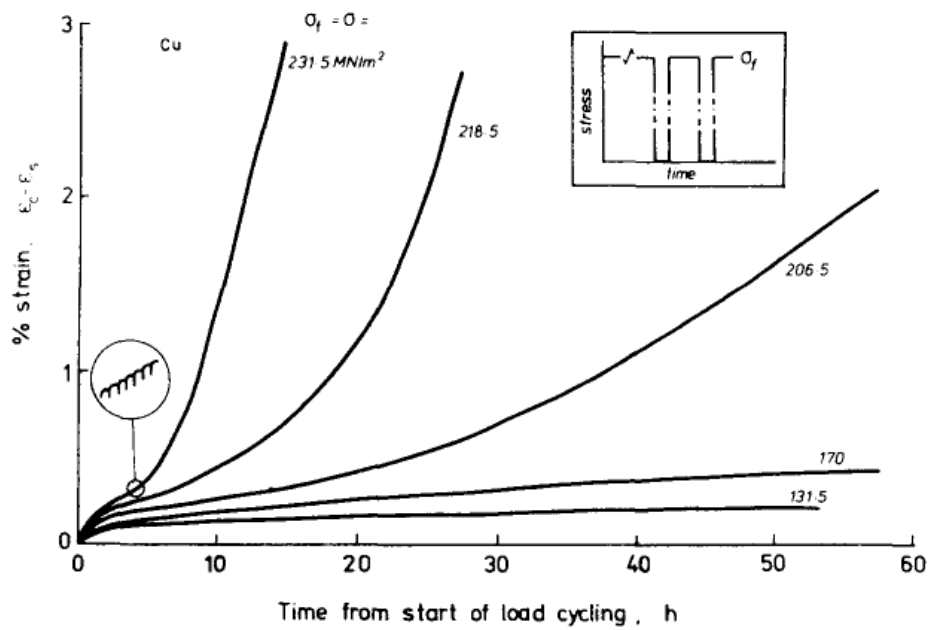
(b)

FIGURE 2.30 Envelopes of creep curves produced by cyclic loading at room temperature showing the effect of applied stress: (a) C-Mn steel [2] (b) copper [1].

During the same period, Shetty and Meshii performed separate static and cyclic creep tests for pure iron at the same stress levels [5]. By comparison of the static and cyclic creep curves (FIGURE 2.31), they found that at relatively longer times (> 2-3 hours), the cyclic creep definitely showed "cyclic creep acceleration". Nevertheless, the same group of researchers observed an interesting creep behavior on aluminum. They found for aluminum, the cyclic stresses could either enhance or retard the creep accumulation under different conditions [4]. FIGURE 2.32 shows two extreme examples for each case. In fact, Kennedy effect is not a universal rule that can be applied to any metals under any conditions. Other researchers have also observed "cyclic creep retardation" in their studies [97-99]. Wang and Chen [99] performed similar static and cyclic creep tests for pipeline steel X52, and they found that the creep deformation was significantly reduced by cyclic stresses at room temperature, as shown in FIGURE 2.33.
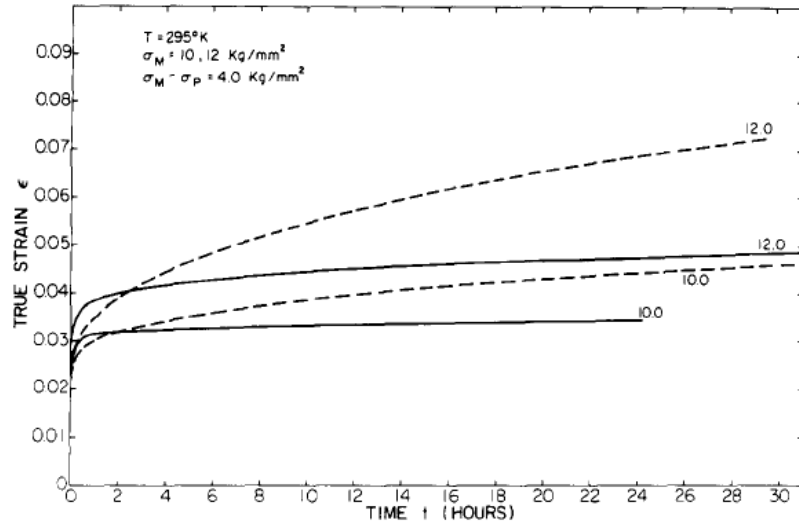
FIGURE 2.31 Typical static (solid lines) and cyclic (broken lines) creep curves for pure iron at room temperature (295 °K) and at two stresses, 10 and 12 kg/mm^2. [5]
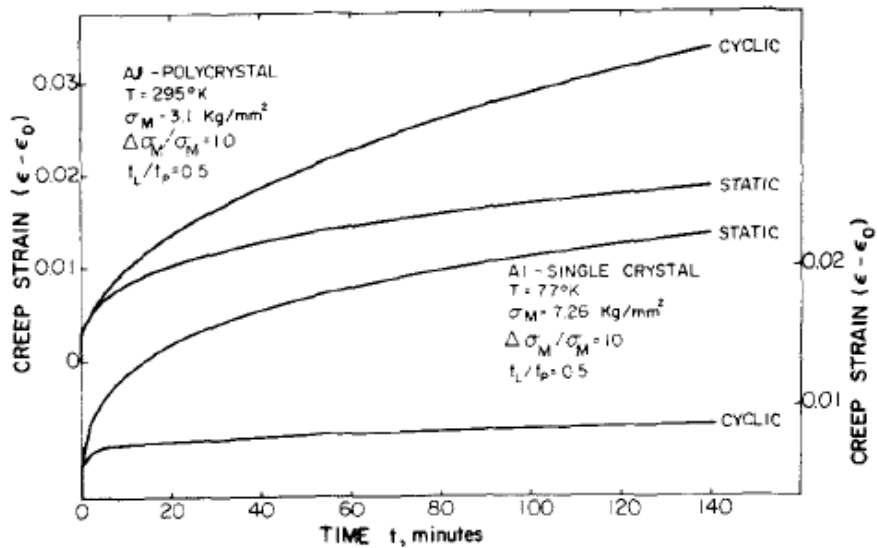
FIGURE 2.32 Comparison of cyclic and static creep curves of aluminum. Top pair illustrates cyclic stress acceleration behavior of polycrystal aluminum at 295 °K; bottom pair illustrates cyclic stress retardation behavior of single crystal aluminum at 77 °K. [4]
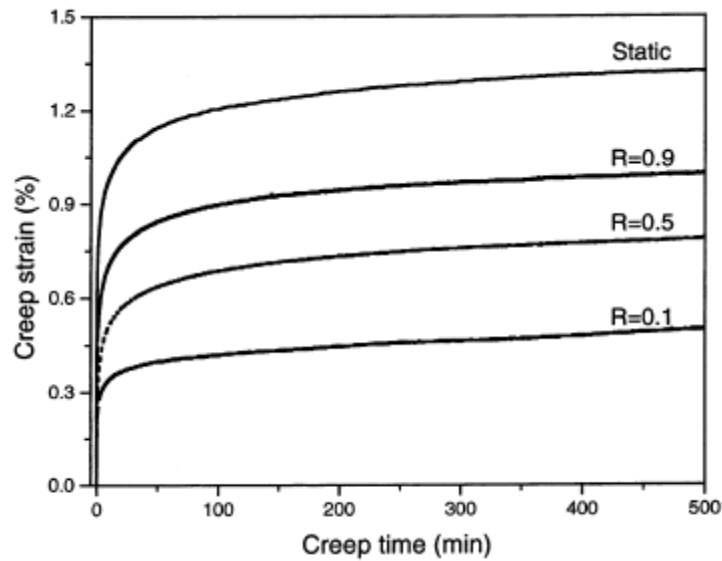
FIGURE 2.33 Comparison of creep curves obtained under static and cyclic loading with

various R-ratio for X52 pipeline steel. [99]

Cyclic stress acceleration and retardation are affected by various experimental parameters, especially the applied stress. Above a threshold stress, cyclic stress was observed to enhance creep deformation, while below the threshold stress, cyclic stress was observed to retard creep deformation. Experimental results indicated that the threshold stresses are significantly influenced by temperature, which means the cyclic creep behavior of aluminum will also depend on temperature. Shetty and Meshii [4] pointed out that the threshold stress increases with decrease of temperature. Therefore, the cyclic creep retardation observed at 77 °K (FIGURE 2.32) is actually due to the applied stresses were smaller than threshold stress at that temperature, and this

threshold stress could not be studied because of necking in the material. It is worth mentioning that for aluminum at room temperature, cyclic creep acceleration predominates (FIGURE 2.32).

Reasons for the dramatic effects of the cyclic stresses on creep deformation have been explored in a number of researches. In Bennett, Evans and Parkins' studies, they believed that the essential feature of creep induced by cyclic loading is the recovery of properties that occurs during unloading [2]. Recovery could occur in two ways: (a) mobile screw dislocation segments may leave their slip planes by cross-slip aided by fluctuations in internal stress encountered during reverse movement, (b) obstacle dislocations may become rearranged because of the altered state of internal stress. The general trends of these results showed that the Kennedy effect is more significant at room temperature when the stress is high. Similarly, Shetty and Meshii [5] also explained the creep deformation enhanced by cyclic stresses in pure iron using the cross slip model, which is based on the attraction of oppositely signed screw dislocations on parallel slip planes leading to mutual annihilation [100]. In their studies for aluminum [4], Shetty and Meshii identified the cyclic creep acceleration (or retardation) was caused by the dislocation rearrangement which may produce less (or more) cyclic strain-hardening. Similarly, Wang and Chen [99] believed that room temperature creep is a result of the glide of mobile dislocations, and the cyclic creep retardation they observed for X52 at room temperature was due to the cyclic-hardening of the material. Microscopically, cyclic-hardening could happen when dislocation cells form in the material, which could significantly reduce the amounts of mobile dislocations by adding them into the cells.

55

Moreover, there are evidences of dislocation cell formation caused by cyclic loading under certain conditions [3, 98, 101]. Several researchers have suggested that the occurrence of cyclic creep acceleration or retardation depends on whether the material will exhibit cyclic hardening or softening behavior under specific conditions [4, 97, 99]. The tension-tension loading mode in Wang and Chen's study is one of the factors favoring cyclic hardening, based on Chai and Laird's results [97, 99]. Yang and Wang also argued that the cyclic hardening and softening may depend on the microstructure and the material itself [102]. The temperature dependence of the threshold stress could be explained by stacking fault energy (SFE). Feltner and Laird have pointed out that the threshold stress is affected by the SFE of the material because softening is easier for material with a higher SFE [103]. Various FCC materials' SFE have been proved to increase with temperature [104-106].When the SFE is high, the cross slip is easier to happen. That is, the threshold stress above which cyclic softening will occur is lower when SFE is high, or when temperature is high. On the other hand, the threshold stress observed in FCC materials (Al and Cu) [107, 108] was not observed in BCC pure iron [5]. This may be attributed to the fact that the cross slip is relatively easy in pure BCC metals, where it is observed even at lower stresses [5].

In summary, all of the above mentioned mechanisms involve the dislocation movement in the material under cyclic creep. The strain rate caused by dislocation motion can be described using the Orowan equation [109]

$$\dot{\varepsilon} = \rho_m \cdot b \cdot v \qquad\qquad 2.3$$

Where ρ_m is the mobile dislocation density, b is the Burgers vector, and v is the dislocation velocity. Therefore, the increase (or decrease) of the creep strain rate is a result of the increase (or decrease) of the mobile dislocation density or velocity, or a combination of both. Most of the mechanisms discussed above have mainly attributed the strain rate change to the mobile dislocation density change induced by cyclic loading.

2.5.3 Effect of Cyclic Stresses on SCC

As discussed in Section 2.2.3, several mechanisms of SCC are based on the assumption that sufficient plastic deformation is present at the crack initiation site or crack tip. Both slip dissolution model and corrosion tunnel model assume that there are emerging slip bands on the material surface, which is an indication of plastic deformation in the material. Localized surface plasticity model will only work when the brittle surface film is ruptured, and plastic deformation is the most important factor to cause it. Moreover, the plastic deformation could enhance hydrogen intake in the hydrogen embrittlement model. Therefore, plastic deformation is a critical factor for SCC, and larger plastic deformation enhances SCC susceptibility.

In the case of cyclic creep acceleration, low frequency cyclic stresses could induce room temperature creep (i.e., plastic deformation) on various materials, as we just discussed in Section 2.4.1. Hence, the low frequency cyclic stresses will enhance SCC by inducing plastic deformation/creep at the crack tip or crack initiation site. This could work in several ways. First, by producing a larger amount of plastic deformation compared to static loading, cyclic loading increases the probability of rupturing the brittle surface film at the crack tip, which leads to a higher stress corrosion crack initiation and propagation rate. Secondly, since cyclic loading could induce an increased transient creep or strain rate right after each unloading and reloading process, this sudden deformation could rupture the brittle film, leaving little time for the protective film to repair itself in the corrosive environment. This means that higher strain rates may facilitate anodic dissolution that can result in a higher crack initiation and propagation rate. Additionally, in the case of film induced cleavage model, the transient increased creep/strain rate induced by cyclic loading provides the fast strain rate that is required for this mechanism to work (Section 2.2.3.2.2). Thirdly, since SCC is a rate-sensitive phenomenon, and it only occurs within a certain strain rate range (FIGURE 2.28), the creep/strain rate increase due to cyclic loading at the crack tip or crack initiation site could bring itself back into the SCC strain rate range, when the creep/strain rate is exhausted by static loading. This means, the protective surface film will be constantly ruptured as it is formed at the alloy surface, depending on the corrosive environment. Moreover, if the increased strain rate is maintained (indicated by the constant slope of the cyclic creep strain curve in FIGURE 2.29), the SCC process will proceed continuously.

In contrast, when the cyclic stresses result in cyclic creep retardation, the effects of cyclic stresses on SCC are expected to be the opposite of what was mentioned in earlier section.

Effect of cyclic stresses on SCC has been extensively studied in literature, but very little research has been done on the effect of room temperature creep induced by cyclic loading on SCC. Oehlert and Atrens [109] discussed the possible interaction between room temperature creep and SCC in their studies for three different high strength steels. They concluded that the transient creep can have an influence on SCC in high strength steels in aqueous solutions. "The mobile dislocations can assist hydrogen transport through the metal and the transient creep strain can rupture the protective film on the surface of the metal and assist the crack initiation." However, there were no experimental data provided to support their arguments regarding the effects on SCC. In contrast to that, Wearmouth and his coworkers obtained some evidence of prestrain retarding subsequent SCC failure [110]. In SCC tests, they observed an increase in time to failure and threshold stress when a Mg-Al alloy was prestrained in air. Smialowski and Konstanski found some correlations between the creep coefficient, an index of creep strain, and the crack initiation and propagation rate for an austenitic stainless steel in boiling 35% $MgCl_2$ [111]. As can be seen in FIGURE 2.34, the creep coefficient and crack initiation and propagation time curves show very similar deflections vs. applied stress levels. These results indicated higher creep coefficient, or higher creep deformation, corresponds to shorter crack initiation and propagation time. However, in order to compare the creep test and the SCC test results, the creep tests were done at 125°C, so

the creep effects are not strictly what we are interested in, namely the room temperature creep. In addition, these creep tests were purely monotonic instead of cyclic ones.
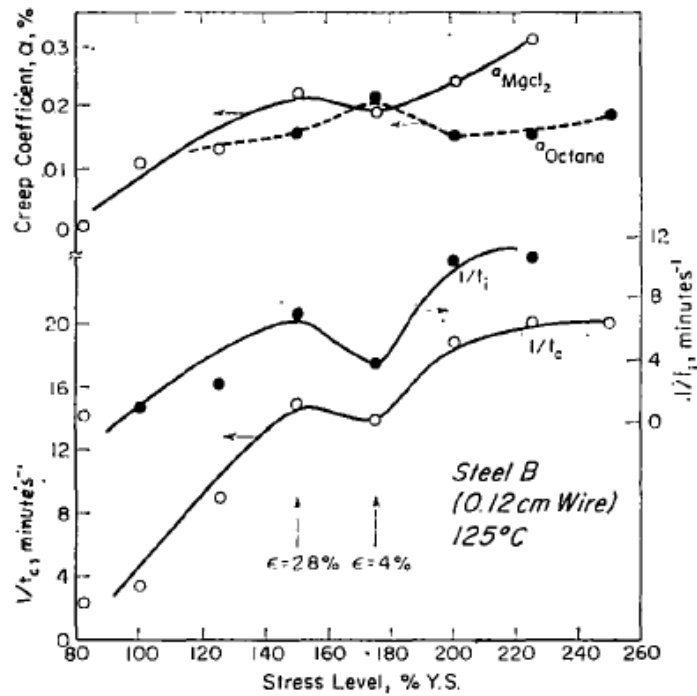
FIGURE 2.34 The effect of applied stress on reciprocal cracking time, reciprocal induction time, creep coefficient in boiling MgCl₂, and creep coefficient in boiling octane for an austenitic stainless steel. [111]

The researches on cyclic loading effect on room temperature creep were relatively active in 1970s, when DSSs were just developed. In a survey of the literature, we found

there was no study done on the effect of room temperature cyclic creep for DSSs. It is one of the purposes of this work to investigate the cyclic creep behavior of DSSs at room temperature.

2.6   Motivation

Based on the discussion in the previous sections, we know that the production and application of DSSs have increased dramatically during the last decade. According to S. Jacques [112] from Industeel, in desalination plants, some companies have completely shifted from austenitic stainless steels to duplex grades. In recent years, due to the rising nickel prices, cost of DSS with lower nickel content is even more favorable. However, SCC failures of DSSs under different service conditions have been reported, and in many cases, the stresses in these applications are not strictly static [113, 114]. FIGURE 2.35 shows the environment induced cracking of a DSS 2205 scraper arm in a continuous digester under intermittent loading. The examination of the cracking under microscope reveals it was a typical CF failure, which features cracking without branches. FIGURE 2.36 shows a crack found in a DSS 2205 black liquor evaporator, in a pulp mill, after three-year service. Failure analysis of this part showed that the damage was caused by vibrations or cyclic loading experienced by the evaporator.
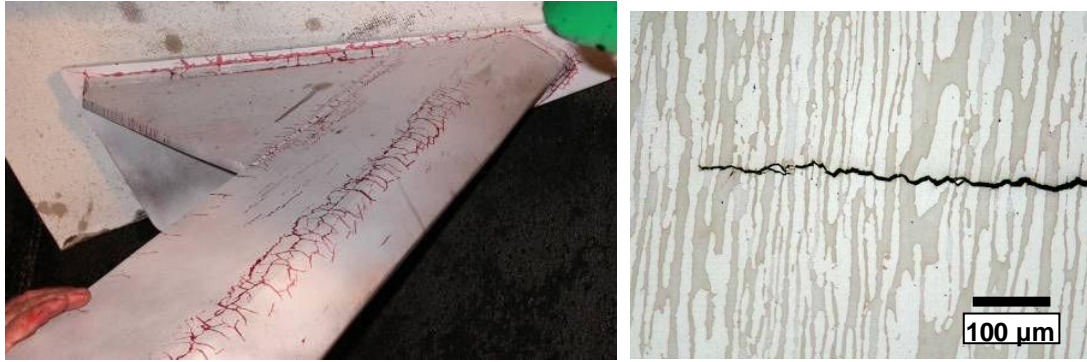
FIGURE 2.35 SCC of DSSs in a DSS 2205 scraper arm under intermittent load. [114]

FIGURE 2.36 Leakage in a DSS 2205 evaporator due to vibrations or cyclic loads. [113]

Effects of cyclic stresses on SCC and CF of DSSs have been studied in various corrosive environments [45, 115-120]. However, most of these studies are about the effects of high frequency cyclic stresses. Even for the so-called low frequency cyclic stresses, the frequencies were in the range of 1 to 0.001 Hz. No systematic study has been done on

the effects of cyclic loadings below 0.001 Hz, on SCC of DSSs in any corrosive environments. Under very low frequency, however, the cyclic creep behavior of the material will be affected. Hence, the cyclic creep acceleration or retardation is certainly expected to influence SCC of DSSs. Furthermore, in the existing literature, more attention has been given to the investigation of stress corrosion crack propagation processes, rather than the crack initiations caused by cyclic loading. Researchers also put emphasis on completely reversed cyclic loadings, and very little work has been done on tension-tension cyclic loading effects on SCC of DSSs. Unlike the general corrosion (uniform corrosion), localized corrosion attack like SCC and CF, usually results in catastrophic consequences, such as sudden rupture or explosion. Hence, with more and more austenitic stainless steels being replaced by DSSs, SCC and CF problems of DSSs deserve more attention and understanding. Therefore, in this research work, we will focus on the low frequency tension-tension cyclic loading effects ($\sim 10^{-5}$ Hz) on stress corrosion crack initiations of DSS 2205 in acidified chloride and sulfide-containing caustic environments.

CHAPTER 3 EXPERIMENTAL PROCEDURES

3.1   Materials

The duplex stainless steel (DSS) 2205 materials used in this study have three batches. One batch of the material came from round bars (denoted as "2205B"). The other two batches were obtained from the Outokumpu stainless steel company, in the form of hot-rolled plates (denoted as "2205A" and "2205C", respectively). Both of hot-rolled materials had been annealed during production.

Chemical compositions of these different batches of DSS 2205 were sent out for analysis using combustion, inert gas fusion and ICP atomic emission techniques. The results are listed in TABLE 3.1. From this data, it seems that there is no significant difference in the chemical composition of these selected material batches. They all meet the compositional requirement for standard DSS 2205 specified in ASM Metals Handbook [121].

TABLE 3.1 Chemical composition of different batches of DSS 2205 used in this study.

	Element											
	Fe	C	Mn	Si	P	S	Cr	Ni	Mo	Cu	V	N
2205B (Bar)	Bal.	0.023	1.24	0.44	0.023	0.004	22.3	5.17	3.22	0.21	0.11	0.16
2205A (Plate #1)	Bal.	0.022	1.40	0.49	0.028	<0.003	22.6	4.97	3.10	0.37	0.06	0.14
2205C (Plate #2)	Bal.	0.016	1.33	0.18	0.024	<0.003	22.6	5.61	3.21	0.22	0.07	0.14

Nevertheless, the tensile stress-strain behavior of these materials is quite different from each other, as can be seen from FIGURE 3.1. The bar material (2205B) showed maximum ductility, and its stress-strain curve is analogous to 2205C plate material in shape, featuring a large amount of strain-hardening after yielding. In contrast, 2205A plate material had higher yield strength and did not exhibit significant strain-hardening or ductility compared to the other two batches of DSS. Moreover, the mechanical properties (i.e., stress-strain curve and yield strength) of 2205A are quite unique, rather different than what we usually see in literature for annealed DSS 2205. Although 2205C had lower ductility than the bar materials (2205B) but the two showed a stress-strain behavior which is fairly typical for annealed DSSs.
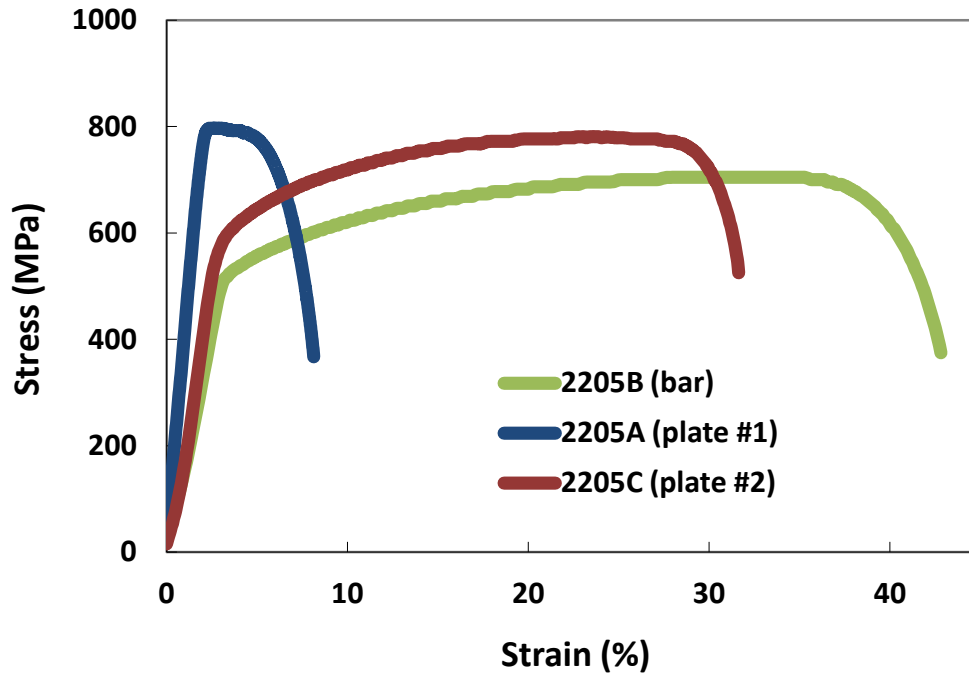
FIGURE 3.1 Stress vs. strain behaviors of different DSS 2205 materials tested in air, strain rate is 1×10^{-6} s^{-1}.

2205A material does not show strain-hardening behavior after yielding as this batch of plate had been cold worked after annealing. During that cold work process, the dislocations must have been locked preventing the material from further strain hardening.

To check the above stated effect of cold work, another test was done to understand the difference between DSS 2205A and 2205C batches. In this test, an annealed 2205C sample was prestrained to 742 MPa, and then the tensile behavior was tested. Test results showed that the stress vs. strain behavior of the prestrained 2205C was very

analogous to that of 2205A (FIGURE 3.2). Based on the material history and our tests to confirm it, in this study, 2205A material was used to study the effect of cold-working on stress corrosion cracking (SCC) and low frequency corrosion fatigue (CF) of DSS 2205.
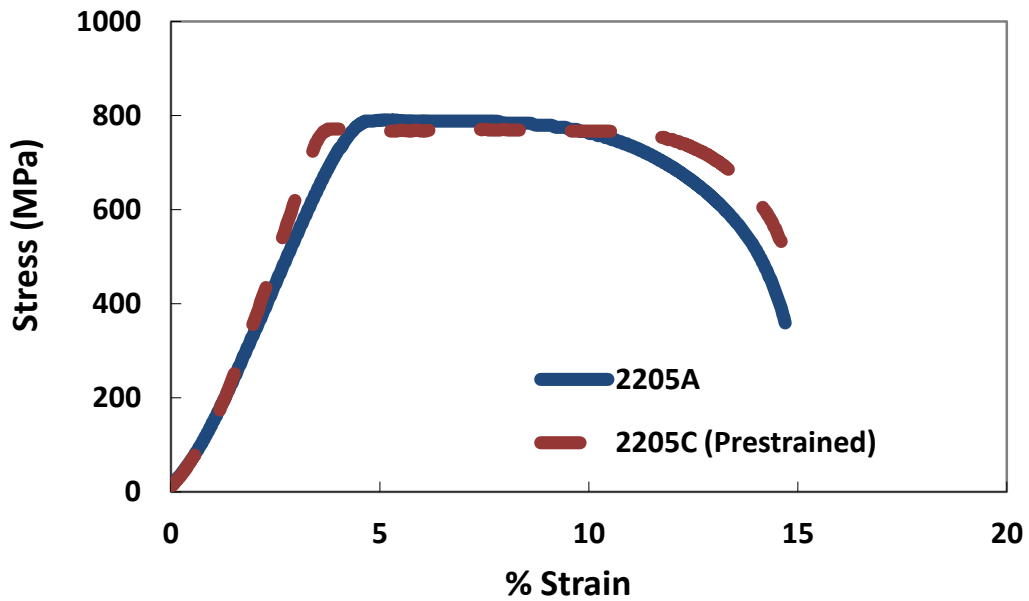
FIGURE 3.2 Stress vs. strain behaviors of as-received 2205A material and prestrained 2205C material. Tested in NaCl solutions, strain rate is 1×10^{-6} s^{-1}.

Microscopic images of these materials showed their phase morphologies are different as well (FIGURE 3.4). These microstructures are for the cross-section perpendicular to the rolling direction of the plate material or the extrusion direction for the bar material. Lighter phases in these micrographs are austenite, while the darker phases are ferrite.

2205A and 2205B have cylinder-shape austenite phases, distributed uniformly in ferrite phase. Hence the cross sections have rounder austenite phases, as shown in FIGURE 3.4 (a) and (b). However, the 2205C material has pancake-shape austenite phase, so the cross section pictures show that the austenite phases are elongated in one direction versus the other, as can be seen in FIGURE 3.4 (c).
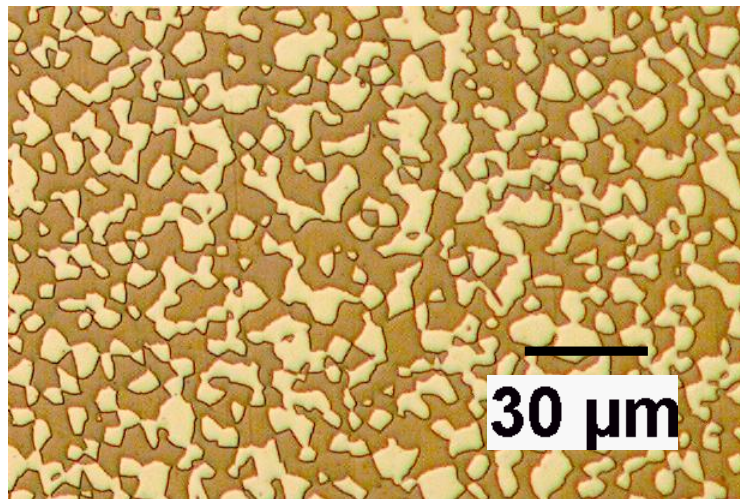
(a) 2205B

FIGURE 3.3 Phase morphologies of DSS 2205 materials.
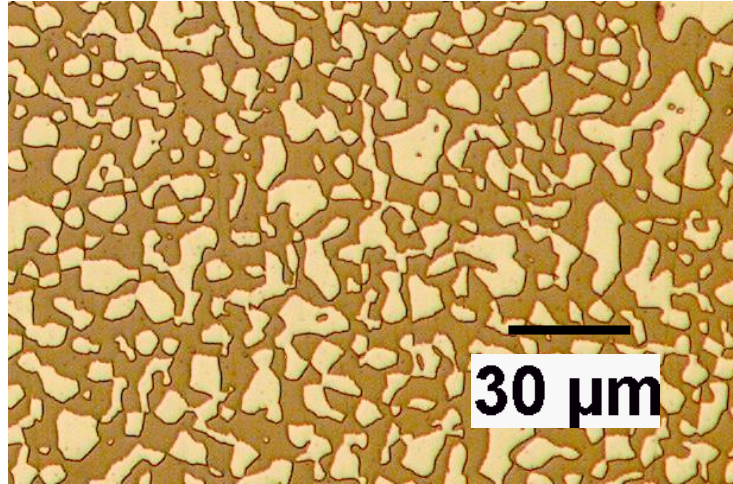
(b) 2205A
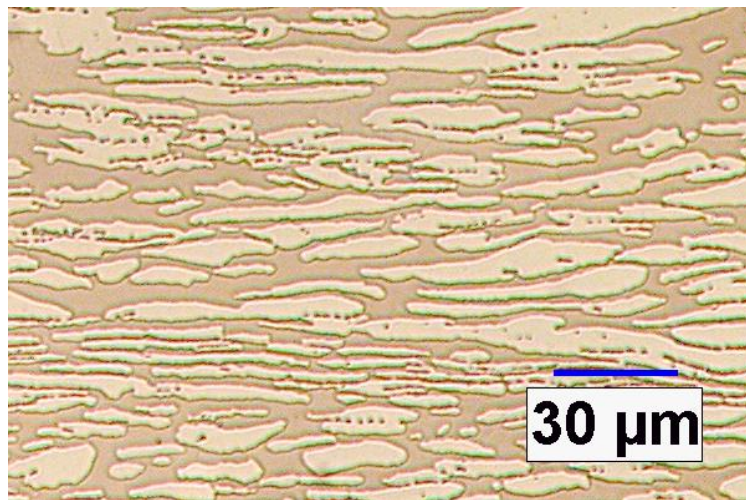
(c) 2205C

FIGURE 3.4 Continued.

Based on these micrographs, phase ratios of these DSS 2205 materials were quantified

using image analysis software to get the ferrite/austenite ratios for each material used.

Moreover, the ferrite numbers of these materials averaged from 10 measurements

were also measured by FERRITSCOPE® MP30. Results in TABLE 3.2 showed that the ferrite contents obtained by the two methods were consistent.

TABLE 3.2 Phase ratios of DSS 2205 materials used in this study.

Material	Avg. ferrite/austenite from Image analysis	Ferrite number from Ferritescope
2205B	56.3 / 43.6	61.2
2205A	60.8 / 39.1	63.3
2205C	46.2 / 53.8	53.1

Microstructure characterization results shown in micrographs and in TABLE 3.2 indicates that there are phase ratio and phase morphology differences among these materials, which is normal for different DSS products. The phase ratios are in normal range for DSSs, and both types of phase morphologies have been reported in numerous published literature for annealed DSSs [34-36, 80, 83, 90]. Most importantly, the difference between the mechanical behaviors of selected DSS batches has been identified, since this has the most significant influence on SCC of DSSs.

3.2   Sample Preparation

The DSS 2205 bars or plates were machined into smooth-gage tensile samples with the length of the sample along the rolling direction. The geometry of the samples is shown

in FIGURE 3.5. The gage section is 1" long and 1/8" in diameter. Prior to each test, the sample was ground with SiC paper down to 2000 grit, and then polished with diamond paste and suspension to 0.3 μm.
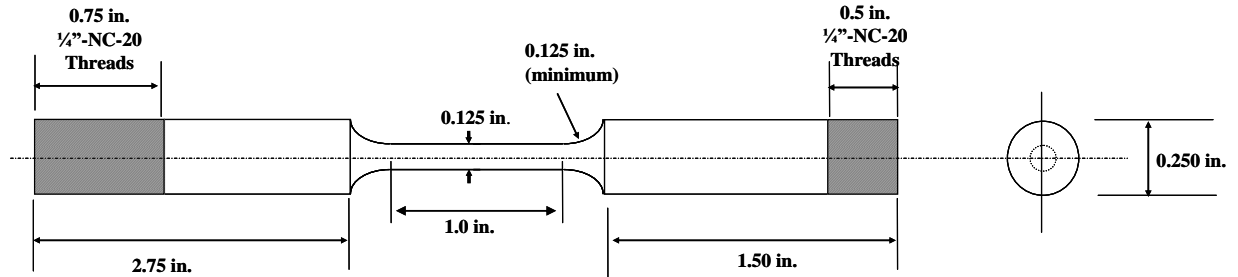
FIGURE 3.5 Geometry of DSS 2205 samples.

Polished tensile samples were used for the slow strain rate tests (SSRT), static and cyclic creep tests, as well as low frequency CF tests. The reason of using the smooth-gage tensile sample instead of notched-sample was to investigate the crack initiation process, rather than crack propagation. Besides, mirror polishing also helped us identified where the cracks initiate and why.

3.3   Testing Environments

The two corrosive environments investigated in this work were acidified NaCl solution at room temperature and caustic WL solution at 170 °C. WL solution is composed of 150

g/L NaOH + 50 g/L Na$_2$S, and it is a caustic solution used in the pulp and paper industry to cook wood chips and produce pulp and fibers.

Nowadays, almost all new pressure vessels and auxiliary equipment to handle the pulping liquors in new and existing pulp mills are made out of DSSs. Field experience and laboratory studies have shown that the WL may cause severe SCC or CF in DSSs above 120 °C [44, 45, 50, 113, 122-125]. At other end of environmental spectrum for this study, the concentrated chloride environment is frequently found in offshore structures, due to evaporation of water [126, 127] as well as in a number of processes in chemical industry. And the SCC and CF of DSSs have also been extensively studied in laboratories [32, 34, 35, 39, 42, 127, 128]. Main reason for studying these practically important environments was to develop an understanding of the mechanisms for low frequency CF and SCC in very different environments where one is highly alkaline and other is acidic.

To achieve the required acidity, the pH of the NaCl solution was adjusted using diluted HCl or NaOH. The pH of the WL solution was not adjusted, and its value is about 12 at room temperature.

3.4   Experimental Procedures

3.4.1   Polarization Testing

The conditions under which DSS 2205 are susceptible to SCC in WL has been established by previous studies [57]. Bhattacharya's results showed that DSS 2205 is susceptible to

SCC in WL at 170 °C and open circuit potential (OCP). However, optimum conditions for SCC of DSS 2205 in acidic chloride environments at room temperature are not very well characterized. Therefore, efforts were focused on characterizing optimum electrochemical conditions for the acidic NaCl environment. In order to identify the optimum pH value and potential range for SCC of DSS 2205 in the acidic NaCl solution, potentiodynamic polarization tests were performed.

Corrosion of metallic materials in aqueous environment is an electrochemical process, hence it is crucial to understand the polarization behavior of DSS 2205 in the studied environment. Polarization behavior of materials can provide useful information regarding surface conditions, corrosion susceptibility, and corrosion rate at different potentials. Commonly used polarization techniques include potentiodynamic, potentiostatic and cyclic potentiodynamic polarization tests. In this study we predominately used anodic potentiodynamic polarization and potentiostatic polarization methods. Potentiodynamic polarization tests done at different scan rates have also been used to determine the potential range for SCC susceptibility of an alloy in a given environment. Use of anodic potentiodynamic techniques to determine the SCC susceptibility of materials was proposed by Zakroczmski and Parkins [129]. The test method is purely electrochemical and assumes that the SCC mechanism involves the film rupture and anodic dissolution at the crack tip. In an anodic potentiodynamic polarization test, current are drawn out of the metal by applying an external voltage. The deficiency of electrons makes the potential of the metal change in the anodic (or more positive) direction. The rate of potential change is controlled during the test, and

73

the current is measured at different potential values. Since the current density is proportional to the corrosion rate, the current density changing with potential is an indicator of corrosion rate at different potentials.

FIGURE 3.6 shows a typical experimental setup for a three-electrode electrochemical cell for potentiodynamic polarization tests. The alloy sample being tested serves as the working electrode. In this study, platinum foil was used for counter electrode, and the reference electrode was saturated calomel electrode (SCE). The model of potentiostat used in this study was "Gamry reference 600".
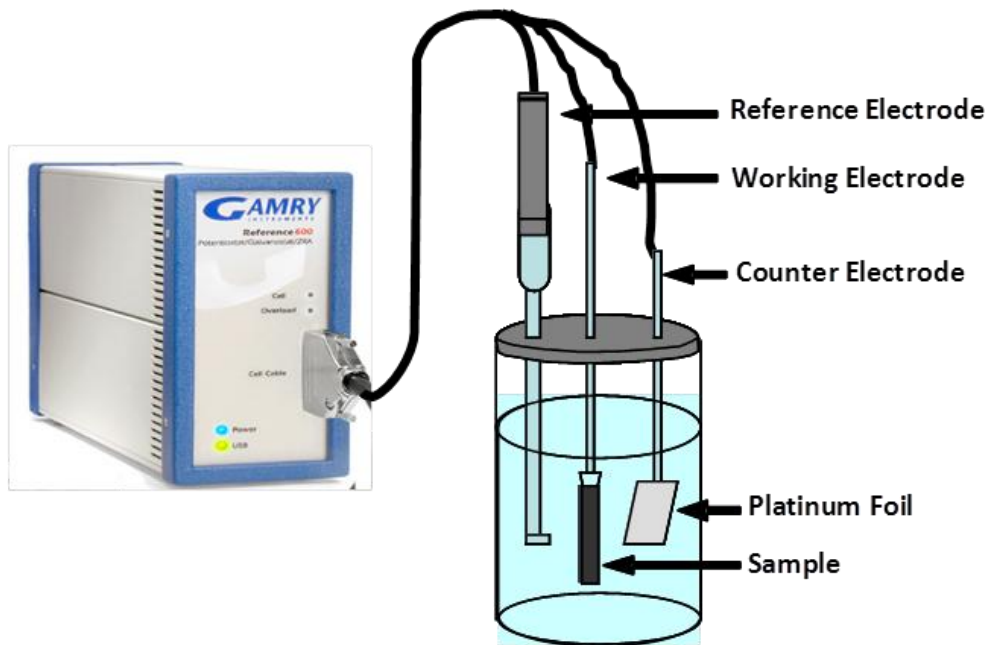
FIGURE 3.6 Experimental setup for potentiodynamic polarization tests.

The key outcome of a potentiodynamic polarization test is the polarization curve, which is a potential versus current density curve. A schematic anodic polarization curve is shown in FIGURE 3.7. Point A represents the equilibrium point of the system. Region B is the active region, where the metal oxidation (corrosion) takes place. In this region the current density or corrosion rate increases with potential increase. Region E is the passive region characterized by a low current density. This indicates the surface passive film is stable, so the corrosion rate falls to very low values. When the potential reaches point F, the stable surface film breaks down. Then the current density or corrosion rate increases again with increasing potential in the transpassive region G.
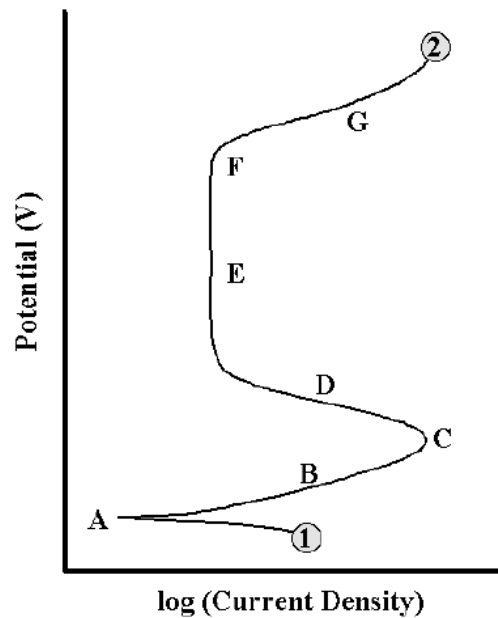
FIGURE 3.7 A schematic anodic polarization curve. [130]

SCC generally occurs for systems with material showing the passivation behavior, or those exhibiting an active-passive transition region in their polarization curves. In Section 2.2.1, when the potential dependence of SCC was discussed, it has been pointed out that the main potential range of SCC is the active-passive transition region (labeled as Zone 2 in FIGURE 2.5).

More specific electrochemical conditions (or narrower potential range) promoting SCC were also determined by slow- and fast-scan polarization of the material in the corrosive environment. At slow-scan rate, the surface passive film will have sufficient time to form, which represents the surface of an exposed sample. At fast-scan rate, there may not be enough time for the film to form before the potential is increased to even higher values, which represents the crack tip under stress. This difference between passive films could result in a large difference in current densities. The corresponding potential range is expected to be where SCC would occur. FIGURE 3.8 shows an example of high purity iron tested in caustic solution at 100 °C. The slow and fast scan rates are 1V/h and 100 V/h, respectively. The large difference in current density is marked using an arrow in the plot, and the potential range of SCC is around -1 V (SCE).
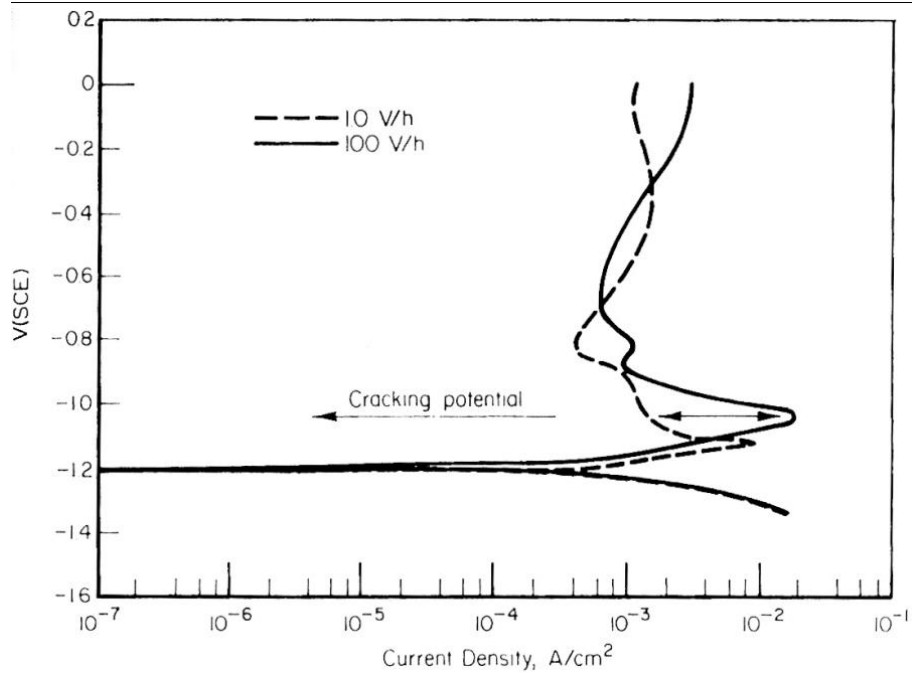
FIGURE 3.8 Potentiodynamic polarization curves for high-purity (carbon) iron tested at 100 °C in deaerated aqueous 35 wt.% NaOH at scan rates of 1 and 100 V/h. [131]

The slow- and fast-scan polarization behavior also provides information regarding the relative SCC intensities of different materials in different environments. In this way, we could compare the SCC intensities of DSS 2205 in solutions with different pH values through an SCC parameter, P_{SCC}, so that we can identify the optimum pH value for SCC to occur. This parameter was proposed by Fang and Staehle [132], and it is defined as

$$P_{SCC} = [R_{SR}(E)][i(E)_{fast}] = [R_{SR}^2(E)][i(E)_{slow}] \qquad 3.1$$

where $R_{SR}(E)$ is the scanning rate ratio as a function of potential E for current densities i measured at fast and slow scan rates,

$$R_{SR}(E) = \frac{i(E)_{fast}}{i(E)_{slow}} \hspace{6cm} 3.2$$

The parameter P_{SCC} is an indicator of SCC intensity. It assumes that the SCC intensity is proportional to the probability of occurrence of SCC times the current density corresponding to the fast scan, as illustrated by the first part of EQUATION 3.1. The probability of occurrence of SCC is represented by scanning rate ratio $R_{SR}(E)$, because at potential values where large current density difference exists, there is more chance of SCC happening. The reason that current density corresponding to the fast scan $i(E)_{fast}$ was related to P_{SCC} is because it is proportional to the dissolution velocity at the crack tip. Baek *et al.* have plotted P_{SCC} for Alloy 600 in 10 wt.% NaOH solution at 315 °C. Fast and slow scans were measured at 1200 mV/min and 20 mV/min, respectively (FIGURE 3.9). The peak value of P_{SCC} quantifies the SCC intensity, and the corresponding potential range -0.25 V (Ni) is the SCC potential range.
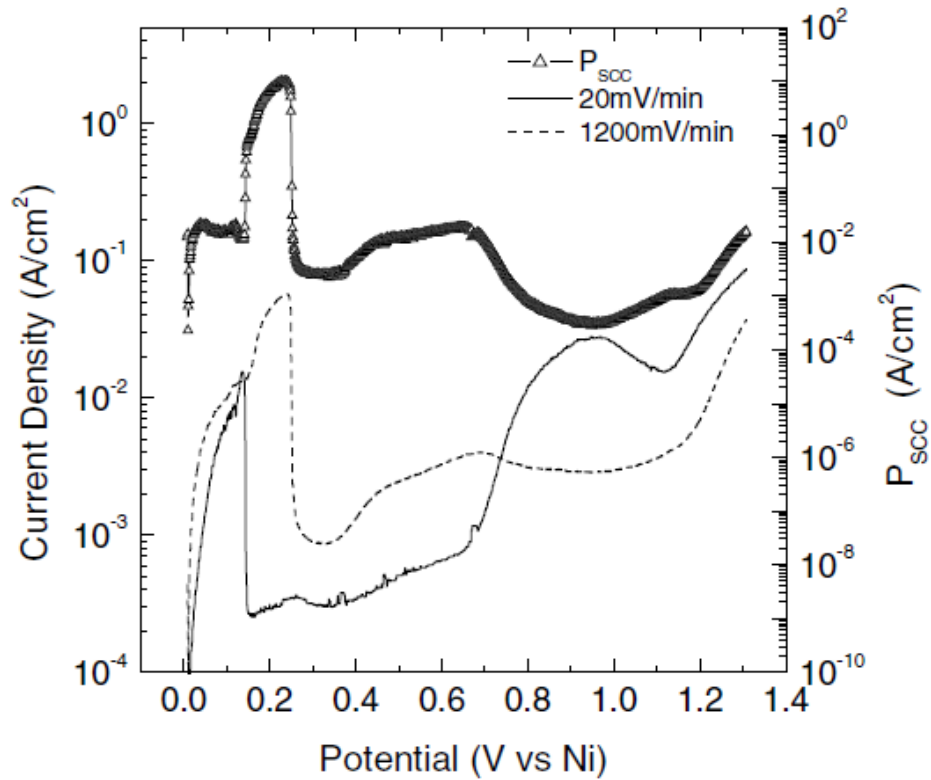
FIGURE 3.9 Fast and slow scanning polarization curves and SCC parameter P$_{SCC}$ as a function of potential for Alloy 600 in 10 wt.% NaOH solution at 315 °C. [133]

3.4.2 SSRTs

To study the stress corrosion crack initiation and propagation in selected environments, SSRT method was used throughout this study. SSRT could also be done at specific applied potential values within the potential range, as predicted by the polarization tests. There are a number of SCC test methods available, such as constant load or constant strain methods, but SSRT was specifically selected as it can also provide

information on the effect of strain rate on SCC susceptibility, which is very relevant for understanding the role of cyclic stresses parameters.

The standard practice of SSRT is outlined in ASTM G129. In this study, smooth cylindrical samples exposed to a corrosive environment were pulled at a constant extension rate (FIGURE 3.10). This is why SSRT is also known as constant extension rate testing (CERT). In fact, CERT is a more precise name for this type of tests, because the extension rate is constant during the testing, but the true strain rate changes with time. Therefore, when a strain rate is specified for a SSRT, it is actually the initial strain rate. Room temperature SSRT were conducted in a glass cell, while the high temperature tests were conducted in an autoclave equipped on a SSRT rig, as shown in FIGURE 3.11 (a) and (b). Inside the autoclave, the specimen is electrically isolated using the PTFE tubes and ceramic washers, as shown in FIGURE 3.12.

Motor

Load Cell

Environment Cell

Specimen

Test Rig
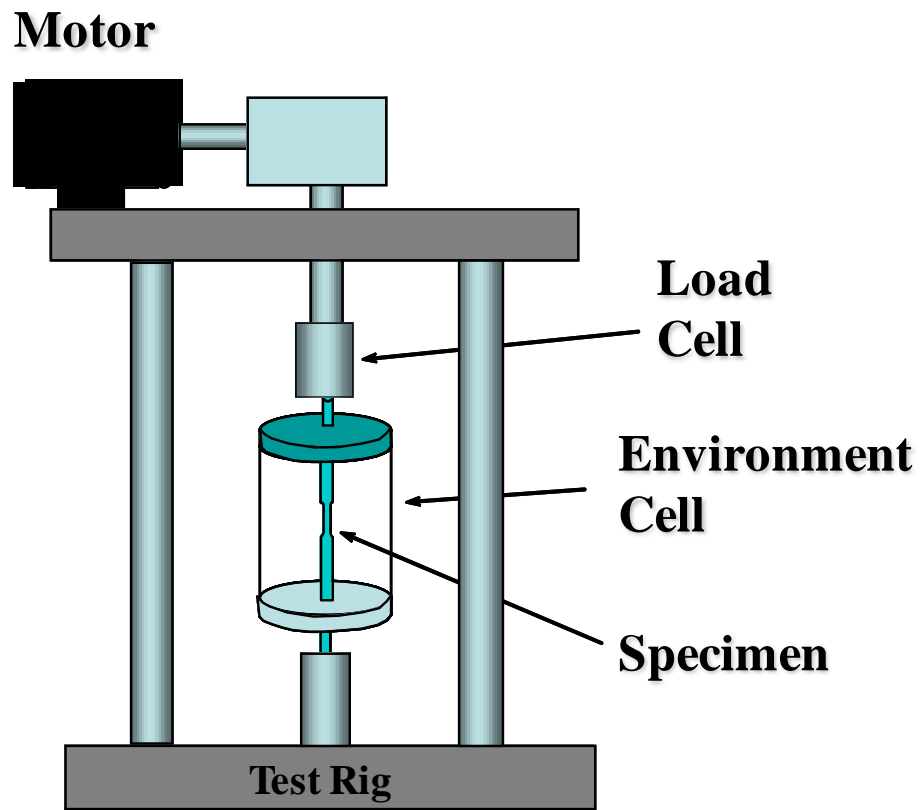
FIGURE 3.10 Schematic drawing of SSRT rig.

(a)
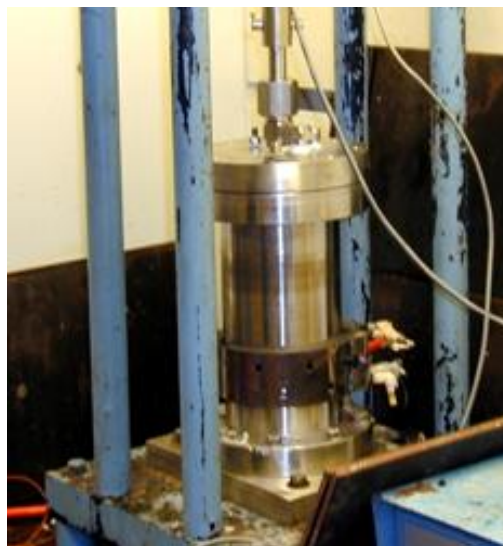
(b)

FIGURE 3.11 Environmental cells for SSRT (a) glass cell for room temperature tests (b) autoclave for high temperature tests.
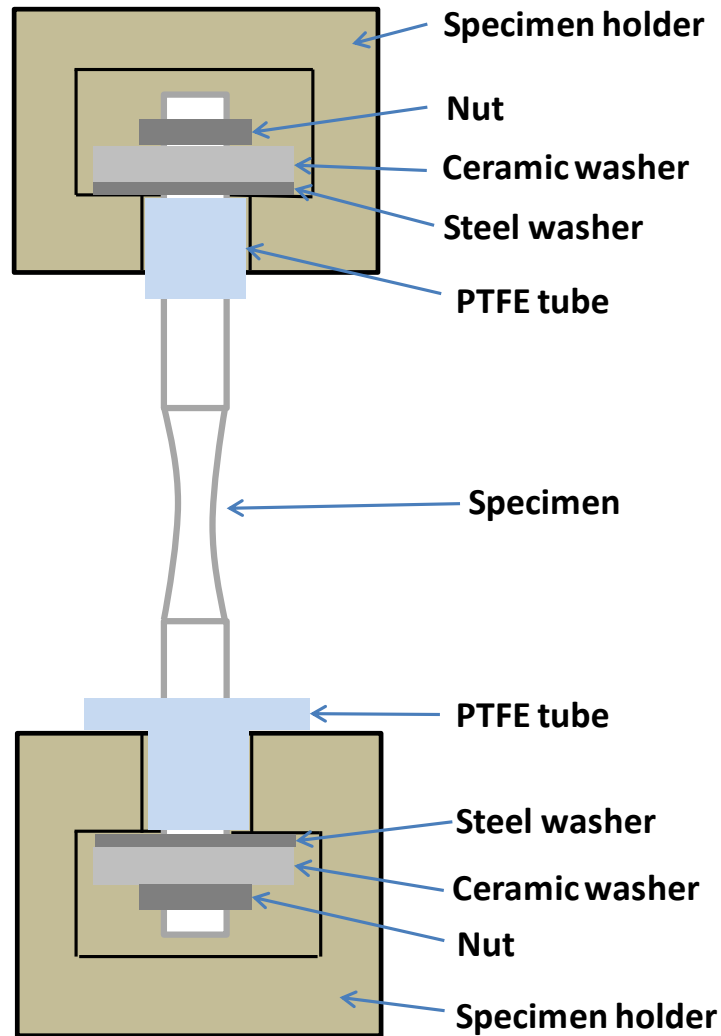
FIGURE 3.12 Electric isolation for the sample inside the autoclave.

A Wenking® potentiostat was used to apply the constant potential when the specimen needed to be polarized during the SSRT. In case when the transient current was also measured during SSRTs, Gamry Reference 600 potentiostat was used.

SCC resistance of materials was evaluated by comparing parameters such as time-to-failure ratio, percentage reduction of area, crack velocity, crack density, and so on. After

each test, the fractured sample was sectioned, mounted, and polished. Crack morphologies were observed by examining the mounted sample under microscope. Parameters like crack velocity and crack density were also quantified in such way.

SSRTs were conducted for DSS 2205 at different potential values and different strain rates to investigate the SCC susceptibility and intensity in acidic NaCl environment. Similarly, SSRTs were also performed for cold-worked DSS 2205 under same conditions to illustrate the cold-working effect.

Interrupted SSRTs were performed to study the crack initiations of DSS 2205 in NaCl and WL environments. Threshold stress and strain for crack initiations were identified by examining the sample after testing under optical microscope and scanning electron microscope (SEM).

3.4.3 Static and Cyclic Creep Tests

Effect of low frequency cyclic stresses on the creep behavior of DSS 2205 was investigated. DSS contains almost equal volume fraction of austenitic phase with face centered cubic (FCC) crystal structure, and ferritic phase with body centered cubic (BCC) crystal structure. Therefore, the two phases also have different mechanical properties, especially plastic deformation behavior. The roles of the individual phases in plastic strain accumulation were studied by conducting static and cyclic creep tests on DSS 2205, austenitic stainless steel 304L (FCC), and ferritic stainless steel 430 (BCC).

The static creep tests were carried the cyclic creep tests were accomplished by retrofitting the creep machine, as shown in FIGURE 3.13. Instead of using a constant

load, a container with known amount of water was attached to the loading beam was used to apply a given load to the specimen. Typical tensile samples were again used in all creep tests. Cyclic loading was applied by pumping water into and out of the container at a controlled rate. The two pumps were connected to two programmed timers, so that the pumps work intermittently to apply predetermined cyclic loads to the sample. An Epsilon® extensometer with the range of $\pm10\%$ was hooked on the sample using springs, to measure the elongation of the specimen. To prevent the extensometer from slipping on the smooth sample, special cylindrical fixtures were fitted on the shoulder of each tensile sample to help the extensometer stay in place. The fixtures were machined such that the knife edges of the extensometer fitted perfectly into the grooves. These fixtures were attached to the sample shoulders by screws, as can be seen in FIGURE 3.13. Actual load on the test sample was monitored and recorded by load cell attached to the load-train.

FIGURE 3.13 Creep test setup.

In order to compare the creep test results under static and cyclic loading, two types of creep tests have been performed. The first type was pure static and pure cyclic creep test. In this case, either static or cyclic loading was applied to the specimen through the whole test, and the maximum stress of the cyclic loading equals to the stress of static loading. The minimum loads for all cyclic stress tests were the same, which was the

weight of the bucket, which was about 160 lbs. However, the maximum value of applied

load was different for each test, as mentioned in results. A schematic load profile of low

frequency cyclic stress in pure cyclic creep tests is shown in FIGURE 3.14. The loading

rate for the pure cyclic creep tests was 4 lb/s. The second type of creep test is static-

cyclic creep test, in which the static loading followed by cyclic loading was applied to the

same specimen. The load profile in static-cyclic creep tests is schematically shown in

FIGURE 3.15. In static-cyclic creep tests, the pre-straining effect was included, because

the specimens were being strained by the static loading before the cyclic loading started.

In contrary to the pure cyclic creep tests, the minimum stress in static-cyclic creep tests

was zero. Other than that, the frequency for the static-cyclic creep tests and pure cyclic

creep tests were different, as can be seen in FIGURE 3.14 and FIGURE 3.15.

All creep tests were performed at room temperature in air. In this way, the high

temperature effect on creep was eliminated.
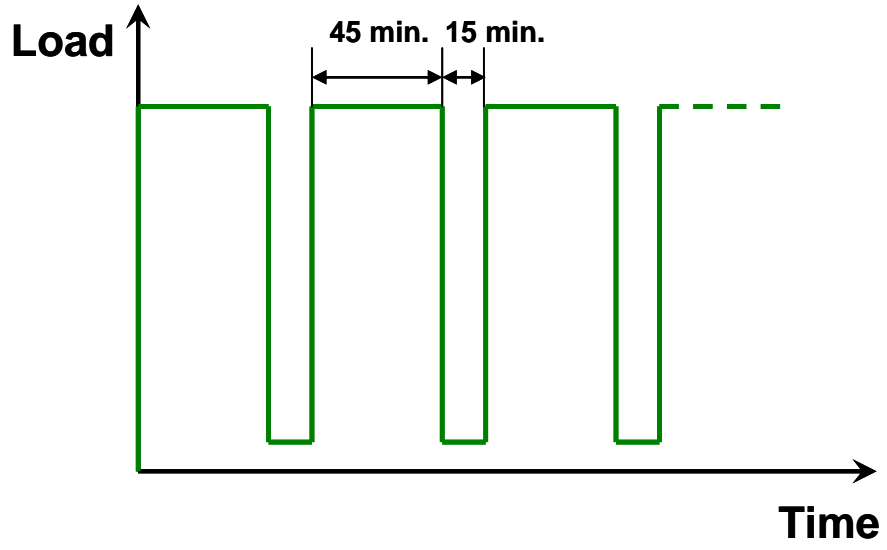
FIGURE 3.14 Load profile for pure cyclic creep tests.
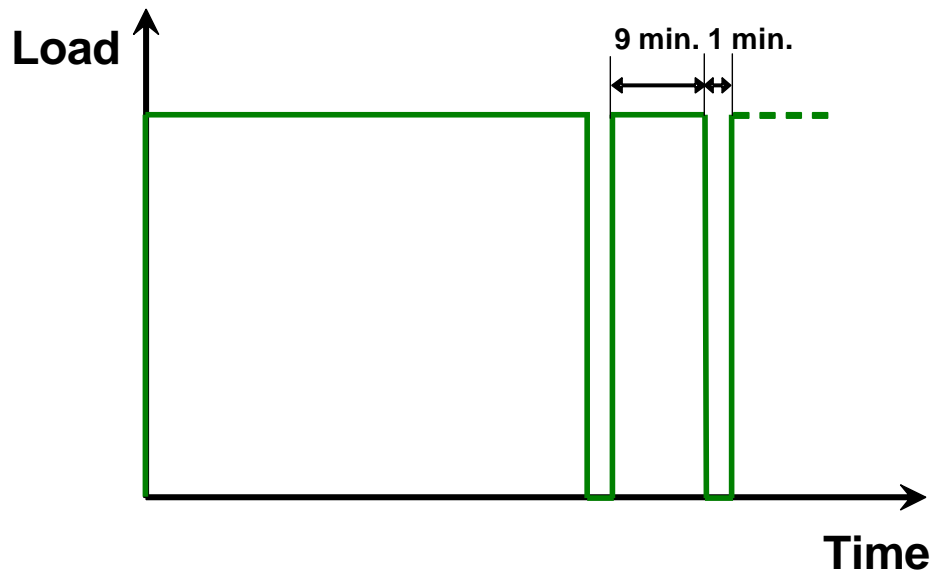
FIGURE 3.15 Load profile for static-cyclic creep tests.

Separate cyclic and static creep tests were performed for DSS 2205 at different stress levels. The cyclic stress effect was revealed by comparing the results of static and cyclic tests at the same stress level, and the stress level effect was illustrated by comparing the cyclic creep tests at different maximum stresses.

Cyclic and static creep strains were compared using cyclic creep acceleration parameter [5], which is defined as

$$\frac{\varepsilon_{cn} - \varepsilon_{c1}}{\varepsilon_{st_n} - \varepsilon_{st_1}} \qquad\qquad 3.3$$

where $\varepsilon_{cn} - \varepsilon_{c1}$ is the total strain in the n-th stress cycle minus the strain in the first cycle under cyclic loading and $\varepsilon_{st_n} - \varepsilon_{st_1}$ is the strain occurring during the same period of time in the static creep test.

In order to understand the role of the two phases or two different crystal structures of DSS 2205 (BCC vs. FCC) in strain accumulation process, cyclic and corresponding static creep tests were also conducted for ferritic SS 430 (BCC) and austenitic SS 304L (FCC). Although the composition of 304L and 430 is not exactly the same as for the austenitic and ferritic phases for the DSS 2205, but these alloys were selected for the following reasons. First, although the chemical composition can play an important role, the purpose of this study is to distinguish the creep behaviors of different crystal structures in the strain accumulation process. Second, the commercially available stainless steel grades that have the closest chemical compositions to the two phases of DSS 2205 (TABLE 3.3) are Sea-Cure® (BCC) and 316L (FCC). However, Sea-Cure® is only available in

thin tubes which cannot be machined to tensile samples. As for 316L, although it has 2-3%

of molybdenum, which it is closer to the austenite phase of DSS 2205 in terms of

chemical composition, but typically chromium content for 316L is lower. However,

mechanical behavior of 316L is very similar to that for the 304L.

TABLE 3.3 Average measured chemical compositions of DSS 2205 and its individual

phases and the nominal composition of SS 430, SS 304L.

Alloy	Element				
	Fe	Cr	Ni	Mn	Mo
2205C	bal.	22.6	5.61	1.33	3.21
α	bal.	24.76	3.94	1.13	5.37
γ	bal.	21.71	6.67	1.69	3.16
430	bal.	16-18	0.75	1.00	0.00
304L	bal.	18-20	8-12	2.0	0.00

In addition to the pure static and cyclic creep tests, SS 430 and SS 304L were also tested

in static load followed by cyclic creep tests (denoted as "static-cyclic creep tests"). In

this type of tests, a static load was applied to a specimen for a certain period of time,

and then cyclic loading of the same stress level was applied to the specimen. In these

tests, the creep strain rate of the material was exhausted before the cyclic loading was

applied, because the creep rate decreased rapidly under constant loading at room

temperature. Through these test results, the effect of strain rate before cycling was investigated.

3.4.4   Low Frequency CF Tests

Under the conditions that the DSS 2205 is susceptible to SCC, low frequency CF tests were performed in acidic chloride as well as WL environments.

CF tests were also conducted on SSRT machine with a programmable logic controller (PLC) connected to it. PLC controls the maximum and minimum stress levels of the cyclic loading. The loading mode was tension-tension with a triangular waveform, as shown in FIGURE 3.16. Effects of stress level and stress ratio (ratio of minimum stress to maximum stress) were studied by varying them in each test. In the same corrosive environment, identical extension rate was used for CF tests. Frequency, on the other hand, changes with stress range, since tests were done at constant extension rate. However, frequencies for all CF tests in this study were in the range of 10^{-5} Hz.
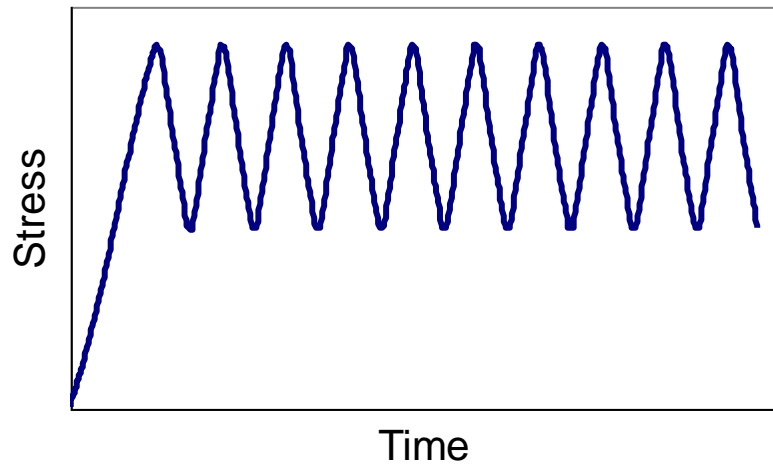
FIGURE 3.16 Tension-tension triangular loading profile for CF tests.

Due to the small size of the crack initiations in the CF tests, smooth sample surfaces were examined under SEM. Crack size and density were recorded during the examination.

Work hardening effect on CF was studied using the cold-worked DSS 2205 under same conditions.

3.4.5   Microhardness Measurement

In order to demonstrate the load sharing or strain distribution between the two phases of DSS 2205, microhardness measurements were done on samples strained to different plastic deformations. Since strain rate has an influence on the mechanical properties of materials, samples were strained using interrupted SSRTs. In this way, the hardness results are comparable to the results of the CF tests, which are also performed at the same strain rate.

Strained tensile samples were sectioned, mounted and polished to 0.05 μm. With this surface finish, the phases were visible under microscope, so no further etching was required for these samples. A Buehler microhardness tester was used to measure the Vickers hardness. Load applied was 100 gf, and the loading time was 10 sec.

CHAPTER 4 ENVIRONMENTAL EFFECT ON STRESS CORROSION

CRACKING OF DUPELX STAINLESS STEEL 2205

4.1 Introduction

Numerous reported failure cases and laboratory studies have suggested that seawater or formation water evaporating on a hot metal surface could provide a concentrated chloride-containing environment in which stress corrosion cracking (SCC) is possible, and this can be a significant hazard for marine applications of DSSs such as offshore pipelines [37, 134-136]. The results from these papers illustrated that high concentration and elevated temperature favor SCC of duplex stainless steels (DSSs) in chloride environment. In Cottis and Newman's review on SCC resistance of DSSs, they pointed out that SCC of stainless steels is more likely to happen in hot, concentrated MgCl$_2$ solutions, certainly at temperatures greater than 130 °C [134]. Under evaporative seawater conditions, Hinds and Turnbull identified a threshold temperature of SCC between 70 °C to 80 °C for a 22Cr and a 25Cr DSS, when the applied stress is 90% $\sigma_{0.2}$ [136]. Huizinga and his co-workers [135] reported a failure of 22%Cr DSS pipework on an offshore platform in the North Sea (UK). Their investigation revealed that the pipework works at a temperature of about 140 °C, with no or very little oxygen, and the failure was caused by the extremely high level of chloride concentration due to evaporation. Other than simulating the evaporation of seawater, researchers have also conducted tests in hot concentrated chloride solutions. Tseng and Tsai compared the SCC behavior

of 22%Cr DSS in three chloride-containing environments: 3.5 wt.% NaCl at 80 °C, 40 wt.% $CaCl_2$ solution at 100 °C, and boiling 45 wt.% $MgCl_2$ at 155 °C [35, 36]. Their slow strain rate test (SSRT) results showed that DSS 2205 is susceptible to SCC in both $CaCl_2$ and $MgCl_2$ solutions, but resistant to SCC in NaCl solution. Further investigation confirmed that the SCC resistance exhibited by DSS in NaCl should be attributed to the lower concentration of the NaCl solution used in these tests. At 90 °C, DSS 2205 is susceptible to SCC in 26 wt.% NaCl solution when the electrochemical potential is around and above pitting potential [33].

At room temperature, SCC of DSSs is still possible in concentrated chloride solutions but only when a favorable external potential is applied. Mill-annealed DSS UNS S32550 (25%Cr, 6%Ni, 3%Mo) loaded to 90% of yield strength in a boiling 35% $MgCl_2$ solution was found to be immune to SCC under open circuit potential (OCP), but becomes susceptible to SCC when an external potential of 135 mV more positive than OCP was applied [137]. OCP is the equilibrium potential of the electrochemical cell, when there is no external voltage applied. Sanchez *et al.* [38] found that at OCP, both DSS 2304 and DSS 2205 were resistant to SCC in a 50 g/L NaCl solution at room temperature. On the contrary, when a 300 mV (SCE) potential was applied, lean DSS 2304 was susceptible to SCC under the above conditions, but DSS 2205 was still resistant to SCC due to its better corrosion resistance. However, in a more concentrated and acidified NaCl solution, e.g., 26 wt.% and pH 2.0, DSS 2205 was susceptible to SCC within a certain potential range of -245 mV (SCE) to -500 mV (SCE), at room temperature [34].

In summary, the SCC of DSSs is more likely to occur at higher temperature in concentrated chloride environment. At room temperature, SCC is possible when a favorable electrochemical potential is applied. Lower pH of the solution also helps in promoting SCC of DSSs.

Cold-worked commercial stainless steel has been found to corrode at the same rate as an annealed stainless steel in natural waters [138], but in hydrochloric acid, cold-working increased the corrosion rate several fold [139]. Khatak *et al.* found that the SCC susceptibility of type 316 SS in boiling $MgCl_2$ increases with increasing of prior deformation [140]. Moreover, Garcia *et al.* found that prior cold-working could change the SCC mode of type 304 SS in chloride environment [141]. The intergranular SCC of solution annealed 304 SS will change to transgranular SCC with the increase of cold-working degree level. Kwon and Kim [137] reported that the cold work of DSS UNS S32550 significantly increases the SCC susceptibility in boiling 35% $MgCl_2$ by shifting the critical cracking potential in the negative direction. Critical cracking potential is the potential below which the material is immune to SCC.

In order to understand the SCC of DSS 2205 in NaCl solution, the role of environmental parameters on SCC was studied, specifically, the effect of solution pH and applied potential. Prior work has shown that DSS 2205 is susceptible in very concentrated caustic solutions, including the white liquor (WL) environment used in the pulp and paper industry [50, 57]. However, this chapter focuses on the NaCl environment. In addition, the effect of cold work on the SCC of DSS 2205 in the two environments was

96

illustrated by comparing the SCC results of as-received (mill-annealed) and cold worked material.

4.2   Results and Discussion

4.2.1   Effect of pH

The effect of solution pH values on SCC of DSS 2205 were studied by potentiodynamic polarization tests at room temperature. The solution used was 26 wt.% NaCl solution, and the pH value was adjusted using diluted HCl. Both bar and plate annealed DSS 2205 materials were used in these tests for comparison, denoted as 2205B and 2205C respectively. Slow- and fast-potential scan rates were used for DSS 2205B to illustrate the SCC intensity at different pH values. The pH values and the scan rates used in these tests are listed in TABLE 4.1.

TABLE 4.1 Potentiodynamic polarization test matrix.

Material	pH	Scan Rate (mV/s)
2205B	2 3 4 5	1
	2 3 4 5	10
2205C	2 3 4 5	1

The anodic potentiodynamic polarization curves of DSS 2205B and 2205C at 1 mV/s are summarized in FIGURE 4.1 and FIGURE 4.2, respectively. The anodic polarization behavior for the two batches of materials was similar. An active/passive transition peak was observed at pH = 2 and 3. At pH = 4 and 5, both bar and plate DSS2205 material exhibited spontaneous passivation, as they showed a better corrosion resistance in the active region. These results revealed the possibility of SCC in 26 wt.% NaCl solutions with pH = 2 and 3, because film-induced SCC mechanism is possible for the material/environment systems that exhibit an active/passive transition peak. Moreover, the potential range where the SCC occurs is near this transition region, as highlighted in FIGURE 4.1 and FIGURE 4.2. From these polarization curves, a decrease of OCP with the decrease of pH value was observed, indicating a decrease of SCC resistance with decreasing of pH values. That is, DSS 2205 should experience the most severe SCC in NaCl solution with pH = 2 among the pH values tested.
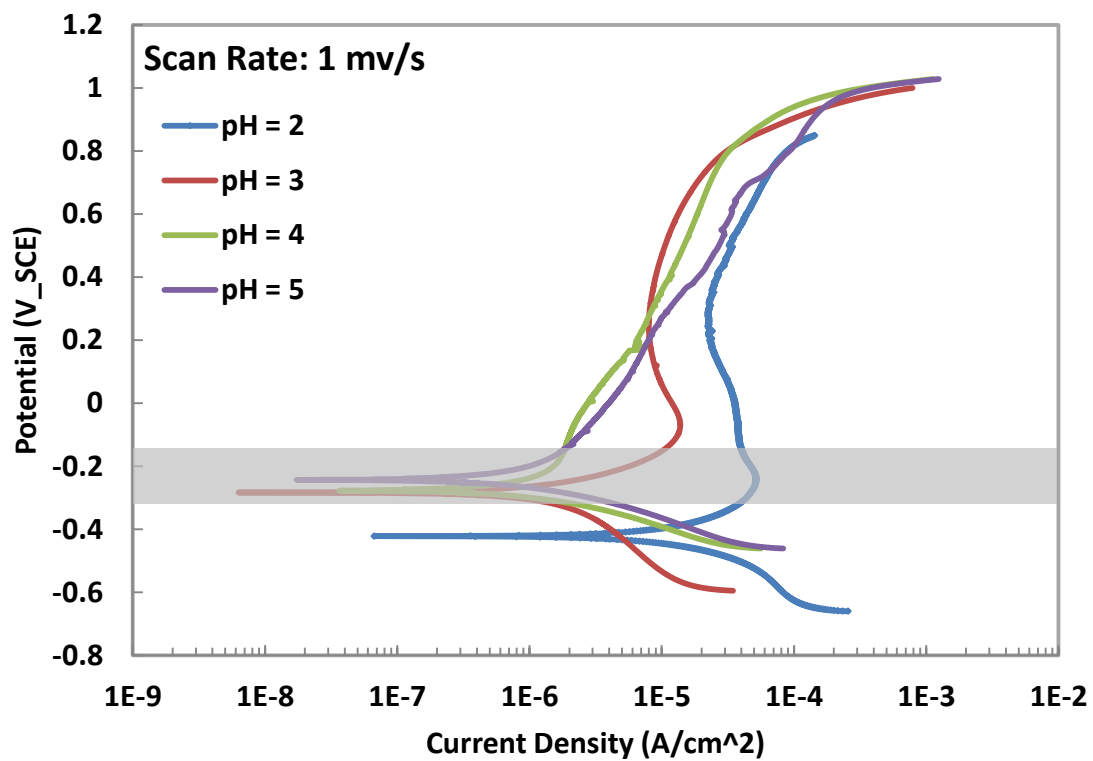
FIGURE 4.1 Potentiodynamic polarization curves of DSS 2205B at room temperature in 26 wt.% NaCl solution with pH ranging from 2.0 to 5.0 at a scan rate of 1 mV/s.
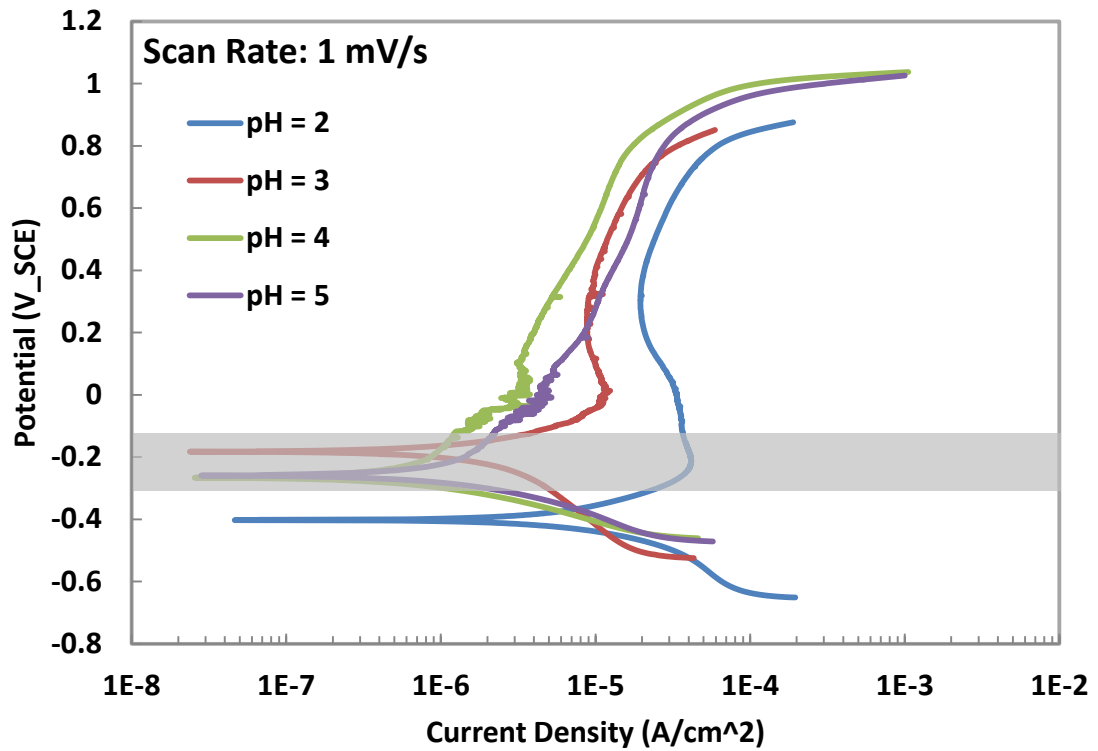
FIGURE 4.2 Potentiodynamic polarization curves of DSS 2205C at room temperature in 26 wt.% NaCl solution with pH ranging from 2.0 to 5.0 at a scan rate of 1 mV/s.

Slow- and fast-scan polarization tests confirmed the conclusion above quantitatively. SCC susceptibility parameter P_{SCC}, which was defined in Section 3.4.1, could be used to quantify the SCC intensity. Combining EQUATION 3.1 and EQUATION 3.2, P_{SCC} can be calculated by the following equation

$$P_{SCC}(E) = \frac{\left(i_{fast}(E)\right)^2}{i_{slow}(E)} \qquad\qquad 4.1$$

where $i_{fast}(E)$ is the current density obtained by a fast scan rate, and $i_{slow}(E)$ is the corresponding current density at a slower scan rate. Since the fast- and slow-scan current densities are functions of potential E, $P_{SCC}(E)$ changes with potential as well. In order to determine the effect of pH on SCC intensity, anodic polarization tests at scan rate of 1 mV/s and 10 mV/s were conducted for DSS 2205B in NaCl solutions with pH = 2 and 3. Fast and slow scan polarization curves are plotted together for comparison, as shown in FIGURE 4.3 (a) and FIGURE 4.4 (a). The $P_{SCC}(E)$ values calculated by EQUATION 4.1 are also plotted in the same figure. The results demonstrated that SCC in pH = 2 solution should be more severe than that in pH = 3 solution, indicating by the much larger peak value of $P_{SCC}(E)$ in pH =2 solution, as shown in the zoomed graphs of FIGURE 4.3 (b) and FIGURE 4.4 (b). The potential range corresponding to the peak value of $P_{SCC}(E)$ coincides with the OCP range of the slower scan curve in both cases. As discussed in Section 3.4.1, at this potential range, there is more chance of SCC happening. That is, within this potential range, the passive film can be formed, but not stable. Hence this potential range provides the possibility of keeping the crack tip active while the rest of the sample surface passive.
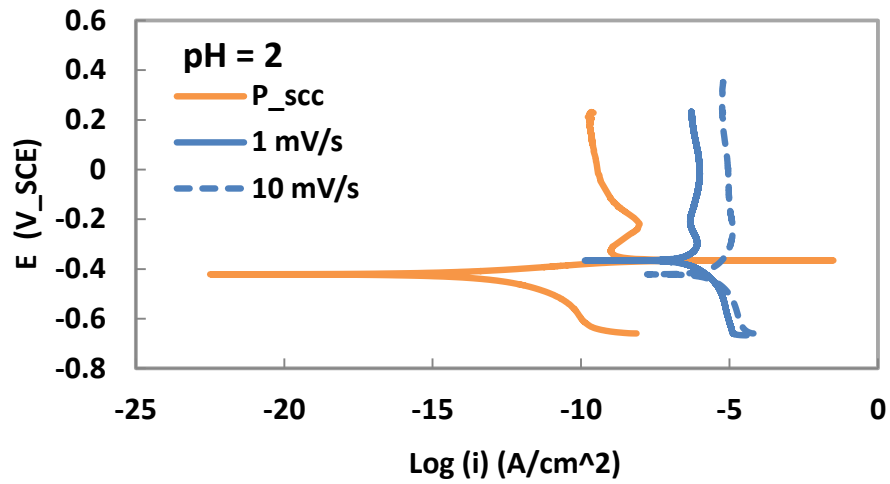
(a)
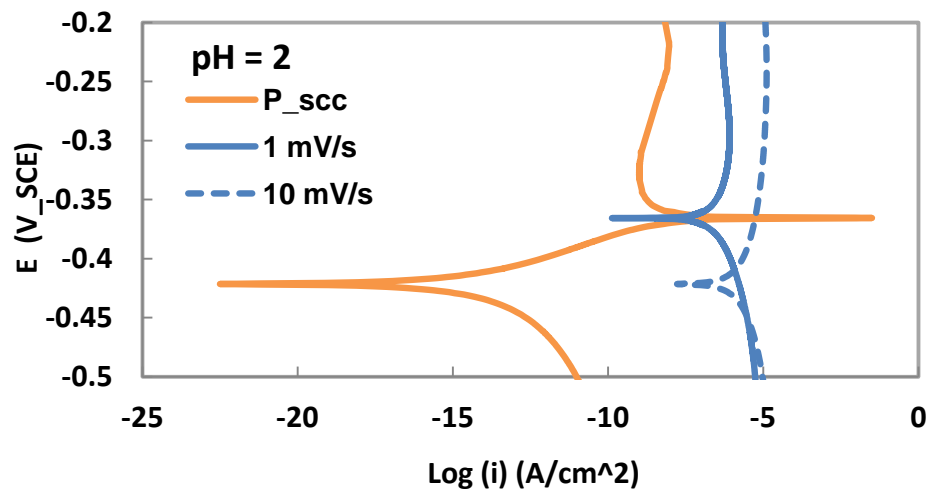
(b)

FIGURE 4.3 (a) Anodic polarization curves of DSS 2205B in 26 wt.% NaCl solution with pH = 2, at slow and fast scan rates and corresponding SCC intensity parameter P_{SCC}. (b) Blow up of the potential range of P_{SCC} peak.

102
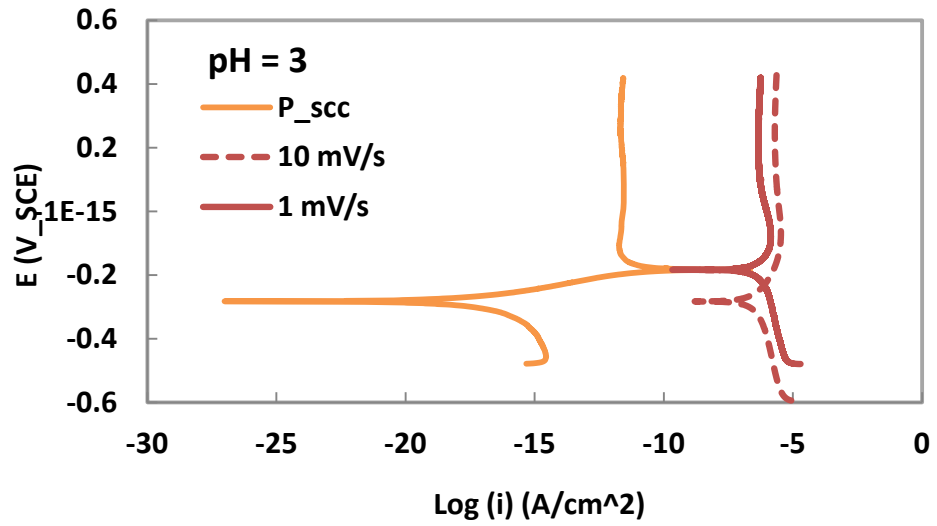
(a)
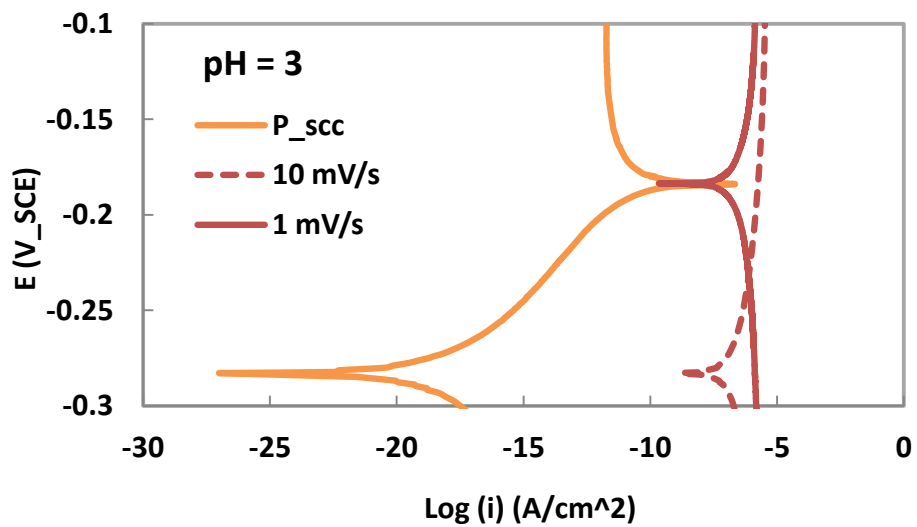
(b)

FIGURE 4.4 (a) Anodic polarization curves of DSS 2205B in 26 wt.% NaCl solution with pH = 3, at slow and fast scan rates and corresponding SCC intensity parameter P_{SCC}. (b) Zoomed graph of the potential range of P_{SCC} peak.

Liu and Wu [142] have investigated the pH influence on alloy 254SMO (19.9% Cr, 17.9% Ni, 6.0% Mo) in 3.5% NaCl solution. They also observed active/passive transient peaks in polarization curves obtained in solutions with pHs ranging from 0.1 to 3, and spontaneous passivation behavior in curves at solution pH values of 4 and 5. They attributed the different polarization behaviors to the composition of surface film formed in different pH solutions. XPS analysis was performed on the surface passive film formed in weak (pH = 5) and strong (pH = 0.8) acid solutions, and they found that the outermost layer of the films are iron oxides and chromium hydroxide, $Cr(OH)_3$, respectively. The inner layer of the film formed in the two solutions was primarily Cr_2O_3. Although alloy 254SMO has a significantly higher Ni content than DSS 2205, there is hardly any nickel oxides detected in the surface film of 254SMO. Hence, considering the similar electrochemical behavior exhibited by the two types of DSSs, it is reasonable to expect that DSS 2205 may have a similar passive film compositions with DSS 254SMO.

In summary, anodic potentiodynamic polarization test results showed that concentrated NaCl with pH = 2 provides the most aggressive environment for SCC to occur, compared to other acidic pH values tested in this study. Subsequent SSRT and cyclic corrosion fatigue (CF) testing for chloride environment are all conducted in 26 wt.% NaCl solution with pH 2.

4.2.2 Effect of Potential

Although the electrochemical polarization tests could predict a rough potential region where SCC could happen, actual tests are needed to test and quantify the SCC

susceptibility of any given alloy under those conditions. SSRT were selected for this study SCC susceptibility and compare environmental effects on SCC. SSRT with applied potential were used to evaluate the SCC behavior of DSS 2205 at specific electrochemical conditions. A series of SSRT were performed within a wide range of potential to ensure the SCC potential range is covered, and the tests were conducted at room temperature in 26 wt.% NaCl solution with pH 2, at an initial strain rate of 1×10^{-6} s^{-1}. After the SSRT was over, the samples were further characterized to quantify the percentage reduction of area (% RA) and % elongation. One half of the failed tensile samples was sectioned, mounted and polished to measure the crack length into the metal. Crack velocity for each test was calculated by measuring the maximum crack depth for SCC for each test, which was used to compare the SCC intensity. Percentage reduction of area was defined using the following equation

$$\% \ RA = \frac{A_0 - A_f}{A_0} \times 100\% \qquad\qquad 4.2$$

where A_0 and A_f are the original and final sample cross section area, respectively. When SCC happens, the fracture tends to be brittle, hence the % RA will decrease compared to ductile failure. Therefore, smaller % RA corresponds to more severe SCC. Crack velocity was calculated using the largest crack length divided by the total test time. FIGURE 4.5 shows the effect of the applied potential on the two parameters. Results in FIGURE 4.5 indicated that DSS 2205 is susceptible to SCC in acidified NaCl solution in a wide potential range from -375 mV to -520 mV (SCE).
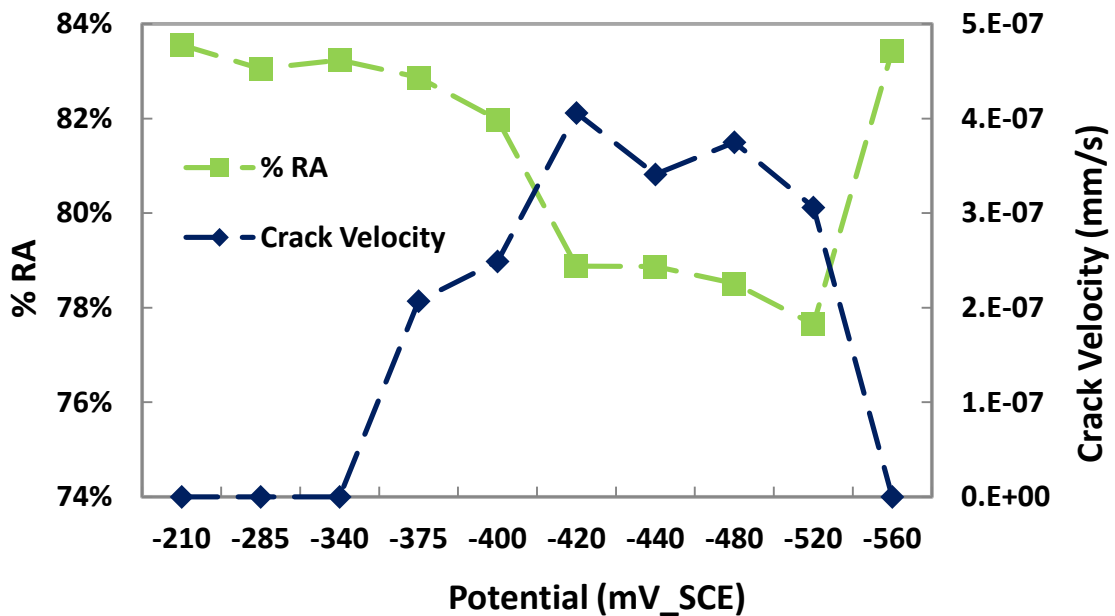
FIGURE 4.5 Percentage reduction of area and crack velocity at different potentials obtained by testing DSS 2205B in 26 wt. % NaCl with pH = 2, tested by SSRT at a strain rate of $1×10^{-6}$ s^{-1}.

Besides, the reduction of ductility of materials could also be reflected by the SSRT curves. In FIGURE 4.6, the ductility of DSS 2205 was significantly reduced when the material was tested in chloride environment, compared to in air. Moreover, as the potential decreases from -285 to -420 mV (SCE), the SCC intensity increases (FIGURE 4.5) and the ductility decreases. The SSRT curves obtained at -285, -375, and -420 mV (SCE) in FIGURE 4.6 have illustrated this trend, although the difference is not very large.
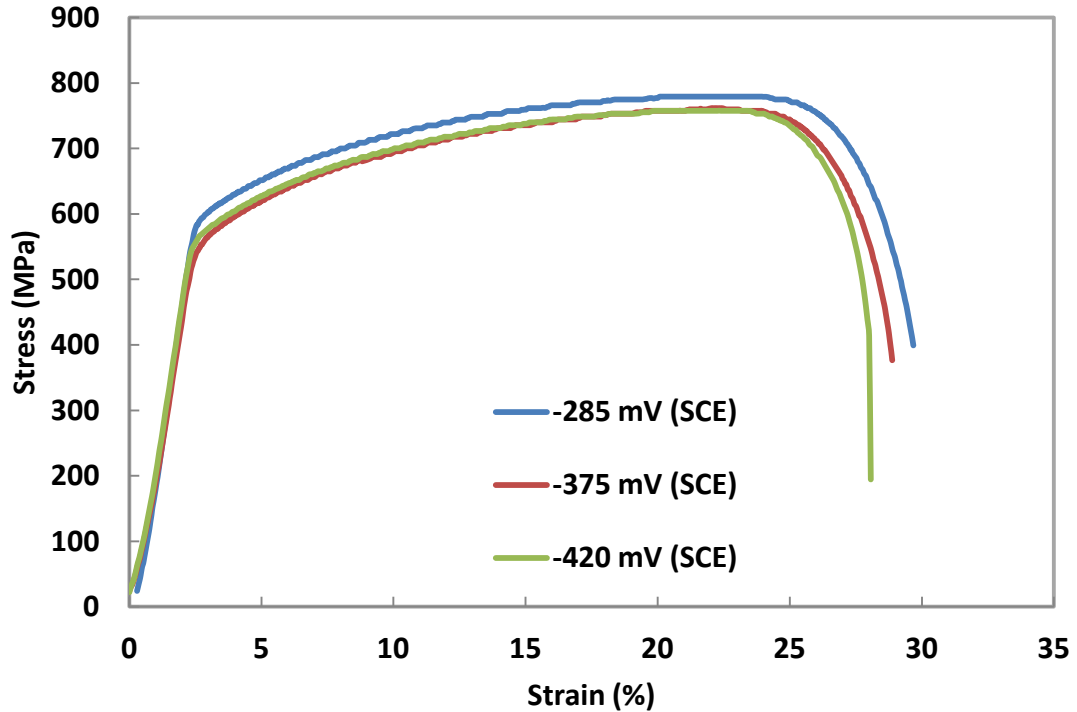
FIGURE 4.6 SSRT curves of DSS 2205 tested in air and 26 wt.% NaCl of pH = 2 under different applied potentials. SSRTs were performed at room temperature and at a strain rate of 1×10^{-6} s^{-1}.

Visual inspection of the tensile sample surfaces at a magnification of 10X (FIGURE 4.7) confirmed the effect of the applied potential illustrated by the results in FIGURE 4.5 and FIGURE 4.6. At lower and higher potential values of -285 mV (SCE) and -560 mV (SCE), there is no cracking observed on the sample surface, and the samples fractured in a ductile manner. At medium potential values of -375 mV (SCE) and -420 mV (SCE), DSS 2205 was found to be susceptible to SCC. From the observation of the sample surfaces, SCC was more severe at -420 mV (SCE) than at -375 mV (SCE). This is consistent with the

results of FIGURE 4.5 and FIGURE 4.6, e.g., smaller % RA, higher crack velocity, and smaller ductility for the sample tested at -420 mV (SCE). This potential range was also consistent with the potential range predicted by the peak value of P_{SCC} (E) in FIGURE 4.3. Within this potential range, the film rupture induced SCC is readily to happen.

On all the samples showing SCC, the cracks mainly appear in the necking region, indicating the importance of plastic deformation in SCC of DSS 2205 under the testing conditions. The sectioned crack morphologies of the cracking shown in FIGURE 4.7 (b) and (c) are illustrated in FIGURE 4.8 (a) and (b), respectively. Under -375 mV (SCE), the cracks appeared mainly in the region with significant plastic deformation, as indicated by the curved crack shape in FIGURE 4.8 (a). On the other hand, under a potential of -420 mV (SCE), both curved and straight cracks were observed in FIGURE 4.8 (b), indicating SCC occurred with less plasticity at this potential. Besides, the cracks generated at -420 mV (SCE) are longer in depth than those generated at -375 mV (SCE).
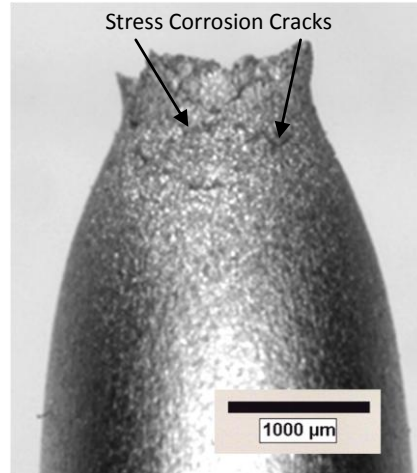
(a) -285 mV (SCE)　　　　　　　　　　(b) -375 mV (SCE)
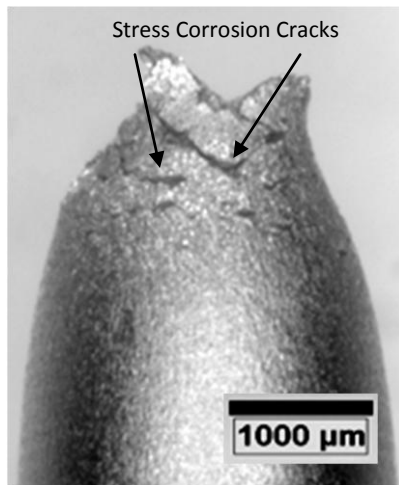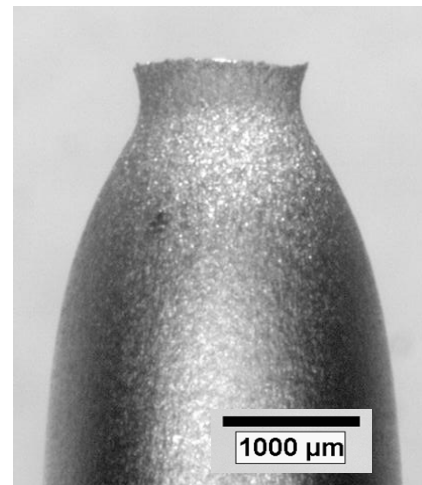
(c) -420 mV (SCE)　　　　　　　　　　(d) -560 mV (SCE)

FIGURE 4.7 Effect of applied potential on SCC of DSS 2205, illustrated by surface cracking after SSRT in 26 wt.% NaCl solution of pH = 2 at different potential values: (a) -285 (b) -375 (c) -420 (d) -560 mV (SCE).
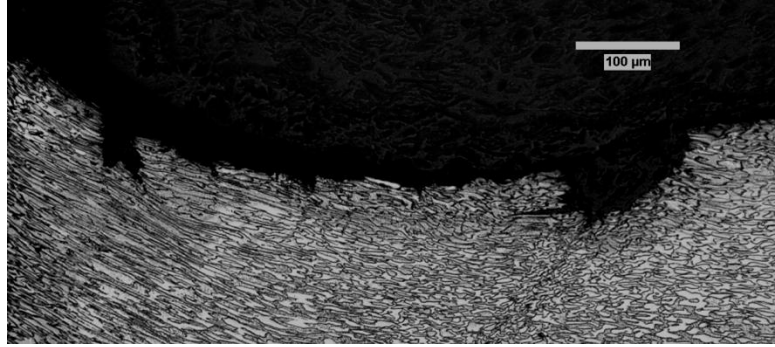
(a)
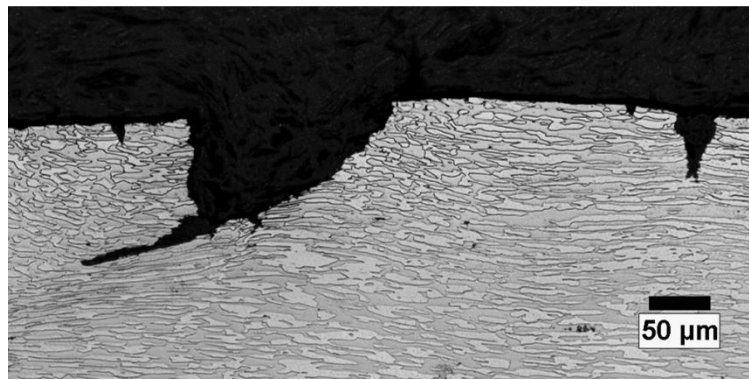
(b)

FIGURE 4.8 Cracking morphology of DSS 2205 tested in 26 wt.% NaCl of pH = 2 at

potentials of (a) -375 mV (SCE) and (b) -420 mV (SCE).

Tsai and Chou [34] have investigated the potential effect for the DSS 2205 in chloride

system. They found a similar SCC susceptible potential range as we obtained. They also

observed a very negative potential range (-800 ~ -1500 mV (SCE)) where DSS 2205 was

attacked by hydrogen assisted cracking. However, the 10 specific potential values they

studied spread over a much larger potential range, about 1400 mV. The present study,

on the other hand, focused on the SCC susceptible potential range close to the open circuit potential of DSS 2205, and the 10 potential values studied were within 350 mV. Therefore, this work revealed a more detail potential effect on SCC of DSS 2205 in acidic NaCl solution.

In summary, SCC behavior of DSS 2205 in acidic NaCl solution at room temperature is affected by applied potential. In 26 wt.% NaCl of pH 2, DSS 2205 is susceptible to SCC in the potential range of -375 mV (SCE) to -520 mV (SCE). Right above and below this potential range, DSS 2205 is immune to SCC in this environment. Within this potential range, various SCC mechanisms involving film rupture could work, such as slip-dissolution model, film induced cleavage model, and localized surface plasticity model. Since this is a potential range where passive film could form but is not stable, it is possible to keep the crack tip active but the rest of the surface passive. With a large anodic current at the crack tip, the passive film cannot repair itself to protect the crack tip from active dissolution. On the other hand, the rest of the sample surface is protected by the passive film formation.

4.2.3   Effect of Cold Working

As discussed in Section 4.1, the cold-worked stainless steels are more susceptible to SCC and have a higher corrosion rate, compared to the annealed stainless steels. Moreover, cold-working is involved in many manufacturing processes of stainless steels, such as cold rolling, drawing, pressing, extruding *et al.* Hence, it is important to investigate the cold-working effect on SCC of DSSs.

In the present study, effect of cold-working on SCC of DSS 2205 was studied in both chloride and WL environments, by comparing the SSRT results of two batches of materials: 2205B (annealed) and 2205A (cold-worked). SSRTs for chloride-containing environment were performed at room temperature at a strain rate of 1×10^{-6} s^{-1}. The test solution is 26 wt.% NaCl of pH 2, and an external potential of -375 mV (SCE) was applied throughout the test. Since the polarization behavior for the two materials is similar, the potential range applied was the same. For WL environment, SSRT were conducted at an initial strain rate of 2×10^{-6} s^{-1} in an autoclave at 170 °C. No external potential was applied in WL tests.

After the SSRT, samples tested in WL environment were covered with a thick layer of black film. The film composition has been characterized using X-ray diffraction by A. Bhattacharya [57]. She found that the film mainly consisted of magnetite (Fe_3O_4) and a certain amount of nickel sulfide (NiS_2) was also present in the film. After each test, the sample was cathodically polarized, and the surface film was removed mechanically by hydrogen bubbles generated on the sample surface. Hence, the sample surfaces looked corroded, but the samples tested in chloride environment were still shiny after the tests. SCC was observed on the surface of both type of DSS alloy samples under the optical microscope, as shown in FIGURE 4.10 and FIGURE 4.10. However, visual inspection indicated that the SCC was more severe for cold-worked material in both environments.
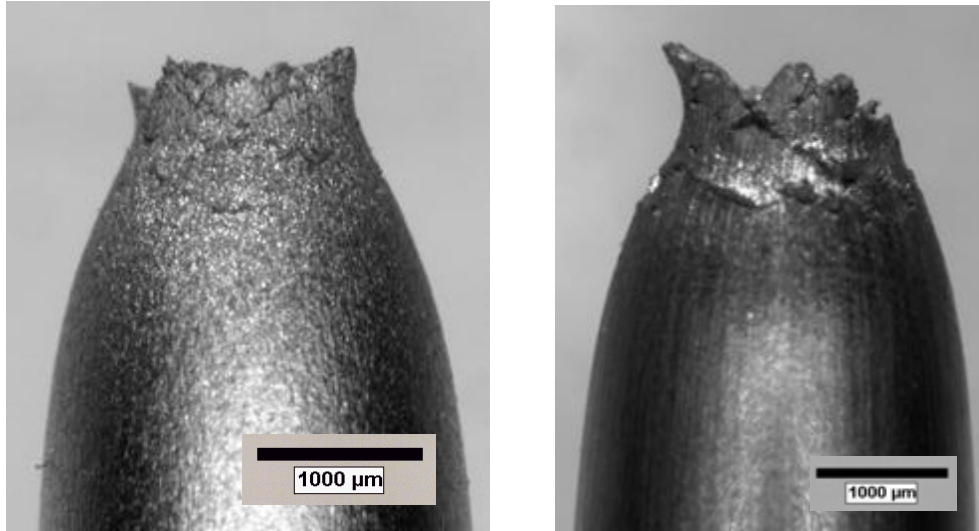
FIGURE 4.9 SCC of (a) annealed (b) cold-worked DSS 2205 in 26 wt.% NaCl solution of

pH = 2 under a potential of -375 mV (SCE) at room temperature.
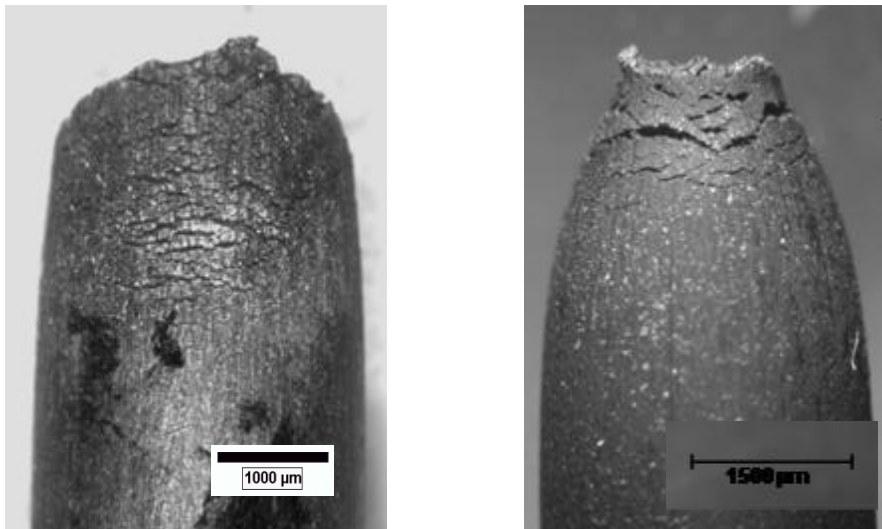
FIGURE 4.10 SCC of (a) annealed (b) cold-worked DSS 2205 in WL solution at OCP at

170 °C.

To compare the SCC intensity quantitatively, crack velocities and crack densities were measured, and the results are listed in TABLE 4.2. Both crack velocity and crack density for cold-worked DSS 2205 are larger than annealed DSS 2205, and this is true for both environments. These characteristics are also illustrated by the micrographs in FIGURE 4.11 and FIGURE 4.12. In annealed DSS 2205, larger plastic deformation is required for SCC to occur as compared to the cold-worked DSS 2205. The cracks in annealed samples were mainly found in the necking region of specimens while the cracks found in the cold-worked specimens have been observed in non-necking region as well.

TABLE 4.2 Crack velocities and crack densities of as-received and cold-worked DSS 2205.

DSS 2205	NaCl		WL	
	Crack Velocity (mm/s)	Crack Density (/mm)	Crack Velocity (mm/s)	Crack Density (/mm)
As-Received	2.98×10^{-7}	4	3.13×10^{-7}	17
Cold-worked	1.13×10^{-6}	8.5	1.8×10^{-6}	38.3
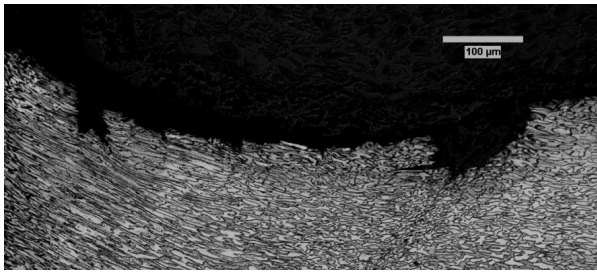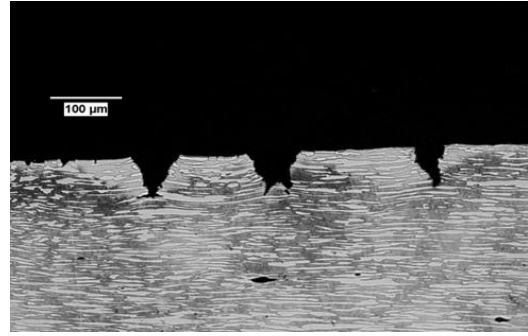
(a)   (b)

FIGURE 4.11 SCC of (a) annealed DSS 2205 and (b) cold-worked DSS 2205 in 26 wt.%

NaCl solution of pH = 2 at a potential of -375 mV (SCE) at room temperature.
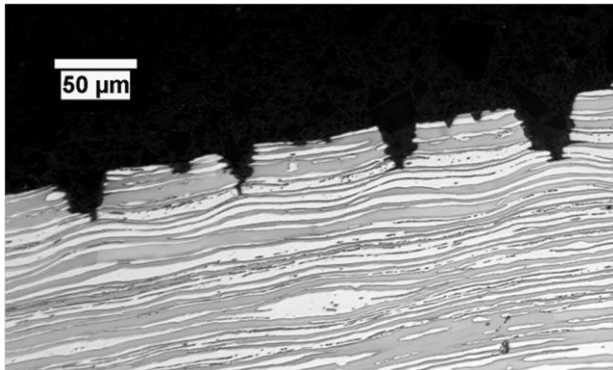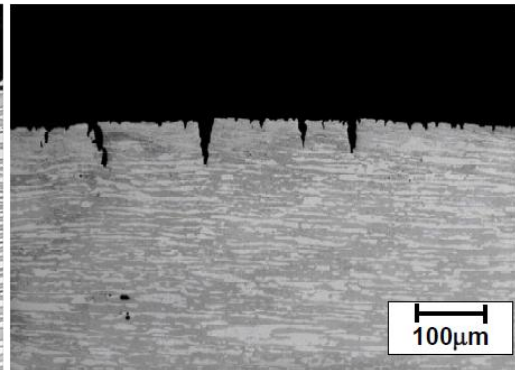
(a)   (b)

FIGURE 4.12 SCC of (a) annealed DSS 2205 and (b) cold-worked DSS 2205 in WL

solution at OCP at 170 °C.

115

The harmful effects of cold-working on SCC have been extensively studied for various alloy/environment systems, but there is hardly any satisfactory mechanism established. Residual stresses induced by cold-working within the material have been used to explain the cold-working effect by many researchers [143, 144]. Using hardness measurements, X-rays, SEM and TEM analyses, Cigada and his co-workers [144] concluded the increase in internal micro-stresses may be responsible for the detrimental influence of cold-working on SCC of austenitic stainless steel 304L and 316L in chloride environment. Bhattacharya *et al.* [143] have clearly demonstrated that annealed DSS 2205, which was immune to SCC in WL, became susceptible to SCC after more internal stresses were induced by preloaded to yield strength. However, other authors do not agree, because the residual stress, measured in a calorimeter (usually < 7 cal/g), is less than sufficient to account for an appreciable change in free energy. Hence this probably is not responsible for the increase of corrosion rate [145]. Foroulis and Uhlig [139] explained that the decrease in SCC resistance of cold-worked pure iron was not due to the presence of the cold-working introduced imperfections themselves, but rather the lower hydrogen overvoltage at these imperfection sites. Hence the imperfections worked as an anode while the rest of the sample surface as a cathode of a galvanic electrochemical cell, and the imperfections got preferentially attacked and served as the SCC initiation sites.

In summary, cold-working significantly enhanced SCC of DSS 2205 in both acidic chloride and caustic WL environments.

4.2.4 Crack Initiation

After the SSRT, sample surfaces were examined under optical microscope. Multiple cracks were observed, and they are mainly in the necking region of the fractured samples. Then one half on the failed tensile sample for each test was mounted in epoxy and polished to 0.05 μm. Then they were etched using 40% NaOH solution for a few seconds at 3 V to reveal the phases of DSS 2205. Crack initiations were observed under optical microscope. FIGURE 4.13 (a) and (b) are showing the stress corrosion crack initiations of DSS 2205 in acidic NaCl environment. The darker phase in the figures is ferrite phase (α), while the lighter phase is austenite phase (γ). These micrographs clearly illustrated the key characteristics of SCC in the acidic NaCl environment is the preferential attack of ferrite phase. Cracks were growing within ferrite phase, and jumped over austenite phase.
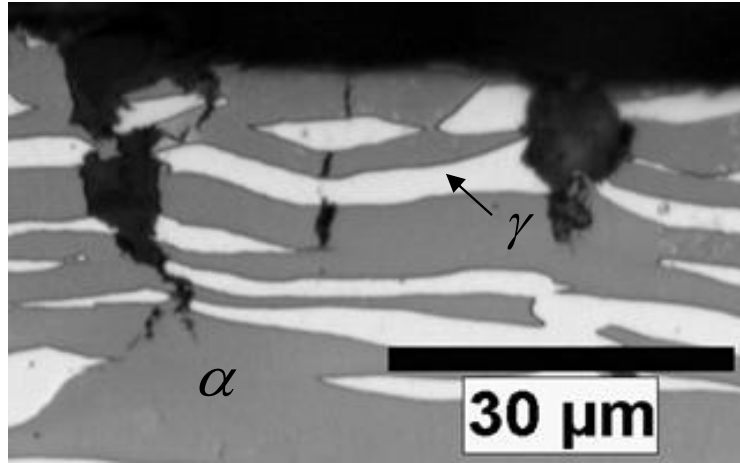
(a)
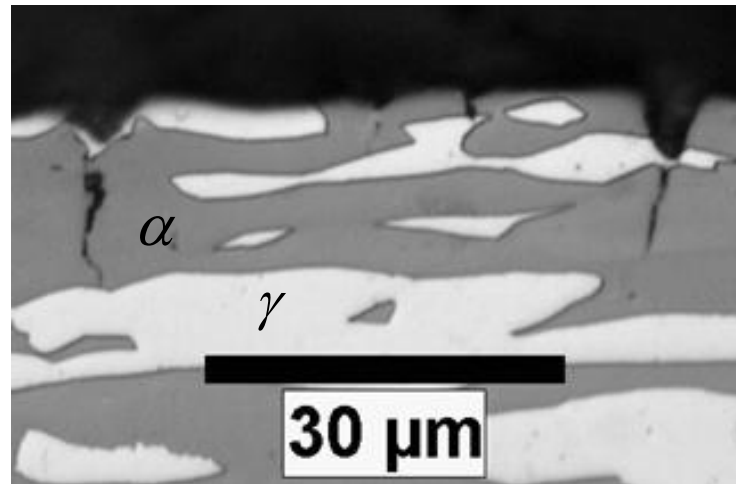
(b)

FIGURE 4.13 Stress corrosion crack initiations of DSS 2205 in 26 wt.% NaCl of pH = 2 at

room temperature.

It has been reported by many authors that ferrite phase is preferentially attacked by SCC in chloride-containing environment [33, 34, 39, 42, 43, 134, 146, 147], at both room temperature and elevated temperatures. Most authors have explained this preferential attack by selective dissolution of ferrite phase due to the potential difference between the two phases, as shown in the schematic drawing of FIGURE 4.14. In galvanic corrosion, when two electrically connected metals are immersed to an electrolyte, the metal that is more electrochemically active, or has a lower corrosion potential, will corrode and hence protect the other metal. In this case, between the two phases of DSSs, ferrite phase has a lower corrosion potential. Lo *et al.* [43] found that in mixed H_2SO_4/HCl solution, there are two anodic peaks in the active/passive transient region of the polarization curve of DSS 2205. The lower peak corresponds to dissolution of the ferrite phase, while the higher to the austenite phase. That is, ferrite phase has a more active corrosion potential and a larger corrosion current than austenite phase under this condition. Similarly, Fourie and Robinson [148] observed that austenite phase is 20 mV nobler than ferrite phase in electrochemical potential when DSS was exposed to 1M H_2SO_4 + 0.5M NaCl solution at 60 °C. Using micro-electrochemical technique, Park and his co-workers performed polarization tests on each individual phase of a 25%Cr DSS in pH 5.6 acetate buffer solution [149]. From the polarization curves they obtained, a lower corrosion potential and higher corrosion current was again observed for ferrite.
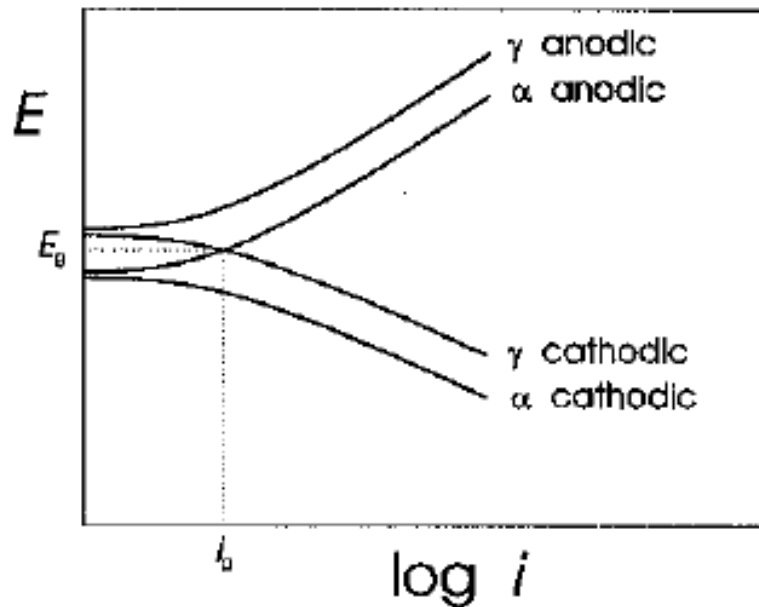
FIGURE 4.14 Schematic drawing illustrating the sacrificial protection of austenite by ferrite. [134]

Some authors have explained the selective dissolution of ferrite phase in chloride environment from the difference in the passive films of the two phases. Schmidt-Rieder *et al.* [146] believed that the relative stability of austenite phase compared to the ferrite phase is partially related to the passive film. Because the content of nitrogen is as high as 4 atom% in the film formed on austenite phase, while it is absent in the film on ferrite phase. Since nitrogen is beneficial in improving corrosion resistance, the passive film on austenite phase was reported to be more protective. Using Auger electron spectroscopy (AES), Vigal *et al.* found a difference in Cr/Fe ratio in passive films of the DSS phases [90]. In the inner layer of the passive film formed on DSS UNS S31803, the value of Cr/Fe ratio

is approximately 0.51 on ferrite and 0.58 on austenite. Further investigation revealed a linear relationship between Cr/Fe ratio and corrosion potential for phases of various stainless steels in chloride containing environment, as shown in FIGURE 4.15. Results in FIGURE 4.15 clearly demonstrated the strong connection between the passive film composition and the corrosion potential of the material. Consequently, the lower Cr/Fe ratio in ferrite phase will result in a lower corrosion potential as compared to austenite phase. According to this relationship, the average Cr/Fe ratio on the film formed on DSS 2205 should be different in 26 wt.% NaCl solution with different pH values. FIGURE 4.3 and FIGURE 4.4 showed at a scan rate of 1 mV/s, the OCP of DSS 2205 in pH = 2 solution which was -365 mV (SCE) was lower than that in pH = 3 solution which was -180 mV (SCE). Hence, the Cr/Fe ratio in surface film formed in pH = 2 solution was much lower than that formed in pH = 3, as labeled by the black diamonds in FIGURE 4.15. Since higher Cr/Fe ratio in surface film corresponds to relatively higher SCC resistance, DSS 2205 should be more resistant to SCC in 26 wt.% NaCl of pH = 3. Apparently, this is consistent with the SCC intensity predicted by parameter P_{SCC} in Section 4.2.1.
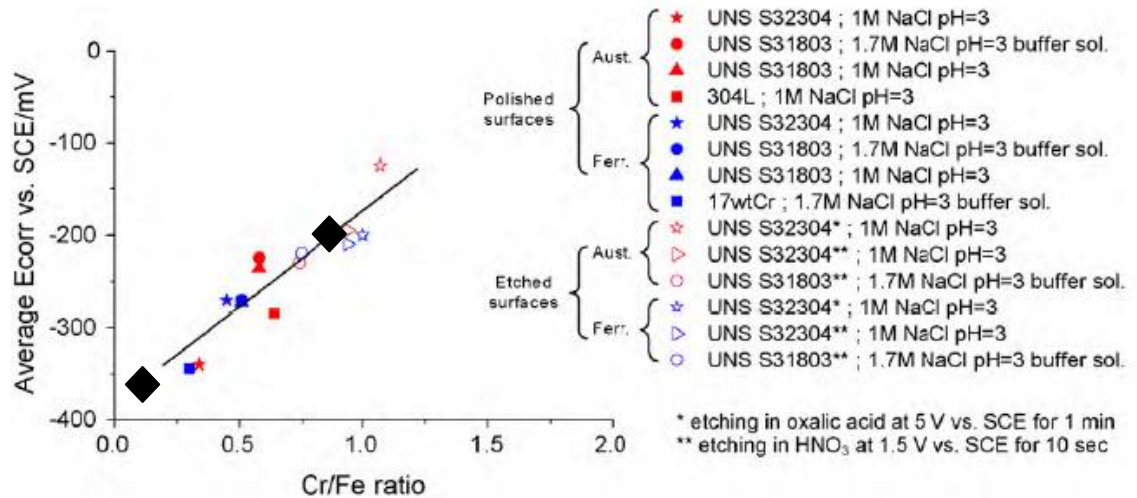
FIGURE 4.15 Linear relationship between the corrosion potential of metallic phases and the Cr/Fe ratio in the passive film. [90]

Moreover, some researchers identified an influence of the alloying element content of DSSs have on this preferential attack of ferrite in chloride environment. Sridhar and Kolts [150] found for a low nitrogen DSS (25.2%Cr, 11.8%Ni, 4.01%Mo, 0.006%N), selective dissolution occurs in austenite phase when the material is exposed to 10% ferric chloride. On the contrary, in the same environment, for DSS Ferralium Alloy 255 with normal nitrogen content (25.6%Cr, 5.7%Ni, 3.4%Mo, 0.17%N), ferrite phase is preferentially attacked. This is because nitrogen is austenite stabilizing element, hence in DSSs with high nitrogen content, almost all nitrogen is dissolved in the austenite phase. Since nitrogen is beneficial in improving corrosion resistance, the austenite phase becomes cathodic to ferrite. Consequently, austenite phase is galvanically protected by ferrite phase [36]. Cottis [134] has also mentioned, in principle it is possible to make the

122

two phases equally corrosion resistant by manipulating the content of Ni and Mo. Ni and Mo can improve the corrosion resistance of the material, and they segregate to different phases, e.g., Ni to austenite and Mo to ferrite. Therefore, the higher the Mo content of a DSS, the more similar is the corrosion behavior of the two phases in chloride environment.

The crack initiation mode of DSSs is also a function of environment. Some data obtained by Sridhar and Kolts [150] showed that for Ferralium Alloy 255, in phosphoric and sulfuric acid environments, selective dissolution occurs in austenite rather than ferrite. In the study of SCC behavior of DSS 2205 in WL environment, Bhattacharya [57] found stress corrosion cracks initiated in the austenite phase of DSS 2205 in WL solution at 170 °C. FIGURE 4.16 is a picture of DSS 2205 surface crack initiations taken under SEM, and it shows that numerous cracks initiated from austenite phase. In her study, the preferential attack of the austenite phase in WL environment was attributed to the tensile residual stresses of austenite phase. Since tensile residual stresses promote the emergence of slip bands on the sample surface, anodic dissolution will happen readily at the slip bands (slip-dissolution mechanism).
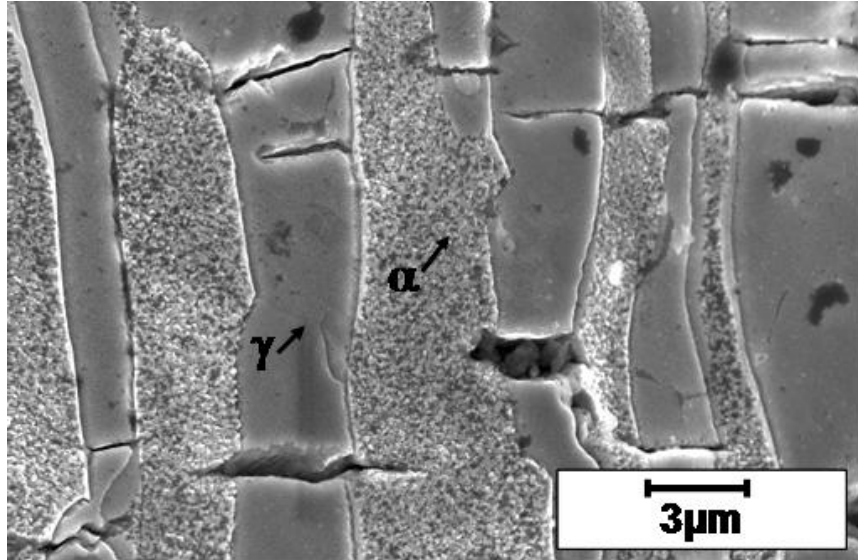
FIGURE 4.16 Crack initiation sites in the austenite phase in 2205 as received DSS under SSRT in sulfide-containing caustic solution at 170 °C. [57]

In summary, SCC initiation in DSS surface may be affected by the composition of the base material phases, the compositions of the protective film formed on each phase, and the corrosive environment. SCC of DSS 2205 initiated in ferrite phase when the material was tested in 26 wt.% NaCl solution of pH 2. On the other hand, the crack initiations were found in austenite phase in WL environment.

4.2.5   Threshold Stress/Strain for Crack Initiation

The threshold stress/strain for stress corrosion crack initiation of DSS 2205 in chloride and WL environments were determined by interrupted SSRT. In interrupted SSRT, the test was stopped at a certain stress/strain level before the sample fractured. The stress vs. time curves for the interrupted SSRT for DSS 2205 samples in chloride environment

are shown in FIGURE 4.17. For comparison, a complete SSRT curve, Sample #6, is also included in this plot. After the test, the sample surface was examined under optical microscope and SEM, and the residual plastic strain was measured, which are also labeled in FIGURE 4.17.

Among the interrupted SSRT, only Samples #4 and #5 showed the evidence of SCC. Sample #4 was strained to ultimate tensile strength (UTS), hence the cracks actually initiated before UTS, and the threshold strain for stress corrosion crack initiation in this environment is above 2%. Cracks were mainly found in the necking region, indicating that the plastic deformation is very important in initiating and propagating these cracks. Curve #2 represents the interrupted SSRT in which the sample was loaded to the YS and then the strain was held constant for about 27000 seconds before unloading it. This was done so that the sample was exposed to the corrosive environment for the same amount of time as Sample #4. The purpose of this test was to isolate the time effect from the effect of the applied stress/strain. No signs of SCC were found on Sample #2, which means that without straining the material to a higher level of plastic strain, exposing it to the corrosive environment at yield strength is not sufficient for crack initiation to happen.
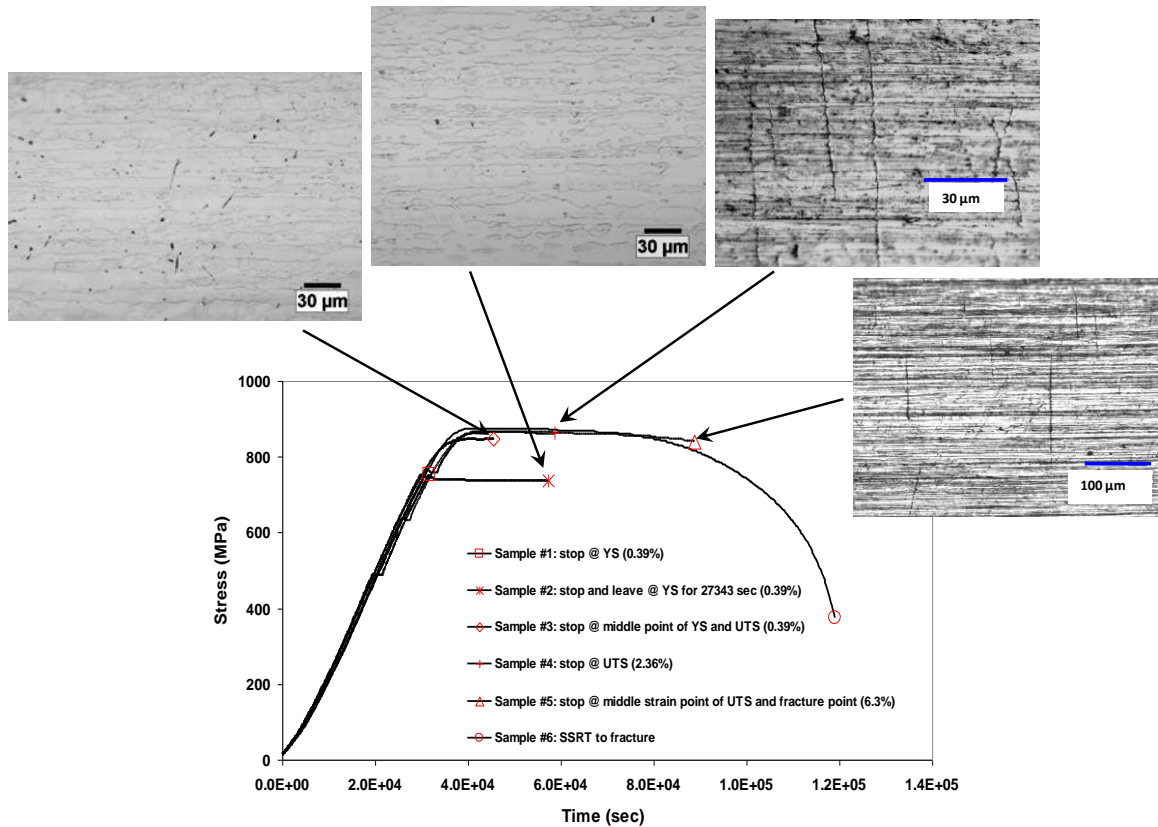
FIGURE 4.17 Stress vs. time curves of interrupted SSRTs for DSS 2205 in 26 wt.% NaCl of pH 2 at a strain rate of 1×10^{-6} s^{-1} at room temperature.

Similarly, FIGURE 4.18 shows the stress vs. time curves for the interrupted SSRT of DSS 2205 in WL at 170°C. Curve for Sample #7 is for a sample tested to failure for comparison. The percentage plastic strains measured after each test are also listed in FIGURE 4.18. Among the interrupted SSRTs, Samples #5 and #6 with applied strain beyond UTS, showed the evidence of SCC. Multiple cracks initiated and propagated mainly in the necking region for both samples, as shown in the SEM pictures in FIGURE 4.18. Unlike the specimens tested in chloride environment, the specimen strained to

UTS in WL did not show any cracking. Hence it even requires more plastic deformation for crack initiation of DSS in WL environment. The threshold strain for crack initiation in WL was found to be above 3.0% plastic strain. Curve for Sample #2 represents the test in which the sample was loaded to YS and then strain was held constant for about 20000 seconds. And no cracking on Sample #2 was observed. Results from interrupted SSRT in WL at 170 °C showed that for DSSs higher amount of plastic deformation is required for SCC initiation, corrosive environment alone is not sufficient for stress corrosion crack initiation. SCC in WL showed different features as in chloride environment: crack initiation sites or phases were different in the two environments, e.g., ferrite in chloride and austenite in WL (FIGURE 4.13 and FIGURE 4.16); both the crack density and crack velocity of samples tested in WL were larger than in chloride environment (TABLE 4.2). However, the results of the interrupted SSRT showed that crack initiations in the two environments both required a large amount of plastic deformation.
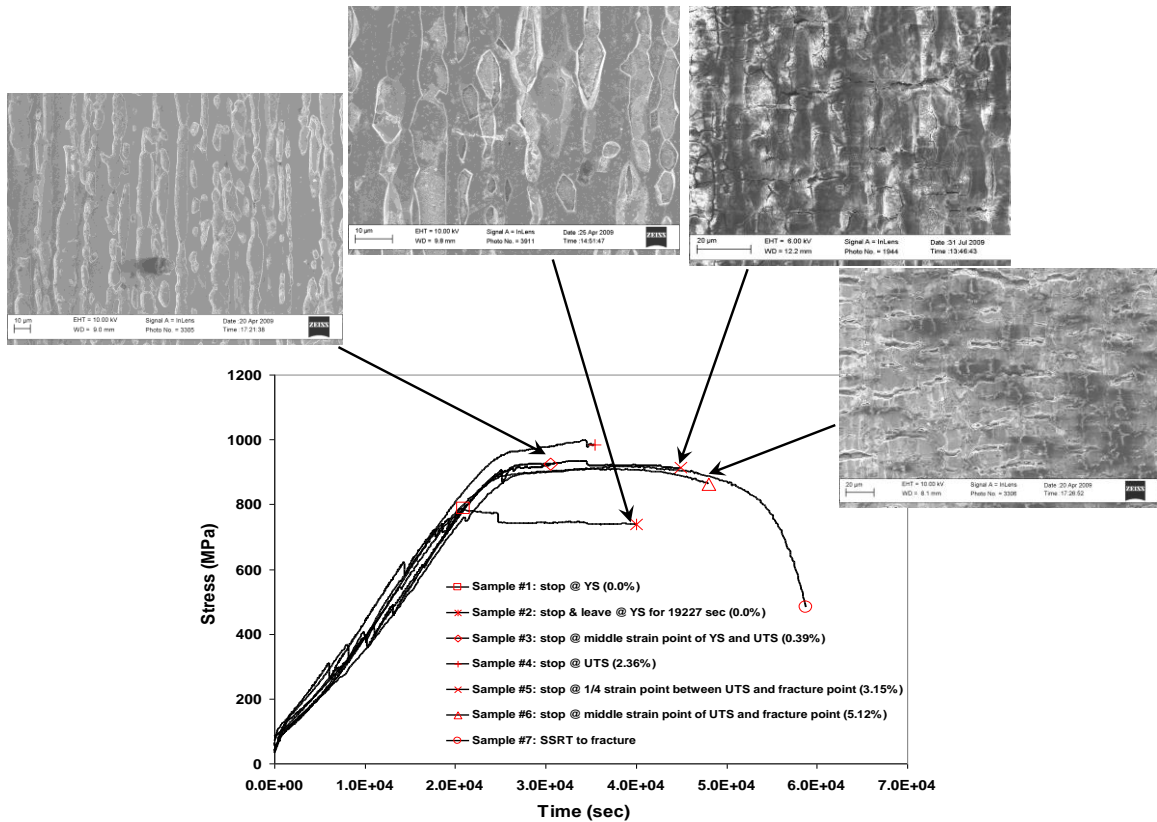
FIGURE 4.18 Stress vs. time curves of interrupted SSRTs for DSS 2205 in WL solution at a strain rate of 2×10^{-6} s^{-1} at 170 °C.

In summary, the plastic deformation is very important for stress corrosion crack initiations of DSS 2205 in both acidic chloride and WL environments. Straining the material at or below yield strength and exposing the material in these corrosive environments cannot initiate cracks. Threshold strains for stress corrosion crack initiations in acidic chloride and WL environments are about 2.3% and 3.1%, respectively.

4.3   Conclusions

From the study of environmental effects on SCC of DSS 2205, the following conclusions could be drawn:

❖ SCC behavior of DSS 2205 in acidic NaCl solution at room temperature was affected by both pH values and applied potential.

❖ Anodic potentiodynamic polarization test results showed that among the acidic pH values tested in this study, pH = 2 provided the most aggressive environment for SCC to occur in 26 wt.% NaCl solution at room temperature.

❖ SSRT results indicated that DSS 2205 was susceptible to SCC in the potential range of -375 mV (SCE) to -520 mV (SCE), in 26 wt.% NaCl of pH 2. Right above and below this potential range, DSS 2205 was immune to SCC in this environment.

❖ SCC initiations of DSSs were affected by the compositions individual phases and their protective film, and the corrosive environment. SCC of DSS 2205 initiated in ferrite phase when the material was tested in 26 wt.% NaCl solution of pH 2, and the crack initiations were found in austenite phase in WL environment.

❖ Cold working significantly enhanced SCC of DSS 2205 in both acidic chloride and caustic WL environments.

❖ Plastic deformation was crucial for stress corrosion crack initiations of DSS 2205 in both acidic chloride and caustic WL environments. Straining the material at or below yield strength and exposing the material in these corrosive environments cannot initiate cracks. Threshold plastic strains for stress corrosion crack

initiations in acidic chloride and WL environments are 2.3% and 3.1%, respectively.

CHAPTER 5 CYCLIC STRESS EFFECT ON CREEP BEHAVIOR OF

DUPLEX STAINLESS STEEL 2205

5.1   Introduction

Discussions in previous chapters have demonstrated that there are two key parameters regarding the stress corrosion crack initiation of duplex stainless steel (DSS) 2205 in acidic chloride and caustic white liquor (WL) environments, namely, plastic deformation and strain rate at the crack tip. In CHAPTER 4, the results of interrupted slow strain rate tests (SSRTs) conducted in the two corrosive environments revealed that a certain amount of plastic deformation was required for stress corrosion crack initiation of DSS 2205. In CHAPTER 2, it has been pointed out that stress corrosion cracking (SCC) occurs in a critical range of strain rate. For most of the metals / aqueous systems, this critical range is around 10^{-6} s^{-1}. FIGURE 2.28 indicated that above and below this critical range, materials are immune to SCC. Therefore, to maintain the strain rate at the crack tip is crucial. For film-induced crack propagation mechanism, strain rate at the crack tip needs to be sufficiently high to constantly break the newly surface protective film, so that the fresh metal could be exposed to the corrosive environment. Otherwise, the crack propagation will cease because of the protection of passive film.

In the presence of low frequencies cyclic loading (especially less than 0.01 Hz), room temperature creep of metallic materials could be enhanced or retarded as compared to static loading. Compared to relatively high frequency strain accumulation behavior, the

strain accumulation behavior of DSS 2205 under low frequency cyclic loading was expected to be different. Accordingly, the strain rate will change as well because of the change in strain. As illustrated by the schematic drawing of Kennedy effects in FIGURE 2.29, the strain rate decreases with time under static loading, but after cyclic loading starts, the cumulative strain rate keeps constant with time. Therefore, cyclic stresses could have a significant influence on the stress corrosion crack initiation of DSS 2205 in acidic chloride and caustic WL environments.

Although creep is much more pronounced at elevated temperatures, we will focus on room temperature creep in this study. Because the room temperature creep phenomenon is important to understand SCC and corrosion fatigue (CF) behavior at low temperatures. Room temperature tests also eliminate the high temperature influence and illustrate the low frequency cyclic loading effect on strain accumulation behavior of materials, especially during the unloading process of low frequency cyclic loading. The enhancement and retardation of room temperature creep induced by cyclic loading are called "cyclic creep acceleration" and "cyclic creep retardation", respectively. Extensive review of related publications revealed that both cyclic creep acceleration and retardation have been reported for materials with different crystal structures, i.e., BCC and FCC structures.

Cyclic creep acceleration was observed on BCC materials, such as pipeline carbon steel [2], pure iron [5], and FCC materials, such as copper [1, 98], aluminum [3, 4], and polycrystalline lead [94]. Similarly, cyclic creep retardation was reported for BCC

materials, such as X-52 pipeline steel [99], and FCC materials, such as aluminum and copper [4, 98]. As discussed in these papers, the cyclic loading effect on creep behavior of metallic materials was due to the recovery of material properties during unloading. Generally speaking, this recovery could occur in two ways: (a) obstacle dislocations may become rearranged because of the altered state of internal stress, (b) mobile screw dislocation segments may leave their slip planes by cross-slip aided by fluctuations in internal stress encountered during reverse movement [2], or the attraction of oppositely signed screw dislocations on parallel slip planes may lead to mutual annihilation. Between these two recovery mechanisms, the second one or the cross slip model was accepted by most people. Moreover, even under cyclic stresses without dwelling at maximum stress level or pure triangle wave shape cyclic stresses, a pronounced macroscopic cyclic stress induced creep has also been observed by Feltner [3] in aluminum under a cyclic stress with a frequency of 0.18 Hz and stress ratio of zero.

Nevertheless, there is no research published on the room temperature cyclic creep behavior of DSSs. Since DSSs are mixtures of two phases with different crystal structures, i.e., BCC structure of ferrite phase and FCC structure of austenite phase, the room temperature cyclic creep behavior of DSS 2205 was expected to exhibit characteristics of both BCC and FCC structures.

5.2 Results and Discussion

Pure static and pure cyclic creep tests were conducted to illustrate the effect of low frequency cyclic stress on the room temperature creep behavior of DSS 2205. That is in each test, the static or cyclic loading was applied from the beginning and throughout the whole test. The lengths of these tests were all about 220 hours. The frequency of the cyclic loading is 1/3600 Hz, and the dwell time at the maximum and minimum stress was roughly 45 minutes and 15 minutes, respectively. The loading profile for pure cyclic creep tests was schematically shown in FIGURE 3.14. Changes in the sample dimension, measured as creep deformation, were recorded with a knife-edge extensometer, attached to the sample with a special fixture to prevent any errors during measurements. Cumulative creep deformation was plotted against time. Results from the pure static creep test and the pure cyclic creep test with the maximum stress equal to the static creep stress were compared to illustrate the cyclic stress effect. Different maximum stress levels were selected to demonstrate the maximum stress effect. Similar tests were also performed on stainless steels with different crystal structures representing the two phases of DSS , i.e., stainless steel (SS) 304L with γ, face centered cubic (FCC), and SS 430 with α, body centered cubic (BCC) crystal structure. TABLE 5.1 is the summary of pure static and pure cyclic creep tests for the three stainless steels.

TABLE 5.1 Summary of pure static and pure cyclic creep tests with the maximum stress levels for different materials.

Material	Stress Type	Max. Stress (MPa)
DSS 2205	Static	620 513 400 330
DSS 2205	Cyclic	620 513 400
SS 304L	Static	545 435
SS 304L	Cyclic	545 435
SS 430	Static	670 592
SS 430	Cyclic	670 592

Static-cyclic creep tests or tests starting with static loading followed by cyclic loading were also carried out to illustrate the effect of low frequency cyclic stresses on the room temperature creep behavior of DSS 2205. In these tests, cyclic loading was applied to specimens that had been pre-strained under static loading for a certain amount of time. Specifically, in this study the static loading was applied for 4.75 hours, and then cyclic loading was applied for 5 hours. The frequency of the cyclic loading is 1/600 Hz, and the dwell time at the maximum and minimum stress was 9 minutes and 1 minute, respectively, as shown in FIGURE 3.14. After each test, the cumulative creep strain was plotted against time, and the two portions of the creep strain curve generated by static

and cyclic loading were compared to demonstrate the cyclic stress effect on room temperature creep behavior of DSS 2205. Different maximum stress levels were selected to demonstrate the maximum stress effect. Furthermore, by comparing these results with pure static and cyclic creep tests, the effect of pre-straining could also be illustrated. Similar tests were also performed for SS 304L and SS 430 to show the crystal structure effect on creep behavior of materials. TABLE 5.2 shows the maximum stresses used in the static-cyclic creep tests for each material.

TABLE 5.2 Summary of static-cyclic creep tests with the maximum stress levels for different materials.

Material	Stress Type	Max. Stress (MPa)
DSS 2205	Static-Cyclic	620 640 660
SS 304L	Static-Cyclic	500 550 600 620 640
SS 430	Static-Cyclic	620 640 660 680

5.2.1   Pure Static and Cyclic Creep Test Results

In order to determine the stress levels to be applied for the creep tests, the stress vs. strain behavior of DSS 2205, SS 304L and SS 430 steels were determined using the same

creep machine frame which was used for the creep tests. Tensile samples were loaded

at a rate of 4 lbs/s in air at room temperature, as shown in FIGURE 5.1. Since the stress

vs. strain behavior of materials change with loading rate or strain rate, the curves shown

in FIGURE 5.1 are different than those obtained under the slow strain rates. From the

small plot showing mainly the elastic parts of the three curves, the elastic limits were

around 400 MPa, 500 MPa and 300 MPa for DSS 2205, SS 430 and SS 304L, respectively.
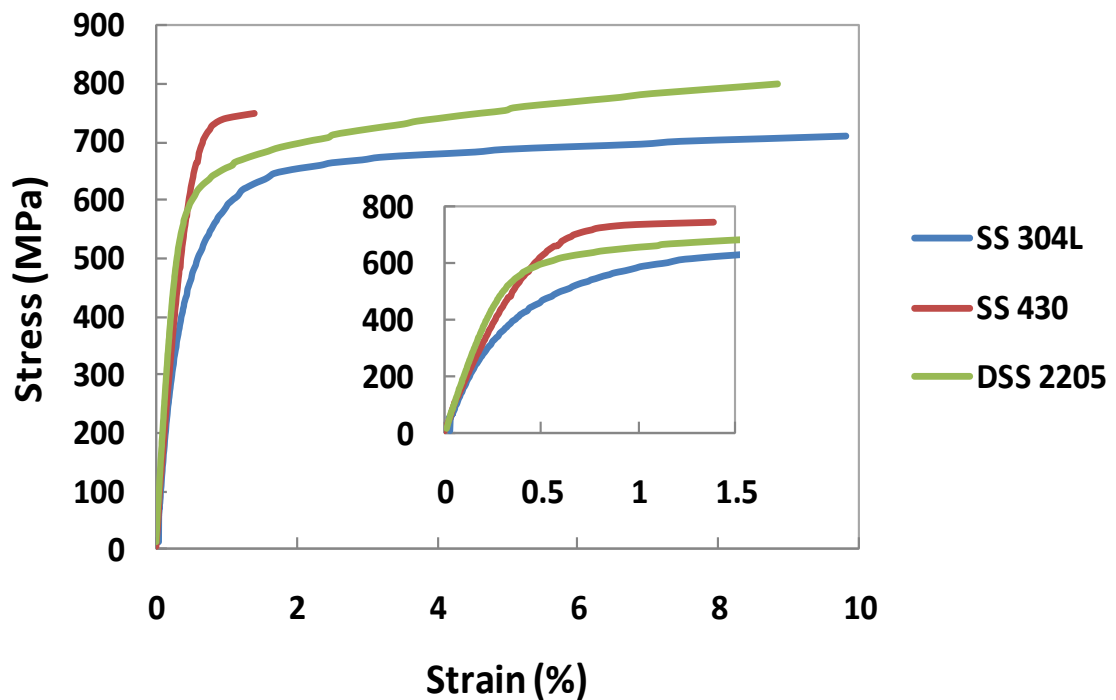
FIGURE 5.1 Stress vs. strain curves of DSS 2205, SS 304L and SS 430 obtained under a

loading rate of 4 lbs/s.

The strain accumulation curves of DSS 2205 under pure static and cyclic loadings are plotted in FIGURE 5.2. Solid lines represent the creep strains generated by cyclic loading, while dashed lines are the creep strains of DSS 2205 under static loading. Except for the two green curves which are using the vertical axis on the left, all other curves use the axis on the right. These results showed that cyclic creep acceleration occurred in DSS 2205 at room temperature. Under the same maximum stress, low frequency cyclic loading enhanced strain accumulation of DSS 2205 at room temperature, as compared to static loading. Moreover, the extra amount of strain induced by cyclic loading, indicated by $\Delta\varepsilon$ in FIGURE 5.2, increased with increasing of the stress level. Stress level has been reported to be the most important parameter influencing the cyclic creep behavior of various metallic materials at room temperature [1, 2, 4, 98]. In the case of cyclic creep acceleration, the effect of cyclic stresses will be more pronounced, or the extra strain induced by cyclic loading will be larger. In addition, the extra strain $\Delta\varepsilon$ almost diminished around the stress level of 400 MPa, which is the elastic limit of DSS 2205 under this loading condition. Below the elastic limit, at a cyclic stress of 330 MPa, the creep strain hardly changed with time. These results showed that the cyclic creep acceleration was observed above the elastic limit of DSS 2205 at room temperature, indicating that cyclic creep acceleration occurred with the presence of plastic deformation.
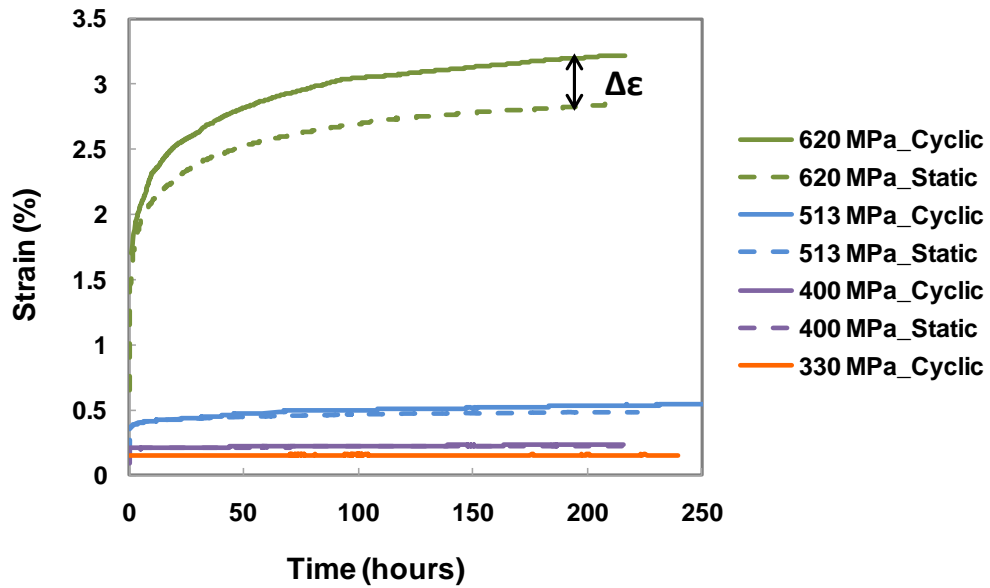
(a)
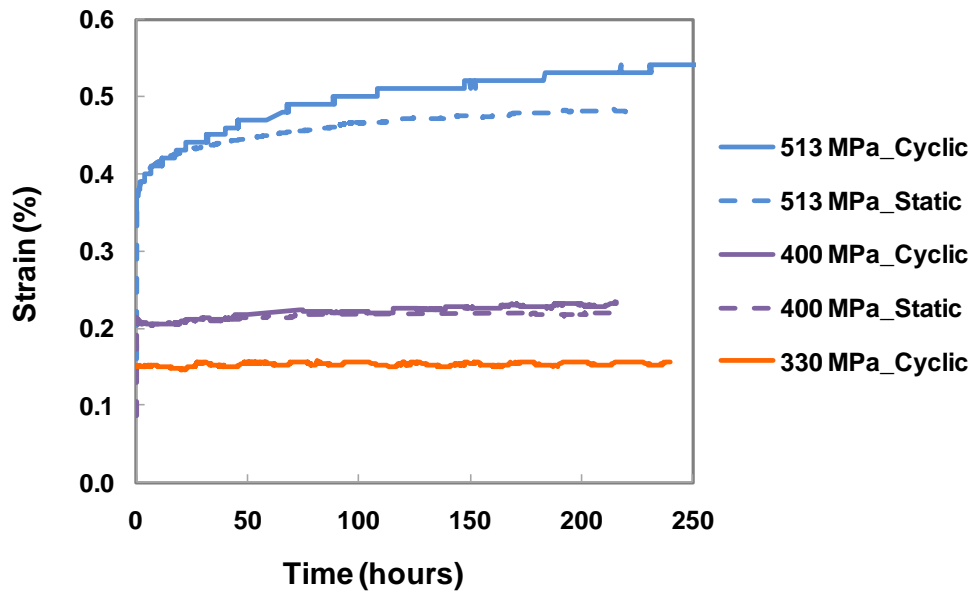
(b)

FIGURE 5.2 (a) Total strain curves for DSS 2205 under pure static and cyclic loading at room temperature. (b) Zoomed plot of the lower stress level total strain curves. The solid lines represent the envelopes of the creep curves produced by cyclic loading, and the dashed lines represent the creep curves produced by static loading.

However, contrary to DSS 2205, for both SS 304L and SS 430, cyclic creep retardation was observed on specimens without any pre-straining at room temperature. As shown in FIGURE 5.3 and FIGURE 5.4 the creep strain generated by cyclic loading was smaller than that generated by static loading of the same stress level. In fact, the lower stress levels in these figures, i.e., 435 MPa in FIGURE 5.3 and 592 MPa in FIGURE 5.4, correspond to the same initial strain level 0.414. However, all stress levels used in the tests of SS 304L and SS 430 were higher than their elastic limits. Hence the cyclic creep retardation observed on these materials could not be attributed to stress level effect. As discussed in Section 5.1, cyclic creep retardation has been found in both BCC and FCC materials. Our results further confirmed that this phenomenon is not crystal structure dependent.

There are two possible mechanisms for cyclic creep retardation to occur. One is due to cyclic-hardening of the material. As discussed by Wang and Chen [99], microscopically, the cyclic-hardening could happen when dislocation cells form in the material, which could significantly reduce the amounts of mobile dislocations by adding them into the cells. The other mechanism assumes that cyclic loading does not affect the microstructures of the material. Hence strain accumulation only occurs during the time when the peak stress was applied. If that is true, for the same total testing time, strain accumulated in pure cyclic creep test should be less than that in pure static creep. In FIGURE 3.14, the load profile of pure cyclic creep tests indicated that peak stress was applied for 3/4 of the total test time. Therefore, if the second mechanism works, the cumulative creep strain produced by pure cyclic loading at any time T should equal to

the creep strain produced by pure static loading at ¾T. Observation of the creep curves from FIGURE 5.3 and FIGURE 5.4 showed, there is no such relationship existing between the cumulative creep strains generated by static and cyclic loading. In another word, the cyclic creep retardation observed on SS 304L and SS 430 in this study was mainly due to the cyclic-hardening induced by the cyclic loading.
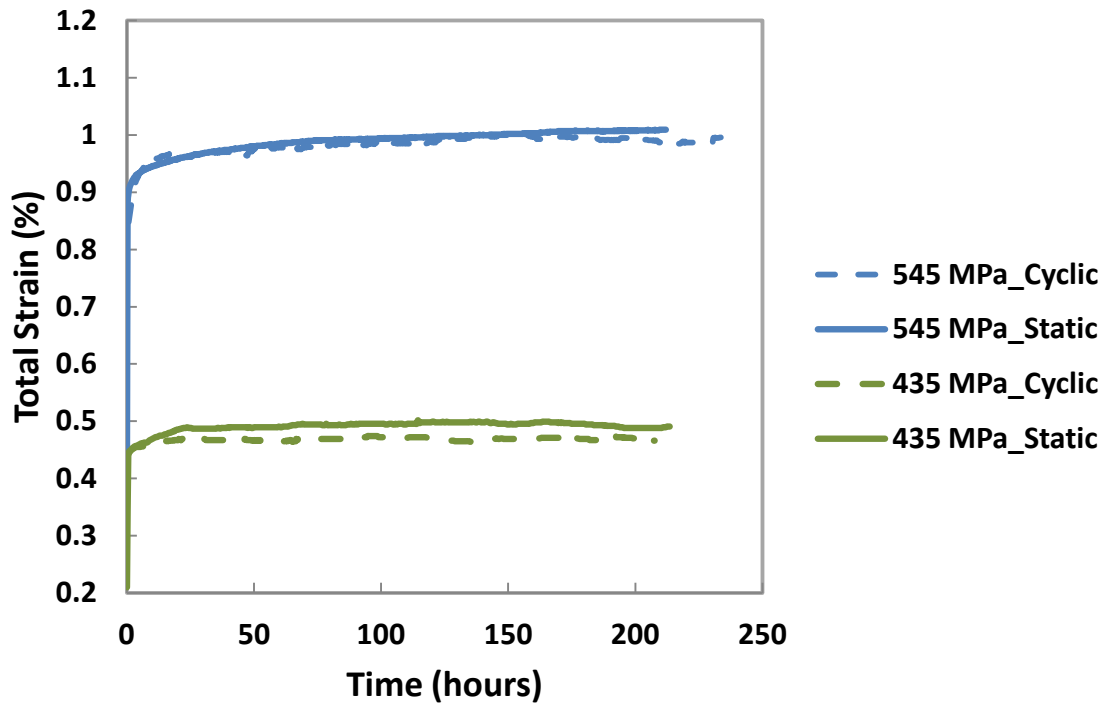
FIGURE 5.3 Total strain curves for SS 304L under static and cyclic loading at room temperature. The dashed lines represent the envelopes of the total strain curves produced by cyclic loading, and the solid lines represent the total strain curves produced by static loading.
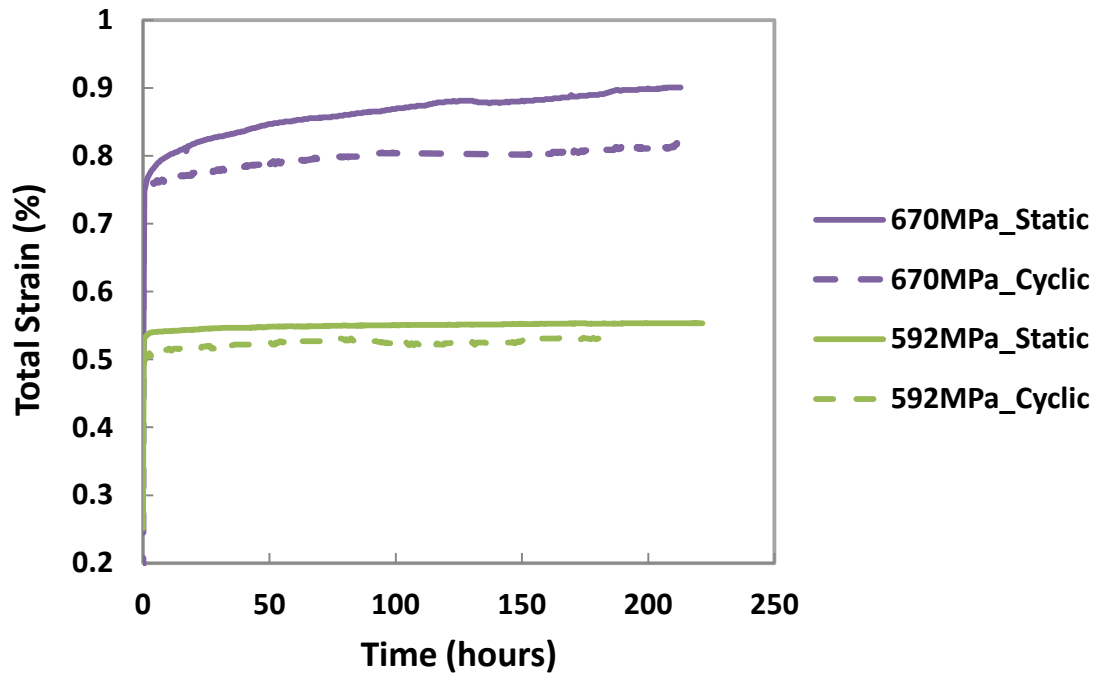
FIGURE 5.4 Total strain curves for SS 430 under static and cyclic loading at room temperature. The dashed lines represent the envelopes of the total strain curves produced by cyclic loading, and the solid lines represent the total strain curves produced by static loading.

Since SS 304L and SS 430 have different yield strengths, creep test results from the same applied stress level do not represent similar conditions for the two materials. Moreover, the two phases of DSS 2205 have different microstresses during the loading process, because of the existence of the initial residual stress. However, they have similar macro-strains, although local micro-strains vary due to local inhomogeneties, shape and the mechanical properties of the two phases. Hence, the strain accumulation behavior of

the two materials has been compared with similar initial applied strain. Under static

loading, SS 430 accumulated more strain than SS 304L, especially at higher strain level of

0.6% total strain, as shown by the two purple curves in FIGURE 5.5. When the initial

strain was relatively lower, the two materials did not show any difference in strain

accumulation behavior under static loading.
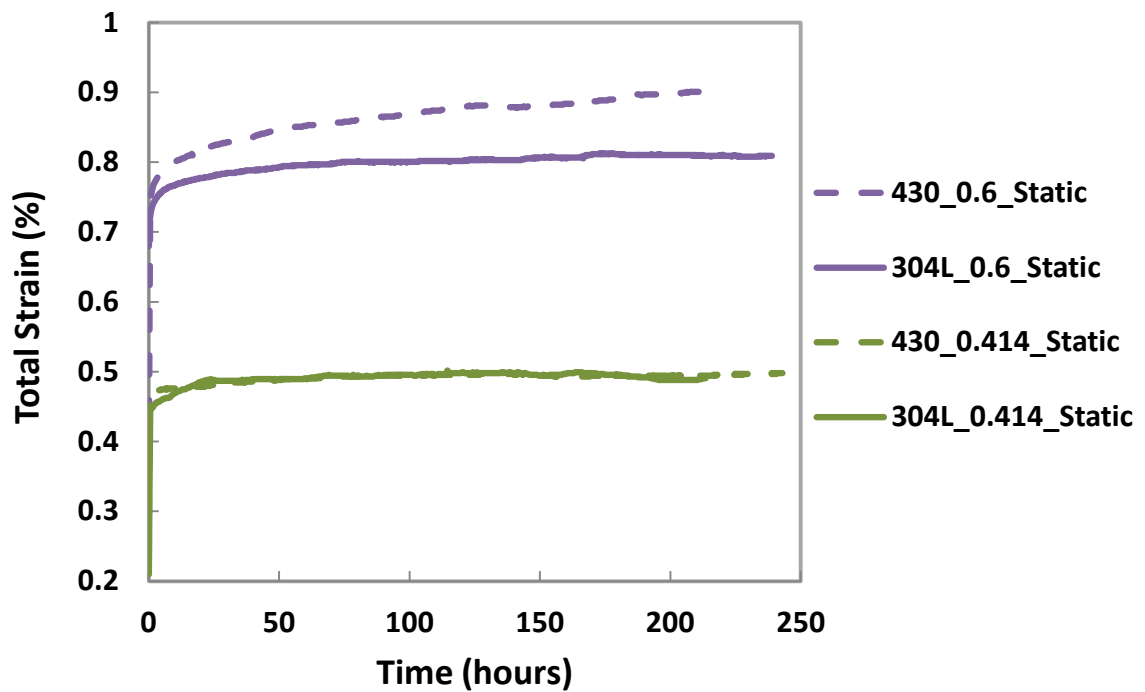
FIGURE 5.5 Total strain curves for SS 304L and 430 tested at same initial strain level

under static loading.

5.2.2 Static Creep Analytical Model

Before discussing the results of static-cyclic creep tests, a static creep analytical model is introduced here, since this model was used to analyze the static-cyclic creep test data for results in Section 5.2.3.

This creep model [151] describes the strain accumulation behavior of metals vs. time under constant load at room temperature, and it can be shown as

$$\varepsilon = \left(\frac{S}{B}\right)^{\frac{1}{m+n}} \cdot \left(\frac{m+n}{n} \cdot t\right)^{\frac{n}{m+n}} \qquad\qquad 5.1$$

where ε is the plastic strain, S is the maximum stress of the cyclic loading, B is strength coefficient, m is strain-hardening exponent (slope of $logS - log\varepsilon$ curve for constant $\dot{\varepsilon}$), and n is rate sensitivity (slope of $logS - log\dot{\varepsilon}$ curve for constant ε). The model is based on the creep stress vs. strain behavior

$$S = B\dot{\varepsilon}^{n}\varepsilon^{m} \qquad\qquad 5.2$$

EQUATION 5.2 is derived from the empirical linear relationship observed between log plastic strain and log time in many metallic materials, particularly at room temperature [152]. In this relationship, the strain is considered as a function of stress and strain rate (or time). At room temperature, the creep rate at constant stress continuously decreases as long as a metallurgical reaction does not occur, and the creep rate diminishes rapidly.

With the assumptions of neglecting the rate-history effect and Bauschinger effect, the creep behavior can be determined by integration:

$$t = \int \frac{d\varepsilon}{\dot{\varepsilon}}$$ <div align="right">5.3</div>

Rewriting EQUATION 5.2 as $\dot{\varepsilon} = \left(\frac{S}{B}\right)^{\frac{1}{n}}\left(\frac{1}{\varepsilon}\right)^{\frac{m}{n}}$, then substituting it into EQUATION 5.3, gives us

$$t = \int \frac{d\varepsilon}{\left(\frac{S}{B}\right)^{\frac{1}{n}}\left(\frac{1}{\varepsilon}\right)^{\frac{m}{n}}} = \left(\frac{S}{B}\right)^{-\frac{1}{n}} \cdot \frac{n}{m+n} \varepsilon^{\frac{m+n}{n}}$$ <div align="right">5.4</div>

By Rearrange EQUATION 5.4, we obtain EQUATION 5.1. Therefore, EQUATION 5.2 is essentially an equation describing strain as a function of stress and time. The advantage of using this equation is that it does not assume the effects of stress and time are separable variables, as many other models do [153].

However, in this study, we used total strain in EQUATION 5.1, and the reasons are discussed as follows. First of all, the instantaneous plastic strain caused by the initial sudden application of stress cannot be separated out from the instantaneous total strain. Because when the stress is sufficiently high, an initial plastic deformation will occur as well [154]. Moreover, it is difficult to perform the loading in a well-defined instantaneous manner [155] and record the stress and strain data in a truly instantaneous way. Secondly, EQUATION 5.1 is based on the empirical linear relationship between log-plastic strain and log-time. Hence as long as the total strain

data has the same linear relationship with time, the model in EQUATION 5.1 can be used for the total strain. The only difference will be the values of the fitting parameters of B, m and n. The results of static-cyclic creep tests showed that the static part of the creep curve does follow the linear relationship described above, as is shown in FIGURE 5.6, FIGURE 5.7 and FIGURE 5.8. Therefore, this analytical model could be used to describe the static creep behavior of these three tested materials.
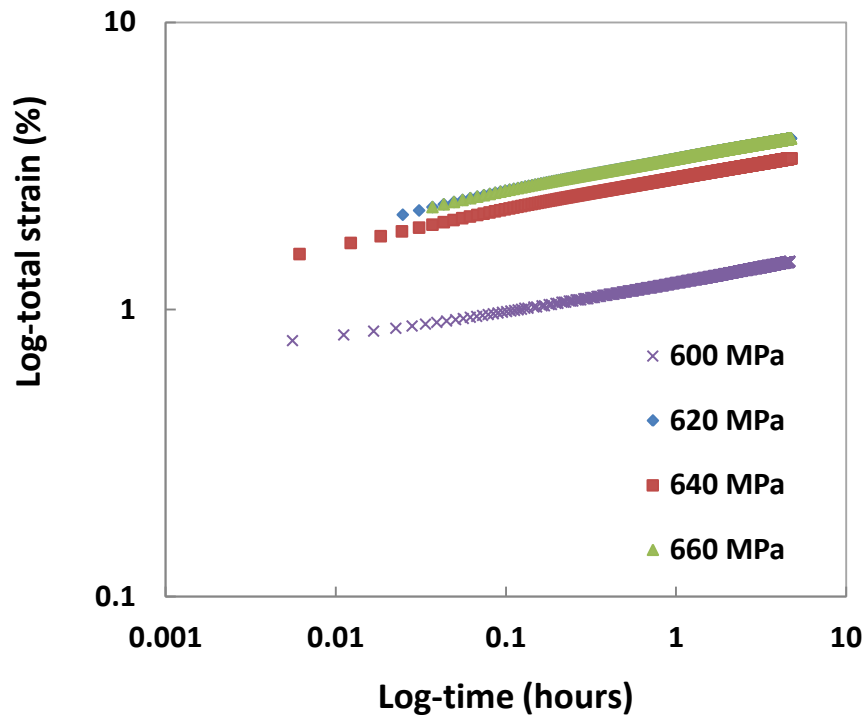
FIGURE 5.6 Linear relationship between log-total creep strain and log-time for DSS 2205 static creep data.
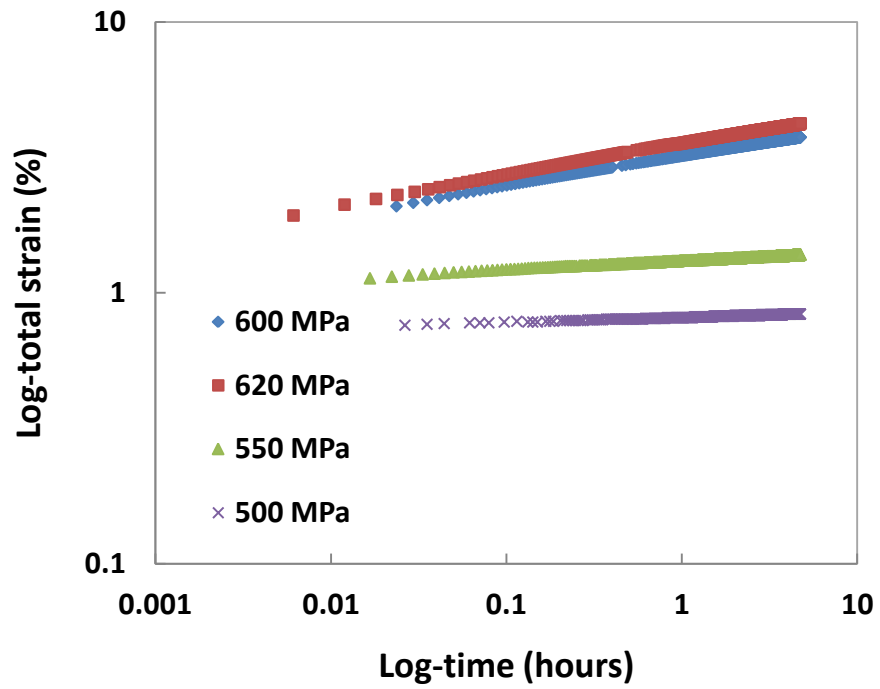
FIGURE 5.7 Linear relationship between log-total creep strain and log-time for SS 304L static creep data.
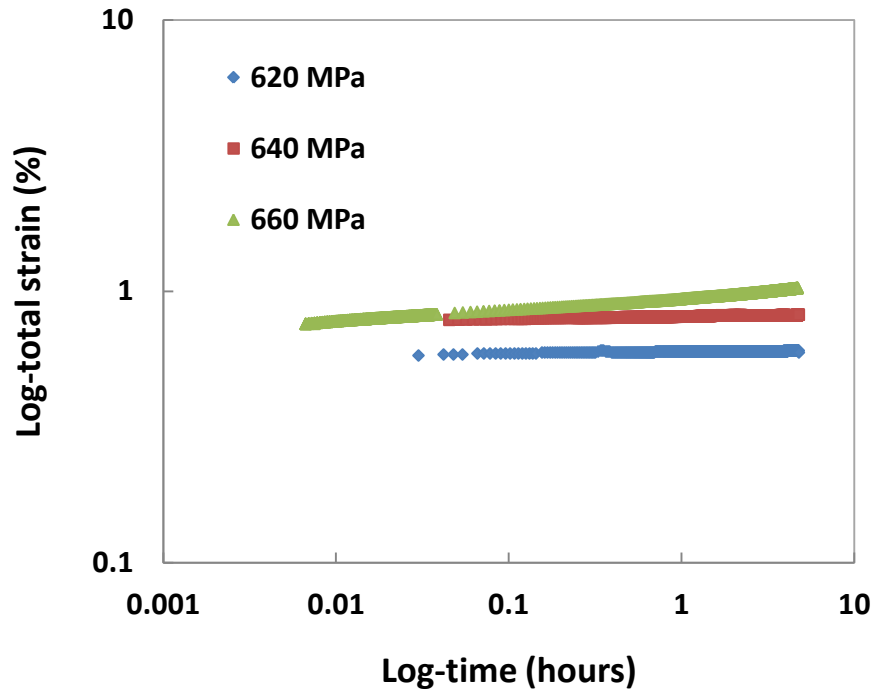
FIGURE 5.8 Linear relationship between log-total creep strain and log-time for SS 430 static creep data.

5.2.3 Static-Cyclic Creep Test Results

The effect of pre-straining on cyclic creep behavior of materials at room temperature has also been investigated by the static-cyclic creep tests. The total creep strain vs. time curves are shown in FIGURE 5.9, FIGURE 5.10 and FIGURE 5.11 for DSS 2205, SS 304L and SS 430 respectively. As separated by the vertical dashed lines in the plots, the static loading was applied for about 4.75 hours, and the cyclic loading was applied after that for about 5 hours. The solid lines are the creep strain generated by the static and cyclic loadings, and the dashed lines are the fitted curves using EQUATION 5.1 from the static

creep data. The data fitting was accomplished by MATLAB codes (APPENDIX A) using the least square method, as shown in FIGURE 5.12. The curve-fit line, red line in FIGURE 4.12, illustrates how the data for the dashed lines, static creep line extrapolation, in FIGURE 5.9, FIGURE 5.10 and FIGURE 5.11 were obtained. Data for the dashed portion of static creep curves was generated by data fitting the blue stars using the creep model. The corresponding parameter values of B, m and n were then generated by the MATLAB codes and are shown in the plot as well. Initial estimated values of B, m and n were required to run the codes, and their values were adjusted to fit the data until the sum of the errors between the data and the fitting curve at each data point reached the minimum value, which was in fact how the least square method worked. According to the physical meanings of these curve fitting parameters, an estimate for each parameter was determined. Strength coefficient B and strain hardening exponent m usually have the values 10^6 and 1/3 respectively [151]. Rate sensitivity n varies greatly with temperature, and at room temperature it is very small [151], hence an estimate value of 1/600 was used.
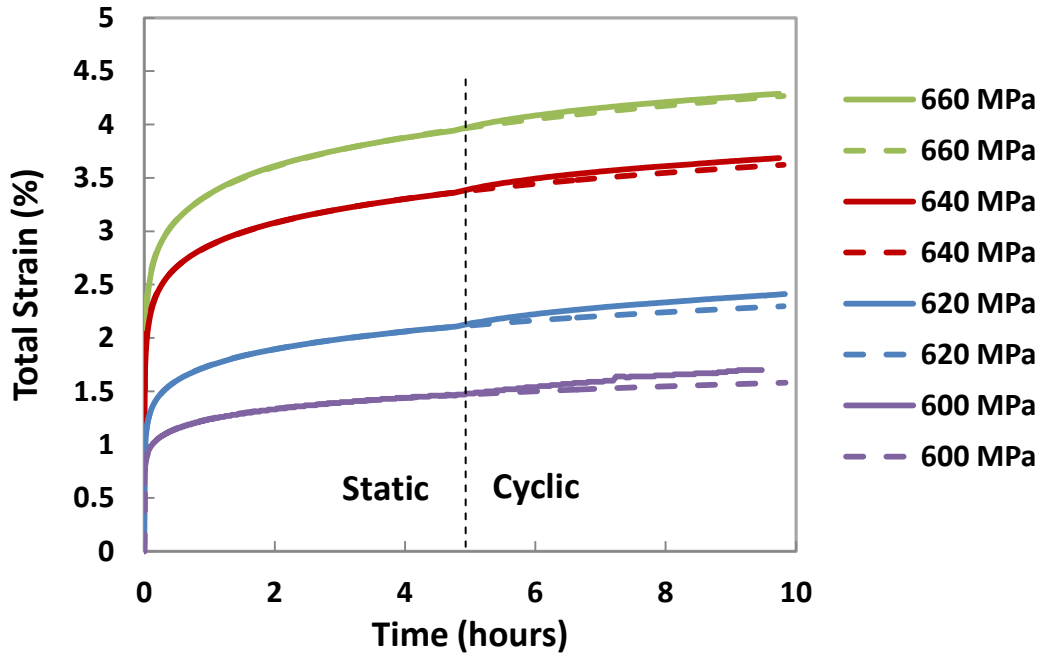
FIGURE 5.9 Solid curves represent the cumulative total strain of DSS 2205 in static-cyclic creep tests; dashed curves represent the total strain of DSS 2205 generated by the analytical model.
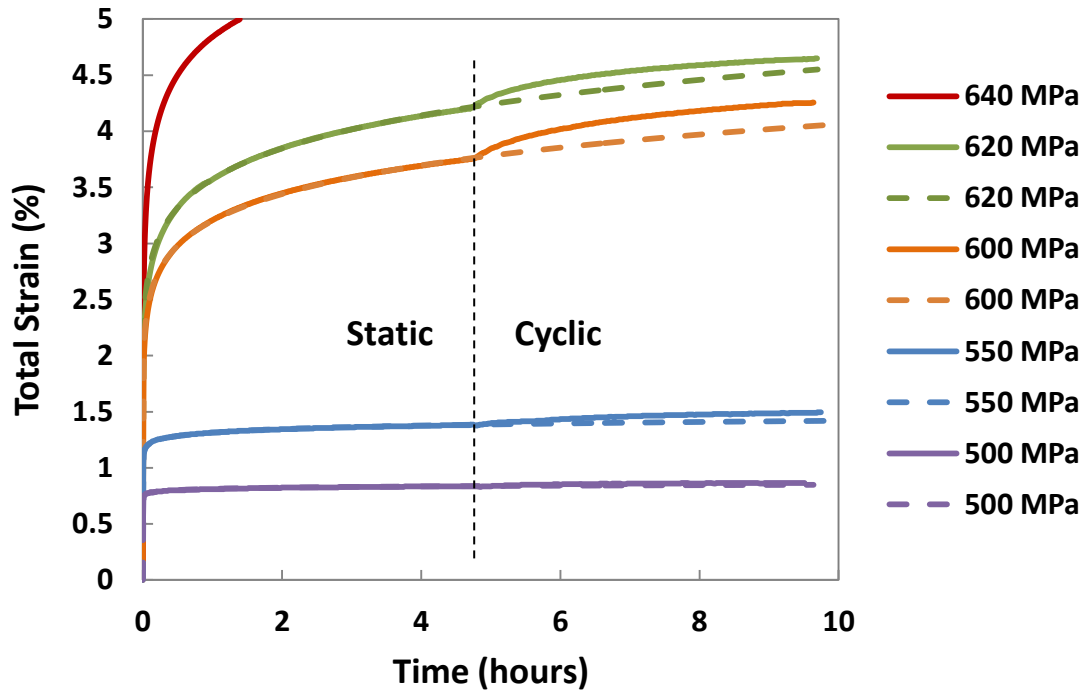
FIGURE 5.10 Solid curves represent the cumulative total strain of SS 304L in static-cyclic creep tests; dashed curves represent the total strain of SS 304L generated by the analytical model.
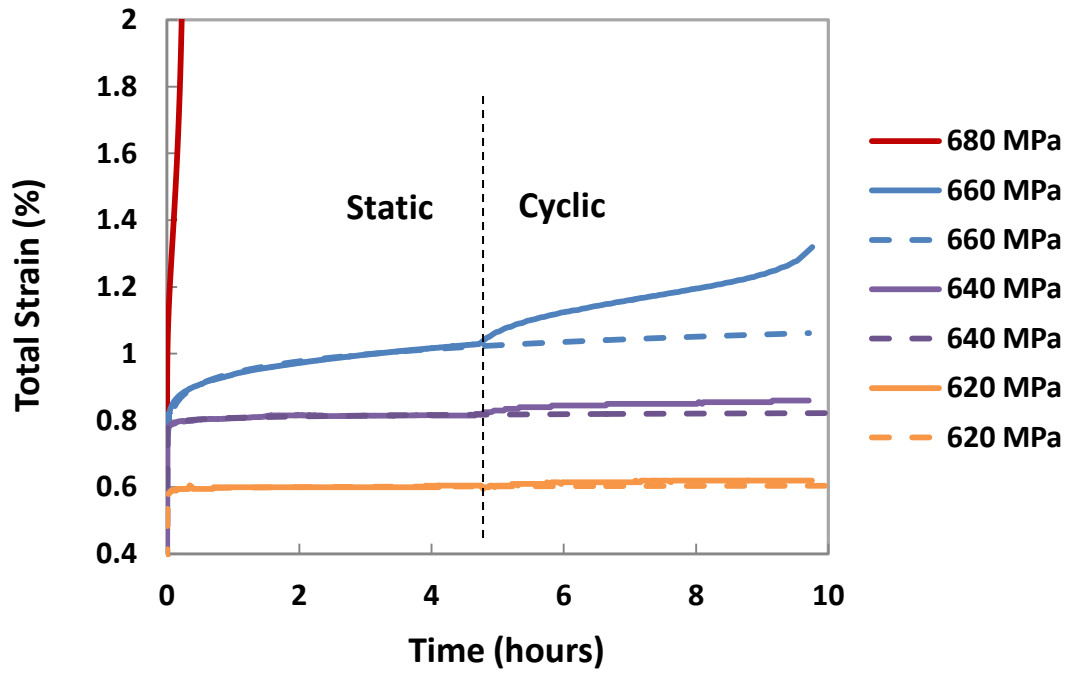
FIGURE 5.11 Solid curves represent the cumulative total strain of SS 430 in static-cyclic

creep tests; dashed curves represent the total strain of SS 430 generated by the

analytical model.

Creep Curve Fitting

B = 90290.168

n = 0.0031111

m = 0.025554
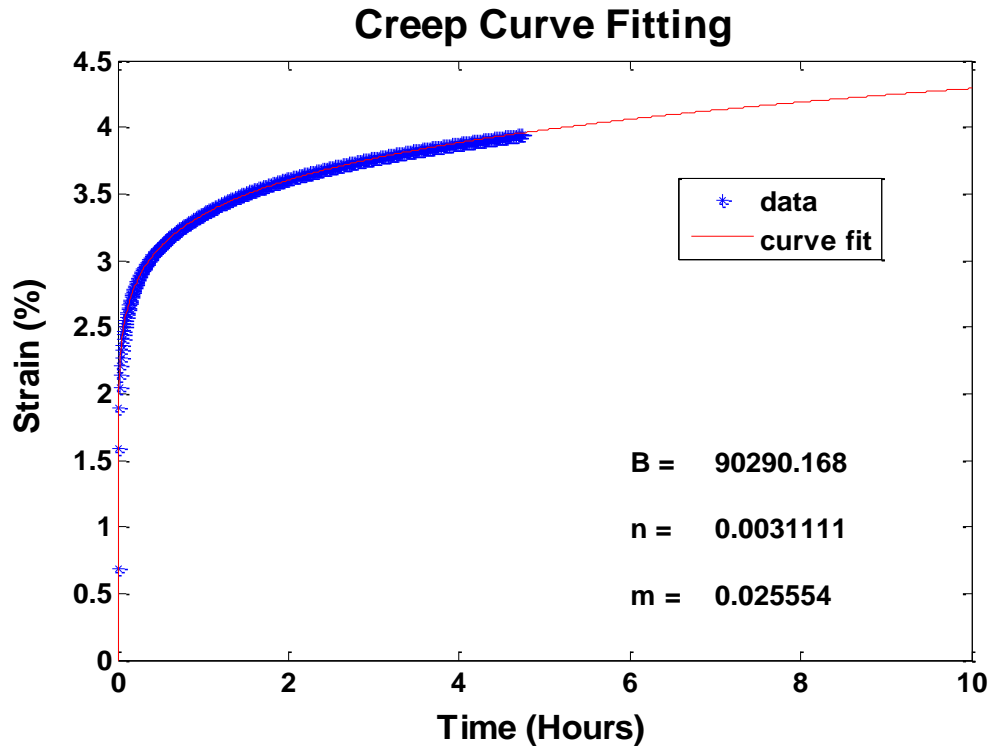
FIGURE 5.12 Curve fitting using creep model of EQUATION 5.1 for the static creep data obtained for DSS 2205 under 660 MPa. The blue stars are total strain data, and the red line represents the fitted curve using this data and the creep model.

For the three tested materials, creep strain increased with an increase in the applied stress level. The strain levels that SS 430 could reach were much smaller than those for DSS 2205 and SS 304L, and this could be explained by the limited ductility of SS 430.

Under the pre-straining condition, cyclic creep acceleration happened to all three stainless steels with different crystal structures. This is a significant difference from the pure static and cyclic creep behavior of SS 304L and SS 430, which exhibited cyclic creep

retardation, as illustrated by FIGURE 5.3 and FIGURE 5.4. These results strongly suggested that pre-straining could significantly enhance the cyclic creep strain accumulation under the same stress level as the pre-straining. Furthermore, it could even change the nature of cyclic creep accumulation of both stainless steels from retardation to acceleration. In fact, in the presence of pre-straining, the cyclic creep acceleration was always observed, regardless of the crystal structure type of the materials, i.e., BCC or FCC [1, 2, 4]. It was discussed in Section 5.1 that the cyclic creep behavior was associated with dislocation rearrangement. Therefore, when the dislocation density and the total stored energy were increased with increasing pre-straining, the probability and the driving force for dislocation rearrangement were both increased as well [97]. However, it was worth mentioning that with or without pre-straining, DSS 2205 always exhibited cyclic creep acceleration at room temperature.

5.2.4 Creep Strain Ratio

The cyclic creep acceleration parameter "creep strain ratio" was used to quantify the cyclic stress effect on the creep behavior of the three stainless steels. The creep strain ratio was defined by Shetty and Meshii [5] as

$$\frac{\varepsilon_{cn} - \varepsilon_{c1}}{\varepsilon_{st_n} - \varepsilon_{st_1}} \qquad 5.5$$

where $\varepsilon_{cn} - \varepsilon_{c1}$ is the difference between the total strain after the n-th stress cycle minus the total strain in the first cycle, and $\varepsilon_{st_n} - \varepsilon_{st_1}$ is the corresponding static creep strain occurring during the same time interval, as labeled in FIGURE 5.13.
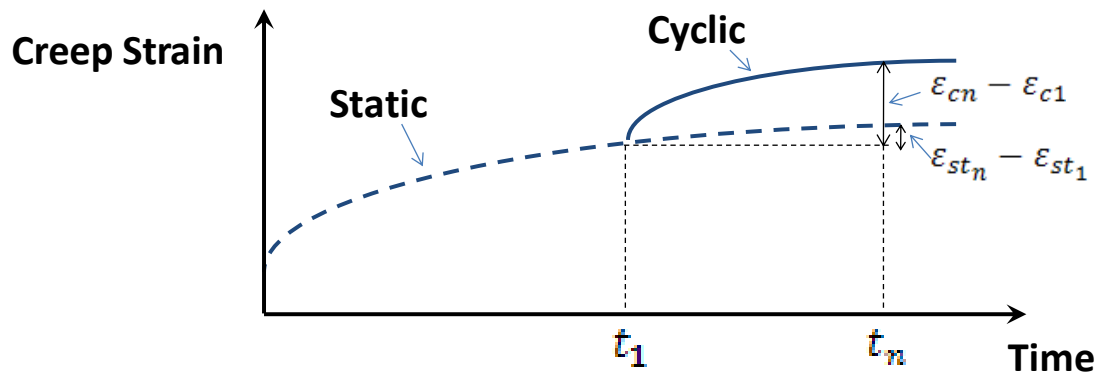
FIGURE 5.13 Schematic drawing illustrating the definition of creep strain ratio.

From the definition of creep strain ratio, it measured the cyclic creep strain normalized by the strain caused by static loading of the same stress level during the same time period. The advantage of using this parameter, instead of the absolute values of the total creep strain is that this parameter quantified the magnitude of the additional creep strain caused by cyclic stress, as compared to static stress. From the static-cyclic creep test data and the extrapolated data from the creep model in, FIGURE 5.9, FIGURE 5.10 and FIGURE 5.11, the creep strain ratios were calculated and are plotted in FIGURE 5.14, FIGURE 5.15 and FIGURE 5.16.

The creep strain ratios decreased with the increasing of the number of cycles. In other words, the effect of cyclic loading on creep strain accumulation was greatest upon the application of the cyclic loading, and then it decreased with time. The only exception is

the creep strain ratio of SS 430 under the cyclic stress of 660 MPa, as shown in FIGURE 5.16. This was due to the stress was too large and mechanical instability occurred to the material, as illustrated by the cumulative static-cyclic creep curve of SS 430 under 660 MPa cyclic stress in FIGURE 5.11.

Another distinct feature exhibited by the creep strain ratios data was that the maximum creep strain ratios were generally obtained at lowest or intermediate stress levels, as shown in FIGURE 5.14, FIGURE 5.15 and FIGURE 5.16. Similarly, in Shetty and Meshii's study for pure iron [5], the maximum creep strain ratio was observed at intermediate stress levels, whereas at the highest stress level they investigated, the creep strain ratio was the minimum values among all stress levels. Although the absolute creep strain value of $\varepsilon_{cn} - \varepsilon_{c1}$ may be large at higher stress levels, but the denominator $\varepsilon_{st_n} - \varepsilon_{st_1}$ was large as well, which makes the ratio of the two quantities even smaller. On the other hand, because of the extremely small strain $\varepsilon_{st_n} - \varepsilon_{st_1}$ generated by static stress at lower stress levels, the creep strain ratio became relatively large. That is equivalent to say that at lower stress levels, when the static stress could hardly generate any additional strain with time, the application of the cyclic loading retriggered the almost-stopped strain accumulation again. Although the absolute creep strain induced by cyclic loading at the lower stress levels was not large, but the mobile dislocations generated by the cyclic loading through rearrangement, were large in amount compared to the existing mobile dislocations before cycling started. Similarly, at higher stresses, the absolute cyclic creep strain values were large, but at these stress levels, pure static stress could still produce a fair amount of strain, or there were still a relatively large

156

amount of mobile dislocations in the material before cycling started. Thus, microscopically the effect of cyclic loading on generating additional mobile dislocations was not as great as at lower stresses. In this way, the creep strain ratio could be considered as a measurement of the amount of mobile dislocations generated by cyclic stresses as compared to the existing mobile dislocation amount produced by pre-straining (under static load).
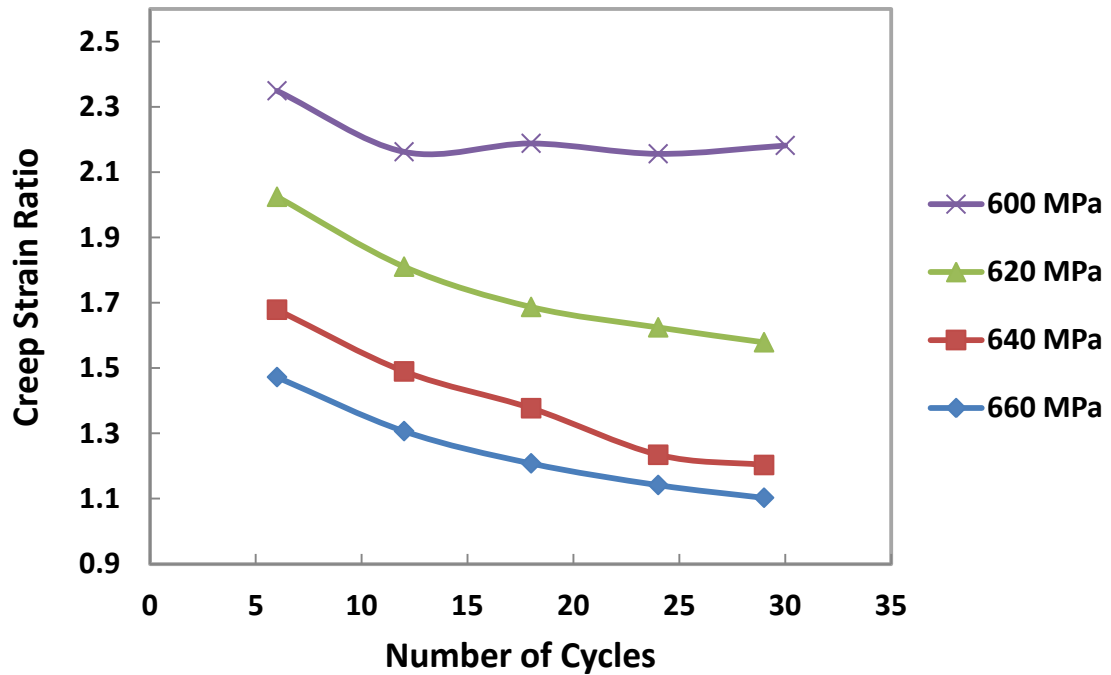
FIGURE 5.14 Creep strain ratio obtained from the creep strain data in FIGURE 5.9 for

DSS 2205.
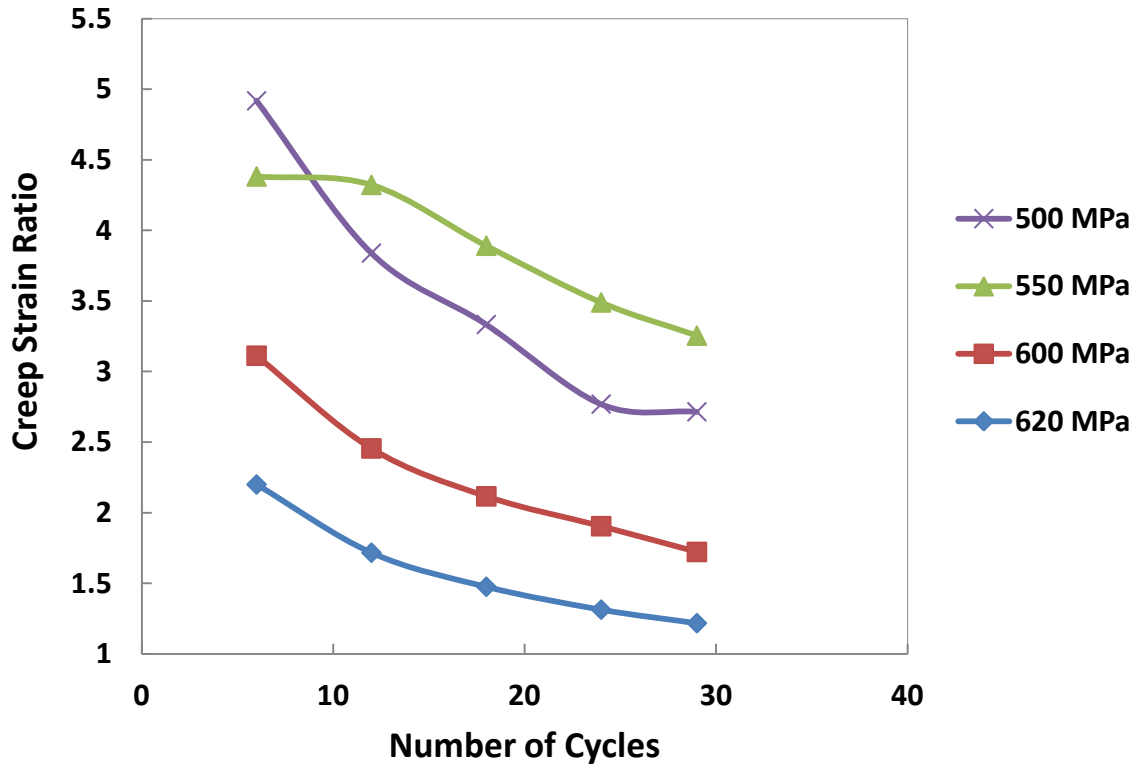
FIGURE 5.15 Creep strain ratio obtained from the creep strain data in FIGURE 5.10 for

SS 304L.
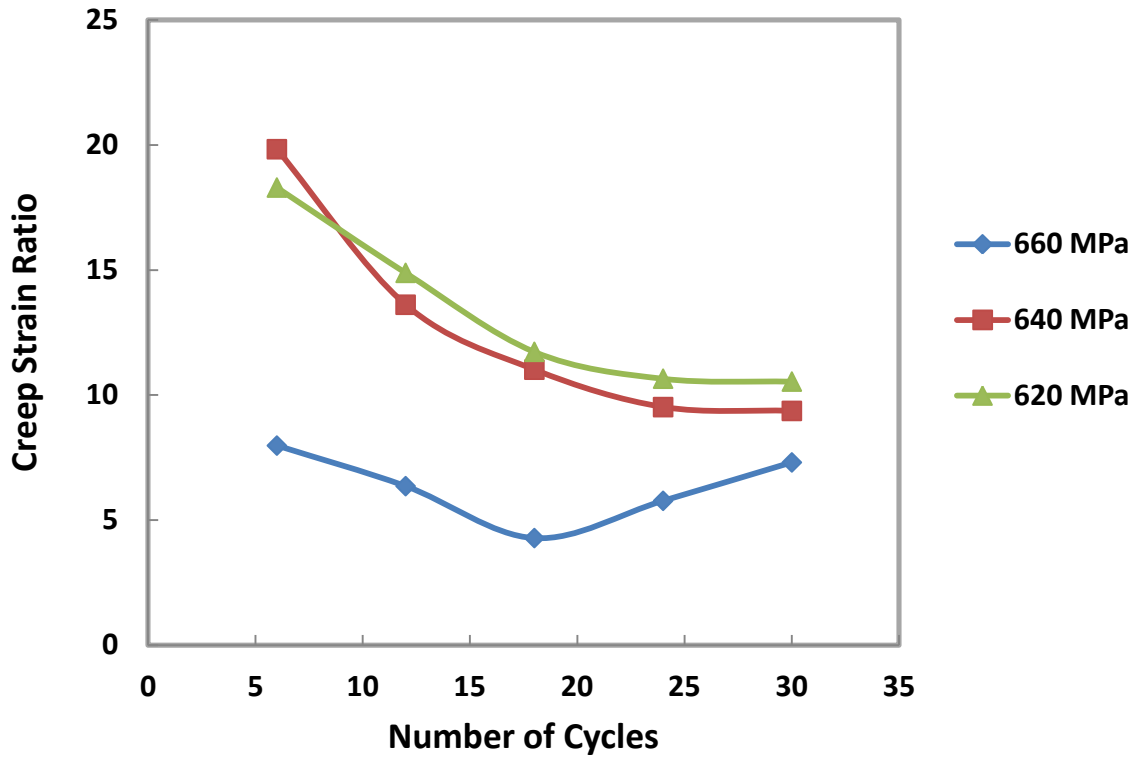
FIGURE 5.16 Creep strain ratio obtained from the creep strain data in FIGURE 5.11 for

SS 430.

The effect of different crystal structures on cyclic creep acceleration was also reflected

by the creep strain ratio of SS 304L (FCC) and SS 430 (BCC). Comparing the results in

FIGURE 5.15 and FIGURE 5.16, it is clear that the creep strain ratio values for SS 430

were much larger than those for the SS 304L. The creep strain ratio for SS 430 could be

as large as 20, but the largest creep strain ratio for SS 304L was less than 5. This means

that at the similar stress level, the mobile dislocations were more easily generated by

cyclic loading in BCC material than in FCC material. This is counter-intuitive, as the FCC

materials are more ductile due to large number of closed packed slip systems available at room temperature, whereas the BCC does have more slip planes, but are not close-packed. However, our results (which will be discussed in details in Section 5.2.3) also indicate that the austenite grains strain-harden more than the BCC-ferrite grains under cyclic loading parameters tested.

There were two ways that the mobile dislocations could be generated, as discussed in Section 5.1. First, Obstacle dislocations may become rearranged because of the altered state of internal stress. Second, mobile screw dislocation segments may leave their slip planes by cross-slip aided by fluctuations in internal stress encountered during reverse movement, and it could be called as cross slip model. It is well known that the metals with BCC crystal structures could cross slip extensively [156], because BCC materials have many possible slip planes intersecting along the <111> close-packed direction. Therefore, if the second mechanism works, the BCC crystal material SS 430 should exhibit a higher cyclic creep acceleration behavior. This may explain why the BCC material SS 430 has a much higher creep strain ratio values than FCC material SS 304L as well as DSS 2205. It also suggested that the cross slip model could be used to explain the cyclic creep acceleration of stainless steels at room temperature.

Based on the above discussions and considering the phase crystal structures, the cyclic creep behavior of DSS 2205 was controlled by the strain accumulation behavior of the two phases. Under low frequency cyclic loading, ferrite phase (BCC) enhanced strain accumulation through extensive dislocation cross-slips, whereas the austenite phase

(FCC) tended to weaken the cyclic stress effect on creep strain accumulation through cyclic strain hardening.

5.3   Conclusions

From the study on the creep behavior of DSS 2205, SS 304L and SS 430 under low frequency cyclic loading at room temperature, the following conclusions could be drawn.

❖ Cyclic creep acceleration was observed for DSS 2205 at room temperature under both cyclic creep conditions, with or without pre-straining.

❖ Cyclic creep acceleration of DSS 2205 at room temperature occurred above the yield strength.

❖ For all three stainless steels investigated, DSS 2205, SS 304L and SS 430, creep strain increased monotonically with the an increase in stress level, under both pure static and cyclic and static-cyclic creep conditions.

❖ Cyclic creep retardation was observed on SS 304L and SS 430 in pure cyclic creep tests at room temperature, and it was mainly due to the cyclic-hardening induced by the cyclic loading. Cyclic creep acceleration and retardation were not crystal structure dependent.

❖ Pre-straining could significantly enhance the cyclic creep strain accumulation under the same stress level as used for the static pre-straining.

❖ All three stainless steels, DSS 2205, SS 304L and SS 430, exhibited cyclic creep acceleration under static-cyclic creep test conditions, or when they were pre-

strained at the same stress level as the cyclic stress for 4.75 hours before the cyclic stress was applied.

❖ The decrease of creep strain ratio with the number of cycles indicated that the effect of cyclic loading on creep strain accumulation was greatest during initial cycles, and then it decreased with time/number of cycles.

❖ The cross slip model could be used to explain the cyclic creep acceleration of stainless steels at room temperature. Specifically, mobile screw dislocation segments may leave their slip planes by cross-slip aided by fluctuations in internal stress encountered during reverse movement. Steel tested with BCC crystal structure was more susceptible to cyclic creep acceleration, because of the extensive cross slips happening in this type of structure.

❖ The cyclic creep behavior of DSS 2205 was controlled by the strain accumulation behavior of the two phases. Under low frequency cyclic loading, ferrite phase (BCC) enhanced strain accumulation through extensive dislocation cross-slips, whereas the austenite phase (FCC) may resist the cyclic stress effect on creep strain accumulation through cyclic strain hardening.

CHAPTER 6 CYCLIC STRESS EFFECT ON STRESS CORROSION

CRACKING OF DUPLEX STAINLESS STEEL 2205

6.1   Introduction

Previous work on mild steel tested in sea water has shown that deterioration of mechanical properties under cyclic loading is very small when either high frequency or low stress level were applied [126]. However, this study also showed that the environmental induced damage in mechanical properties was more severe under high stress/ultra-low frequency cyclic fatigue loading [126]. Structures may experience low frequency loads under various scenarios. For example, the large changes of the still-water bending moment when the loading condition goes from ballast to fully loaded and back, or the low frequency changes of stresses related to the temperature changes (day/night), and for offshore structures, changes of wind and wave directions [126]. As for high stresses, in a study of the practical load history to the North Sea offshore tabular structures, Pook [157] showed the possibility of having stresses in a structure above the yield stress at higher applied stress levels. Another source of high stress-low frequency loads in ships is slamming or crash into other structures. According to Aertssen [158], peak stress of 110% yield stress for mild steel caused by wave bending and slamming for ships was found to occur 2 or 3 times per hour, which is a frequency less than 0.001 Hz. Below 10^{-2} Hz and under constant amplitude loading, the crack growth rate increased by a factor of 2 for every 10-fold reduction in frequency [126].

The insufficient corrosion fatigue (CF) resistance in the standard grades of stainless steels is due to a variety of deficiencies in these materials [159]. Austenitic stainless steels, such as 304 and 316, usually have low fatigue strength because of their low yield strength. Moreover, they are quite susceptible to stress corrosion cracking (SCC) in various corrosive environments. Ferritic stainless steels, such as 430 and 446, have high fatigue crack propagation rates at stress intensities greater than half the fracture toughness, K_c, because of their low ductility and toughness. Martensitic stainless steels, such as 410, have higher yield strength and good toughness in the tempered condition, but their low chromium content significantly decreases their corrosion resistance. Hence, the development of duplex stainless steels (DSSs) has successfully exhibited an improved CF behavior compared to other related alloys. They have the corrosion resistance, ductility, and toughness of austenitic stainless steels, and high strength and the SCC resistance of ferritic stainless steels.

The deleterious effects of corrosive environment on fatigue lives of various alloys, including DSSs, have been proved in numerous studies, especially in chloride-containing environment. Makhlouf *et al.* [120] compared the CF crack propagation of a DSS (X6CrNiMoCu 25-6 type) in air at room temperature and in artificial sea water at 70 °C. At a frequency of 0.1 Hz and a stress ratio of 0.1, the CF crack growth rate was about 1.7 orders of magnitude higher than that in air. Girones and his co-workers [117] also performed low cycle fatigue tests on super DSS SAF 2507 in a frequency range of 0.26 ~ 0.76 Hz, in air and artificial sea water at room temperature. The results indicated a remarkable reduction in fatigue life in the presence of the corrosive environment,

especially for high strain amplitudes. Tseng *et al.* [128] found the CF crack growth rate of 22%Cr DSSs was higher in 3.5 wt.% NaCl solution at 80 °C than the crack growth rate generated in air. In this corrosive environment, the experimental results also indicated that the effect of nitrogen content on CF crack growth rate depended on the fatigue frequency. Specifically, the CF crack growth rate was affected by the nitrogen content of the material at a lower fatigue frequency of 0.1 Hz, but not affected at a frequency of 1 Hz. In this system, the SCC mechanism was hydrogen embrittlement. At 1 Hz, the environmental effect was not pronounced due to the high frequency, whereas at 0.1 Hz, the increase of nitrogen content reduced the ferrite content, hence the contribution of hydrogen embrittlement was decreased.   In another CF study of DSS 2205 at a frequency of 47.5 Hz and stress ratio of -1, Stevens [160] also compared the S-N curves obtained in air and in artificial sea water at 55 °C. He found the fatigue lives of DSS 2205 were significantly lowered by the corrosive environment. Johansson and Groth [161] conducted fatigue experiments on DSS 2205 at 50 Hz in air and in 0.01 N NaCl solution. They found the endurance limit of the material, which was 420 MPa in air, dropped to 220 MPa in NaCl solution at room temperature. Further reduction in fatigue endurance limit was observed when the CF tests were run at higher temperatures. However, very little work has been done on CF behavior of DSS in caustic sulfide-containing solutions, as compared to acidic chloride environments. In paper machine white water environment, Perdomo and Singh *et al.* [45, 162] studied crack initiation and propagation behavior of a few cast DSS materials at a frequency of 25 Hz with a stress ratio of 0.5. They found the microstructural changes caused by different heat treatment

conditions had a significant influence on the threshold stress intensity for crack propagation of DSSs.

Although extensive studies have been done on CF behavior of DSSs, almost all of them were done at relatively higher frequencies. The lowest frequency investigated in the published work was 0.01 Hz. It is a well known fact that CF behavior of metals is frequency dependent, hence the CF behavior of DSSs at ultra-low frequency or strain rate ($<10^{-3}$ Hz) was not fully understood. At lower frequencies, the effect of the cyclic creep induced plastic deformation is large; hence the low frequency is expected to influence the CF crack initiation behavior of DSS 2205. In a mixed acid solution of 2M H_2SO_4 + 0.7 M HCl, Tsai and Lo [163] reported a significant reduction in fatigue lives of DSS 2205, compared to the fatigue life in air. Moreover, the test results showed that at all three potential values they investigated, i.e., open circuit potential (OCP), -300 mV (SCE), and -240 mV (SCE), the CF lives of DSS 2205 decreased when the frequency decreased from 10 Hz to 5 Hz to 1 Hz.

Most of the published research on CF of DSSs is focused on the crack propagation process, and only very few were dedicated to CF crack initiation behavior. Tsai and Lo [163] performed interrupted CF tests for DSS 2205 in mixed 2 M H_2SO_4 + 0.7 M HCl solution at different potential values. The CF tests were stopped at 40% fatigue lives to observe the crack initiations. They found that under the applied potential of -300 mV (SCE), the cracks were sharp at 10 Hz, but blunt at 1 Hz, indicating more corrosion occurred in the crack tip at lower frequency. Through the interrupted CF tests, they also

studied the selective dissolution effect on fatigue crack initiations. Micrographical examination of the fatigued sample surfaces suggested that the cracks initiated in the phase with a lower selective dissolution rate. Because the selective dissolution removed the slip bands or the stress concentration sites in that phase [65].

Variables influencing the CF behavior of DSSs are not only the loading parameters, Moskovitz and Pelloux [159] concluded that the main structural variables affecting the corrosion-fatigue crack initiation and crack propagation in acidic chloride solution are: volume fraction of austenite and ferrite, microstructural orientation of the different phases, intermetallic precipitates and grain boundary carbides.

6.2   Results and Discussion

In the present study, the CF behavior of DSS 2205 in both acidic chloride and caustic white liquor (WL) environments was investigated in the ultra-low frequency range, which has never been done in these systems. We focused on the effect of the mechanical loading parameters, i.e., stress level and stress ratio to understand how these parameters help effect crack initiation as well as propagation. Crack initiation was defined as the cracking or debonding propagating into matrix of the material in this study.

6.2.1 Low Frequency CF Behavior of DSS 2205 in Acidic Chloride Environment

DSS 2205 tensile samples were tested under low frequency cyclic loading conditions to study the low frequency CF behavior of this alloy in 26 wt.% NaCl solution with pH = 2 at room temperature. A potential of -375 mV (SCE) was applied throughout the tests as the alloy shows SCC susceptibility under these electrochemical conditions. All CF tests were performed on a modified slow strain rate test (SSRT) rig with capability of cyclic loading. These tests were done with an initial strain rate of 1×10^{-6} s^{-1}. Stress level and stress ratio were varied in each test to investigate their effects on CF crack initiation of DSS 2205 in this environment. The test matrix is outlined in TABLE 6.1. In this table, the stress levels are presented as the percentage of yield strength (YS) of DSS 2205 in the acidic NaCl solution obtained under the same slow strain rate 1×10^{-6} s^{-1}, 530 MPa. Cyclic frequency in these tests was determined by the applied stress range and strain rate, hence changed slightly in each test, but fell into the range of 10^{-5} Hz for all tests described here. Because of the extremely low frequencies, the test durations were typically long. For example, the test #3, which was conducted at the maximum stress equal to 140% YS and stress ratio of 0.1 took roughly 30 days to complete 47 cycles.

TABLE 6.1 Maximum stress, stress ratio and number of cycles used for the CF tests of DSS 2205 in acidic chloride environment.

Test No.	Max. Stress	Stress Ratio	Cycles
#1	110% YS	0.1	32
#2	120% YS	0.1	32
#3	140% YS	0.1	47
#4	140% YS	0.5	47
#5	140% YS	0.8	47

In order to investigate the CF crack initiation of DSS 2205, after a certain amount of cycles, the CF tests were stopped and the samples were unloaded to examine their surfaces under scanning electron microscope (SEM). In contrary to notched or flat specimen, round smooth tensile specimens do not have a specific crack initiation site. Hence search for crack initiation required a very thorough examination of the entire surface of each tensile sample after test, which was a very time-consuming task. However, as the main aim of this study was to understand the crack initiation under low-frequency cyclic loading conditions, therefore smooth tensile specimens were used in this study.

To compare the crack initiation under cyclic and monotonic loading, interrupted monotonic SSRT were also performed for DSS 2205 in acidic NaCl environment. By comparing the cyclic fatigue and monotonic SSRT results obtained under the same

maximum stress, the effect of cyclic stresses and the crack initiation mechanism were illustrated.

6.2.1.1 Crack Initiation

Visual inspection performed on all CF test sample surfaces showed that cracks initiated exclusively from intermetallic precipitates. FIGURE 6.1 is showing the micrographs of crack initiations observed on DSS 2205 samples, tested in acidic NaCl solution under cyclic loading. Some of the crack initiations were confined within the precipitates, and many of them propagated into the base material. All of the cracks were propagating in the direction perpendicular to the direction of applied stresses. Similarly, Laitinen and Hanninen [164] studied the effect of non-metallic inclusions on high-cycle fatigue resistance of powder metallurgical fabricated and hot isostatically pressed DSSs in chloride- and sulphate-containing aqueous solution at room temperature. They found that the CF crack initiation occurred at material defects, especially oxide inclusions.
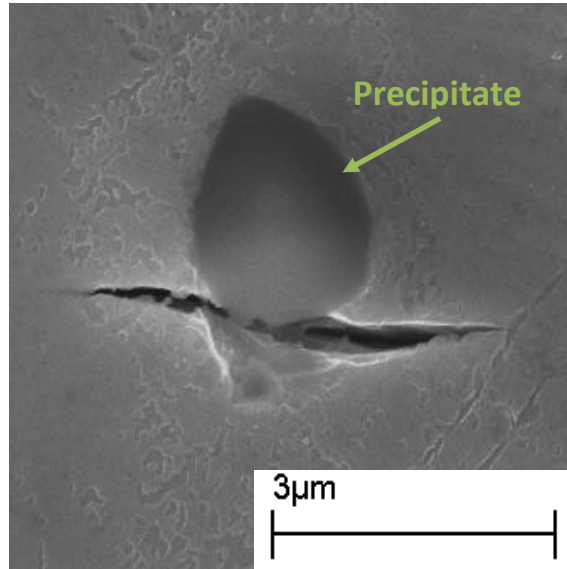
(a)
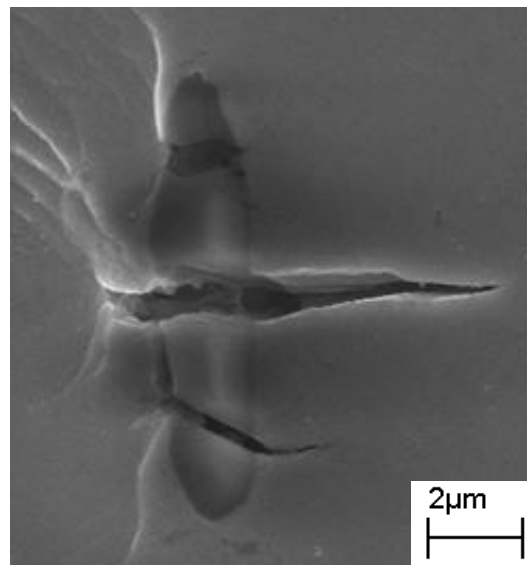
(b)

FIGURE 6.1 SEM micrographs showing crack initiation at damaged precipitates for DSS 2205 in 26 wt.% NaCl solution with pH = 2 after 47 cycles at strain rate of 1×10^{-6} s^{-1} with an applied potential of -375 mV (SCE) under maximum stress of 140% YS and stress ratio of 0.5.

Metallographic examination of the DSS 2205 bar material (denoted as "2205B" in CHAPTER 3) showed that there are many oval shape intermetallic precipitates on the surface as well as inside the material. FIGURE 6.2 shows the micrographs of polished DSS 2205 with precipitates in the material. In these pictures, the dark dots are precipitates, and the lighter and darker phases are austenite and ferrite phases, respectively. Hence the precipitates exist in both phases. To find out the chemical composition of the precipitates, the energy disperse X-ray electron spectroscopy (EDS) equipped on the SEM was used on a number of different precipitates from different specimens, and an example of the typical EDS spectra for these precipitates is shown in FIGURE 6.3. Similar compositional results were obtained on all of the precipitates, and TABLE 6.2 shows the weight percentage of the elements in the precipitates, averaged from six different EDS results. From these results, the O and Mn content of these precipitates is high, about 35% and 23% respectively. Precipitates also contained significant amount of Al and Cr along with a small amount of Ti. However, sulfur was not detected in these precipitates. Although this type of precipitates are not well characterized in DSSs, Park and Kwon [165] have reported similar intermetallic precipitates in Fe-18Cr alloy with addition of Mn.
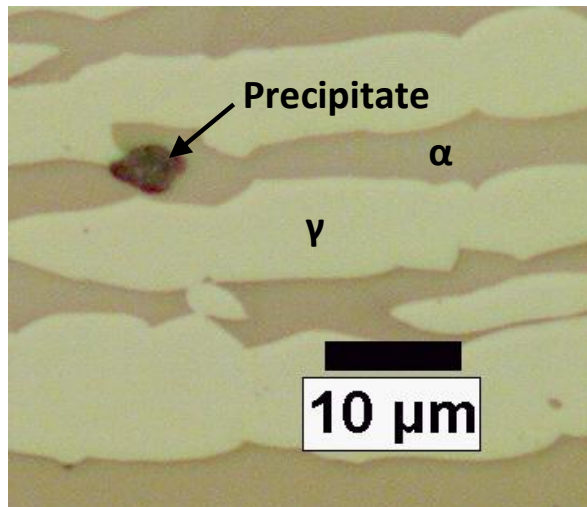
(a)
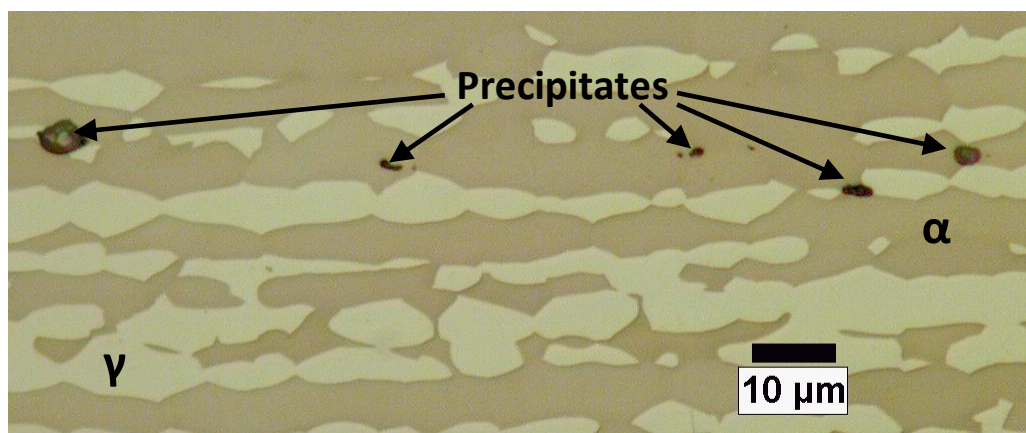
(b)

FIGURE 6.2 Micrographs of inclusions in DSS 2205.
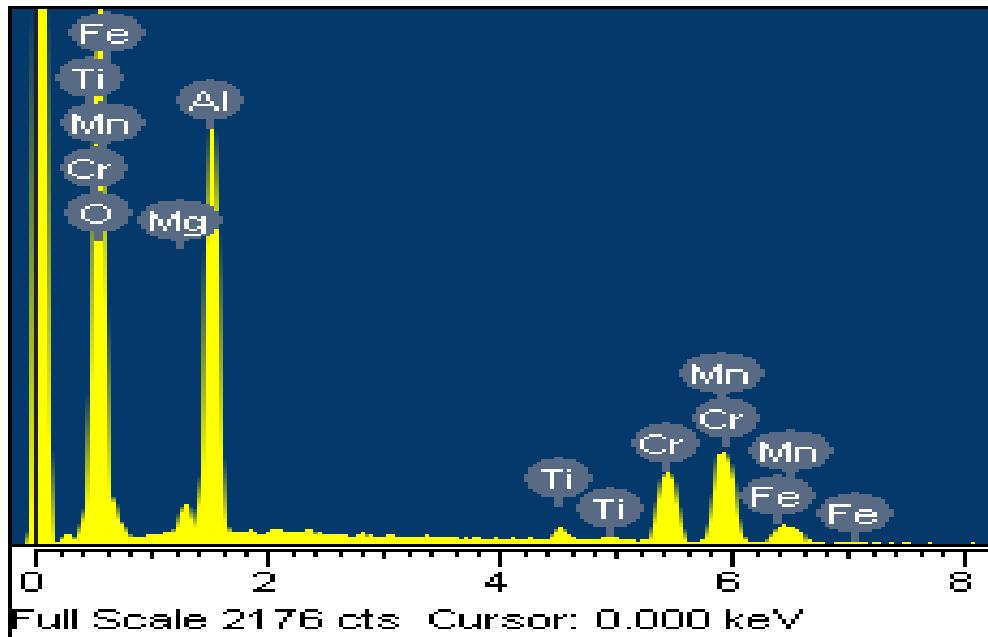
FIGURE 6.3 EDS spectra of intermetallic precipitate in DSS 2205.

TABLE 6.2 Averaged chemical composition of intermetallic precipitates, showing crack initiation in DSS 2205.

Element	O	Mg	Al	Ti	Cr	Mn	Fe	Total
Weight. %	35.14	1.18	19.42	1.37	15.28	23.65	3.69	100.00

Further testing and examination of the surface damage on cyclically loaded tensile samples revealed the role of the corrosive environment and cyclic stress during the crack initiation in DSS 2205. To illustrate the effect of the corrosive environment, a cyclic fatigue test was also performed under the same condition as test #3 in TABLE 6.1, but in air. FIGURE 6.4 and FIGURE 6.5 are SEM graphs showing the precipitate damages after

fatigue testing in air and in acidic NaCl solution, respectively. The major difference in the damages is especially exhibited by the damage of the smaller precipitates. In acidic NaCl environment, the small precipitates were dissolved out of the material, leaving numerous small pits on the surface of the material (FIGURE 6.5). In air, however, small precipitates are not dissolved or damaged at all, as shown in FIGURE 6.4. This phenomenon was found in all specimens tested in NaCl environment, indicating the attack of the corrosive environment at the interface between the precipitates and the base material. It was clear from the examination that the interface between the precipitates and the matrix was preferentially attacked in tested environment. Small pits were seen at the area of smaller precipitates, whereas the larger precipitates were still present with the interfaces attacked, as is shown in FIGURE 6.5. Equivalent micrograph for the sample tested in air did not show any cracks in the smaller precipitates, whereas the larger precipitates did show cracks in the precipitate or at the interface. Since the small precipitates are relatively shallow, they are easily removed by the corrosion attack at the interface while for the larger precipitates, embedded deeper into the base material, were still present in the material, as is shown in FIGURE 6.5.

(a)   (b)
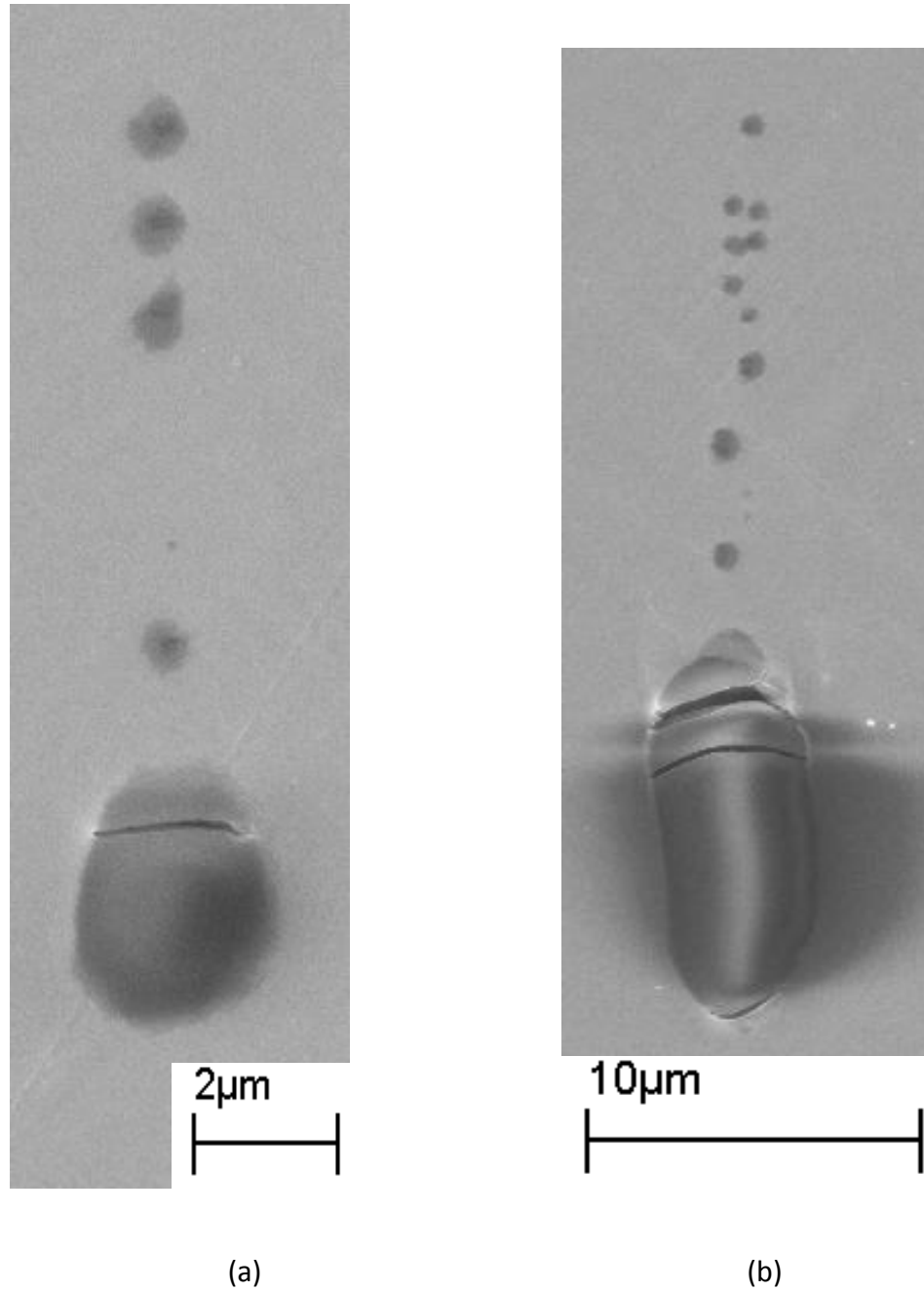
FIGURE 6.4 SEM micrographs showing damages of precipitates for DSS 2205 in air after

cyclic fatigued 47 cycles, under a maximum stress of 140% YS, stress ratio of 0.1, and

at a strain rate of 1×10^{-6} s^{-1}.
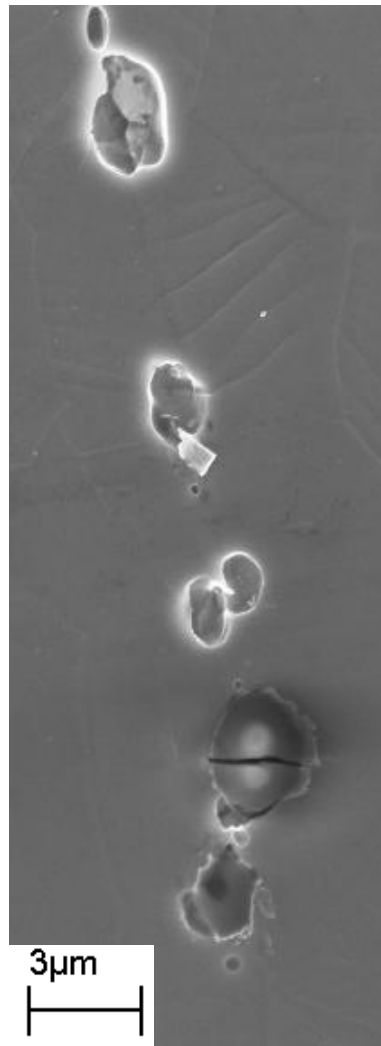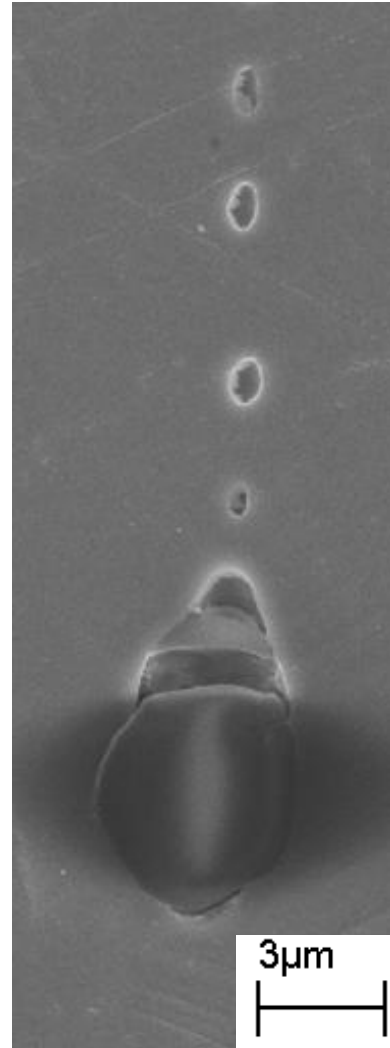
(a)   (b)

FIGURE 6.5 SEM micrographs showing damage of precipitates for DSS 2205 in 26 wt.% NaCl solution of pH = 2 after cyclic fatigued at strain rate of $1 \times 10^{-6}\ s^{-1}$ with an applied potential of -375 mV (SCE) (a) 32 cycles at maximum stress of 120% YS and stress ratio of 0.1 (b) 47 cycles at maximum stress of 140% YS and stress ratio of 0.8.

The preferential corrosion attack at the precipitate interfaces can be attributed to the galvanic effect that caused the interface to be more active compared to the precipitates. To understand the alloy composition at the precipitate/alloy interface, EDS analysis was carried out for a number of precipitates and their interfaces. TABLE 6.3 shows the averaged EDS results with major alloying elements near the precipitates. The Mn content was 50% lower than that in the base material, but concentration of other alloying elements did not change much from the base alloy in interface areas. The depletion of Mn may be due to the enrichment of Mn in the precipitates. Jang *et al*. found the SCC resistance of cast DSS CD4MCU increased in 3.5% NaCl + 5% H_2SO_4 aqueous solution, when the Mn content increased from 0.8% to 2.0% [166]. Thus, the decrease Mn content near the precipitates may also have assisted the preferential corrosion attack at the interface.

Detrimental effect of Mn on localized corrosion has also been reported in some other studies [165, 167], but the reasons were mainly attributed to the Mn-containing precipitates formed because of the addition of Mn. Pardo *et al*. [167] found the detrimental effect of Mn on pitting corrosion behavior of austenitic stainless steel 304 and 316 in chloride environment was mainly due to the presence of MnS inclusions which acted as pitting initiators. Similarly, Park and Kwon [165] also found that the decrease of localized corrosion resistance for Fe-18Cr alloy in NaCl solution was caused by the increase in the number and size of Mn-containing oxides, acting as initiation sites for pitting corrosion. However, we did not see any sulfur in the Mn containing precipitates in tested DSS 2205 samples.

TABLE 6.3 Averaged chemical composition of material near precipitates, obtained by EDS.

Element	Cr	Mn	Ni	Mo	Fe	Total
Weight %	24.35	0.70	4.51	3.91	66.52	100.00

In order to illustrate the effect of cyclic stresses on damage accumulation and crack initiation, two constant extension rate tests were interrupted at 140% YS and ultimate tensile strength (UTS). These tests were conducted under the same environmental conditions as the cyclic CF tests. FIGURE 6.6 is shows the micrographs of the surface damage for the two specimens after the tests were interrupted. Comparing to the CF crack initiation of DSS 2205 under the same conditions in FIGURE 6.1, the main characteristic of crack initiation under constant extension loading was that the cracks were all confined within the precipitates and did not propagate into the matrix for the constant extension tests. Even after applied strain equivalent to the UTS, cracks did not propagate into the base material. Whereas when the specimen was cyclically loaded under a maximum stress of 140% YS and stress ratio of 0.5, at multiple sites the cracks propagated from cracked precipitates into the base material, only after 47 cycles, as is shown in FIGURE 6.1. Therefore the cyclic stress has largely enhanced the crack initiation for DSS 2205 exposed to acidic NaCl environment.
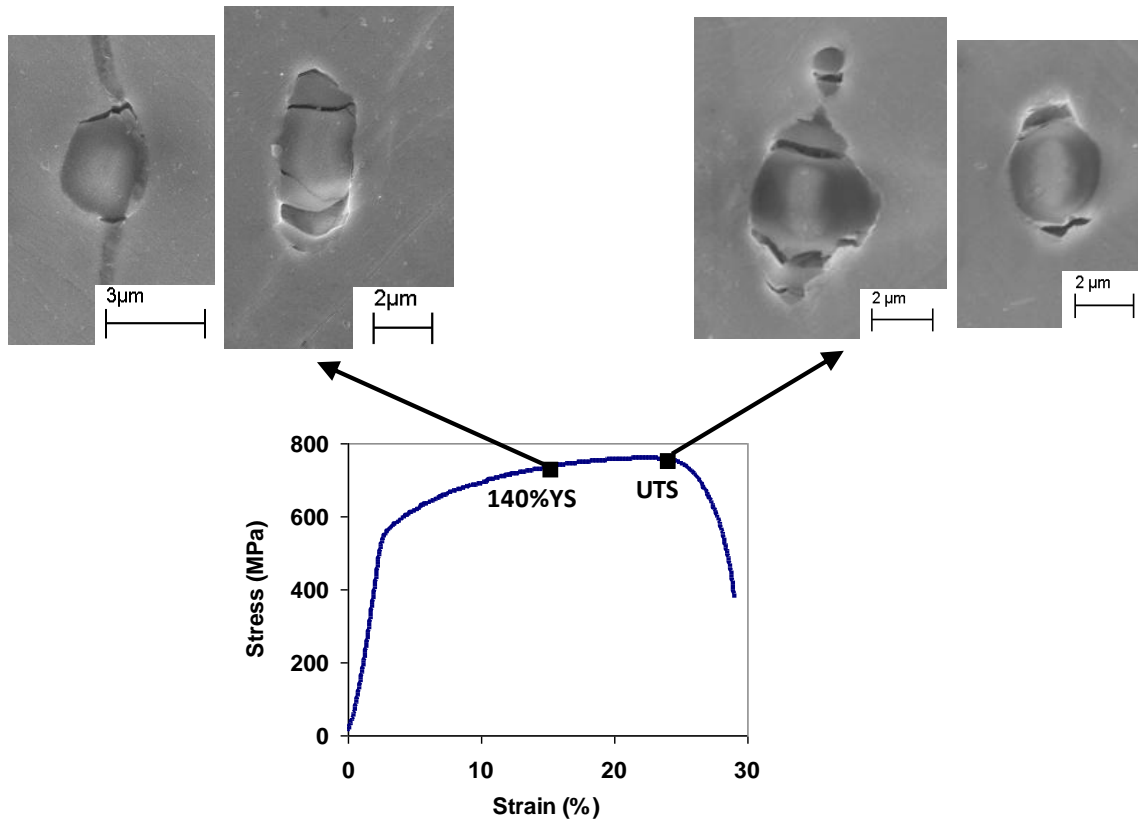
FIGURE 6.6 SEM micrographs showing crack initiation for DSS 2205 after monotonic SSRT test in 26 wt.% NaCl solution of pH = 2 with an applied potential of -375 mV (SCE) at a strain rate of 1×10^{-6} s^{-1}.

SSRT test results presented in CHAPTER 4 have shown that the SCC of DSS 2205 in acidified NaCl environment initiated from ferrite phase. However, the CF test results showed that the crack initiation predominately occurred at precipitates. This is because the stress corrosion crack initiation observed on the cross section of fractured DSS 2205 specimens was caused by corrosion attack under significant plastic deformation, especially after localized strain accumulation and necking had set in the sample. On the

other hand, the CF crack initiation at precipitates on the un-fractured specimens did not require similar applied plastic deformation. Hence, there were still crack initiations at precipitates under monotonic SCC condition, but with an increase in the applied strain in SSRT, cracks also initiated in ferrite phases, especially in the necked area.

6.2.1.2 Effect of Stress Level

The effect of maximum stress of the cyclic loading on CF crack initiation was illustrated by comparing the crack initiations of Test #1, #2 and #3 in TABLE 6.1. After each CF test, the whole gage section of the specimen was examined under SEM, and crack initiations were recorded through pictures. Then the crack initiation characteristics and crack lengths were measured and compared.

For CF crack initiation in specimens of Test #1, #2 and #3, one common feature was that the crack initiations in all these cases were confined within the intermetallic precipitates. Hence in this case, the crack initiation started with precipitate damage. The crack lengths were associated with the specific sizes or widths of the precipitates. FIGURE 6.7 shows the SEM micrographs illustrating the typical precipitate damages after CF tests under different maximum stress levels. From FIGURE 6.7, under maximum stress of 110% YS, no precipitate cracking was observed on this specimen, and the CF crack initiation occurred by the corrosion attack at the interface of precipitate and base alloy. For small precipitates, this corrosion attack completely destroyed the bonding between the precipitate and the base material. For larger precipitates, complete interface did not get attacked in the test time period, but the attack was sufficient to start a small crack at

the interface of precipitates and the base material, as shown in the first column of

FIGURE 6.7. With an increase in the maximum stress level, cracking of precipitates was

observed on the sample surface. Moreover, the larger the stress, the more open were

the cracks in these broken precipitates, as illustrated by the last two columns of FIGURE

6.7. At the maximum stress of 120% YS, the cracks in the precipitates were closed, but

when stress increased to 140% YS, the cracks were quite open. Plastic deformation in

the base metal, associated with the open cracks in precipitate, is also clear in FIGURE 6.7.

Therefore, the CF crack initiation or intermetallic precipitate damage of DSS 2205 in the

acidic NaCl environment was mainly controlled by the maximum stress of the cyclic

loading. The corrosive solution could attack the precipitate boundary, and assist the

debonding of precipitates. The reason that no cracks propagated into the base material

is due to the small stress ratio, 0.1, used in these tests. The stress ratio effect on CF

crack initiation is discussed in the next section.
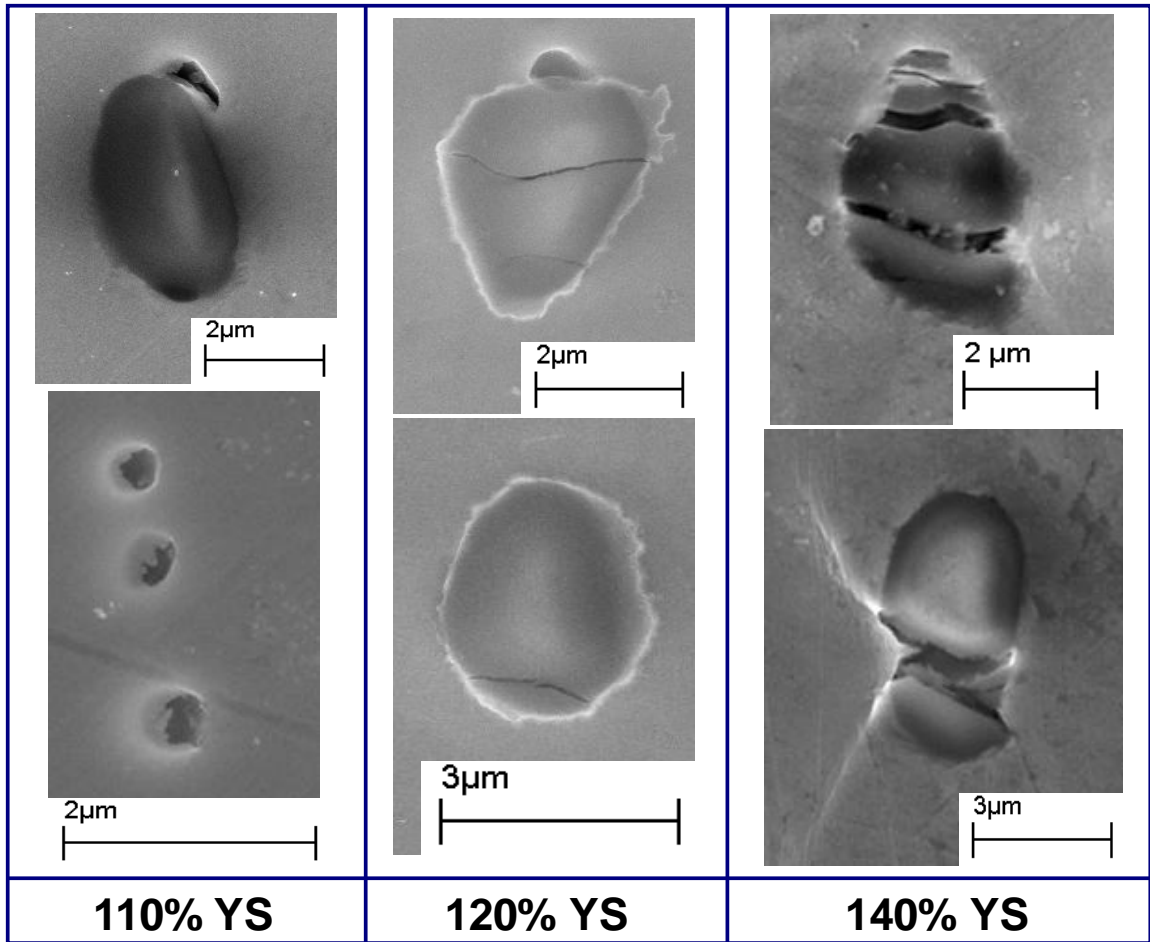
FIGURE 6.7 SEM micrographs showing crack initiation for DSS 2205 after CF tests in 26 wt.% NaCl solution of pH = 2 at a strain rate of 1×10^{-6} s^{-1} with an applied potential of -375 mV (SCE), at stress ratio 0.1 and various maximum stress levels.

6.2.1.3 Effect of Stress Ratio (R)

The effect of stress ratio, minimum stress/maximum stress (R), of the cyclic loading on the CF crack initiation was illustrated by comparing the crack initiations of Test #3, #4 and #5 in TABLE 6.1. While keeping the maximum stress constant, three stress ratios

were selected in this study, and they are 0.1, 0.5 and 0.8. In order to demonstrate the

effect of stress ratio, the cracks were divided into several groups by length. The crack

density, which is the number of cracks in a certain group averaged from 7.366 mm^2 of

area thoroughly examined, is plotted in FIGURE 6.8. Results in FIGURE 6.8 show that the

overall crack density increased with an increase in the stress ratio. For stress ratio R =

0.1, there were no large cracks found on the sample surface, corresponding to no data

for crack lengths larger than 5 μm. This is consistent with the results in FIGURE 6.7,

where crack initiations were all confined within the precipitates and no cracks

propagated into the base material. For all crack length ranges, the crack densities for the

sample tested at R = 0.8 were generally more than those of R = 0.5, especially in the

intermediate range shown in FIGURE 6.8.
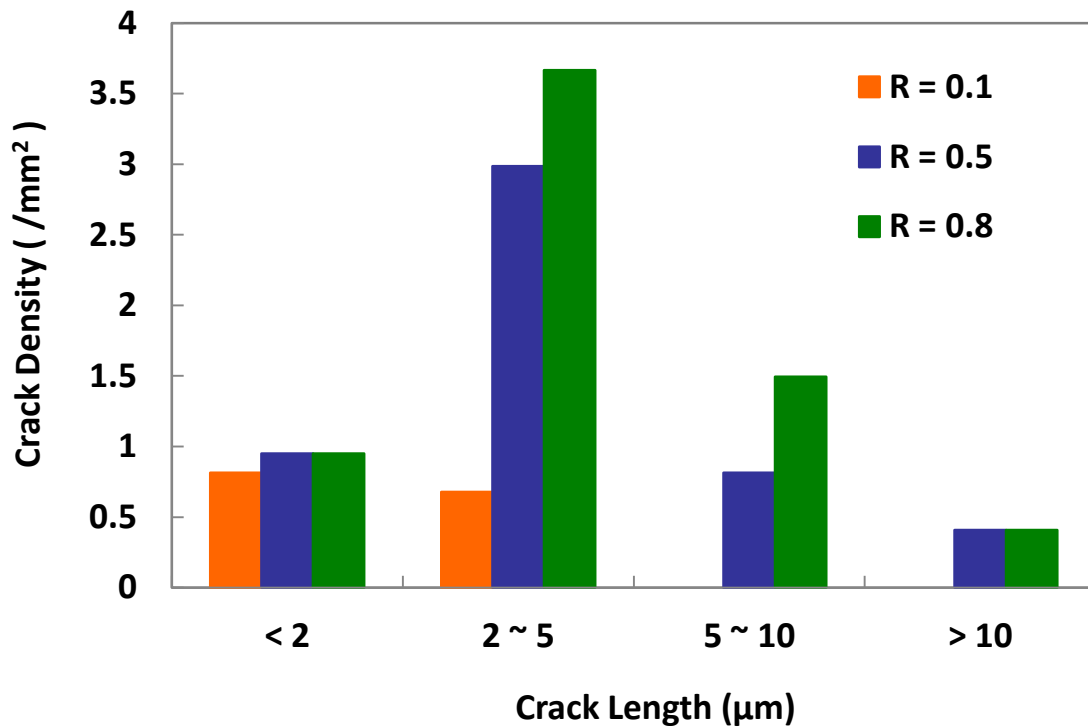
FIGURE 6.8 Averaged crack density for different crack length ranges for DSS 2205 after 47 cycles of CF tests in 26 wt.% NaCl solution of pH = 2 at a strain rate of 1 × 10⁻⁶ s⁻¹ with an applied potential of -375 mV (SCE), at maximum stress 140% YS and various stress ratios.

With the same maximum stress level, stress ratio changes correspond to changes in the stress range. Since the CF tests were conducted under constant extension rate, larger stress ratio means smaller stress range and shorter unloading time for each cycle. Thus, the stress ratio effect can also be related to the effect of unloading time. The results shown in this chapter indicated that the shorter unloading time enhanced CF crack

initiation and propagation of DSS 2205 in acidic NaCl environment. During unloading process, the passive film on the material surface can repair itself, because there are no tensile stresses to break the film. Hence, the less time for the surface film to repair, the easier for the cracks to initiate and propagate. These results suggest that under low frequencies tested, the crack initiation and propagation behavior of DSS 2205 in acidic NaCl environment was greatly controlled by the passivation and repassivation of the surface film.

Generally speaking, at relatively higher frequency range ($> 10^{-2}$ Hz), lower frequencies increases the corrosion attack at crack tip, resulting in higher CF crack propagation rates in DSSs [128, 163]. Because lower frequencies give the corrosive environment sufficient time to attack the crack tip. However, the low frequency CF test results here showed that the effect of frequency or stress ratio was contrary to that. Hence the frequency effect on CF behavior of metallic materials was totally changed when the frequency decreased to as low as 10^{-5} Hz. The main reason is that the effect of repassivation became remarkable at the ultra low frequencies because of the prolonged unloading time.

6.2.1.4 Summary

To summarize the crack initiation and propagation process of DSS 2205 in acidic NaCl environment, FIGURE 6.9 could be used for illustration. First, applied stresses cause the cracking of the precipitates and/or debonding at the interface between the precipitates and the base material, as shown by the first SEM micrograph of FIGURE 6.9. In addition,

the corrosive environment also preferentially attacks the interface of precipitates and base material. Then, during the loading process of each cycle, stress concentration at the crack initiation sites assist propagation of these cracks, as shown by the rest of the micrographs in FIGURE 6.9. However, during unloading of each cycle, the crack propagation stops, and the surface passive film may be repaired during that period of time.

The damage, i.e., cracking and debonding of precipitates was mainly determined by the maximum stress level, and the higher the maximum stress the larger is the crack opening. Additionally, the propagation of the CF crack was significantly influenced by the stress ratio (R), or the unloading time of each cycle. Specifically, the larger stress ratio, or shorter unloading time, promoted CF crack propagation.
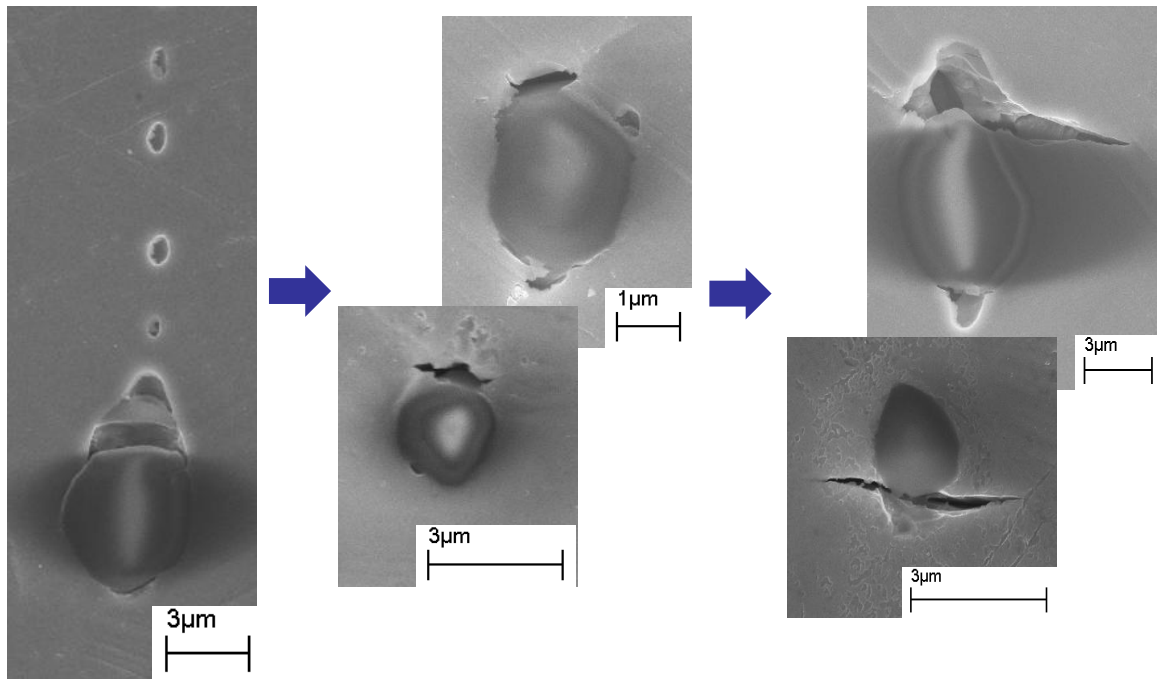
FIGURE 6.9 CF crack initiation and propagation of DSS 2205 in 26 wt.% NaCl solution of pH = 2 at a strain rate of 1×10^{-6} s^{-1} with an applied potential of -375 mV (SCE).

6.2.2   Low Frequency CF Behavior of DSS 2205 in Caustic WL Environment

Preferential attack on different phases or microstructure of DSSs not only depends on the alloy composition and processing history but also on the environmental parameters. Previous results had shown that the austenitic phase is more susceptible to stress corrosion crack initiation in hot caustic environment, especially when sulfides are also present in the solution. However, low-frequency CF behavior of DSS in hot sulfide containing caustic solutions has not been studied. To understand the effect of low frequency stress fluctuations on crack initiation, DSS 2205 tensile samples were tested under low frequency CF conditions in caustic WL solution at 170 °C. Caustic WL solution

was composed of 150 g/L NaOH + 50 g/L Na_2S. No external potential was applied. An initial strain rate 2×10^{-6} s^{-1} was used for all CF tests. Similar to the CF tests for acidic NaCl environment, maximum stress level and stress ratio were varied in each test to investigate their effect on CF crack initiation of DSS 2205 in WL. The test matrix is listed in TABLE 6.4. In this table, the stress level is presented as the percentage of YS of DSS 2205 in the caustic WL solution (500 MPa), obtained under the same slow strain rate 2×10^{-6} s^{-1}. Frequency, which was a function stress range and strain rate, changed in each test, but they were all in the range of 10^{-5} Hz.

TABLE 6.4 Maximum stress, stress ratio and number of cycles used for CF tests of DSS 2205 in acidic chloride environment.

Test No.	Max. Stress	Stress Ratio	Cycles
#1	110% YS	0.5	123
#2	110% YS	0.5	173
#3	140% YS	0.1	123
#4	140% YS	0.5	123
#5	140% YS	0.8	123

To study the CF crack initiation of DSS 2205 in WL environment, the tests were interrupted after a certain number of cycles, and the sample surface were examined under SEM. Since the specimen was tested in the caustic WL solution at high

temperature, after the test the sample surface was covered with a thick layer of black corrosion product film. In order to examine the sample surface, the film was mechanically removed by hydrogen bubbles generated on the DSS sample surface. The hydrogen bubbles were produced at the surface by cathodically polarizing the DSS sample in a mixed acid solution of 2 g/L acetylsalicylic acid + 25 ml/L H_2SO_4, with an externally applied voltage of 3 V.

Interrupted monotonic SSRTs were also performed for DSS 2205 in caustic WL environment. By comparing the cyclic fatigue and monotonic SSRT results obtained under the same maximum stress, the effect of cyclic stresses on crack initiation was illustrated.

6.2.2.1   Crack Initiation

Visual inspection of sample surfaces under SEM revealed that unlike the specimens tested in acidic NaCl environment, specimens tested in WL had a relatively rough surface under the corrosion film and showed significant corrosion on the surface. On all specimens with cracks, the cracks initiated from one phase, as shown in FIGURE 6.10. EDS results showed the composition of this phase was high in Ni and low in Cr as compared to the nominal composition of DSS 2205, indicating that the cracks preferentially nucleated in the austenite phase.
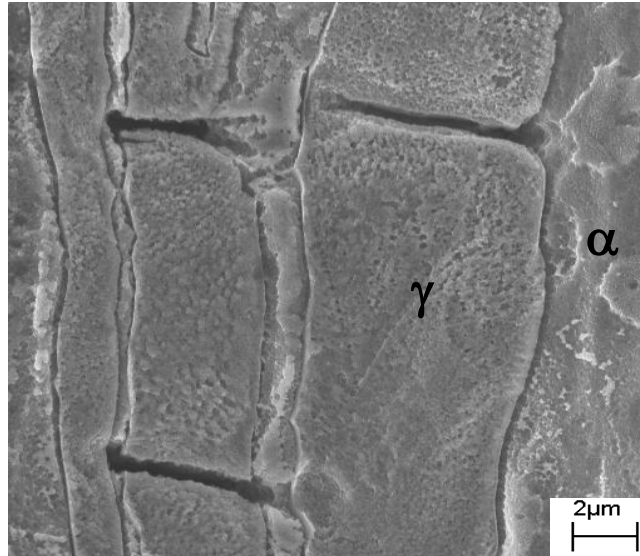
FIGURE 6.10 SEM micrograph showing crack initiation sites of DSS 2205 after CF testing in caustic WL at 170 °C: interrupted after 173 cycles maximum stress 110% YS, stress ratio 0.5, and at a strain rate of 2×10^{-6} s^{-1}.

Examination of CF samples showed that most of the cracks were confined within the austenite phase, and stopped at phase boundary. Austenite/ferrite interfaces were observed to act as microstructural barriers. Cracks propagated either along the phase boundary, as shown in FIGURE 6.11 (a), or jumped over relatively thinner layer of ferrite phase, as shown in FIGURE 6.11 (b). Thus, the crack lengths were associated with the width of the austenite phase.
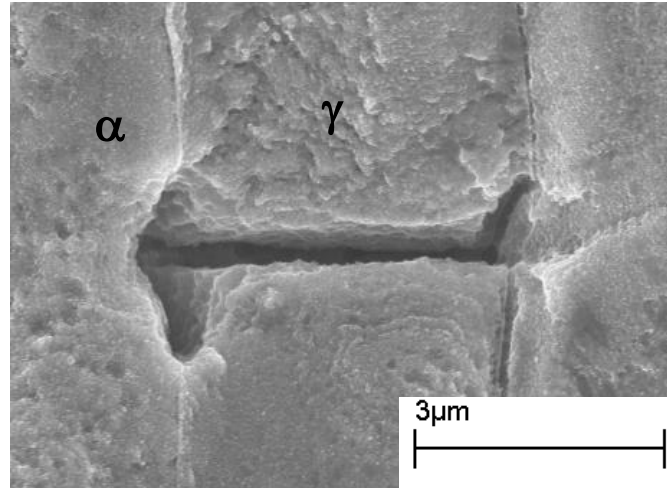
(a)
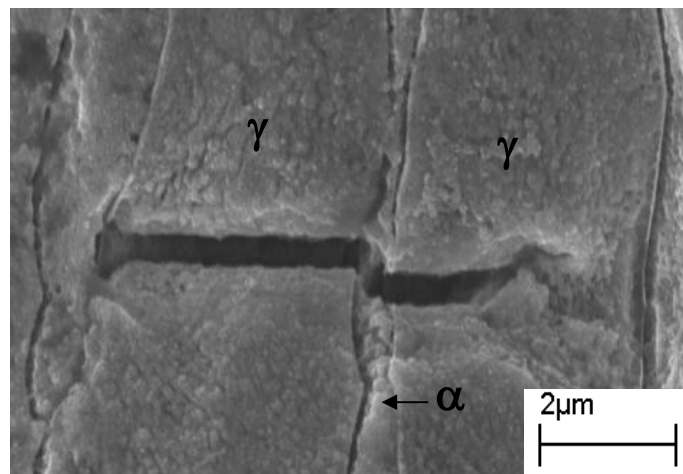
(b)

FIGURE 6.11 SEM micrographs showing crack propagation of DSS 2205 after CF testing in caustic WL at 170 °C: interrupted after 173 cycles, maximum stress 110% YS, stress ratio 0.5, and at a strain rate of 2×10^{-6} s^{-1}.

In order to illustrate the cyclic stress effect, the results of cyclic CF tests and the interrupted SSRTs were compared. SSRT samples were interrupted at 110% YS and UTS respectively. After careful examination, no cracks were observed on both specimens, even for the specimen strained to UTS, as shown in the SEM micrographs of FIGURE 6.12. On the contrary, crack initiation occurred before UTS for specimens tested in acidic NaCl environment, as discussed in Section 6.2.1.1. In fact, these results are consistent with the results of stress corrosion crack initiation threshold stress/strain for DSS 2205A discussed in CHAPTER 4. FIGURE 4.17 and FIGURE 4.18 indicated that crack initiation of DSS 2205 required a larger amount of strain in WL environment than in acidic NaCl environment. Although neither of the interrupted monotonic SSRT specimens showed crack initiation in FIGURE 6.12, serious selective dissolution occurred to the specimen strained to UTS, while the surface of the specimen strained to 110% YS was relatively smoother.
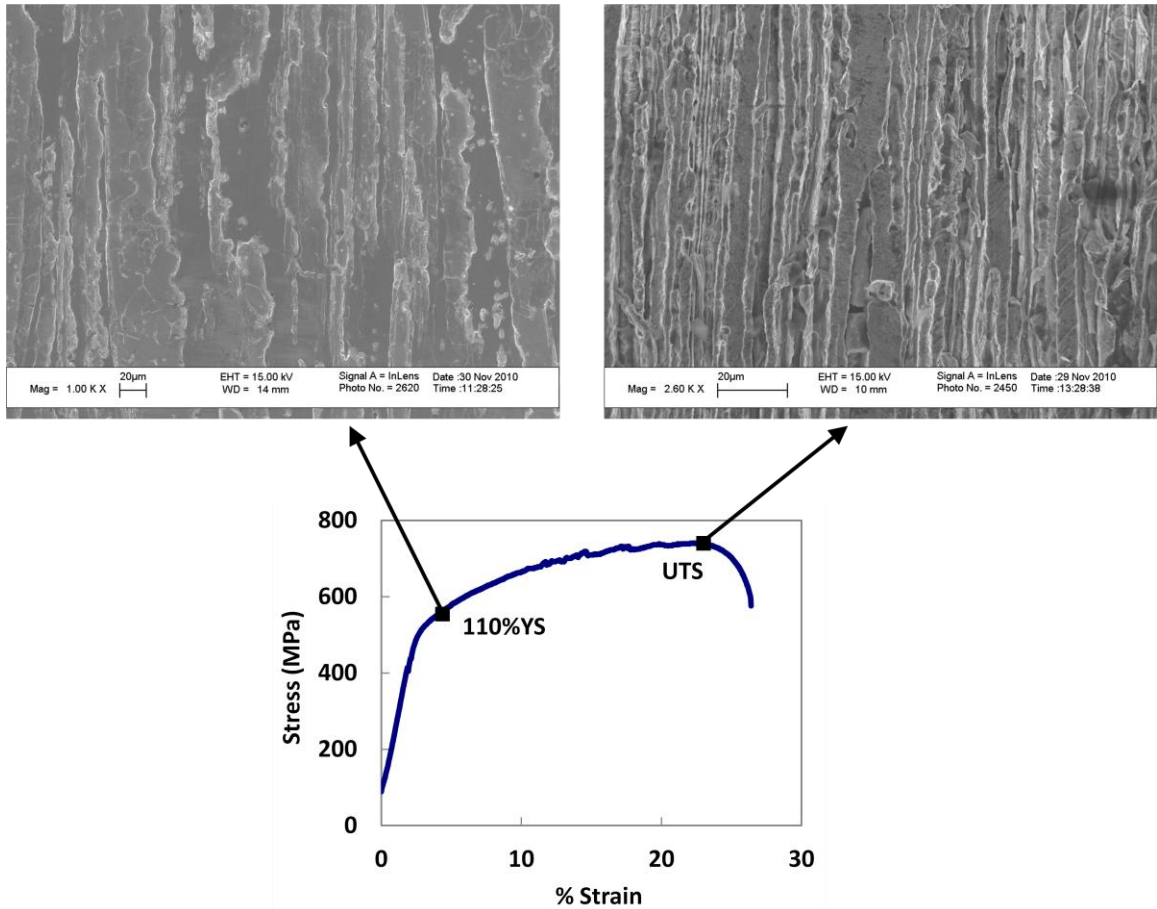
FIGURE 6.12 SEM micrographs showing specimen surfaces of DSS 2205 after interrupted monotonic SSRT tests in caustic WL solution at 170 °C and a strain rate of 2×10^{-6} s^{-1}.

However, crack initiation for DSS 2205 was observed on specimens that were cyclically loaded, even at lower stresses. As shown in FIGURE 6.10 and FIGURE 6.11, CF crack initiated in DSS 2205 under the cyclic loading with a maximum stress of 110% YS. Therefore, the threshold stress for crack initiation was significantly decreased by low frequency cyclic loading. In CHAPTER 4, the stress corrosion crack initiation of DSS 2205

in WL has been shown in austenite phase. Same crack initiation sites of DSS 2205 under SSRT and cyclic loading suggested that the crack initiation mechanism in the two cases was the same. Thus, the effect of cyclic loading was mainly to enhance the crack initiation, through the strain accumulation induced by cyclic loading.

6.2.2.2 Effect of Stress Level

Visual inspection under optical and scanning electron microscopes was done for the CF specimens of Test #1 and #4 in TABLE 6.4, tested in WL, and the characteristics of the surface cracks were compared to illustrate the effect of stress level. FIGURE 6.13 is showing the SEM micrographs of the crack morphologies on these two specimens tested in WL environment under different cyclic loadings. The cracks on the two specimens were similar in length. Most of crack lengths were determined by the width of the austenite phase at the initiation sites, as discussed in Section 6.2.2.1. Crack densities were not quantified, but the visual examination showed that they were similar in the two tests. The only difference between these cracks was the oxide layer observed on the crack walls of the specimen tested under cyclic loading with a maximum stress of 140% YS, as labeled in FIGURE 6.13. EDS was used to identify the composition of the oxide layers, and the results are listed in TABLE 6.5. From the EDS results, the oxygen and sulfide contents were pretty high in these layers, and the Cr content was much higher than the base material as well. This indicated that the film formed at the surface was predominately a mixed oxide of chromium and iron and some sulfide with a small amount of nickel.
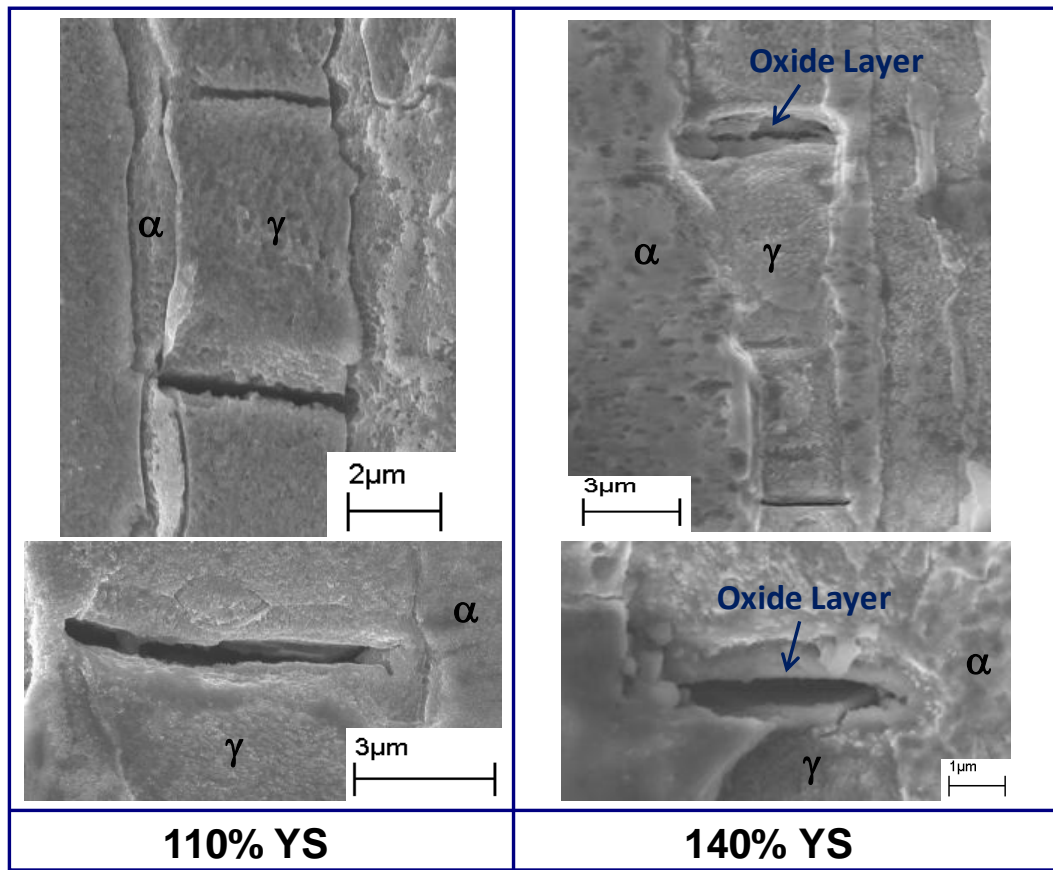
FIGURE 6.13 SEM micrographs showing crack initiation for DSS 2205 after CF tests in WL at a strain rate of 2 × 10^{-6} s^{-1} at OCP, at stress ratio 0.5 and two different maximum stress levels.

TABLE 6.5 EDS results showing the composition of the oxide layers formed on the crack walls of the specimen tested under cyclic loading with a maximum stress of 140% YS at a stress ratio of 0.5 in WL solution at 170 °C.

Element	O	S	Cr	Fe	Ni	Total
Weight. %	14.32	3.37	35.60	41.94	4.76	100.00

Under the same stress ratio 0.5, higher stress level means longer loading and unloading time in each cycle. Hence the thick oxide layer may be formed due to the prolonged exposure time under the higher cyclic stress. Moreover, the cyclic creep test results in CHAPTER 5 showed that the higher maximum stress could accumulate more strain in DSS 2205, as compared to the lower maximum stresses with the same stress ratio. This indicates that it was very likely that the cracks initiated earlier under higher stresses, than the sample tested at the lower stresses, after the tests started. Therefore, when the maximum stress was 140% YS, the opened cracks were exposed to the corrosive environments for a longer time than cracks generated under lower cyclic stresses. The composition of the oxide layers listed in TABLE 6.5 was proved to be the same with the composition of the surface corrosion film, detected by A. Bhattacharya [57]. Using the X-ray photoelectron spectroscopy, Bhattacharya found the corrosion film formed on the surface of DSS 2205 specimen exposed to WL at 170 °C for 15 days was enriched with oxides or sulfides of iron, chromium and nickel, which was consistent with the results we obtained in TABLE 6.5.

6.2.2.3 Effect of Stress Ratio

Effect of stress ratio on CF crack initiation of DSS 2205 in caustic WL environments was done by comparing the results DSS 2205 tested under cyclic loadings with the same maximum stress of 140% YS but different stress ratios 0.1, 0.5 and 0.8. These CF tests were stopped after 123 cycles, and the sample surfaces were examined under SEM. The micrographs are shown in FIGURE 6.14. Based on the SEM examination, CF crack initiations were only observed on the specimen tested under the cyclic stress with a stress ratio of 0.5. At higher and lower stress ratios of 0.8 and 0.1, no crack initiation was observed, as shown in FIGURE 6.14. However, the surface of the specimen tested under a stress ratio of 0.1 was more etched than the one tested under a stress ratio of 0.8. This was predominately due to the longer exposure time for the specimen tested under a smaller stress ratio.

In acidified NaCl environment, CF crack initiation was favored with higher stress ratio, as shown in FIGURE 6.8. However, in caustic WL, medium stress ratio level, R=0.5, promoted crack initiation. Monotonic test results in FIGURE 6.6, show that the cracks initiated in the first cycle when the specimen was loaded to 140% YS in acidic NaCl environment. However, in WL environment the crack initiation did not occur when the DSS 2205 sample was loaded to 140% YS, as indicated by the results in FIGURE 6.12. Therefore, the subsequent cycles in acidic NaCl test accumulated more strain and helped propagate the existing cracks. This is true for both higher and lower stress ratios. The only difference under the two conditions is that at higher stress ratio of 0.8, the unloading time or the time for surface film to repair itself was shorter; hence the crack

propagation rate was higher. However, crack initiation in caustic WL is due to strain accumulation causing film breakdown and film repair during cyclic loading. Therefore the results in FIGURE 6.14 indicate that the strain accumulation induced by cyclic stress of R = 0.8 was not sufficient to initiate cracks, because when the maximum stress was fixed, larger stress range or smaller stress ratio resulted in more pronounced strain accumulation induced by cyclic loading [4]. On the other hand, the film repair during the unloading of cyclic stress with R = 0.1 hindered crack initiation because of the prolonged unloading time. However at stress ratio 0.5, strain accumulation was larger than that at the stress ratio of 0.8, and the film repair time was shorter than that for the stress ratio of 0.1.
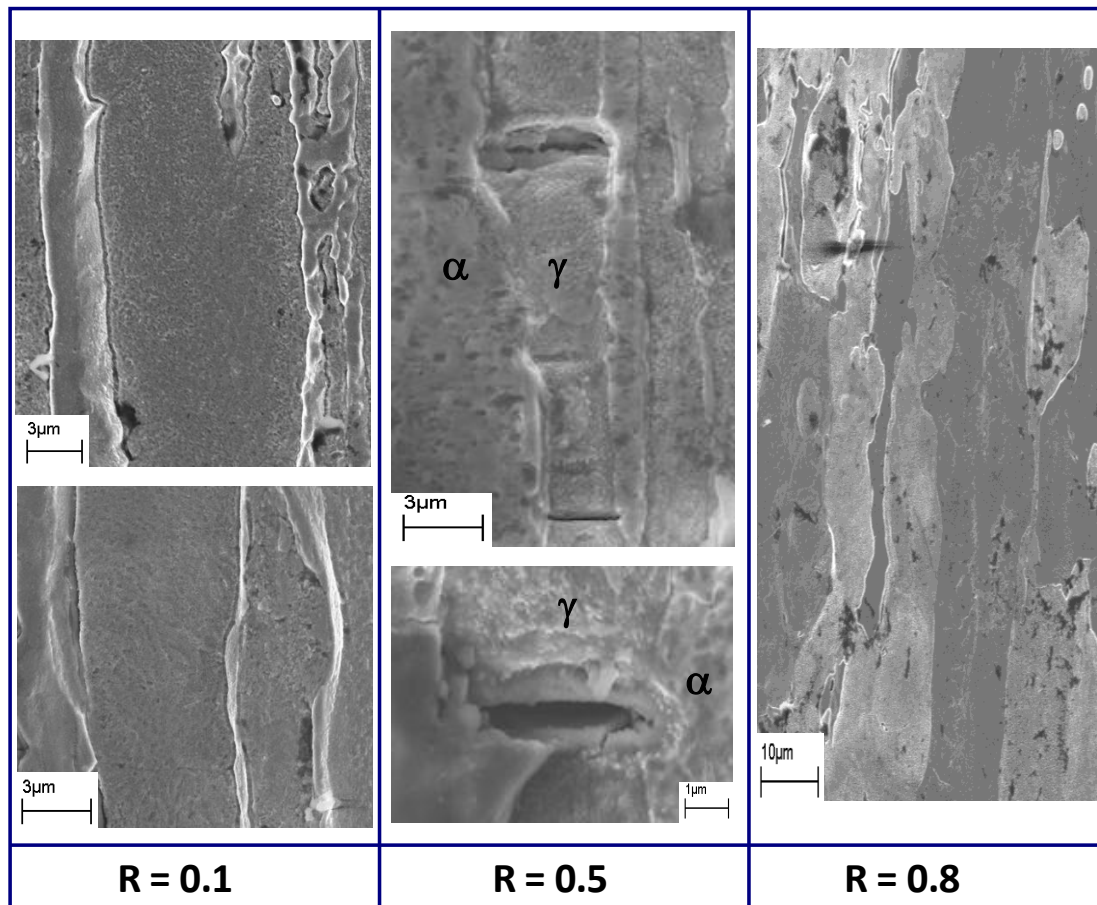
FIGURE 6.14 Crack initiation of DSS 2205 after 123 cycles of CF tests under cyclic loading with a maximum stress of 140% YS but different stress ratios, in WL at 170 °C and a strain rate of 2×10^{-6} s^{-1}.

6.2.2.4 Summary

The CF crack initiation process of DSS 2205 in WL solution at a strain rate of 2×10^{-6} s^{-1} and 170 °C could be summarized as follows. Within the first cycle of the cyclic loading, the strain caused by the monotonic stress was not enough to initiate cracks. With more number of cycles, more plastic deformation was induced by cyclic loading, which

promoted crack initiation. On the other hand, during the unloading process of the cyclic loading, the protective surface film is repaired. However, the film breakdown due to strain accumulation process and the film repair compete with each other. Therefore, at relatively higher or lower stress ratios, when the strain accumulation was insufficient or the film was always repaired before rupture, crack initiation did not occur. Only at stress ratios when the strain accumulation surpassed film repair, crack initiation was observed. Besides, at higher stress level, thick oxide layers formed on the crack walls.

6.2.3　Strain Distribution and Slip Dissolution Mechanism

As was discussed in CHAPTER 4, the preferential attack of the ferrite phase in acidic NaCl environment was due to the potential difference between the two phases of DSS 2205 during SCC. In caustic WL environment, the stress corrosion crack initiation in austenite phase have been explained using the slip-dissolution model by Bhattacharya [57]. The argument was based on the tensile residual stress in austenite phase, hence the austenite phase yields first and the plastic flow lines appear in austenite phase. However, observation of the surface plastic flow lines and the EDS results showed that at higher plastic deformations, slip bands appeared in ferrite phase. As shown in FIGURE 6.15, the plastic flow lines clearly emerged from one phase of the material. EDS results in TABLE 6.6 revealed it was ferrite phase (α) where plastic flow lines were observed, whereas, the smoother region without visible plastic flow lines was austenite phase (γ), as labeled in FIGURE 6.15. Hence, residual stresses could not be used to demonstrate the preferential attack of austenite phase in WL environment, under either monotonic or cyclic loading.

Previous study in our lab showed that the repassivation kinetics of austenite phase was slower, due to the lower Cr composition of austenite phase. Furthermore, in the presence of sulfide, the integrity and stability of the film that formed on austenite phase were compromised [168].
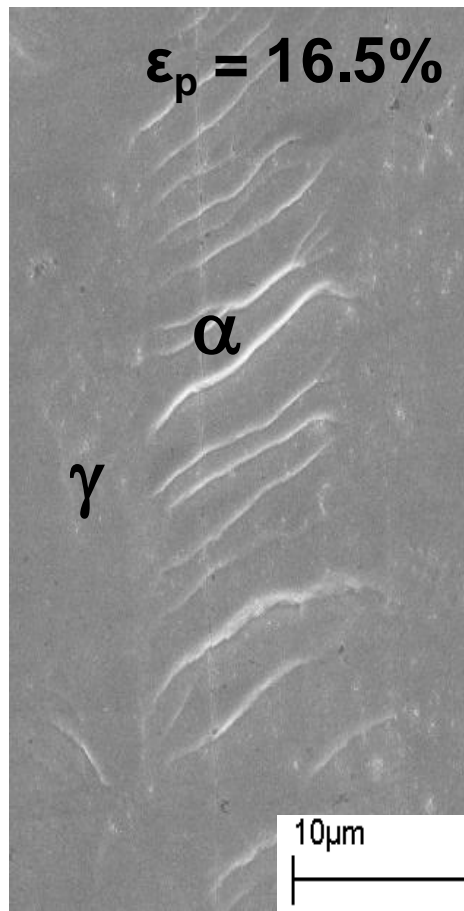
FIGURE 6.15 Surface plastic flow lines of DSS 2205 after being strained in NaCl environment to 16.5% plastic strain.

TABLE 6.6 Chemical composition of different regions of the specimen surface in FIGURE 5.15.

Element	Fe	Cr	Ni	Mn	Mo	Total
γ (Weight %)	65.34	23.21	6.03	1.45	3.96	100.00
α (Weight %)	66.31	24.57	3.66	0.64	4.82	100.00

These results are obviously in contradiction with the residual stress state of the two phases. For that reason, microhardness measurements were performed on the two phases to explore the explanation for it. The microhardness of the two phases was measured at different strain levels. FIGURE 6.16 and FIGURE 6.17 are showing the averaged microhardness values as well as the standard errors. Moreover, in order to correlate the microhardness results to the SCC and CF test results, the specimens for the microhardness tests were strained under the same SCC and CF conditions in acidic NaCl and caustic WL environments.

The microhardness test results had similar trend for the two phases, as shown in FIGURE 6.16 and FIGURE 6.17. When the plastic strain equals to zero, austenite phase was softer than ferrite phase, indicated by its lower hardness value as compared to ferrite phase. With the increase of plastic strain, the hardness of both phases increased because of strain hardening. However, the strain hardening in austenite phase was much more pronounced than for the ferrite phase. Hence, the hardness of austenite phase

exceeded the hardness of ferrite phase when the plastic strain was increased to about

3%. With further increase in strain, the hardness value of austenite phase remained

higher than ferrite phase. These results clearly demonstrate that although the austenite

phase was softer at the beginning and has higher tensile stress, it strain hardened

rapidly and became the harder phase in DSS 2205. Therefore, at higher strain levels,

plastic deformation mainly occurred in ferrite phase. This is consistent with the

appearance of slip bands in ferrite phase, as shown in FIGURE 6.15 and TABLE 6.6. In an

in-situ TEM observation of a plastically strained DSS, Zielinski *et al.* found that the slip

transferred from the austenite phase to the ferrite phase through a boundary with a

random orientation relationships [169].
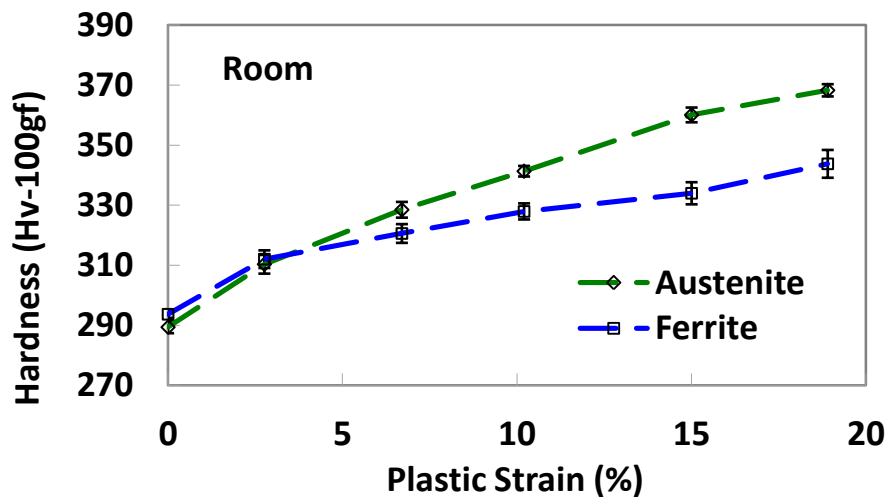
FIGURE 6.16 Microhardness of DSS 2205 after being strained to different plastic strain

levels in 26 wt.% NaCl solution of pH = 2 with an applied potential of -375 mV (SCE) a

strain rate of 2 × 10^{-6} s^{-1} and room temperature.
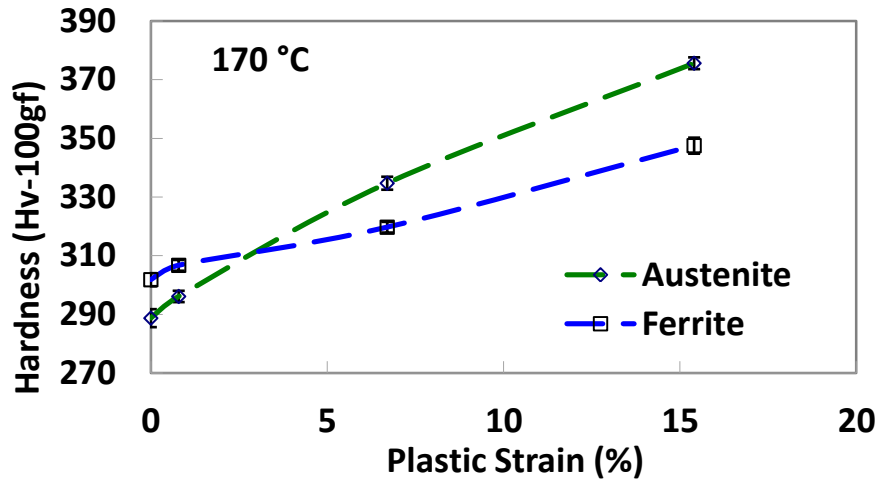
FIGURE 6.17 Microhardness of DSS 2205 after being strained to different plastic strain levels in WL at a strain rate of 1×10^{-6} s^{-1} and 170 °C.

Based on the microhardness results, plastic deformation occurs in the austenite phase first, because of the tensile residual stress in austenite phase and its lower hardness when there is no applied strain. With an increase in the applied or accumulated strain level, plastic deformation predominately occurs in the ferrite phase, due to the higher strain hardening in austenite phase. Under monotonic constant extension rate tests, crack initiation as well as propagation in hot sulfide-containing caustic solutions was observed in austenite phase and evidence of slip-dissolution mechanism was reported (Chasse). However, under cyclic loading conditions, due to strain hardening of the austenite phase, preferential slip bands were found in the ferrite phase rather than the austenite phase. Therefore, slip-dissolution model of crack propagation through austenite phase does not apply under low-frequency cyclic loading.

6.2.4   Effect of Cold Working on CF of DSS 2205

Limited data exists in published literature on the influence of cold-working on CF behavior of metallic materials, especially for DSSs. The harmful effect of cold-working on SCC of DSS 2205 in both acidic chloride and caustic WL environments has been illustrated in CHAPTER 4. In this section, the effect of cold-working on CF behavior of DSS 2205 in these two environments will also be discussed.

6.2.4.1 Acidic Chloride Environment

If the strain hardening changes relative mechanical behavior of the two phases in DSS 2205, it is expected that the cold-worked material will behave differently, both under monotonic constant extension rate tests as well as low frequency CF tests compared to the annealed DSS material. The stress vs. strain behavior under monotonic load was shown in FIGURE 2.1 for both annealed and cold-worked DSS. To test this under cyclic condition, low frequency CF tests were performed on the cold-worked DSS 2205 in acidic NaCl environment under the same conditions described in Section 6.2.1. In order to investigate the stress level effect, various maximum stresses were applied, as listed in TABLE 6.7. A stress ratio of 0.5 was used in all tests, and tests were stopped after a certain number of cycles. After each test, the specimen was examined under optical microscope and SEM, and the occurrence of crack initiation for each specimen was also recorded in TABLE 6.7. CF tests at stress levels below 630 MPa and lower number of cycles did not show any signs of cracks at the end of tests. Crack initiation was observed for specimens tested under a maximum stress of 630 MPa with 250 cycles. Whereas for a sample tested at 870 MPa, cracks were observed after 14 cycles. Number of crack

initiations observed on cold-worked DSS 2205 was very small in both cases. However, the fact of no crack initiation found on most of the test specimens indicates that the cold-working significantly retarded the CF crack initiation of DSS 2205 in acidic NaCl environment. In addition, cracks tended to initiate from pits formed on the sample surface, as is shown in the pictures of FIGURE 6.18. It is well known that corrosion pits are stress concentration sites, thus the CF crack initiation of cold-worked DSS 2205 in acidic NaCl environment was mainly influenced by the local stress state, rather than the applied normal stress.

TABLE 6.7 CF test summary for cold-worked DSS 2205 in acidic chloride environment.

Maximum Stress (MPa)	Cycles	Crack Initiation
280	11	No
400	31	No
630	250	Yes
700	40	No
750	12	No
768	69	No
780	15	No
830	11	No
850	53	No
870	14	Yes
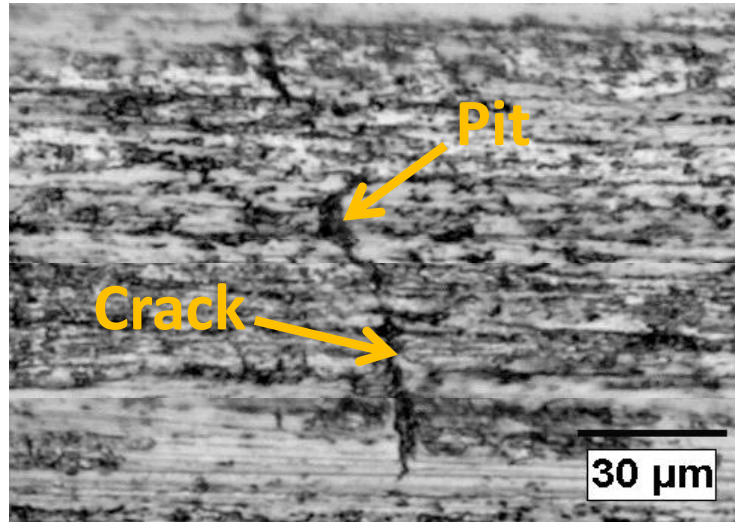
(a)
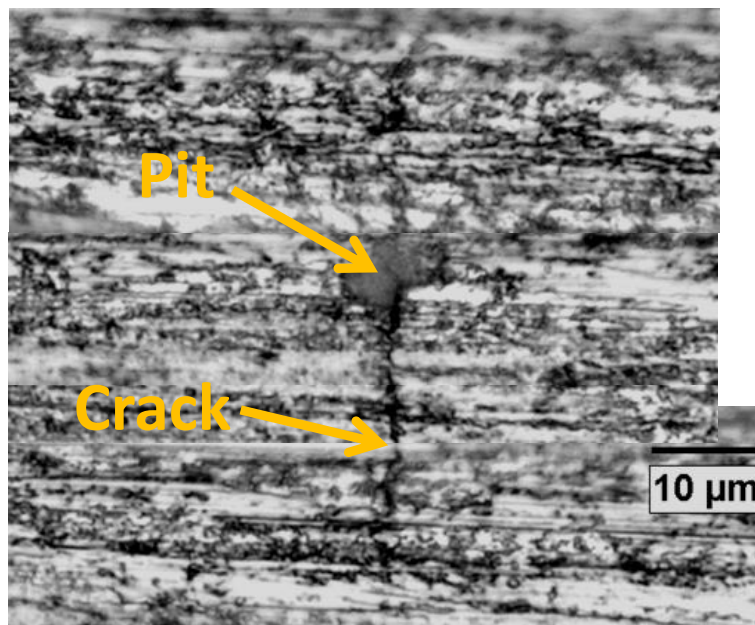
(b)

FIGURE 6.18 CF crack initiation of cold-worked DSS 2205 in 26 wt.% NaCl solution of pH = 2, with an applied potential of -375 mV (SCE) at room temperature, after 250 cycles under a maximum stress of 630 MPa.

6.2.4.2 Caustic WL Environment

Low frequency CF tests were also performed on the cold-worked DSS 2205 in caustic WL environment at 170°C, under the same conditions described in Section 6.2.2. In

TABLE 6.8, a stress ratio of 0.5 was used in all tests. After each test, the specimen were

cleaned and the film formed at the surface was cathodically removed to examine these

samples   under SEM. Crack initiation was observed for specimens tested under a

maximum stress of 560 MPa and 850 MPa. Similar to the CF tests of cold-worked DSS

2205 in acidic NaCl environment, no trend could be found because of the small

population of crack initiations observed on cold-worked DSS 2205 tested in WL

environment. Besides, crack initiations were found on specimens tested under lowest

maximum stress level, 560 MPa. However, SEM micrographs in FIGURE 6.18 revealed

that the CF cracks usually initiated from precipitates, which indicated the crack

initiations were mainly controlled by the local stress concentration or plasticity. This

explained the appearance of CF crack initiation under lower stress level. Nevertheless,

the effect of cold-working on CF crack initiation of DSS 2205 in WL was also found to

impede the crack initiation, similar to that in acidic NaCl environment.

TABLE 6.8 CF test summary for cold-worked DSS 2205 in caustic WL environment.

Maximum Stress (MPa)	Cycles	Crack Initiation
560	11	Yes
700	40	No
792	12	No
800	69	No
850	12	Yes
890	11	No
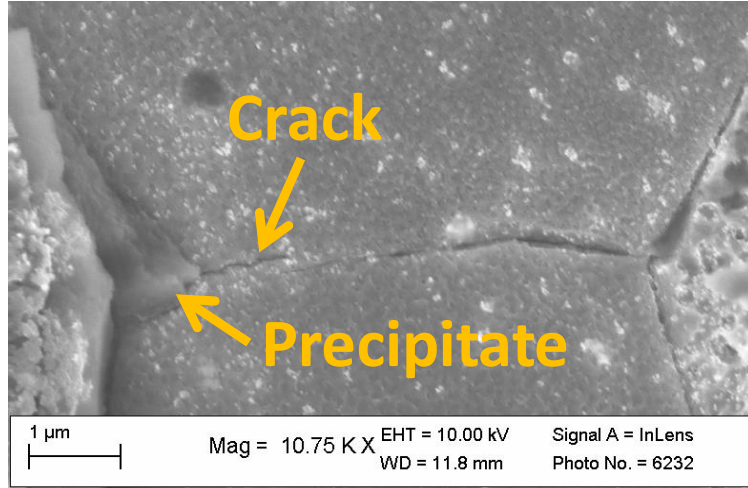
(a)
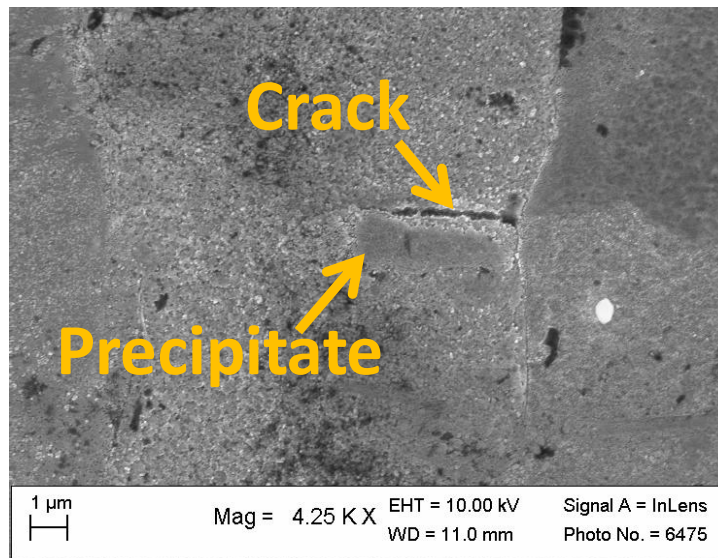
(b)

FIGURE 6.19 CF crack initiation of cold-worked DSS 2205 in WL solution at 170 °C: (a) after 11 cycles under a maximum stress of 560 MPa (b) after 12 cycles under a maximum stress of 850 MPa.

6.2.4.3 Summary

In both acidic NaCl and caustic WL environments, CF crack initiation was retarded by cold-working of DSS 2205. Local stress concentration or local plasticity was the key parameter for crack initiation. Therefore, the CF crack initiation of cold-worked DSS 2205 was usually associated with microstructural features such as pits or precipitates. In addition, the yield strength of the material was significantly increased by cold-working but the ductility decreased significantly. There was very little strain hardening after the yield point for the cold-worked DSS 2205 (FIGURE 3.1). However, it was shown by the results in CHAPTER 4 that the initiation of stress corrosion cracks required a large amount of plastic deformation for cold-worked DSS 2205.

As discussed in CHAPTER 4, the SCC was enhanced by cold-working of DSS 2205 in both acidic NaCl and caustic WL environments. This detrimental effect of cold work has been reported for pure iron and austenitic stainless steels, and is attributed to the residual stresses induced by cold-working or the lower electrochemical potential of the imperfections induced by cold-working [139, 143, 144]. However, under cyclic loading, the effect of cold-working on crack initiation of DSS 2205 was reversed. Since cyclic stress induced creep has a large influence on CF crack initiation of DSS 2205 in the two environments, the cold-working effect could be explained by its effect on creep deformation. In CHAPTER 2, it was pointed out that the phenomenon of cyclic creep acceleration could be attributed to the increase of mobile dislocation density caused by cyclic loading. In this case, the dislocation density was saturated by prior cold-working, and the mobility of dislocation was decreased by prior cold-working. Both of the effects

that cold-working had on dislocations reduced the creep strain accumulation and resulting into the change in the creep strain rate due to cyclic loading. Therefore, the stress corrosion crack initiation of DSS 2205 under cyclic loading was significantly retarded by cold-working, as compared to annealed state.

6.3   Conclusions

Work in this chapter was to understand the CF behavior of DSS 2205 under very low frequency cyclic loading in acidic NaCl and caustic WL environments. The following conclusions could be drawn from these results.

In acidic NaCl environment,

- ❖ When the intermetallic precipitates (which are especially rich in O, Mn, Al and Cr) exist in DSS 2205, CF cracks always initiated from these precipitates in acidic NaCl environment.

- ❖ Corrosive environment was found to preferentially attack the interface of precipitates and base material, because of the depletion of Mn in base material at the interface.

- ❖ Low frequency cyclic stresses significantly enhanced crack initiation of DSS 2205 in acidic NaCl environment.

- ❖ CF crack initiation or intermetallic precipitate damage of DSS 2205 in the acidic NaCl environment was determined by the maximum stress of the cyclic loading. The higher the maximum stress the larger the crack opening.

❖ The propagation of the CF crack was significantly influenced by stress ratio, or the unloading time of each cycle. Specifically, the larger stress ratio, or shorter unloading time, promoted CF crack propagation.

In caustic WL environment,

❖ CF cracks initiated exclusively from austenite phase.

❖ The crack lengths were associated with the width of the austenite phase. Most of the cracks were confined within the austenite phase, and stopped at phase boundary. Some of the cracks jumped over relatively thinner layer of ferrite phase.

❖ Threshold stress for crack initiation was significantly decreased by low frequency cyclic loading.

❖ Same crack initiation sites of DSS 2205 under monotonic and cyclic loading suggested that the crack initiation mechanism in the two cases was the same. Thus, the effect of low frequency cyclic loading was mainly to enhance the crack initiation, through the strain accumulation induced by cyclic loading.

❖ Crack initiation occurred at intermediate stress ratios when the strain accumulation surpassed film repair.

❖ Stress level did not have much influence on crack initiation. At higher stress level, thick oxide layers were formed on the crack walls.

❖ Although the austenite phase was softer at zero plastic strain and has higher tensile residual stress, it strain hardened rapidly and became the harder phase in

DSS 2205. At higher strain levels, plastic deformation mainly occurred in ferrite phase. Hence, slip-dissolution model could not be used to explain the mechanism of SCC and CF crack initiation of DSS 2005 in WL environment.

Cold-worked DSS 2205

❖ The stress corrosion crack initiation of DSS 2205 under cyclic loading was significantly retarded by cold-working, as compared to annealed DSS 2205 in both environments investigated. Cyclic creep deformation of cold-worked DSS 2205 was decreased, because the dislocation density was saturated by prior cold-working, and the mobility of dislocation was decreased by prior cold-working.

❖ CF crack initiation of cold-worked DSS 2205 in both environments was controlled by the local plasticity, rather than the nominal stress or strain. The local plasticity was usually associated with microstructural features such as pits or precipitates.

CHAPTER 7 CONCLUSIONS AND PROPOSED MECHANISM FOR EFFECT OF LOW-FREQUENCY CYCLIC STRESSES ON STRESS CORROSION CRACKING INITIATION

7.1   Introduction

The stress corrosion cracking (SCC) of metallic materials in corrosive environments are controlled by various factors: material related factors such as alloy composition, microstructure, and secondary phases; stress related factors such as magnitude of the tensile stress or stress intensity factor, residual stress, and stress state; environmental factors like temperature, pressure, pH, and electrochemical potential. Furthermore, in the case of duplex stainless steels (DSSs), the different chemical compositions and mechanical properties of the two phases add more complexity to this problem.

In this study, the SCC and low frequency corrosion fatigue (CF) behavior of DSS 2205 was studied in two distinct corrosive environments, i.e., acidic NaCl solution and sulfide containing caustic solution, white liquor (WL) solution. Primary objective of this research was to understand the interaction of different environments with the DSS 2205 alloy under ultra-low frequency ($\sim$$10^{-5}$ Hz) cyclic stresses to initiate stress corrosion cracks. In fact, this is the first study on ultra-low frequency CF in DSSs. In this chapter, the major results and conclusions of this study are summarized and discussed.

Ultra-low frequency cyclic stress effect on SCC behavior of DSS 2205 was investigated based on the hypothesis that low frequency cyclic loading does not change the basic electrochemical reactions involved in the preferential corrosion attack of the two phases in the two corrosive environments; low frequency cyclic stresses only facilitate the stress corrosion crack initiation by accumulating an extra amount of strain and increasing the strain rate to break the protective film continuously to propagate that crack. Competing process for the film-induced stress corrosion crack initiation or growth processes is the repassivation on surface or crack, which may repair the protective film, especially during the unloading period.

The discussion of results in this chapter is separated into three main parts: first, the effect of ultra-low frequency cyclic loading on strain accumulation behavior of DSS 2205 without corrosive environments; second, the combined effect of ultra-low frequency cyclic loading and acidic NaCl environment on stress corrosion crack initiation behavior of DSS 2205; third, the combined effect of ultra-low frequency cyclic loading and caustic WL environment on stress corrosion crack initiation behavior of DSS 2205.

7.2   Effect of Ultra-low Frequency Cyclic Stress

The effect of ultra-low frequency cyclic stresses on strain accumulation behavior of DSS 2205 was studied. The reason is that the SCC results from this study showed that the plastic deformation was essential for stress corrosion crack initiation of DSS 2205 in both acidic NaCl and caustic white liquor (WL) environments (Section 4.2.5). Below yield

strength, DSS 2205 was immune to stress corrosion crack initiation in the two corrosive environments tested. It was also known from previous studies [57, 168] that the crack initiation under constant strain conditions, even above the yield stresses may not cause SCC of DSS in these environments. In existing publications, there is no study has been done on the ultra-low frequency cyclic loading effect on strain accumulation behavior of any DSSs at room temperature.

In the absence of corrosive environments, the effect of ultra-low frequency cyclic loading on strain accumulation in the two phases of DSS could be demonstrated by the schematic shown in FIGURE 7.1. The major effect of the ultra-low frequency cyclic stress is to increase the cumulative strain and strain rate of DSS 2205, even at room temperature. Both pure static and cyclic creep and static-cyclic creep test results clearly demonstrate this in Section 5.2. Since the passive film, which is mainly composed of chromium oxide formed on the sample surface, is much more brittle than the base material, strain accumulation induced by the low frequency cyclic loading causes this film to break locally at the sample surface, as shown in the second drawing of FIGURE 7.1.

The cross slip model explains the cyclic creep acceleration of stainless steels at room temperature. Specifically, mobile screw dislocation segments may leave their slip planes by cross-slip aided by fluctuations in the internal stress encountered during reverse loading movement. Due to the dual-phase microstructure, the cyclic creep behavior of DSS 2205 is controlled by the strain accumulation behavior of the two phases. Under

ultra-low frequency cyclic loading, ferrite phase (BCC) enhances strain accumulation through extensive dislocation cross-slips, indicated by the larger number of slip bands generated in ferrite phase (α) than in austenite phase (γ), as shown in FIGURE 6.15 and also depicted in the schematic in FIGURE 7.1. Whereas the cyclic stress effect on creep strain accumulation for the austenite phase (FCC) tends to weaken due to cyclic strain hardening of this phase. This can be attributed to the fact that materials with BCC crystal structures are more susceptible to cyclic induced strain accumulation than materials with FCC crystal structure, because of the extensive cross slip happening in BCC material, as proved by the results of creep strain ratios for the two materials obtained in Section 5.2.4. Furthermore, microhardness measurement of the two phases of DSS 2205 (Section 6.2.3), with different amounts of cold work, also illustrated that although the austenite phase is softer at zero plastic strain and has higher tensile residual stress, it strain hardens rapidly as the strain increases and becomes the harder phase in DSS 2205. Hence at higher strain levels, plastic deformation mainly occurred in the ferrite phase.
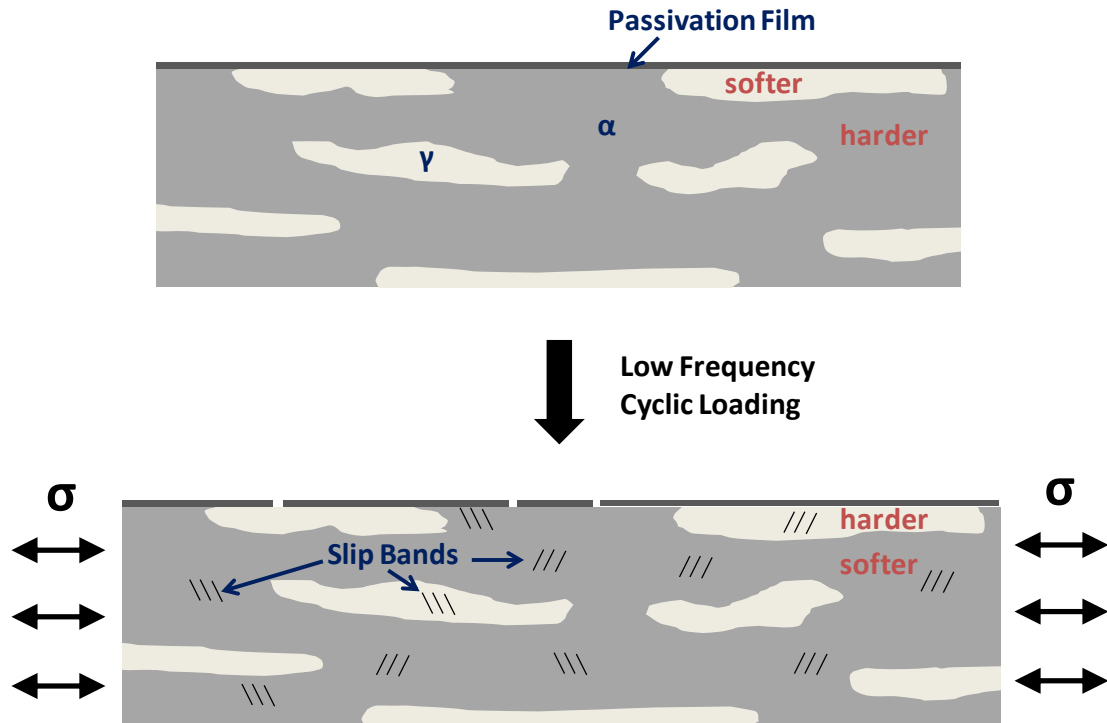
FIGURE 7.1 Schematic Illustration of the effect of low frequency cyclic loading on DSS 2205 deformation in air.

The effect of low frequency cyclic loading on strain accumulation of stainless steels (SS) is enhanced by pre-straining, because the effect of cyclic loading on SS 304L and SS 430 changed from retarding to accelerating the strain accumulation with pre-straining (Section 5.2.1 and Section 5.2.3). Moreover, this effect of cyclic loading on the creep strain accumulation is greatest during the initial cycles of cyclic tests, and then it decreases with time. Cumulative creep strain increases monotonically with an increase in the of stress level, with or without pre-straining.

7.3　Combined Effect of Ultra-low Frequency Cyclic Stress and Acidic Chloride Environment

In presence of corrosive environment, i.e., acidic NaCl solution, the ultra-low frequency cyclic stress facilitates the stress corrosion crack initiation through its effect on the strain accumulation as well as strain rate change. This was verified by the comparison of crack initiation under monotonic and cyclic loading in Section 6.2.1.1. The mechanism of stress corrosion crack initiation for DSS 2205 under ultra-low frequency cyclic loading in acidic NaCl environment could be illustrated by the schematic in FIGURE 7.2. Since the material used in this part of the study was the bar material (denoted as 2205B in Section 3.2) which contains Mn-, O-, Al-, Cr- and Ti-containing intermetallic precipitates, the crack initiation process is significantly influenced by the precipitates, as shown by micrographs in FIGURE 6.1.

One important fact revealed by the slow strain rate test (SSRT) results, discussed in Section 4.2.4, is that the SCC of DSS 2205 in acidified NaCl environment initiated from the ferrite phase, which is consistent with the results in literature [33, 34, 39, 42, 43, 134, 146, 147]. However, under cyclic loading conditions, as shown in FIGURE 7.2, the crack initiation predominately occurred at intermetallic precipitates in the same environment. This is because the stress corrosion crack initiation observed on the cross section of fractured DSS 2205 specimens (SSRT results in FIGURE 4.13 and FIGURE 4.16) is caused by the corrosion attack under significant plastic deformation, especially after the localized strain accumulation and necking had set in the sample. On the other hand, the CF crack initiation at precipitates on the un-fractured specimens does not require

similar applied plastic deformation. Hence, there are still crack initiations at precipitates under monotonic SCC condition, but with an increase in the applied strain in SSRT, cracks also initiate in ferrite phases, especially in the necked area.

With the accumulated strain induced by the ultra-low frequency cyclic loading, cracking of precipitates and debonding between the precipitates and base material occurs. In addition, the corrosive environment also preferentially attacks the interface of precipitates and the matrix. For small precipitates, the whole interface is attacked, and they are completely dissolved out and leave small pits on the sample surface, as shown in FIGURE 6.5 and depicted in the second and third schematic in FIGURE 7.2. Then, during the loading process of each cycle, stress concentration at the crack initiation sites, or precipitates, assist propagation of these cracks. Energy-dispersive x-ray spectroscopy (EDS) results showed that the intermetallic precipitates are high in O, Mn, Cr and Al, whereas the interface material is depleted with Mn, making the interface more susceptible to corrosion attack. However, during unloading of each cycle, the crack propagation stops, and the surface passive film is repaired during that period of time, because there are no tensile stresses to break the film. In this study, crack initiation is defined as the cracks propagating into the matrix of the material. Mere cracking of the precipitates is not considered as crack initiation under CF tests.
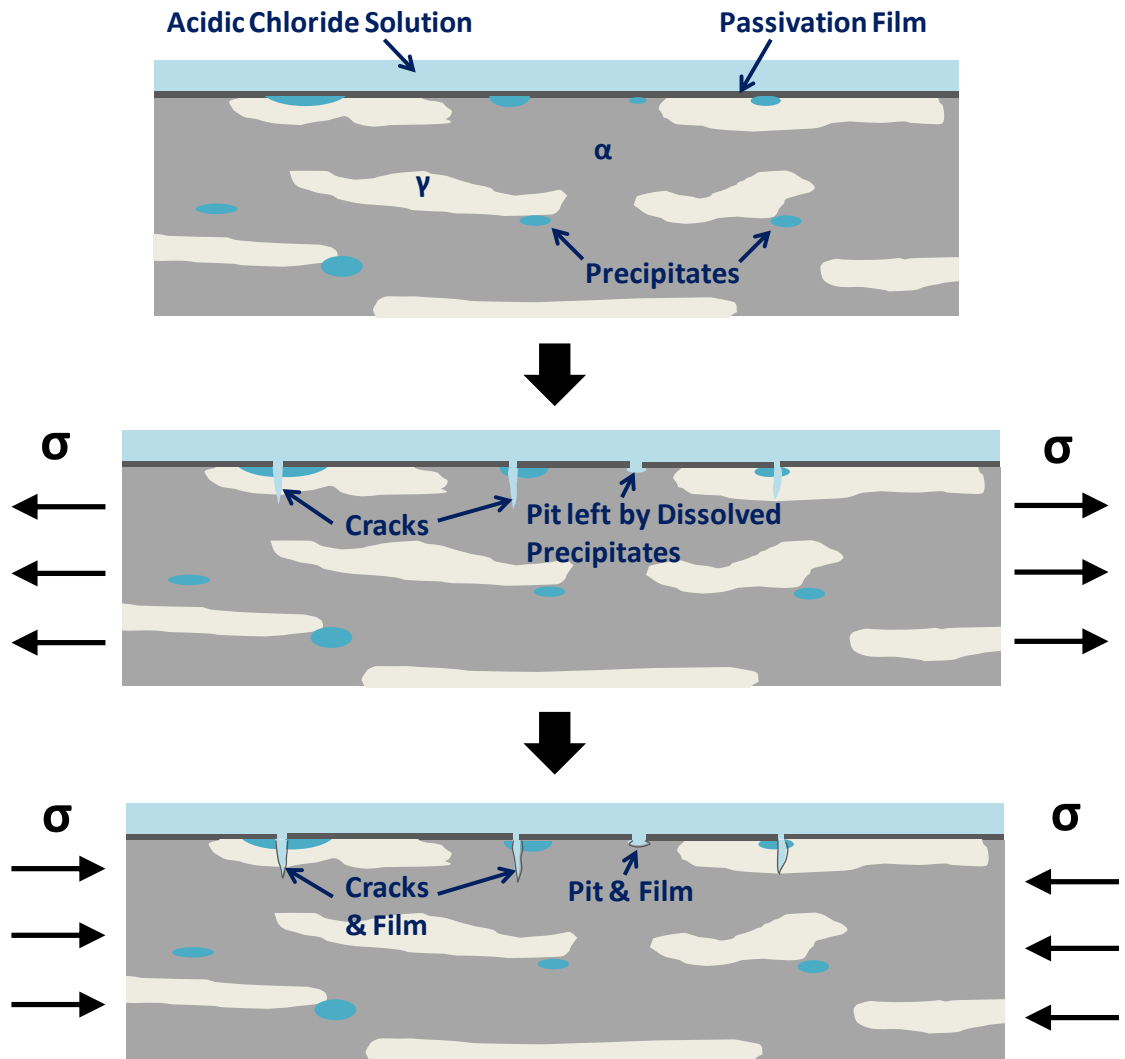
FIGURE 7.2 Schematic drawing illustrating the CF crack initiation of DSS 2205 in acidic NaCl environment.

Test results in Section 6.2.2.2 and Section 6.2.2.3 showed that the process described in FIGURE 7.2 was influenced by the maximum stress and stress ratio of the ultra-low frequency cyclic loading. CF crack initiation is favored by the higher maximum stress as well as higher stress ratio. Higher maximum stress generates larger crack opening,

which promotes the contact of the newly exposed material to the corrosive environment. Under the same maximum stress, the effect of stress ratio is associated with the unloading time within each cycle of the cyclic loading. Higher stress ratio, corresponding to shorter unloading time, results in less time for the surface film to repair, which also promotes the crack initiation and propagation in this environment. In another word, these results suggest that under the low frequencies investigated in this study, the crack initiation and propagation behavior of DSS 2205 in acidic NaCl environment is greatly controlled by the passivation and repassivation of the surface film. This frequency effect is contrary to the general effect of stress ratio at relatively higher frequency range (> 10^{-2} Hz), i.e., lower frequencies increases the corrosion attack at crack tip, resulting in higher CF crack propagation rates in DSSs [7, 12]. Hence indicated by the results of this study, the frequency effect on CF behavior of metallic materials is totally changed when the frequency decreases to as low as 10^{-5} Hz. The main reason is that the effect of repassivation became remarkable at the ultra low frequencies because of the prolonged unloading time.

In this environment, the results of SSRT and potentiodynamic polarization tests showed that the SCC behavior of DSS 2205 is influenced by the pH value of the solution and the electrochemical potential, as discussed in CHAPTER 4. Higher acidity of the NaCl solution generates more severe SCC of DSS 2205 in this environment. DSS 2205 is susceptible to SCC in 26 wt.% NaCl of pH = 2 under the electrochemical potential range from -375 mV (SCE) to -520 mV (SCE). Right above and below this potential range, DSS 2205 was

immune to SCC in this environment. These effects are similar to the results obtained in other publications [33, 34].

7.4 Combined Effect of Ultra-low Frequency Cyclic Stress and Caustic WL Environment

Similar to the results in acidic NaCl solution, the ultra-low frequency cyclic stress also facilitates stress corrosion crack initiation through its effect on strain accumulation and strain rate change in caustic WL environment. However, the details of the mechanism of environmental effect are different in these two environments tested. In Section 6.2.2.1, the crack initiations of DSS 2205 under monotonic and cyclic loading were compared. The results showed that under low frequency cyclic loading, crack initiation occurred at a much lower maximum stress level, as compared to monotonic loading. The crack initiation and propagation process of DSS 2205 under ultra-low frequency cyclic loading in WL environment is schematically shown in FIGURE 7.3.

The most distinctive feature of crack initiation under this condition is that the cracks exclusively initiate from the austenite phase, which is the same as the stress corrosion crack initiation under monotonic loading, as previously found by Bhattachary and Chasse [44, 48, 57, 143, 168]. This proved the hypothesis of ultra-low frequency cyclic loading does not change the preferential attack of the two phases in the two corrosive environments, and low frequency cyclic stresses only facilitate stress corrosion crack initiations by accumulating an extra amount of strain and increasing the strain rate to

break the protective film. Upon loading, at where the passivation film is ruptured, the austenite phase is preferentially attacked, and crack initiate at these sites. Moreover, most of the crack propagation stops at phase boundary. Austenite/ferrite interfaces act as microstructural barriers. Cracks propagate either along the phase boundary, or jump over relatively thinner layer of the ferrite phase, as shown in FIGURE 7.3. Thus, the crack lengths were associated with the width of the austenite phase. During the unloading process, passivation film is formed on the surface and the crack walls. The longer the exposure time is, the thicker the film is.
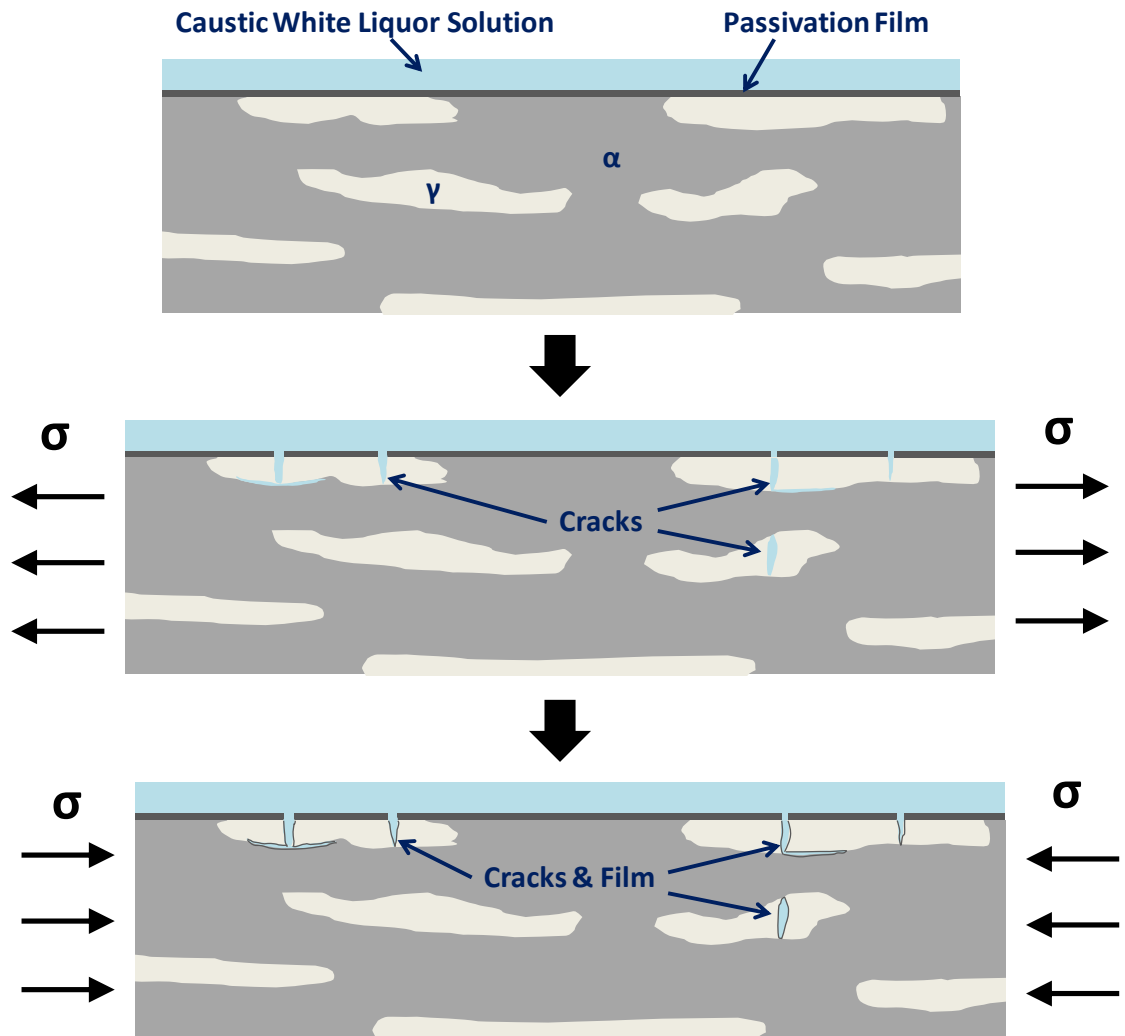
FIGURE 7.3 Schematic drawing illustrating the CF crack initiation of DSS 2205 in caustic WL environment.

Contrary to the results in acidic NaCl environment, the maximum stress level and stress ratio affect the crack initiation and propagation of DSS 2205 under low frequency cyclic loading in caustic WL in a different way. Maximum tress level does not show much

influence on crack initiation, and this may be attributed to the threshold stress is lowered by the cyclic loading and is smaller than the testing stress levels. At higher maximum stress levels, thick oxide film is formed on the crack walls, due to the longer exposure time to the corrosive environment as compared to lower stress levels. As for the stress ratio, intermediate stress ratios promote stress corrosion crack initiation. Because between the two competing processes, i.e., strain accumulation induced by low frequency cyclic loading and passivation film repair during unloading process, the strain accumulation and the corresponding increase in strain rate generated at intermediate stress ratios surpass the protective film repair. Whereas at lower frequency, the passive film repair dominates due to the prolonged unloading time, and at higher frequency, the strain accumulation caused by low frequency cyclic loading is small. These results for the first time illustrated the CF behavior of metallic materials at such low frequencies in this corrosive environment.

7.5 Effect of Cold-working on SCC of DSS 2205 under Monotonic and Ultra-low Frequency Cyclic Loading

Effect of prior cold-working on SCC and CF behavior of DSS 2205 in the two corrosive environments were also studied through SSRT and low frequency CF tests on cold-worked DSS 2205 material.

Results of Section 4.2.3 and Section 6.2.4 showed that cold-working significantly enhances the stress corrosion crack initiation of DSS 2205 under monotonic loading in

both acidic NaCl and caustic WL environments. This is reflected by an increase in the crack density and crack velocity in cold-worked DSS 2205, as compared to annealed material (TABLE 4.2). However, the crack initiation sites are the same for both cold-worked and annealed DSS 2205, namely, ferrite phase in acidic NaCl and austenite phase in caustic WL environment.

In contrary to the results under monotonic loading, cold-working largely retards the stress corrosion crack initiation of DSS 2205 under ultra-low frequency cyclic loading as compared to the annealed DSS 2205, in both acidic NaCl and caustic WL environments. This could be attributed to the limited strain accumulation induced by low frequency cyclic loading for cold-worked DSS 2205, because the dislocation density was saturated by prior cold-working, and the mobility of dislocation was decreased by prior cold-working. CF crack initiation of cold-worked DSS 2205 in both corrosive environments is determined by the local plasticity, rather than the applied stress or strain level. The local plasticity is usually associated with microstructural features such as pits or precipitates.

The harmful effects of cold-working on SCC have been extensively reported for various alloy/environment systems [143, 144], but there is hardly any satisfactory mechanism that is well established. However, there is no research has been done for the cold-working effect on stress corrosion crack initiation at such low frequencies.

CHAPTER 8 PRACTICAL IMPACT AND FUTURE WORK

8.1   Practical Impact and Recommendations

This work filled the void that existed in the knowledge base for the effects of ultra-low frequency ($\sim 10^{-5}$ Hz) cyclic loading on stress corrosion cracking (SCC) of duplex stainless steel (DSS) alloys in corrosive environments, as well as the effect that cold-working has on the stress corrosion crack initiation behavior of DSSs under monotonic and cyclic loading. The completion of this work led to an understanding of the stress corrosion crack initiation behavior of annealed and cold-worked DSS 2205 under low frequency cyclic loadings in two distinct corrosive environments: acidic NaCl and caustic WL solutions. Armed with this knowledge, researchers and engineers will be more confident when they are designing DSS structures exposed to either acidic or caustic solutions under ultra-low frequency cyclic loadings, as well as the DSS structures that are made of cold-worked materials. Furthermore, since the effect of ultra-low frequency cyclic loadings on SCC has never been studied for any metallic materials, the results of this research could also work as a guidance when structures under this type of loadings are designed using other types of steels.

In actual structures, applied stress levels or design stresses are below yield strength of the material, but the local stresses due to the presence of residual stresses caused by materials processing or welding, may be at or above yield strength of material. Under low frequency cyclic conditions, these areas may be susceptible to extensive strain accumulation and stress corrosion crack initiation. If the environmental factors are

favorable, the DSS structures under SCC susceptible conditions should stay below yield stresses when they are subjected to ultra-low frequency cyclic stresses. Crack initiations in DSS 2205 under these conditions could occur as early as after dozens of the peak cycles.

Under ultra-low frequency cyclic loading, cold-worked DSSs are recommended for the application in the acidic chloride and caustic WL environment, because the strain accumulation behavior of the cold-worked material has been significantly suppressed by the cold-working process. However, cold-working should also be employed with caution. Although cold-working could largely increase the corrosion fatigue (CF) resistance of DSS under ultra-low frequency/high cyclic stresses, but under monotonic loading or once the loading exceeds yielding, the SCC susceptibility may be significantly increased.

Besides, intermetallic precipitates should be strictly avoided in the manufacturing process of DSSs. Otherwise, they will act as CF crack initiation sites at relatively lower cyclic stresses.

Although the SCC susceptibility of DSSs under ultra-low frequency cyclic loading has been revealed in this study, they are still better structural steels than conventional austenitic and ferritic grades. Ferritic stainless steels (SS) with B.C.C. crystal structure could easily accumulate significant plastic strain under ultra-low frequency cyclic loading, and induces a large amount of plastic deformation. Austenitic SSs could not form stable passive film rapidly in caustic sulfide-containing solutions. On the other hand, for DSSs, there is always one phase resists to SCC in the two corrosive environments investigated

in this study. Moreover, the higher strength of DSSs usually leads to thinner thicknesses and less materials; hence DSSs are the more economical options in practical applications.

8.2   Recommendations for Future Work

Although this research work for the first time developed an understanding for the ultra-low frequency cyclic loading effect on stress corrosion crack initiation of DSS 2205 in corrosive environments, more work needs to be done to understand the mechanism of ultra-low frequency CF of DSS 2205.

- ❖ A series of low frequency CF testing should be performed in the acidic NaCl environment using DSS 2205 material without intermetallic precipitates. Since the CF crack initiation of DSS 2205 was significantly influenced by the intermetallic precipitates of the bar material (2205B), it would be useful to know what the crack initiation behavior will be for DSS 2205 in the absence of precipitates in acidic NaCl environment.

- ❖ DSS material properties, such as phase morphology, phase ratio, anisotropy and chemical composition, could be altered to investigate the effect of these parameters on the low frequency CF crack initiation behavior of DSSs. This will help us identify the controlling material parameter(s) in the CF crack initiation process of DSSs, and then help us understand the mechanism of this process.

- ❖ Although the frequencies of the CF tests in this study were altered through the changes of stress level and stress ratio under constant extension rate, the

frequencies of the cyclic stresses were all in the range of 10^{-5} Hz. Therefore, in order to obtain a deep understanding of frequency effect on low frequency CF behavior of DSSs, other frequency ranges could be studied as well, e.g., 10^{-4} Hz and 10^{-3} Hz.

❖ To illustrate the potentiodynamic polarization behavior of the two phases, micro-electrochemical polarization tests could be performed at individual phases of DSS 2205 in acidic NaCl environment at room temperature. The completion of this study would provide direct prove for preferential attack of ferrite phase in acidic chloride environment.

❖ Cyclic creep mechanism or cross-slip model could be confirmed by observation of the changes in crystal structures of the two phases using microstructural characterization technique, such as transmission electron microscopy.

APPENDIX A

MATLAB codes were written to fit the static creep data of the three materials using the creep model in EQUATION 4.1. The codes are saved in two separate m-files.

The first m-file is as follows:

```
clc;clear;


stress = 92824;   % Stress value in psi (changes in each
case)


load timestrain.txt
t = timestrain (:,1);
strain = timestrain (:,2);
[estimates, model] = datafitting_strain(t, strain);


% Plot the Results
plot(t, strain, '*')
hold on
[sse, FittedCurve] = model(estimates);
m = estimates (1);
n = estimates (2);
B = estimates (3);
t_more = (0:0.01:10)';
```

```matlab
FittedCurve_more =
(stress/B)^(1/(m+n))*((m+n)/n*t_more).^(n/(m+n));
plot(t_more, FittedCurve_more, 'r')


xlabel('Time (Hours)', 'FontWeight', 'Bold', 'FontSize', 12)
ylabel('Strain (%)', 'FontWeight', 'Bold', 'FontSize', 12)
title('Creep Curve Fitting','FontWeight', 'Bold',
'FontSize', 14);
legend('data', 'curve fit');
text(6, 0.3, 'm = ', 'FontWeight', 'Bold'); text(7, 0.3,
num2str(m), 'FontWeight', 'Bold');
text(6, 0.5, 'n = ', 'FontWeight', 'Bold');text(7, 0.5,
num2str(n), 'FontWeight', 'Bold');
text(6, 0.7, 'B = ', 'FontWeight', 'Bold');text(7, 0.7,
num2str(B), 'FontWeight', 'Bold');
hold off
```

The second m-file:

```matlab
function [estimates, model] = datafitting_strain(t, strain)
% Call fminsearch with a random starting point.


stress = 92824;
```

```matlab
start_point = [0.3;1/600;100000];    % Recommended values
were used

model = @empfun;

estimates = fminsearch(model, start_point);


% expfun accepts curve parameters as inputs, and outputs
sse,
% the sum of squares error for A * exp(-lambda * xdata) -
ydata,
% and the FittedCurve. FMINSEARCH only needs sse, but we
want to
% plot the FittedCurve at the end.


    function [sse, FittedCurve] = empfun(params)

        m = params(1);

        n = params(2);

        B = params(3);

        FittedCurve =
(stress/B)^(1/(m+n))*((m+n)/n*t).^(n/(m+n));

        ErrorVector = FittedCurve - strain;

        sse = sum(ErrorVector .^ 2);

    end
end
```

REFERENCES

1. Bennett, P.S.G. and J.T. Evans, *Creep stimulated by interrupted loading in copper and copper-1% cadmium.* Materials Science and Engineering, 1979. 38(2): p. 111-122.

2. Evans, J.T. and R.N. Parkins, *Creep Induced by Load Cycling in a C-Mn Steel.* Acta Metallurgica, 1976. 24(6): p. 511-515.

3. Feltner, C.E., *Dislocation arrangements in aluminum deformed by repeated tensile stresses.* Acta Metallurgica, 1963. 11(7): p. 817-828.

4. Shetty, D. and M. Meshii, *Plastic Deformation of Aluminum under Repeated Loading.* Metallurgical and Materials Transactions A, 1975. 6(2): p. 349-358.

5. Shetty, D.K. and M. Meshii, *Influence of carbon on the static and cyclic creep behaviors of alpha iron.* Materials Science and Engineering, 1978. 32(3): p. 283-291.

6. SCHAEFFLER, A.L., Metal Progress, 1960. 77(2).

7. Outokumpu, *http://www.outokumpu.com/applications/upload/pubs_102110190.pdf*.

8. *Practical Guidelines for the Fabrication of Duplex Stainless Steels*. 2009, International Molybdenum Association (IMOA): London, UK.

9. CHARLES, J., *Duplex Stainless Steels - a Review after DSS '07 held in Grado.* Steel Research International, 2008. 79(6).

10. Staehle, R.W., *Stress corrosion cracking and hydrogen embrittlement of iron base alloys*, R.W.S.e. al, Editor. 1977, NACE: Houston. p. 193.

11.   Jones, D.A., *Principles and Prevention of Corrosion*. 2005: Prentice-Hall Inc.

12.   ROBERGE, P.R. January 2005.

13.   Harwood, J.J., *Stress Corrosion Cracking and Embrittlement*, ed. W.D. Robertson. 1956: John Wiley & Sons. 1.

14.   Vermilyea, D.A., *A Film Rupture Model for Stress Corrosion Cracking*, in *Stress Corrosion Cracking and Hydrogen Embrittlement of Iron-Base Alloys*, R.W. Staehle, et al., Editors. 1977, NACE: Houston. p. 208-217.

15.   Staehle, R.W., *Predictions and Experimental Verification of the Slip Dissolution Model for Stress Corrosion Cracking of Low Strength Alloys*, in *Stress Corrosion Cracking and Hydrogen Embrittlement of Iron-Base Alloys*, R.W. Staehle, et al., Editors. 1977, NACE: Houston. p. 180-205.

16.   Scully, J.C., *Stress Corrosion Carck Propagation - A Constant Charge Criterion.* Corrosion Science, 1975. 15: p. 207-224.

17.   Lu, Z. and T. Shoji, *Unified Interpretation of Crack Growth Rates of Ni-base Alloys in LWR Environments.* J. Press. Vess. Technol., 2006. 128: p. 318-327.

18.   Ford, F.P. and P. Andresen, *Corrosion in Nuclear Systems: Environmentally Assisted Cracking in Light Water Reactors*, in *Corrosion Mechanisums in Theory and Practice*, P. Marcus, Editor. 2002, Marcel Dekker: New York. p. 605-642.

19.   Champion, F.A. in *Internal stresses in metals and alloys*. 1948: Institute of Metals.

20.   Logan, H.L., J. Res. Natl. Bur. Stand., 1952. 48.

21.   Parkins, R.N., British Corrosion Journal, 1979. 14: p. 5.

22.   Silcock, J.M. and P.R. Swann, *Environment-Sensitive Fracture of Engineering Materials*, Z.A. Foroulis, Editor. 1979, The Metallurgical Society. p. 133.

23.   Garverick, L., *Corrosion in the Petrochemical Industry*. 1994: ASM International.

24.   Sieradzki, K. and R.C. Newman, PHilosophical Magazine A, 1985. 51(1).

25.   Sieradzki, K. and R.C.Newman, Journal of Phys. Chem. Sol., 1987. 48(11): p. 1101-1113.

26.   Frohmberg, R.P., W.J. Barnett, and A.R. Troiano, Trans. ASM, 1955. 47: p. 892-925.

27.   Johnson, H.H., J.G. Morlet, and A.R. Troiano, Trans. TMS-AIME, 1958. 212: p. 526-536.

28.   Daniels, R.D., R.J. Quigg, and A.R. Troiano, Trans. ASM, 1959. 51: p. 843-860.

29.   Troiano, A.R., Corrosion, 1959. 15: p. 207t-212t.

30.   Troiano, A.R., Trans. ASM, 1960. 52: p. 54.

31.   Uhlig, H.H., in *Physical Metallurgy of Stress Corrosion Fracture*, T.N. Rhodin, Editor. 1959, Interscience: New York. p. 1.

32.   Raman, R.K.S. and W.H. Siew, *Role of nitrite addition in chloride stress corrosion cracking of a super duplex stainless steel.* Corrosion Science, 2010. 52(1): p. 113-117.

33.   Tsai, W.-T. and M.-S. Chen, *Stress corrosion cracking behavior of 2205 duplex stainless steel in concentrated NaCl solution.* Corrosion Science, 2000. 42(3): p. 545-559.

34. Tsai, W.-T. and S.-L. Chou, *Environmentally assisted cracking behavior of duplex stainless steel in concentrated sodium chloride solution.* Corrosion Science, 2000. 42(10): p. 1741-1762.

35. Tseng, C.-M. and W.-T. Tsai, *Environmentally assisted cracking behavior of single and dual phase stainless steels in hot chloride solutions.* Materials Chemistry and Physics, 2004. 84(1): p. 162-170.

36. Tseng, C.-M., W.-T. Tsai, and H.-Y. Liou, *Effect of nitrogen content on the environmentally-assisted cracking susceptibility of duplex stainless steels.* Metallurgical and Materials Transactions A, 2003. 34(1): p. 95-103.

37. Turnbull, A., P. Nicholson, and S. Zhou, *Chemistry of Concentrated Salts Formed by Evaporation of Formation Water and the Impact on Stress Corrosion Cracking of Duplex Stainless Steel.* Corrosion, 2007. 63(6).

38. Sanchez, J., et al., *Stress Corrosion Cracking Behavior of Duplex Stainless Steel by Slow Strain Rate Tests.* Corrosion, 2009. 65(2).

39. Vignal, V., et al., *Influence of long-term ageing in solution containing chloride ions on the passivity and the corrosion resistance of duplex stainless steels.* Corrosion Science, 2011. 53(3): p. 894-903.

40. Oltra, R., et al., *The stress corrosion cracking of duplex stainless steels in environments containing chlorides and H2S. Study of the ferrite phase behaviour.* Corrosion Science, 1987. 27(10-11): p. 1251-1269.

41. Perren, R.A., et al., *Corrosion resistance of super duplex stainless steels in chloride ion containing environments: investigations by means of a new*

microelectrochemical method: II. Influence of precipitates. **Corrosion Science, 2001. 43(4): p. 727-745.**

42. **Bernard, F., V.S. Rao, and H.-S. Kwon,** *A Study on the Repassivation Kinetics and SCC Behavior of Duplex Stainless Steel in Chloride Solution.* **Journal of The Electrochemical Society, 2005. 152(10): p. B415-B420.**

43. **Lo, I.H., et al.,** *Effect of electrolyte composition on the active-to-passive transition behavior of 2205 duplex stainless steel in H2SO4/HCl solutions.* **Corrosion Science, 2006. 48(3): p. 696-708.**

44. **Bhattacharya, A. and P. Singh,** *Stress Corrosion Cracking of Welded 2205 Duplex Stainless Steel in Sulfide-containing Caustic Solution.* **Journal of Failure Analysis and Prevention, 2007. 7(5): p. 371-377.**

45. **Singh, P.M., et al.,** *Stress Corrosion Cracking and Corrosion Fatigue Cracking of a Duplex Stainless Steel in White Water Environments.* **Corrosion, 2004. 60(9).**

46. **Rondelli, G., B. Vicentini, and E. Sivieri,** *Stress corrosion cracking of stainless steels in high temperature caustic solutions.* **Corrosion Science, 1997. 39(6): p. 1037-1049.**

47. **Bhattacharya, A. and P.M. Singh,** *Electrochemical behaviour of duplex stainless steels in caustic environment.* **Corrosion Science, 2011. 53(1): p. 71-81.**

48. **Bhattacharya, A. and P.M. Singh,** *Role of Microstructure on the Corrosion Susceptibility of UNS S32101 Duplex Stainless Steel.* **Corrosion, 2008. 64(6): p. 532-540.**

49. Honda, M., Y. Kobayashi, and A. Tamada, *Stress Corrosion Cracking of Stainless Alloys in Alkaline Sulfide Solutions.* Corrosion, 1992. 48(10): p. 822-829.

50. Bhattacharya, A. and P. Singh, *Effect of Heat Treatment on Corrosion and Stress Corrosion Cracking of S32205 Duplex Stainless Steel in Caustic Solution.* Metallurgical and Materials Transactions A, 2009. 40(6): p. 1388-1399.

51. El-Yazgi, A.A. and D. Hardie, *Stress corrosion cracking of duplex and super duplex stainless steels in sour environments.* Corrosion Science, 1998. 40(6): p. 909-930.

52. van Gelder, K., et al., *The stress corrosion cracking of duplex stainless steel in H2S/CO2/Cl- environments.* Corrosion Science, 1987. 27(10-11): p. 1271-1279.

53. de Moraes, F.D., F.L. Bastian, and J.A. Ponciano, *Influence of dynamic straining on hydrogen embrittlement of UNS-G41300 and UNS-S31803 steels in a low H2S concentration environment.* Corrosion Science, 2005. 47(6): p. 1325-1335.

54. Symniotis, E., *Galvanic Effects on the Active Dissolution of Duplex Stainless Steels.* Corrosion, 1990. 46(1): p. 2-12.

55. Fourie, J.W. and F.P.A. Robinson. in *International Conference on Stainless Steels*. 1991: ISIJ.

56. Leinoen, H.T. and P. Pohjanne, *Stress corrosion cracking susceptibility of duplex stainless steels and their welds in simulated cooking environments.*, in *NACE Corrosion*. 2006: San Diego, CA, USA.

57. Bhattacharya, A., *Stress corrosion cracking of duplex stainless steels in caustic solutions*, in *School of Materials Science and Engineering*. 2008, Georgia Institute of Technology: Atlanta, GA.

58. Wei, R.P. and G. Shim, *Fracture Mechanics and Corrosion Fatigue*, in *Corrosion Fatigue: Mechanics, Metallurgy, Electrochemistry, and Engineering, ASTM STP 801*, T.W. Crooker and B.N. Leis, Editors. 1983, American Society for Testing and Materials. p. 5-25.

59. Talbot, D.E.J. and J.D.R. Talbot, *Corrosion Science and Technology*. second ed. 2007: Taylor & Francis Group, LLC.

60. Duquette, D.J., *Chemo-Mechanical Interactions in Environmentally Induced Cracking.* Corrosion, 1990. 46(6): p. 434-443.

61. Hahn, H. and D. Duquette, *The effect of heat treatment on the fatigue and corrosion fatigue behavior of a CuNiCr alloy.* Metallurgical and Materials Transactions A, 1979. 10(10): p. 1453-1460.

62. Hahn, H.N. and D.J. Duquette, *The effect of surface dissolution on fatigue deformation and crack nucleation in copper and copper 8% aluminum single crystals.* Acta Metallurgica, 1978. 26(2): p. 279-287.

63. Uhlig, H.H. and R.W. Revie, *Corrosion and Corrosion Control -- An Introduction to Corrosion Science and Engineering*. 1985: John Wiley & Sons.

64. Laird, C. and D.J. Duquette, in *Corrosion Fatiuge, NACE-2*, O. Devereux, A. McEvily, and R. Staehle, Editors. 1971, NACE: Houston, TX. p. 88.

65.   Lo, I.H., Tsai, Wen-Ta, *Effect of selective dissolution on fatigue crack initiation in 2205 duplex stainless steel.* Corrosion Science, 2007. 49(4): p. 1847-1861.

66.   Lee, H.H. and H.H. Uhlig, Metallurgical Transactions, 1972. 3: p. 2949-2957.

67.   Gangloff, R.P., in *Environment Induced Cracking of Metals*, R.P. Gangloff and M.B. Ives, Editors. 1990, NACE: Houston, TX. p. 55-109.

68.   Wei, R.P. and R.P. Gangloff, in *Fracture Mechanics: Perspectives and Directions (Twentieth Symposium), ASTM STP 1020*, R.P. Wei and R.P. Gangloff, Editors. 1989, American Society for Testing and Materials: Philadelphia. p. 233-264.

69.   Holroyd, N.J.H. and D. Hardie, Corrosion Science, 1983. 23: p. 527-546.

70.   Ford, F.P., Journal of Pressure Vessel Technology, Transactions of ASME, 1988. 110: p. 113-128.

71.   Ford, F.P., in *Environment Induced Cracking of Metals*, R.P. Gangloff and M.B. Ives, Editors. 1990, NACE: Houston, TX. p. 139-166.

72.   Hudak, S.J., *Corrosion Fatigue Crack Growth: The Role of Crack-Tip Deformation and Film Formation Kinetics*. 1988, Lehigh University: Bethlehem, PA.

73.   Chung, H.M., et al., *Environmentally Assisted Cracking in Light Water Reactors*, in *U.S. Nuclear Regulatory Commission Report NUREG/CR-4667*. 1993.

74.   Stepanov, I.A. and A.G. Salomashenko, *The influence of loading conditions and medium on stress corrosion resistance of materials*, in *Corrosion Fatigue, Proceedings of the First USSR-UK Seminar on Corrosion Fatigue of Metlas heldin Lvov, USSR* R.N. Parkins and Y.M. Kolotyrkin, Editors. 19-22 May 1980.

75. **Johansson, J., M. Odén, and X.H. Zeng,** *Evolution of the residual stress state in a duplex stainless steel during loading.* **Acta Materialia, 1999. 47(9): p. 2669-2684.**

76. **Silberschmidt, V.V. and E. Werner,** *Analysis of thermal residual stresses in duplex-type materials.* **Computational Materials Science, 1999. 16(1-4): p. 39-52.**

77. **Dakhlaoui, R., et al.,** *Effect of residual stresses on individual phase mechanical properties of austeno-ferritic duplex stainless steel.* **Acta Materialia, 2006. 54(19): p. 5027-5039.**

78. **Davis, J.R., ed.** *Stainless Steels.* **1994, ASM International: Materials Park, OH.**

79. **Kamachi, K., et al.** *Thermal fatigue by impact heating and stresses of two phase stainless steels at elevated temperature.* **in** *Prog, in Science and Engineering of Composites.* **1982. Tokyo: ICCM-JV.**

80. **Mary, N., et al.,** *Finite-element and XRD methods for the determination of the residual surface stress field and the elastic–plastic behaviour of duplex steels.* **Philosophical Magazine, 2005. 85(12): p. 1227-1242.**

81. **Baczmański, A., C. Braham, and W. Seller,** *Microstresses in textured polycrystals studied by the multireflection diffraction method and self-consistent model.* **Philosophical Magazine, 2003. 83(28): p. 3225.**

82. **Tavares, S.S.M., et al.,** *Microstructural changes produced by plastic deformation in the UNS S31803 duplex stainless steel.* **Journal of Materials Processing Technology, 2006. 180(1-3): p. 318-322.**

83.   Dakhlaoui, R., C. Braham, and A. Baczmanski, *Mechanical properties of phases in austeno-ferritic duplex stainless steel--Surface stresses studied by X-ray diffraction.* Materials Science and Engineering: A, 2007. 444(1-2): p. 6-17.

84.   Hedström, P., et al., *Load partitioning between single bulk grains in a two-phase duplex stainless steel during tensile loading.* Acta Materialia, 2010. 58(2): p. 734-744.

85.   Van Acker, K., et al., *Neutron diffraction measurement of the residual stress in the cementite and ferrite phases of cold-drawn steel wires.* Acta Materialia, 1996. 44(10): p. 4039-4049.

86.   Pyzalla, A., *Stress and strain measurements: X-rays and neutrons.* Physica B: Condensed Matter, 2000. 276-278: p. 833-836.

87.   Jia, N., et al., *Micromechanical behavior and texture evolution of duplex stainless steel studied by neutron diffraction and self-consistent modeling.* Acta Materialia, 2008. 56(4): p. 782-793.

88.   Lillbacka, R., et al., *Cyclic stress–strain behavior and load sharing in duplex stainless steels: Aspects of modeling and experiments.* Acta Materialia, 2007. 55(16): p. 5359-5368.

89.   Mateo, A., et al., *Cyclic deformation behaviour of superduplex stainless steels.* Materials Science and Engineering A, 2001. 314(1-2): p. 176-185.

90.   Vignal, V., et al., *Influence of the passive film properties and residual stresses on the micro-electrochemical behavior of duplex stainless steels.* Electrochimica Acta, 2010. 55(23): p. 7118-7125.

91.   Navai, F., *Electrochemical behaviour of a type 302 stainless steel in a stress field.* Journal of Materials Science, 2000. 35(23): p. 5921-5925.

92.   Navaï, F. and O. Debbouz, *AES study of passive films formed on a type 316 austenitic stainless-steels in a stress field.* Journal of Materials Science, 1999. 34(5): p. 1073-1079.

93.   Kim, C.D. and B.E. Wilde, *A Review of the Constant Strain-Rate Stress Corrosion Cracking Test*, in *Stress Corrosion Cracking -- The Slow Strain-Rate Technique, ASTM STP 665*, G.M. Ugiansky and J.H. Payer, Editors. 1979, American Society for Testing and Materials. p. 97-112.

94.   Kennedy, A.J., *The Creep of Metals under Interrupted Stressing.* Proc. R. Soc. London, Ser. A, 1952. 213(1115).

95.   Kennedy, A.J., *Creep of Copper under Stress Pulses.* Nature, 1953. 171(4360): p. 927-928.

96.   Taleb, L. and G. Cailletaud, *Cyclic accumulation of the inelastic strain in the 304L SS under stress control at room temperature: Ratcheting or creep?* International Journal of Plasticity. In Press, Corrected Proof.

97.   Chai, H.-F. and C. Laird, *Mechanisms of cyclic softening and cyclic creep in low carbon steel.* Materials Science and Engineering, 1987. 93: p. 159-174.

98.   Lorenzo, F. and C. Laird, *Cyclic creep acceleration and retardation in polycrystalline copper tested at ambient temperature.* Acta Metallurgica, 1984. 32(5): p. 681-692.

99.   Wang, S.-H. and W. Chen, *A study on the pre-cyclic-load-induced burst of creep deformation of a pipeline steel under subsequent static load.* Materials Science and Engineering A, 2002. 325(1-2): p. 144-151.

100.   Shetty, D.K. 1973, Northwestern University.

101.   Chandler, H.D. and J.V. Bee, *Cell structures in polycrystalline copper undergoing cyclic creep at room temperature.* Acta Metallurgica, 1985. 33(6): p. 1121-1127.

102.   Yang, Z. and Z. Wang, *Effect of prestrain on cyclic creep behaviour of a high strength spring steel.* Materials Science and Engineering A, 1996. 210(1-2): p. 83-93.

103.   Feltner, C.E. and C. Laird, *Cyclic stress-strain response of F.C.C. metals and alloys--I Phenomenological experiments.* Acta Metallurgica, 1967. 15(10): p. 1621-1632.

104.   Curtze, S., et al., *Thermodynamic modeling of the stacking fault energy of austenitic steels.* Acta Materialia, 2011. 59(3): p. 1068-1076.

105.   Latanision, R. and A. Ruff, *The temperature dependence of stacking fault energy in Fe-Cr-Ni alloys.* Metallurgical and Materials Transactions B, 1971. 2(2): p. 505-509.

106.   Rémy, L., A. Pineau, and B. Thomas, *Temperature dependence of stacking fault energy in close-packed metals and alloys.* Materials Science and Engineering, 1978. 36(1): p. 47-63.

107.   Bradley, W., S. Nam, and D. Matlock, *Fatigue perturbed creep of pure aluminum at ambient temperatures.* Metallurgical and Materials Transactions A, 1976. 7(3): p. 425-430.

108.   Meshii, M., D.K. Shetty, and Y. Ochiai. in *Proceedings of the 1974 Symposium on Mechanical Behavior of Materials*. 1974. Tokyo, Japan.

109.   Oehlert, A. and A. Atrens, *Room temperature creep of high strength steels.* Acta Metallurgica et Materialia, 1994. 42(5): p. 1493-1508.

110.   Wearmouth, W.R., G.P. Dean, and R.N. Parkins, *Role of Stress in the Stress Corrosion Cracking of a Mg-Al Alloy.* Corrosion Science, 1973. 29(6).

111.   Smialowski, M. and J. Kostanski, *Creep and stress corrosion cracking of austenitic stainless steel in boiling 35% magnesium chloride solution.* Corrosion Science, 1979. 19(12): p. 1019-1029.

112.   JACQUES, S., J. PEULTIER, and P. SOULIGNAC. *Desalination Plants -- Why using Duplex Stainless Steels*. in *Duplex'07*. 2007. Grado, Italy.

113.   Arne Bergquist, L.W., *Duplex 2205: Experiences in Pulp & Paper Industry of a 30 Years Old Steel Grade.* 2010.

114.   Singh, P.M. and J. Mahmood, *TIP3 Project*. 2007.

115.   Armas, A.F., et al., *The influence of temperature on the cyclic behavior of aged and unaged super duplex stainless steels.* Materials Science and Engineering: A, 2008. 491(1-2): p. 434-439.

116.	Comer, A. and L. Looney, *Corrosion and fatigue characteristics of positively polarised Zeron 100 base & weld metal in synthetic seawater.* International Journal of Fatigue, 2006. 28(8): p. 826-834.

117.	Gironès, A., et al., *Influence of artificial seawater on the cyclic response of superduplex stainless steels.* International Journal of Fatigue, 2005. 27(2): p. 197-202.

118.	Gironès, A., et al., *Evaluation of fatigue damage for duplex stainless steels in aggressive environments by means of an electrochemical fatigue sensor (EFS).* International Journal of Fatigue, 2003. 25(9-11): p. 1189-1194.

119.	Llanes, L., et al., *Effect of testing atmosphere (air/in vacuo) on low cycle fatigue characteristics of a duplex stainless steel.* International Journal of Fatigue, 1999. 21(Supplement 1): p. 119-125.

120.	Makhlouf, K., et al., *Corrosion fatigue crack propagation of a duplex stainless steel X6 Cr Ni Mo Cu 25-6 in air and in artificial sea water.* International Journal of Fatigue, 2003. 25(2): p. 167-179.

121.	*ASM Metals Handbook*. 10 ed. Vol. 1.

122.	Leinonen, H.T. *Corrosion Resistance of Duplex Stainless Steel and its Welds in Modern Kraft Batch Cooking*. in *11th International Symposium on Corrosion in Pulp and Paper Industry*. June 2004.

123.	Leinonen, H.T. and P.Pohjanne, *Stress Corrosion Cracking Susceptibility of Duplex Stainless Steels and Their Welds in simulated Cooking Environments*, in *NACE Corrosion*. March 2006.

124.   Harrison, A., *Corrosion control offers paper mills a method of cost control.* Pulp & Paper, 2005. 68(10): p. 135-137.

125.   Bendall, K.C., *Duplex stainless steel in the pulp and paper industry.* Anti-Corrosion Methods and Material, 1997. 44(3): p. 170-173.

126.   Nibbering, J.J.W., *Behaviour of mild steel under very low frequency loading in sea water.* Corrosion Science, 1983. 23(6): p. 645-649, 651-662.

127.   Ladwein, T.L., et al., *The Chloride and Sulfide Stress Corrosion Cracking Behavior of the High Strength Superaustenitic Stainless Steel UNS S34565*, in *CORROSION 2000*. 2000, NACE International: Orlando, Fl.

128.   Tseng, C.-M., H.-Y. Liou, and W.-T. Tsai, *The influence of nitrogen content on corrosion fatigue crack growth behavior of duplex stainless steel.* Materials Science and Engineering: A, 2003. 344(1-2): p. 190-200.

129.   Zakroczmski, T. and R.N. Parkins, *A comparison of potentiodynamic, current decay and straining electrode experiments in assessing the stress corrosion cracking susceptibilities of low alloy ferritic steels.* Corrosion Science, 1980. 20(6): p. 723-727, 729-736.

130.   Enos, D.G. and L.L. Scribner, *The Potentiodynamic Polarization Scan*. 1997, Solartron Instruments.

131.   Rungta, R. and B.N. Leis, *Experimental Methods for the Evaluation of Environmentally Assisted Cracking of Steel in Caustic*, in *Environment-Sensitive Fracture: Evaluation and Comparison of Test Methods, ASTM STP 821*, S.W. Dea,

E.N. Pugh, and G.M. Ugiansky, Editors. 1984, American Society for Testing and Materials: Philadelphia. p. 341-367.

132.   Fang, Z. and R.W. Staehle, *Effects of the Valence of Sulfur on Passivation of Alloys 600, 690, and 800 at 25[degree]C and 95[degree]C.* Corrosion, 1999. 55(4): p. 355-379.

133.   Baek, J.S., et al., *Anodic film properties determined by EIS and their relationship with caustic stress corrosion cracking of Alloy 600.* Corrosion Science, 2003. 45(5): p. 983-994.

134.   Cottis, R.A. and R.C. Newman, *STRESS-CORROSION CRACKING RESISTANCE OF DUPLEX STAINELSS STEELS.* December 1993, UMIST, Corrosion and Protection Center.

135.   Huizinga, S., et al., *OFFSHORE 22CR DUPLEX STAINLESS STEEL CRACKING – FAILURE AND PREVENTION*, in *CORROSION 2005*. 2005, NACE International: Houston, TX.

136.   Hinds, G. and A. Turnbull, *Threshold Temperature for Stress Corrosion Cracking of Duplex Stainless Steel under Evaporative Seawater Conditions* CORROSION, 2008. 64(2): p. 101-106.

137.   Kwon, H.-S. and H.-S. Kim, *Investigation of stress corrosion susceptibility of duplex ([alpha] + [gamma]) stainless steel in a hot chloride solution.* Materials Science and Engineering: A, 1993. 172(1-2): p. 159-165.

138.   Uhlig, H.H., *Corrosion Handbook*. 1948: John Wiley & Sons Inc.

139. Foroulis, Z.A. and H.H. Uhlig, *Effect of Cold-Work on Corrosion of Iron and Steel in Hydrochloric Acid.* Journal of The Electrochemical Society, 1964. 111(5): p. 522-528.

140. Khatak, H.S., et al., *Evaluation of the stress corrosion resistance of cold rolled aisi type 316 stainless steel using constant load and slow strain rate tests.* Journal of Nuclear Materials. 168(1-2): p. 157-161.

141. García, C., et al., *Effects of prior cold work and sensitization heat treatment on chloride stress corrosion cracking in type 304 stainless steels.* Corrosion Science, 2001. 43(8): p. 1519-1539.

142. Liu, C.T. and J.K. Wu, *Influence of pH on the passivation behavior of 254SMO stainless steel in 3.5% NaCl solution.* Corrosion Science, 2007. 49(5): p. 2198-2209.

143. Bhattacharya, A., D. Yang, and P.M. Singh, *STRESS CORROSION CRACKING OF HEAT TREATED 2205 DUPLEX STAINLESS STEEL IN CAUSTIC SOLUTIONS*, in *CORROSION 2009*. 2009, NACE: Atlanta, GA.

144. Cigada, A., et al., *Stress corrosion cracking of cold-worked austenitic stainless steels.* Corrosion Science, 1982. 22(6): p. 559-578.

145. Uhlig, H.H., in *Physical Metallurgy of Stress Corrosion Fracture*, T. Rhodin, Editor. 1959, Interscience: New York. p. 1-17.

146. Rieder, E.S., M. Ashworth, and J.P.G. Farra, *The Effect of Nitrogen on the Stability of the Passive Film on a Zeron 100 Super Duplex Stainless Steel.* Electrochemical and Solid-State Letters, 1999. 2(1): p. 19-21.

147. Tsai, W.T., K.M. Tsai, and C.J. Lin, *SELECTIVE CORROSION IN DUPLEX STAINLESS STEEL*, in *Corrosion 2003*. 2003, NACE.

148. Fourie, J.W. and F.P.A. Robinson, in *Stainless Steels '91*. 1991, ISIJ: Tokyo. p. 111-117.

149. Park, C.-J., H.-S. Kwon, and M.M. Lohrengel, *Micro-electrochemical polarization study on 25% Cr duplex stainless steel.* Materials Science and Engineering A, 2004. 372(1-2): p. 180-185.

150. Sridhar, N. and J. Kolts, *Effects of Nitrogen on the Selective Dissolution of a Duplex Stainless Steel* CORROSION, 1987. 43(11): p. 646-651.

151. Lubahn, J.D. and R.P. Felgar, *Plasticity and Creep of Metals*. 1961: John Wiley & Sons, Inc.

152. Lubahn, J.D., *Creep-Tensile Relations at Low Temperatures*, in *Proc. ASTM*. 1952A. p. 905.

153. Skrzypek, J.J., ed. *Plasticity and Creep: Theory, Examples, and Problems*. ed. R.B. Hetnarski. 1993: Boca Raton, FL.

154. Boyer, H.E., ed. *Atlas of Creep and Stress-Rupture Curves*. 1988, ASM International.

155. Hult, J.A.H., *Creep in Engineering Structures*. 1966: Blaisdell Publishing Company.

156. Van Der Walt, C.M., *Slip in the B.C.C. Metals.* Acta Metallurgica, 1969. 17.

157.   Pook, L.P., *An Approach to Practical Load Histories for Fatigue Testing Relevent to Offshore Structures.* Journal of the Society of Environmental Engineers, 1978. 17(1): p. 22-35.

158.   Aertssen, G., *An estimate of shipping vibration stress based on slamming data of 4 ships.* Int. Shipbuilding Prog., February 1979. 26.

159.   Moskovitz, J.A. and R.M. Pelloux, *Corrosion-Fatigue Behavior of Austenitic-Ferritic Stainless Steels*, in *Corrosion-Fatigue Technology, ASTM STP 642*, H.L.C. Jr., T.W. Crooker, and D.W. Hoeppner, Editors. 1978, American Society for Testing and Materials. p. 133-154.

160.   Stevens, K.J., *Fatigue performance and microanalysis of heat treated 2205 duplex stainless steel.* Materials Science and Technology, 1999. 15(8): p. 903-908.

161.   Johansson, R.E. and H.L. Groth. *Corrosion Fatigue and Fatigue Data for Duplex Stainless Steels*. in *Duplex Stainless Steels '91*. 28-30 Octobre 1991.

162.   Perdomo, J.J. and P.M. Singh, *Corrosion Fatigue of a Heat Treated Duplex Stainless Steel in Paper Machine White Waters.* Corrosion Reviews, 2002. 20: p. 295-316.

163.   Tsai, W.T. and I.H. Lo, *Effects of Potential and Loading Frequency on Corrosion Fatigue Behavior of 2205 Duplex Stainless Steel* CORROSION, 2008. 64(2): p. 155-163.

164.   Laitinen, A. and H. Hänninen, *EFFECT OF NON-METALLIC INCLUSIONS ON CORROSION FATIGUE RESISTANCE OF P/M DUPLEX STAINLESS STEELS.* Fatigue & Fracture of Engineering Materials & Structures, 1996. 19(8): p. 1045-1053.

165.   Park, K. and H. Kwon, *Effects of Mn on the localized corrosion behavior of Fe-18Cr alloys.* Electrochimica Acta, 2010. 55(9): p. 3421-3427.

166.   Jang, Y.H., S.S. Kim, and J.H. Lee, *Effect of different Mn contents on tensile and corrosion behavior of CD4MCU cast duplex stainless steels.* Materials Science and Engineering A, 2005. 396(1-2): p. 302-310.

167.   Pardo, A., et al., *Pitting corrosion behaviour of austenitic stainless steels - combining effects of Mn and Mo additions.* Corrosion Science, 2008. 50(6): p. 1796-1806.

168.   Chasse, K., *A Study on the Mechanism of Stress Corrosion Cracking of Duplex Stainless Steels in Hot Alkaline-Sulfide Solution*, in *School of Materials Science and Technology*. 2011, Georgia Institute of Technology: Atlanta.

169.   Zielinski, W., et al., *Non-uniform distribution of plastic strain in duplex steel during TEM in situ deformation.* Materials Chemistry and Physics, 2003. 81: p. 476-479.